Progress in Materials Science 156 (2026) 101559

Contents lists available at ScienceDirect

Progress in Materials Science

journal homepage: www.elsevier.com/locate/pmatsci

Recent advances and remaining challenges of solid-state electrolytes for lithium batteries

Qing Qiao [a,1], Yingxue Li [a,1], Chang Song [a,1], Mariyam Niyaz [a,1], Yang Zhang [a,1], Songqiang Zhu [b], Tengfei Zhang [c,*], Weiming Teng [b,*], Hongge Pan [d], Xuebin Yu [a,*]

[a] Department of Materials Science, Fudan University, Shanghai 200433, China
[b] Zhejiang Provincial Energy Group Company Ltd., Hangzhou 310023, China
[c] College of Materials Science and Technology, Nanjing University of Aeronautics and Astronautics, Nanjing 210016, China
[d] Institute of Science and Technology for New Energy, Xi'an Technological University, Xi'an 710048, China

ARTICLE INFO

Keywords:
All-solid-state lithium batteries
Solid-state electrolytes
Fundamental research
Industrialization challenges
Academia-industry collaboration

ABSTRACT

All-solid-state lithium batteries (ASSLBs) have garnered significant attention as a next-generation energy storage technology, providing superior safety, enhanced stability, and high energy density. However, current research predominantly remains confined to laboratory-scale demonstrations, with limited translation into scalable technological solutions. Addressing this academia-industry disconnect is critical to unlocking the commercial viability of ASSLBs. This review focuses on bridging this gap by systematically analyzing advancements in solid-state electrolytes (SSEs)—the cornerstone of ASSLB technology. We delve into the structural characteristics, ion transport mechanisms, and performance metrics of various SSEs, alongside a comprehensive summary of modification strategies. Beyond theoretical advancements, we emphasize the practical implications of these strategies in addressing energy density limitations, interfacial instability, and safety concerns. A distinctive feature of this review lies in its multidimensional analysis of early-stage ASSLB industrialization hurdles, integrating perspectives from materials synthesis scalability, electrode processing innovations, device-level performance validation, advanced characterization methodologies, and application-specific requirements. This work not only maps current research frontiers but also establishes actionable guidelines for academia–industry collaboration, offering scientists a roadmap for targeted innovation and equipping enterprises with evidence-based insights to streamline technology development and commercialization strategies.

1. Introduction

Amidst the urgent global demand for clean energy and efficient energy storage, lithium-ion batteries (LIBs) have emerged as the dominant electrochemical storage technology, with widespread deployment across energy storage systems, portable electronic devices, and electric vehicles [1–3]. However, traditional organic liquid electrolytes (LEs) with excellent ionic conductivity have

* Corresponding authors.
E-mail address: yuxuebin@fudan.edu.cn (X. Yu).
[1] These authors contributed equally to this work.

https://doi.org/10.1016/j.pmatsci.2025.101559
Received 12 March 2025; Received in revised form 28 July 2025; Accepted 18 August 2025
Available online 30 August 2025

increasingly exposed fundamental limitations. Their inherent volatility and flammability compound safety risks while constraining LIB deployment in energy-intensive applications [4]. Furthermore, the relatively narrow electrochemical stability windows (ESWs) of LEs cannot accommodate high-voltage cathode materials, thereby limiting further energy density gains in LIBs [5,6].

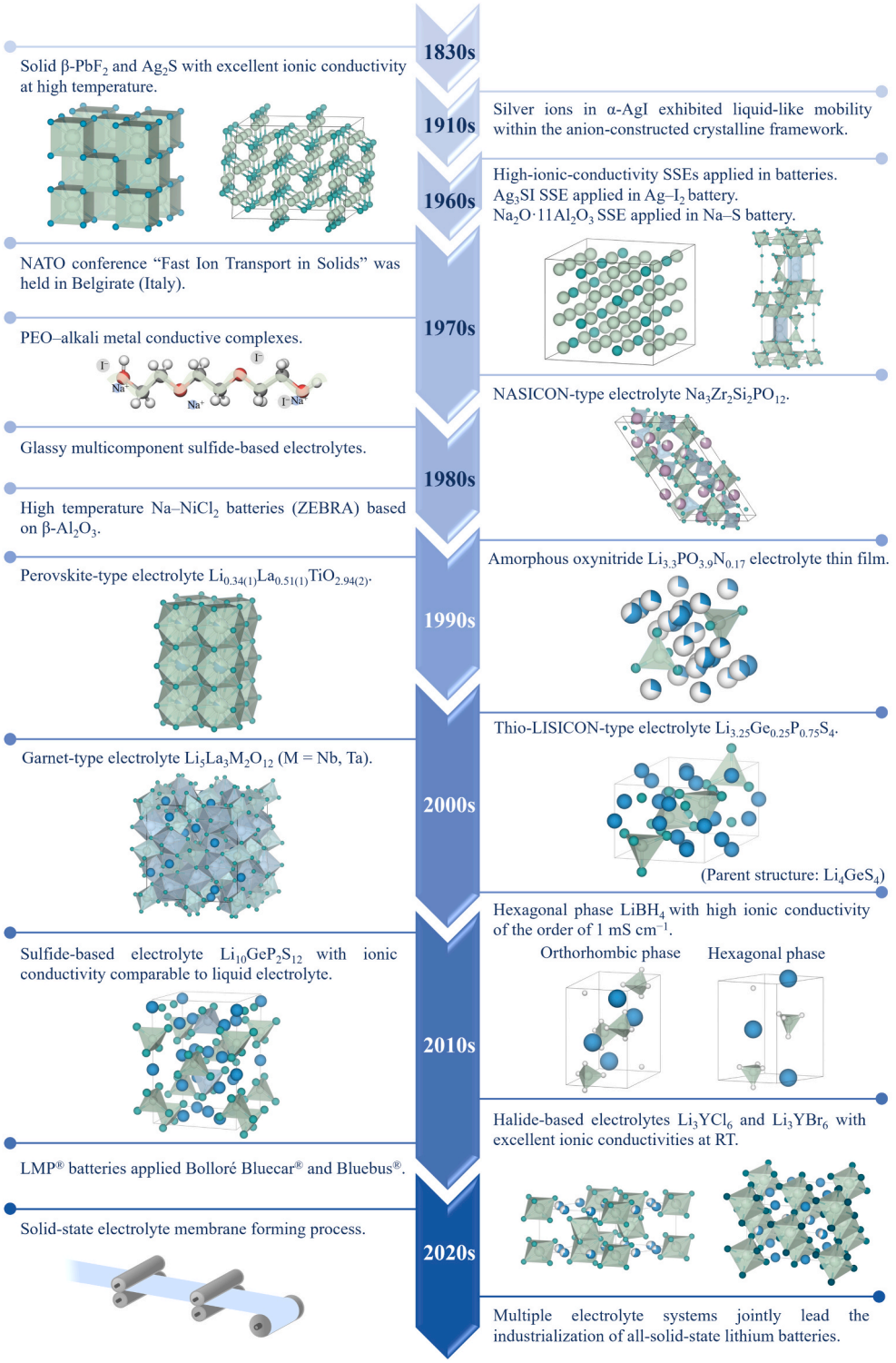

Fig. 1. Schematic diagram of the development history of SSEs. Reproduced with permission from ref. [19,20,22,23,25,26,28,32,36–42,62,67].

In response to these challenges, both the scientific and industrial communities are actively exploring novel electrolyte systems. Advances in materials science theory and machine learning have accelerated the development of solid-state electrolytes (SSEs), including inorganic solid-state electrolytes (ISEs) and solid-state polymer electrolytes (SPEs) [7,8]. And ISEs are primarily classified into four categories: oxide-based SSEs, sulfide-based SSEs, halide-based SSEs, and hydride-based SSEs. These materials exhibit multiple critical advantages for all-solid-state lithium batteries (ASSLBs), enabling higher voltage tolerance, superior energy density, and enhanced safety [9]. Specifically, the core advantages of SSEs manifest across five dimensions: (1) Intrinsic safety and stability. The solid-state form and non-flammability fundamentally eliminate risks of corrosion, combustion, and explosion induced by the leakage and thermal runaway of LEs [10]. SSEs also suppress the dissolution of cathode active materials, significantly improving the long-term cycling stability of lithium batteries. (2) Excellent mechanical strength. Most SSEs can physically block the growth and penetration of lithium dendrites to prevent short-circuit failures [11], while maintaining structural integrity under external impact, compression, puncture, and similar stresses. This is expected to enable safe compatibility with lithium metal anodes and enhance energy density significantly. (3) Wide ESWs. For example, oxide-based SSEs exhibit compatibility with high-voltage cathodes, while hydride-based SSEs can be paired with lithium metal anodes, enabling potential application in high-energy-density systems. (4) Broad temperature applicability. The majority of SSEs exhibit thermal stability, and their ionic conductivity increases with temperature, allowing operation in high-temperature (HT) environment. They also overcome the solidification or increased viscosity common to LEs at low temperature (LT), ensuring functionality in cold conditions [12]. (5) Structural simplification and flexibility. Solid-state design eliminates separators and liquid encapsulation, allowing single-housing multi-cell series configurations to optimize spatial layouts theoretically. As represented by SPEs, SSEs can be fabricated into flexible thin films, holding promise for flexible electronics and wearable devices.

Nonetheless, the commercial application of SSEs still faces numerous scientific and engineering challenges [13]. Firstly, while ionic conductivities comparable to those of LEs have been achieved in some sulfide-based SSEs, most SSEs exhibit unsatisfactory ionic conductivity at room temperature (RT) due to strong ionic interactions, crystal structure constraints, or sluggish polymer chain dynamics. Secondly, inadequate solid–solid contact at the electrode–electrolyte interface results in high interfacial impedance, hindering ion transport [14,15]. This issue is exacerbated by volume changes of cathodes during charge/discharge, leading to interfacial delamination, stress accumulation, and rapid capacity fading. Concurrently, parasitic interfacial reactions further increase impedance and accelerate degradation. Thirdly, scalable manufacturing remains economically challenging because of high raw material costs, complex synthesis protocols, stringent ambient controls, and low production yields [16]. To address these barriers, research has focused on innovative strategies including: structure modification (e.g., lattice doping), interfacial engineering (e.g., artificial solid-state electrolyte interphases (SEIs), buffer layers) [14], composite electrolyte design (e.g., organic–inorganic hybrids) [17,18], and novel manufacturing processes (e.g., thin-film deposition, three-dimensional (3D) printing). Parallelly, industry initiatives, exemplified by Toyota's pilot line for sulfide-based SSEs and QuantumScape's multilayer cell production, are advancing the industrial roadmap toward viable ASSLBs.

Fig. 1 provides a concise overview of the developmental trajectory of SSEs. The inception of solid-state ionic conductor research dates back to the 1830s, when Faraday discovered that solids β-PbF_2 and Ag_2S underwent a sudden transition from insulators to good conductors upon heating [19]. In contrast to conventional conductors relying on electron migration, the conductivity in β-PbF_2 and Ag_2S arises from the rapid mobility of fluoride ions and silver ions, respectively. In 1914, Tubandt et al. [20] proposed an innovative perspective that silver ions within α-AgI exhibit liquid-like mobility within the anion-constructed crystalline framework [21]. Until the 1960s, highly ion-conductive solid-state materials such as Ag_3SI and β-Al_2O_3 ($Na_2O{\cdot}11Al_2O_3$) were successively applied in Ag–I_2 batteries and HT Na–S batteries, marking the breakthrough in practical application of SSEs [22–24]. Subsequently, the landmark NATO conference on "Fast Ion Transport in Solids" held in Belgirate (Italy) in 1972 significantly accelerated the development of solid-state batteries (SSBs) [25]. In 1973, Wright et al. [26] discovered that complexes of poly(ethylene oxide) (PEO) and non-lithium alkali metal salts with low lattice energy (e.g., NaI, NaSCN, and KSCN) exhibited ionic conductivity at elevated temperature, thereby extending the research realm of solid-state ionics to organic polymers. Shortly thereafter, Armand et al. [27] pioneered the proposal of using ion-conducting polymer materials as electrolytes in solid-state LMBs, highlighting their potential for high energy density and sparking extensive academic research on SPEs. During the same period, Goodenough et al. [28] synthesized the sodium super ionic conductor (NASICON)-type SSEs $Na_{1+x}Zr_2Si_xP_{3-x}O_{12}$ via a HT solid-state reaction. This involved partial substitution of P^{5+} with Si^{4+} in $NaZr_2(PO_4)_3$, introducing more Na^+ sites [29]. Subsequently, Li^+-conducting counterparts were derived by substituting sodium ions with lithium ions [30,31]. Initial research on sulfide-based electrolytes emerged in the 1980s, focusing on glassy multicomponent systems such as Li_2S–GeS_2 [32], SiS_2–Li_2S [33], Li_2S–P_2S_5–LiI [34] with ionic conductivity of about 0.1 mS cm^{-1} at RT [35]. In 1986, Coetzer et al. [36] developed the Na–$NiCl_2$ batteries (ZEBRA) based on β-Al_2O_3 SSEs, offering high energy density and excellent safety, albeit requiring operation at 300–350 °C. Oxide-based SSEs are broadly categorized into crystalline and amorphous types. In 1992, Bates et al. [37] at Oak Ridge National Laboratory fabricated amorphous lithium phosphorus oxynitride (LiPON, $Li_{3.3}PO_{3.9}N_{0.17}$) electrolyte films by radio-frequency (RF) magnetron sputtering of a high-purity Li_3PO_4 target under high-purity nitrogen atmosphere. This material exhibited an ionic conductivity of 2.3×10^{-3} mS cm^{-1} at RT, an ESW of 5.5 V (vs. Li^+/Li), good thermal stability, and compatibility with cathodes (e.g., $LiCO_2$ (LCO), $LiMn_2O_4$) and anodes (e.g., lithium metal, lithium alloy), leading to its adoption in commercial thin-film LIBs. Thereafter, perovskite-type [38], garnet-type [39], and other crystalline oxide-based SSEs were discovered and continuously optimized. In 2001, Kanno et al. [40] discovered the first crystalline sulfide-based electrolyte, $Li_{3.25}Ge_{0.25}P_{0.75}S_4$, with an RT ionic conductivity of 2.2 mS cm^{-1}. $Li_{3.25}Ge_{0.25}P_{0.75}S_4$ and its analogues, derived from LISICON-type γ-Li_3PO_4, were named thio-LISICON. A major breakthrough followed in 2011 when Kanno et al. [41] developed the sulfide-based SSE $Li_{10}GeP_2S_{12}$ featuring a novel 3D framework structure. This material exhibited an exceptional Li^+ conductivity of 12 mS cm^{-1} at RT, rivaling or even exceeding that of organic LEs. This discovery sparked intensive research into sulfide-based SSEs, significantly accelerating their application in

ASSLBs. Notably, in 2007, metal hydrides originally developed for solid-state hydrogen storage made their debut as SSEs [42]. While the ionic conductivity of LT orthorhombic $LiBH_4$ is only 10^{-5} mS cm^{-1}, its HT hexagonal phase reached 1 mS cm^{-1} after phase transition. To overcome this limitation, researchers have demonstrated strategies for achieving ultrafast Li^+ conduction in hydride-based SSEs at low temperatures, even approaching RT, including anionic complexation [43], incorporation of secondary phases [44,45], interfacial modification [46–48], and composite formation [49–51]. Representative electrolyte materials include $Li_4(BH_4)_3I$ [52], $Li_2B_{12}H_{12}$ [53], $Li(NH_3)_nBH_4$ [54], $(LiBH_4)_x$·AB [44], and HT150-5PMMA [47]. Furthermore, recent studies highlight the potential of metal hydrides with high theoretical specific capacity as anodes in ASSLBs [55–61]. Despite early investigations on halide-based SSEs dating back to the 1930s, their low ionic conductivity hindered research progress. A major milestone was achieved in 2018 when Asano et al. [62] successfully synthesized Li_3YCl_6 and Li_3YBr_6 via high-energy ball milling and annealing processes. These materials demonstrated remarkably high ionic conductivities of 0.51 mS cm^{-1} and 1.7 mS cm^{-1} at RT, respectively, reigniting interest in halide-based SSEs. Subsequently, a series of novel halide-based SSEs including Li_3InCl_6 [63,64], Li_3ScCl_6 [65], and 2LiX-GaF_3 (X = Cl, Br, I) [66] emerged in rapid succession. In the 2010s, the global electric vehicle industry entered a phase of rapid development. Blue Solutions, a subsidiary of French Bolloré Group, identified this trend and leveraged its technological expertise to launch the lithium metal polymer (LMP®) batteries-equipped passenger vehicles, Bluecar® and Bluebus® [67]. Although LMP® batteries exhibited quantifiable deficits in energy density and charge/discharge rates compared to liquid-state LIBs, their SSE design philosophy established a foundational framework for subsequent SSB development. Since the onset of the 2020s, multiple processing technologies have been continuously developed to produce high-performance SSE thin-films suitable for commercial deployment. Industrial players have intensified efforts to advance the commercialization of ASSLBs, focusing primarily on three dominant technological pathways: oxide-based SSEs, sulfide-basedSSEs, and SPEs.

Given the rapid development and continuous iteration of SSE technology, this review comprehensively summarizes the latest

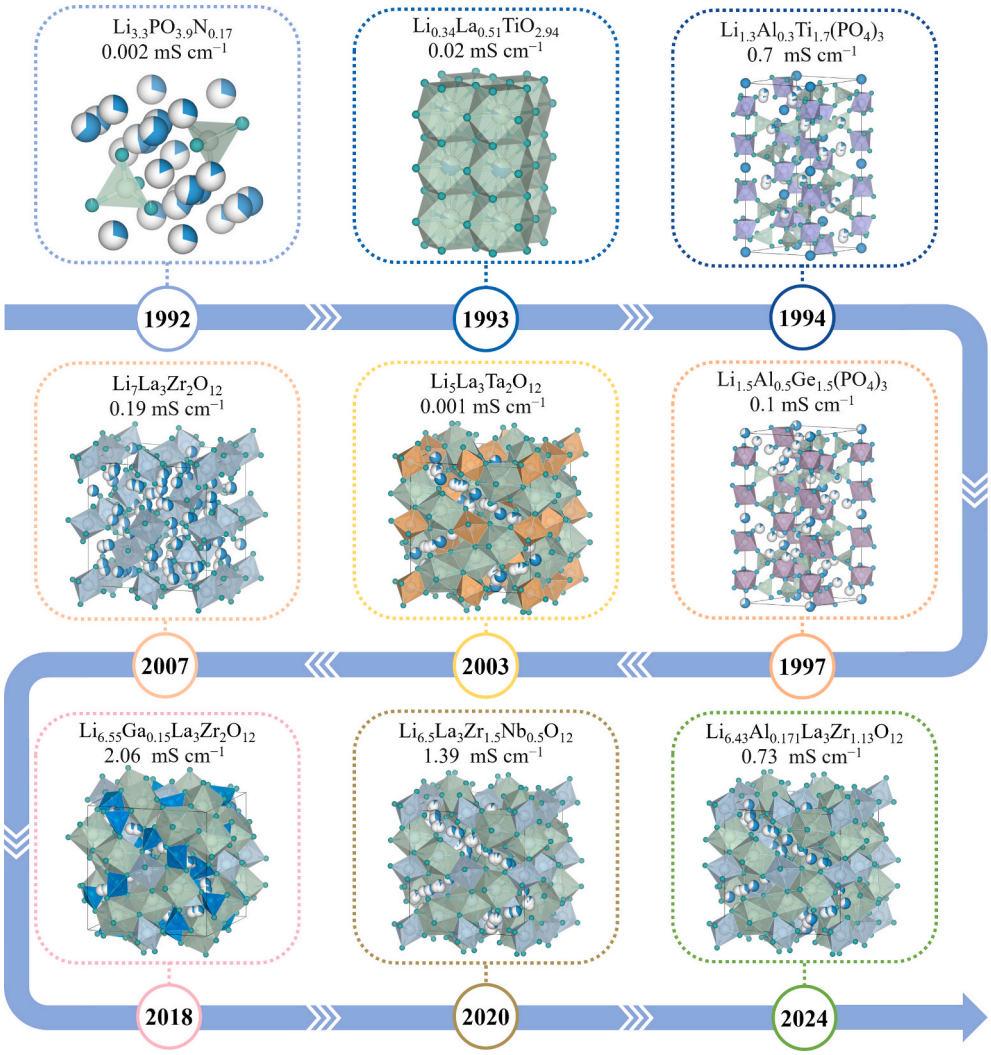

Fig. 2. A brief review of the development of oxide-based SSEs. Reproduced with permission from ref. [30,31,37–39,70,77,103,104].

scientific advances and industrialization trends in SSEs for ASSLBs. It aims to bridge the gap between academic progress and technological innovation, which is an underexplored nexus in prior studies. The review delves into the structural characteristics and ion conduction mechanisms across various SSEs, with a focus on analyzing performance-limiting factors and summarizing improvement strategies. These strategies, encompassing structural optimization, interface design, composite modification, and process refinements, collectively enhance key SSE properties (e.g., ionic conductivity, chemical/electrochemical stability, interfacial compatibility, and mechanical strength) and ultimately augment the energy density and cycle stability of ASSLBs. Furthermore, this review explores the technical hurdles encountered in the commercialization of ASSLBs and the research and development (R&D) trends of various enterprises, covering aspects such as material design, preparation techniques, cost control, and performance evaluation. This work furnishes scientific researchers with an exhaustive and state-of-the-art overview on prevalent research trends. Simultaneously, it delivers robust scientific foundations and actionable insights for industry stakeholders to formulate strategic roadmaps, accelerate technological innovation, and optimize product development. Consequently, this comprehensive review significantly contributes to expediting the development and widespread deployment of ASSLB technology, driving transformative progress in electrochemical energy storage systems.

2. Oxide-based solid-state electrolytes

Oxide-based SSEs exhibit high mechanical strength, moderate ionic conductivity, broad ESWs, and exceptional thermal/chemical stability, showing promise for energy storage. However, their practical adoption faces persistent challenges. Firstly, the cumulative effects of grain boundary resistance and interfacial impedance within oxide-based SSEs typically hinder ion migration, reducing effective ionic conductivity below 0.01 mS cm^{-1}. This necessitates advanced sintering protocols and interfacial engineering strategies, such as rapid sintering or grain boundary modification through doping or secondary phase introduction. Secondly, the inherent mechanical brittleness of rigid oxide ceramics and poor interfacial contact with electrodes induce structural instability during cycling, exacerbating interfacial resistance and triggering dendrite nucleation at localized current hotspots under high current densities. These

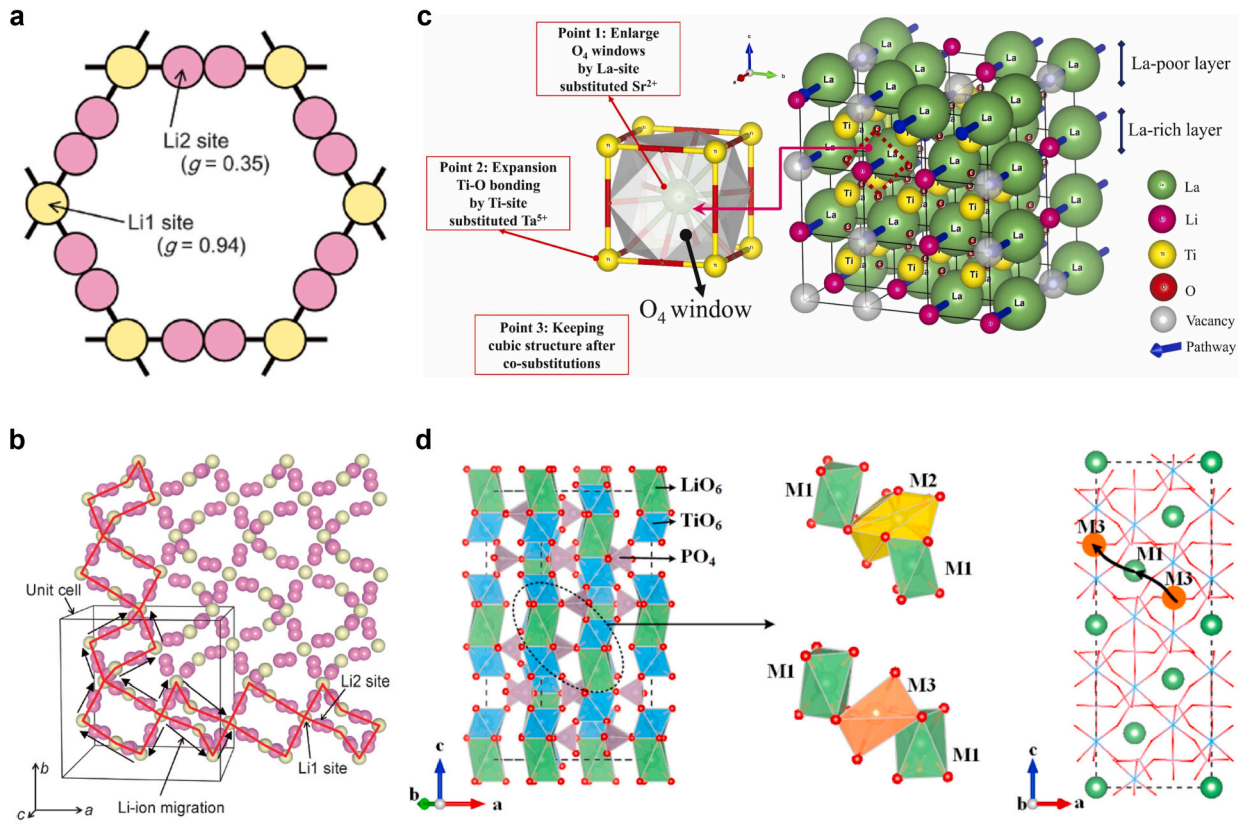

Fig. 3. (a) The loop structures formed by Li atomic arrangement in cubic $Li_7La_3Zr_2O_{12}$. (b) 3D network structure of the Li atomic arrangement in cubic $Li_7La_3Zr_2O_{12}$. Reproduced with permission from ref. [72]. Copyright 2021, Chemistry Letters. (c) Crystal structure of Perovskite-type $Li_{3x}La_{2/3-x}TiO_3$ ($0.04 < x < 0.16$). Reproduced with permission from ref. [84]. Copyright 2024, Journal of Alloys and Compounds. (d) Crystal structure of $LiTi_2(PO_4)_3$, with Li atoms occupying the M1, M2, and M3 sites, and the migration pathway in $LiTi_2(PO_4)_3$. Reproduced with permission from ref. [93]. Copyright 2018, Energy Storage Materials.

limitations are expected to be mitigated by constructing composite architectures that integrate oxide matrices with polymer interlayers or ductile inorganic phases. Furthermore, the manufacturing complexities associated with HT processing and limited scalability of thin-film deposition techniques have intensified interfacial challenges, spurring significant research into LT synthesis methods and composite solid-state electrolyte (CSE) designs. Addressing these multiscale limitations, which span atomic-scale defect chemistry optimization to macroscale mechanical reinforcement, remains pivotal to harnessing the inherent stability advantages of oxide-based SSEs while overcoming their kinetic and interfacial bottlenecks toward viable SSB integration. This chapter systematically discusses these strategies to advance their practical implementation.

2.1. Development based on ionic conductivity

Oxide-based SSEs are generally classified into four primary categories based on crystalline structures: garnet-type, perovskite-type, NASICON-type, and LISICON-type. The representative breakthroughs and research milestones are illustrated in Fig. 2. These materials demonstrate remarkable thermal stability, moderate bulk Li^+ conductivity (0.01–1 mS cm^{-1} at 25 °C), and exceptional mechanical strength (Young's modulus > 150 GPa) [68]. Among these, garnet-type SSEs have attracted particular research attention since Weppner et al. [39] reported the first garnet-like-structured fast lithium-ion conductor $Li_5La_3M_2O_{12}$ (M = Nb, Ta) in 2003 [69]. The general formula of garnet-type SSEs is predominantly $A_2B_3(XO_4)_3$, where A, B, and X occupy the sites of dodecahedron, octahedron, and tetrahedron, respectively. Subsequently, they further prepared zirconium-containing cubic $Li_7La_3Zr_2O_{12}$ (c-LLZO) with a larger cubic lattice constant, higher lithium-ion concentration, and higher densification, achieving high lithium-ion conductivity (0.3 mS cm^{-1} at 25 °C), low activation energy, and good thermal/chemical stability [70]. In 2009, Awaka et al. [71] synthesized the tetragonal-type LLZO (t-LLZO) via solid-state method and sintering at 980 °C. The principal distinctions between t-LLZO and c-LLZO lie in the arrangement of Li atoms and the occupancy of Li sites. The basic structural unit of Li atomic arrangement in c-LLZO is a ring composed of Li1 and Li2 sites (Fig. 3a). These rings interconnect via Li1 sites acting as bridging nodes, forming a 3D network of Li^+ migration pathways throughout the structure, as illustrated in Fig. 3b [72]. Notably, phase transition simulation has revealed the thermodynamic instability of c-LLZO at RT, with spontaneous transformation to t-LLZO with low conductivity [73,74]. This drives intensive research into stabilization strategies, particularly through element doping. The comparative study by Geiger et al. [75] demonstrated that Al contamination from Al-containing ceramic crucibles effectively stabilized c-LLZO, whereas those sintered in Pt crucibles required higher temperatures for phase transformation. In a similar investigation into the impact of crucible materials on electrolyte performance, Liu et al. [76] arrived at slightly different conclusions. Their study reported that 0.25Al-LLZO pellets sintered in platinum crucibles exhibited a higher relative density (96 %), larger grains, and fewer grain boundaries. The material demonstrated an ionic conductivity of 0.448 mS cm^{-1}, which remained stable at 0.36 mS cm^{-1} after 3 months of exposure to air, highlighting its superior environmental stability. In contrast, 0.25Al-LLZO prepared in alumina crucibles displayed lower ionic conductivity and degraded air stability. In addition to the Al, the doping of elements such as Ga [77], Nb [78], Ta [79], and Fe [80] also brings about significant modification effects. Specifically, the RT ionic conductivity of self-textured $Li_{6.55}Ga_{0.15}La_3Zr_2O_{12}$ reaches 2.06 mS cm^{-1}. The high-entropy strategy, through simultaneous doping with multiple elements, has been extensively employed to engineer lattice disorder in garnet-type SSEs. This approach not only stabilizes the cubic phase but also creates percolative pathways for fast lithium-ion conduction. For instance, Jung et al. [81] synthesized stable cubic-phase garnet-type SSEs ($Li_7La_3M_2O_{12}$, M = Zr, Hf, Sn, Sc, Ta, or Nb) by incorporating various dopants, achieving ionic conductivity up to 0.27 mS cm^{-1}. Similarly, Liang et al. [82] designed a cubic-phase fast lithium-ion conductor $Li_7(La,Nd,Sr)_3(Zr,Ta)_2O_{12}$ with an ionic conductivity reaching 0.626 mS cm^{-1}. Crucially, both electrolytes maintain an absence of lithium vacancies, thereby ensuring stability against lithium metal anodes.

Perovskite-type SSEs are characterized by their high bulk Li^+ conductivity of 0.1–1 mS cm^{-1} at ambient conditions, though their overall ionic conductivity is compromised by high grain boundary resistance [83]. ABO_3-structure $Li_{3x}La_{2/3-x}TiO_3$ (LLTO, $0.04 < x < 0.16$) has Li, La (La-rich and La-poor layers) vacancies on the A-sites, and Ti ions on the B-sites coordinated with the oxygen octahedra (Fig. 3c) [84]. Maximum grain conductivity reached 0.143 mS cm^{-1} when x = 0.11, where lithium ions and vacancies attain an optimal ratio in the LLTO framework [85]. Solid-phase reaction and sol–gel processing are the most prevalent synthetic techniques for LLTO, where the parameters (e.g., sintering temperature and duration) significantly influence the properties of resulting materials. For instance, when preparing LLTO by sintering $LiCO_3$, La_2O_3, and TiO_2 precursor powder at 1100–1350 °C, the lithium loss caused by Li_2O volatilization can be alleviated through strategies such as excess incorporation of lithium precursors and precise control of calcination temperature. The diversity of crystal structures further dictates ionic conductivity, where the cubic phase (space group: $Pm\bar{3}m$) exhibits high ionic conductivity due to disordered Li^+ and La^{3+} distribution at A-sites but requires sintering temperatures above 1150 °C for stability. Conversely, the tetragonal phase (space group: P4/*mmm*) obtained via slow cooling or LT annealing demonstrates reduced ionic mobility due to the partial ordering of Li^+ and La^{3+} along the A-sites, and distortion of the [TiO_6] octahedra, which creates bottlenecks around A-site cations [86,87]. Advanced doping strategies address these limitations, as demonstrated by Chen et al. [88]. A 280 % conductivity enhancement (0.3 mS cm^{-1}) in the $Li_{0.33}La_{0.54}Sr_{0.03}Ti_{0.9625}Ta_{0.03}O_3$ electrolyte was achieved through Ta–Sr co-doping, which synergistically optimized structural symmetry, Li^+ concentration, grain boundaries, domain boundaries, and lattice defects. Beyond structural considerations, LLTO exhibits high lithium-ion transference number (t_{Li+} = 0.5–0.9), exceptional air stability, excellent thermal stability, and high oxidation stability, enabling compatibility with high-voltage cathodes [86,89,90]. However, due to the presence of high-valent Ti^{4+} ions, LLTO is incompatible with lithium metal anodes.

Since Hagman et al. [91] first reported $NaM_2(PO_4)_3$ (M = Ge, Ti, Zr) in 1968, Goodenough et al. [28] synthesized NASICON $Na_{1+x}Zr_2Si_xP_{3-x}O_{12}$ via HT solid-state reaction in 1976, partially replacing P atoms with Si atoms and introducing more Na atoms. The

NASICON-type SSEs feature 3D interconnected channels formed by MO_6 octahedra and PO_4 tetrahedra through corner-sharing (Fig. 3d), which become lithium-ion conductors when Na^+ is replaced by Li^+ [92,93]. The general formula of NASICON-type lithium-ion conductor is $Li_{1+x}A_xB_{2-x}(PO_4)_3$ (A = Al, La, In, Ga or Cr; B = Ti, Ge, or Sn), and the most representative are

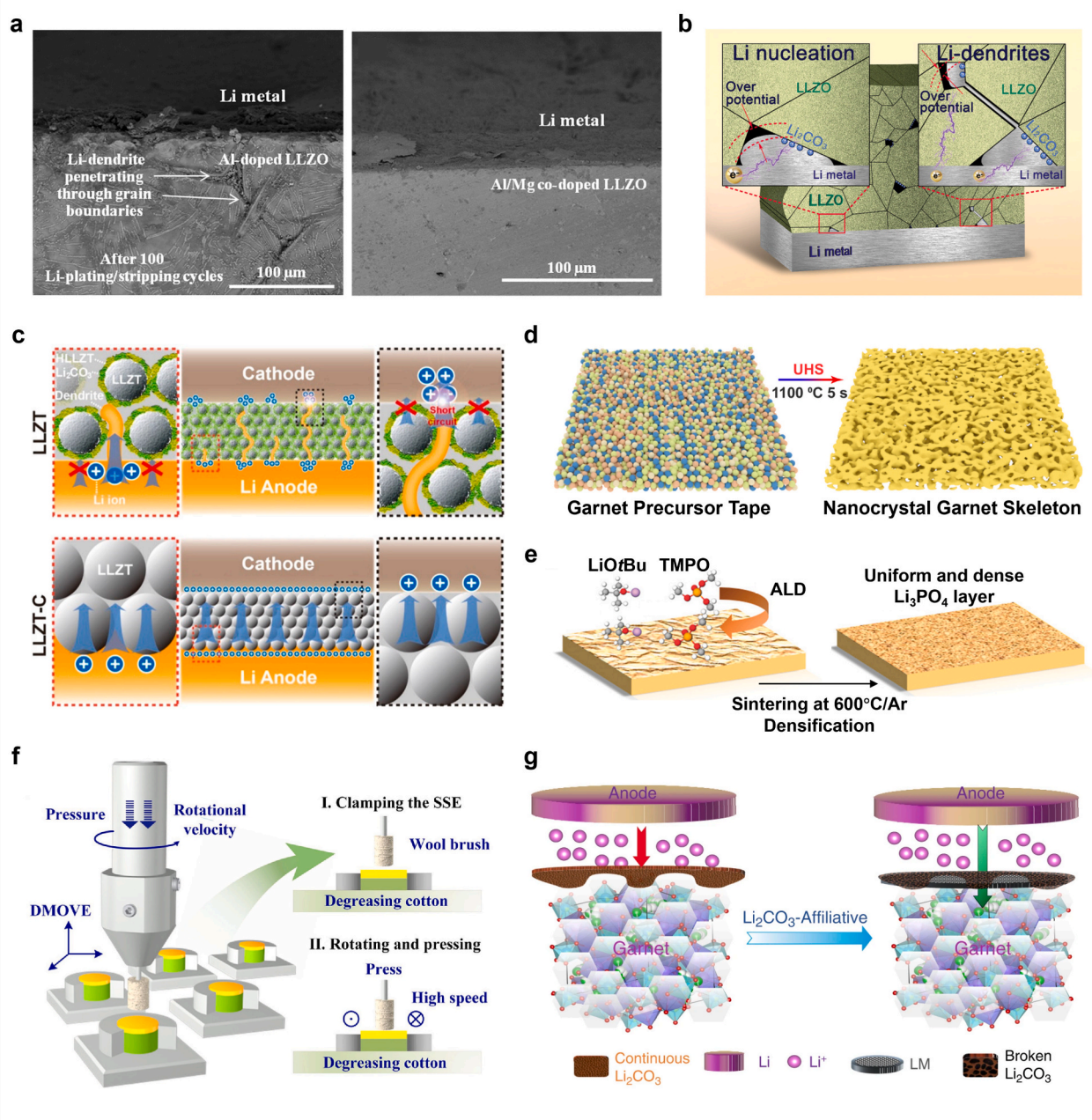

Fig. 4. (a) Cross-section SEM micrographs of Li/Al-doped LLZO (left) and Li/Al/Mg-co-doped LLZO (right) interfaces after 100 cycles (0.1 mA cm^{-2}). Reproduced with permission from ref. [105]. Copyright 2020, ACS Applied Materials & Interfaces. (b) Schematic illustration of lithium nucleation and lithium dendrites growth. Reproduced with permission from ref. [106]. Copyright 2020, Advanced Functional Materials. (c) Schematics of ion transport at the interface between garnet-type LLZT SSE and electrode before and after carbon treatment. Reproduced with permission from ref. [107]. Copyright 2018, Journal of the American Chemical Society. (d) Schematic representation of 3D porous LLZTO skeletons fabricated by UHS. Reproduced with permission from ref. [108]. Copyright 2024, Energy Storage Materials. (e) Schematic diagram of the process for fabricating a dense Li_3PO_4 layer via ALD and sintering. Reproduced with permission from ref. [109]. Copyright 2020, Advanced Materials. (f) Schematic of high-speed mechanical polishing approach for ultraclean LLZTO SSE. Reproduced with permission from ref. [110]. Copyright 2022, Chemical Engineering Journal. (g) Schematic diagram of Li^+ transport at the interface across continuous Li_2CO_3 layers or broken Li_2CO_3 network treated with LM. Reproduced with permission from ref. [111]. Copyright 2020, Nature Communications.

$Li_{1+x}Al_xTi_{2-x}(PO_4)_3$ (LATP) and $Li_{1+x}Al_xGe_{2-x}(PO_4)_3$ (LAGP), with ionic conductivity of 0.1–1 mS cm^{-1} at 25 °C. The common synthesis methods of LATP and LAGP SSEs include solid-state methods (e.g., solid-phase reaction, melt quenching, rapid sintering) and liquid-based methods (e.g., sol–gel, co-precipitation, melt- or evaporation-induced self-assembly) [94]. Among these methods, solid-phase reaction offers the broadest applicability, but faces challenges such as Li loss and potential formation of secondary phases during HT processing, which adversely affect Li^+ conduction. In addition, thermal treatment parameters such as temperature and duration also affect the unit cell volume, phase purity, relative density, and ionic conductivity of NASICON-type SSEs. To mitigate lithium loss, advanced sintering techniques have been developed, including microwave-assisted sintering, spark plasma sintering, and ultrafast sintering. For instance, Liu et al. [95] developed a microwave-assisted ultrafast sintering technique (MAUST) to sinter various ceramic electrolytes in air using a household microwave oven. For the MAUST-LLZTO (Ta-doped LLZO), MAUST-LATP, and MAUST-NZSP pellets sintered for 25 s, the total ionic conductivities were about 0.60, 0.10 and 0.19 mS cm^{-1} at RT, values higher than counterparts sintered by conventional method. Beyond processing optimization, element doping approach plays an equally pivotal role. The incorporation of Al into LATP and LAGP achieves charge balance through lithium modulation, enhancing charge carrier concentration, while the smaller Al^{3+} cations simultaneously promote electrolyte densification, creating interstitial gaps optimized for Li^+ migration and reducing grain boundary resistance, thereby improving overall ionic conductivity. However, compositional control is paramount, as low Al content ($x < 0.3$) introduces heterogeneous phases and excess doping ($x > 0.5$) promotes secondary phase formation, both elevating interfacial resistances. Systematic studies confirm an optimal Al content range of $x = 0.3$–0.5 for maximizing ionic conductivity [96]. Beyond conductivity, LATP and LAGP exhibit exceptional environmental stability and high-voltage tolerance (up to 5 V vs. Li^+/Li), rendering them suitable for high-voltage cathodes. However, similar to LLTO, LATP also demonstrates poor compatibility with Li-metal anodes, while LAGP faces scalability challenges due to its dependence on expensive germanium.

Pioneered by Hong et al. [97] in 1978, the LISICON-type electrolyte $Li_{14}Zn(GeO_4)_4$ demonstrated a resistivity of 8 Ω·cm at 300 °C and a RT ionic conductivity limited to 10^{-4} mS cm^{-1}. Subsequently, LISICON-type SSEs with enhanced ionic conductivity were progressively improved [98,99], including the Li_4GeO_4–$LiVO_4$ [100], $Li_{2+2x}Zn_{1-x}GeO_4$ [101], and Li_2O–V_2O_5–SiO_2 [102] systems. LISICON-type SSEs feature a structure analogous to γ-Li_3PO_4, where Li^+ diffusion is confined to vacancy mechanisms for conductivity enhancement. Nevertheless, they exhibit extreme instability in air, undergoing detrimental reactions. By contrast, their sulfur-substituted derivatives (thio-LISICON) achieve high ionic conductivity on the order of 10 mS cm^{-1} at RT, though with inherent safety risks, which will be detailed in the sulfide-based SSE section.

Beyond the aforementioned four types of crystalline oxide-based SSEs, amorphous oxide-based SSEs represented by LiPON have also been widely explored. Although LiPON exhibits relatively lower ionic conductivity (typically 10^{-5}–10^{-3} mS cm^{-1}), it demonstrates superior chemical stability and a wide ESW. These characteristics make it particularly tailored for thin-film batteries, thereby presenting promising application prospects in electronic devices with lower power requirements. Overall, oxide-based SSEs generally exhibit ionic conductivities in the range of 0.01 to 1 mS cm^{-1} (except for LiPON), which can be improved by element doping, sintering processes optimizing, and additive engineering. Practical implementation of oxide-based SSEs faces multifaceted challenges, particularly interfacial incompatibilities. Insufficient physical contact between oxide-based electrolytes and electrodes induces high interfacial resistance, leading to incomplete electrochemical reactions during cycling and consequent performance degradation. Stability concerns further complicate applications, exemplified by the susceptibility of LLZO to atmospheric H_2O/CO_2 forming detrimental lithium carbonate layers, and the reduction of Ti^{4+} in LATP when paired with lithium metal anodes. These stability limitations, encompassing both chemical and electrochemical degradation mechanisms, underscore the necessity for systematic investigations into failure modes and mitigation strategies, which will be comprehensively analyzed in subsequent sections to guide the development of robust oxide-based SSEs.

2.2. Chemical and electrochemical stability

The intense Coulomb repulsion between lithium ions occupying tetrahedral and octahedral sites in garnet-type electrolytes exacerbates their reactivity with humid air, where H^+/Li^+ exchange at the garnet-moisture interface generates a Li^+-insulating Li_2CO_3 surface layer. This parasitic layer not only impedes interfacial wetting between LLZO and metallic lithium but also induces uneven current distribution, ultimately compromising electrochemical performance [107]. To address these challenges, various strategies have been proposed, including element doping [112], air isolation [106], and grain boundary control [113], to prevent or reduce the formation of Li_2CO_3 and improve the air stability of LLZO. Hwang et al. [114] reported that the dual doping of Ga and Nb elements into LLZO reduced the formation of LiOH and Li_2CO_3 impurity phases, which could be subsequently removed via vacuum drying, thereby restoring the surface morphology. Mukhopadhyay et al. [105] demonstrated that Al/Mg co-doped LLZO conferred superior mechanical robustness compared to single Al-doped LLZO, effectively eliminating interfacial cracks and impurities at Li/LLZO interfaces. The comparative cross-sectional SEM images after 100 cycles at 0.1 mA cm^{-2} are presented in Fig. 4a. Despite these advances, the interfacial instability will be further compounded by electron injection from the anode during cycling, where decomposed Li_2CO_3 layers and intrinsic defects in LLZO generate localized overpotentials. These electrical inhomogeneities promote lithium nucleation within porous structures and dendritic propagation along grain boundaries (Fig. 4b) [106]. An innovative solution, i.e., Ti-doped LLZO ($Li_{56}La_{24}Zr_{15}TiO_{96}$) interlayer, has been developed to address this challenge. Zhou et al. [106] demonstrated that *in situ* formation of a mixed electronic–ionic interphase at the electrolyte/lithium interface during operation homogenized electric field distribution, blocked electron penetration, and maintained ionic transport. Unfortunately, element doping strategies often increase production costs and reduce material compatibility, which may affect the long-term stability of electrolytes and overall battery performance. In this regard, forming a protective barrier via chemical polymerization or chemical vapor deposition techniques to isolate the LLZO surface from ambient air has been proposed as a potential solution. Manuel et al. [115] employed a gas-phase fluorination method to thermally

decompose poly(vinylidene fluoride) (PVDF) at elevated temperatures, generating low concentrations of HF. The HF reacted with Li on the LLZTO surface to form a protective LiF layer. However, during furnace insertion, the LLZTO film was exposed to ambient air, resulting in unintended trace amounts of Li_2CO_3 and LiOH. In response to this issue, Guo et al. [116] introduced dopamine, which undergoes *in situ* polymerization on the LLZO surface initiated by alkaline Li_2CO_3, forming a lipophilic polydopamine barrier layer. This modification enables LLZO to maintain atmospheric stability for 20 days. Given the dual challenges of moisture susceptibility in grain boundary regions with high interfacial energy and their propensity to act as preferential pathways for dendrite propagation [117], grain boundary engineering has become a critical frontier. Duan et al. [118] engineered cubic garnet-type LLZTO with ultrahigh moisture stability, achieved by high relative density, few grain boundaries, water-stable secondary phase of $La_2Zr_2O_7$, and the Li^+-deficient lattice. Extensive research has been conducted to minimize grain boundary effects in SSEs through densification [76,119,120]. As pointed out by Lee et al. [113], the air stability of Ga-LLZTO was significantly improved through three key factors: reduced grain boundary density, increased grain size, and $LiGaO_2$ segregation at grain boundaries resistant to H_2O/CO_2 corrosion.

Current strategies for mitigating Li_2CO_3 formation in garnet-type SSEs have achieved partial success through impurity reduction rather than complete prevention, necessitating complementary purification, surface modification, and chemical conversion approaches to enhance anode–electrolyte interfacial compatibility. Chen et al. [121] employed anhydrous acetic acid (CH_3COOH) to convert surface Li_2CO_3 into ethanol-soluble CH_3COOLi, yielding a lithiophilic interface with reduced interfacial resistance (5 Ω cm^2 at 60 °C). Sun's group [122] immersed LLZTO particles in 1 M hydrochloric acid (HCl) solution for 30 s to effectively remove Li_2CO_3 and obtain a lithiophilic SSE surface, successfully reducing the Li/SSE interfacial resistance by 914 Ω cm^2 at 30 °C. However, it remains challenging to avoid the formation of LiOH as a byproduct during acid etching, underscoring the need for reaction parameter optimization to preserve structural integrity [122,123]. Thermal decomposition strategies offer alternative pathways. As revealed by Goodenough et al. [107], Li_2CO_3 reacts with carbon to convert into Li_2O and CO_2 at 700 °C under inert atmospheres, thereby reducing garnet-type SSE/Li interface resistance to 28 Ω cm^2. The electrode/electrolyte interface state and Li^+ transport behavior before and after modification are shown in Fig. 4c. However, carbon alloying with lithium during pyrolysis introduces new interfacial complexities, while HT calcination near Li_2CO_3 decomposition thresholds (620–1000 °C) risks lithium volatilization and Li-deficient surface phases. Innovative sintering techniques address these limitations. As shown in Fig. 4d, Ping et al. [108] achieved rapid consolidation of sub-50 μm 3D LLZTO scaffolds in just 5 s via ultrafast high-temperature sintering (UHS), minimizing lithium depletion while enhancing ionic conductivity. Unfortunately, the thermal treatment process predisposes Li species to volatilize into Li_2O, leaving Li-deficient impurities on the surface [113,116]. Huang et al. [110] described a high-speed mechanical polishing approach that utilized a powerful centrifugal force at 5000 rpm to thoroughly remove Li_2CO_3 impurities, while stabilizing the process through controlled pressure (Fig. 4f). This approach yielded a lithiophilic LLZTO surface with low interfacial resistance, demonstrating excellent cycling stability against Li metal. However, Dai et al. [124] observed that mechanical polishing appeared to introduce more microcracks near the LLZTO surface or subsurface, and recommended the *in situ* formation of a LiF-rich interlayer on the Li/LLZTO interface to enhance the wettability between SSE and Li anode. Despite these advances, Li_2CO_3 elimination strategies remain transient, as rapid Li_2CO_3 reformation persists upon air re-exposure of treated electrolyte particles.

Surface modification of SSEs with lithiophilic substances (e.g., CoO [125], Ga [111], Li_3PO_4 [109], MgF_2 [126], Al_2O_3, polymer) has emerged as a pivotal strategy to enhance interfacial compatibility and electrochemical stability. Zhang et al. [109] developed a Li_3PO_4 coating on garnet-type SSE through the synergistic integration of atomic layer deposition (ALD) and thermal annealing, with the process shown in Fig. 4e. This strategy enabled conformal contact between the SSE and Li metal while simultaneously forming a Li^+-conducting SEI enriched with Li_2O/Li_3P, resulting in a significantly reduced interfacial resistance of ~ 1 Ω cm^2. Incorporating functional components (such as graphite [127], BN [128], AlF_3 [129], $LiNO_3$ [130], Si_3N_4 [131]) into molten lithium has been established as an effective method to improve the interfacial wettability of solid-state interfaces and enhance the structural stability of anodes. Li et al. [111] prepared LM@LLZT through coating LLZT SSE with liquid metal (LM) Ga, followed by lithiation via immersion in molten lithium. Leveraging the strong Li_2CO_3–LM affinity, LM nanoparticles drive Li_2CO_3 fragmentation into isolated nanodomains, disrupting the continuity of the Li_2CO_3 passivation layer (Fig. 4g). This enables Li^+ transport along the lithiated LM and oxide regions while circumventing insulating Li_2CO_3 particles. Ji et al. [132] introduced Sr_3N_2 into molten Li to form Li–Sr–N composite, in which Li_3N, $Li_{23}Sr_6$, and LiSrN components significantly reduced the interfacial formation energy between LLZTO and Li, resulting in a highly cohesive LLZTO/Li interface. Critically, these approaches eliminate the need for both aggressive Li_2CO_3 removal protocols and costly thin-film deposition technologies.

The strategic conversion of Li_2CO_3 into lithiophilic interfacial layers represents an effective approach to address garnet-type electrolyte interfacial challenges. Guo et al. [139] realized the *in situ* formation of Li_3PO_4 via conversion reaction between molten $NH_4H_2PO_4$ and surface Li_2CO_3, creating an air-stable lithiophilic surface that achieved seamless garnet contact with interfacial resistance reduced to 13 Ω cm^2. Expanding this methodology, subsequent work by the same group [140] engineered a lithiophilic Li_3Bi@Li_3OCl hybrid interlayer through BiOCl–Li *in situ* conversion reactions. Li_3Bi alloy nanoparticles not only augment the affinity of LLZO for Li to form a compact interfacial layer, but also are discontinuously dispersed within the Li_3OCl matrix, effectively suppressing electron tunneling from the Li bulk and Li nucleation at interfaces or grain boundaries. While such conversion strategies demonstrate interfacial optimization, the inherent lithium deficiency created during Li_2CO_3 removal exacerbates dendrite formation risks, necessitating meticulous impurity elimination coupled with lithium compensation mechanisms. Sun et al. [123] addressed this dual challenge through SiO_2-mediated Li_2CO_3 conversion into lithiophilic Li_xSiO_y, which prevented Li_2CO_3 reformation upon exposure to moisture while excess Li_2CO_3 additives counterbalance lithium loss.

Unlike garnet-type LLZO, NASICON-type LATP and LAGP SSEs exhibit superior ambient stability without Li_2CO_3 formation and enhanced processability, rendering them industrially viable. Nevertheless, direct contact between NASICON-type SSE and Li metal triggers rapid reduction reactions, generating three distinct interface types including thermodynamically inert interfaces, mixed

ionic–electronic conducting interfaces, and kinetically metastable interfaces [141,142]. To address these interfacial instabilities, multiple interlayers have been introduced, which can be categorized into three main types. Firstly, flexible polymer-based electrolytes are adopted as interfacial buffer layers. Li et al. [133] employed a sericin protein film with electrochemical stability and electronic insulation properties as an interlayer for Li/LATP interface. The multi-interface compatible modification layer, composed of IL-sericin films, effectively reduced the interfacial resistance of Li/LATP, suppressed volumetric changes and active material dissolution.

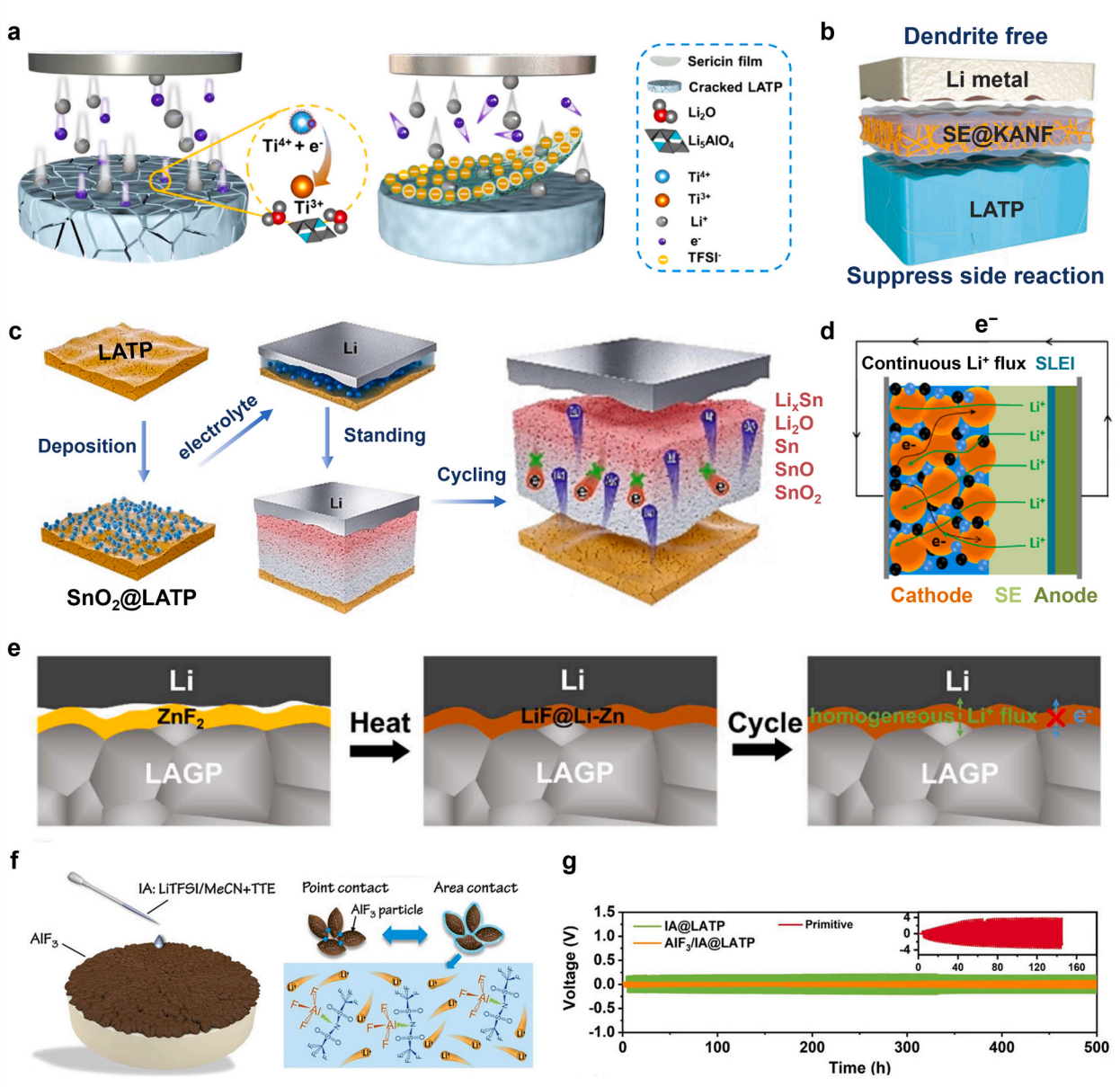

Fig. 5. (a) Schematic representation of the failure mechanism in LATP and the protective mechanism of the sericin film. Reproduced with permission from ref. [133]. Copyright 2022, Energy Storage Materials. (b) Schematic of the SE@KANF composite layer between Li and LATP. Reproduced with permission from ref. [134]. Copyright 2023, Advanced Functional Materials. (c) Schematic illustration of SnO_2 gradient buffer layer suppressing interfacial side reaction and enhancing interfacial adhesion. Reproduced with permission from ref. [135]. Copyright 2023, Journal of Energy Chemistry. (d) Illustration of adding a trace amount of LE to the SSE to improve pore filling and enhance wetting of the Li metal surface. Reproduced with permission from ref. [136]. Copyright 2018, Nano Energy. (e) Interface evolution between metallic Li anode and *in situ*-formed nanoscale ZnF_2 layer coated LAGP pellet. Reproduced with permission from ref. [137]. Copyright 2022, Energy Storage Materials. (f) Schematic illustration of the AlF_3/IA interlayer construction and mechanisms of lithium bis(trifluoromethylsulphonyl)imide (LiTFSI) dissociation and Li^+ transference. (g) Galvanostatic Li deposition/dissolution voltage profile for Li|AlF_3/IA@LATP|Li, Li|IA@LATP|Li cells. Reproduced with permission from ref. [138]. Copyright 2023, Advanced Energy Materials.

Additionally, the layer inhibited the reduction decomposition of LATP and the growth of lithium dendrites (Fig. 5a). However, most polymer-based electrolytes suffer from inherently low ionic conductivity at RT and poor mechanical integrity, which restrict their practical application [143,144]. To circumvent these limitations, Wang et al. [134] engineered an ion-conductive composite layer as a protective barrier for LATP through the *in situ* polymerization of Kevlar aramid nanofiber (KANF) membrane and a solidified electrolyte (SE) (Fig. 5b). The abundant polar functional groups in KANF facilitate uniform Li^+ distribution. Secondly, the *in situ*-formed SSE enabled an intimate Li/LATP interface, significantly diminishing interfacial resistance and facilitating unimpeded and coherent pathways for ion migration. Xia et al. [145] fabricated a 200 nm-thick 3D commercial boron nitride-based release agent (BNRA) layer on LATP through a simple and cost-effective spraying method, effectively suppressing Li/LATP interfacial reactions and thermal runaway. The chemical interactions between BN and Li *in situ* generated Li–N bonds, reducing interfacial resistance and enhancing Li^+

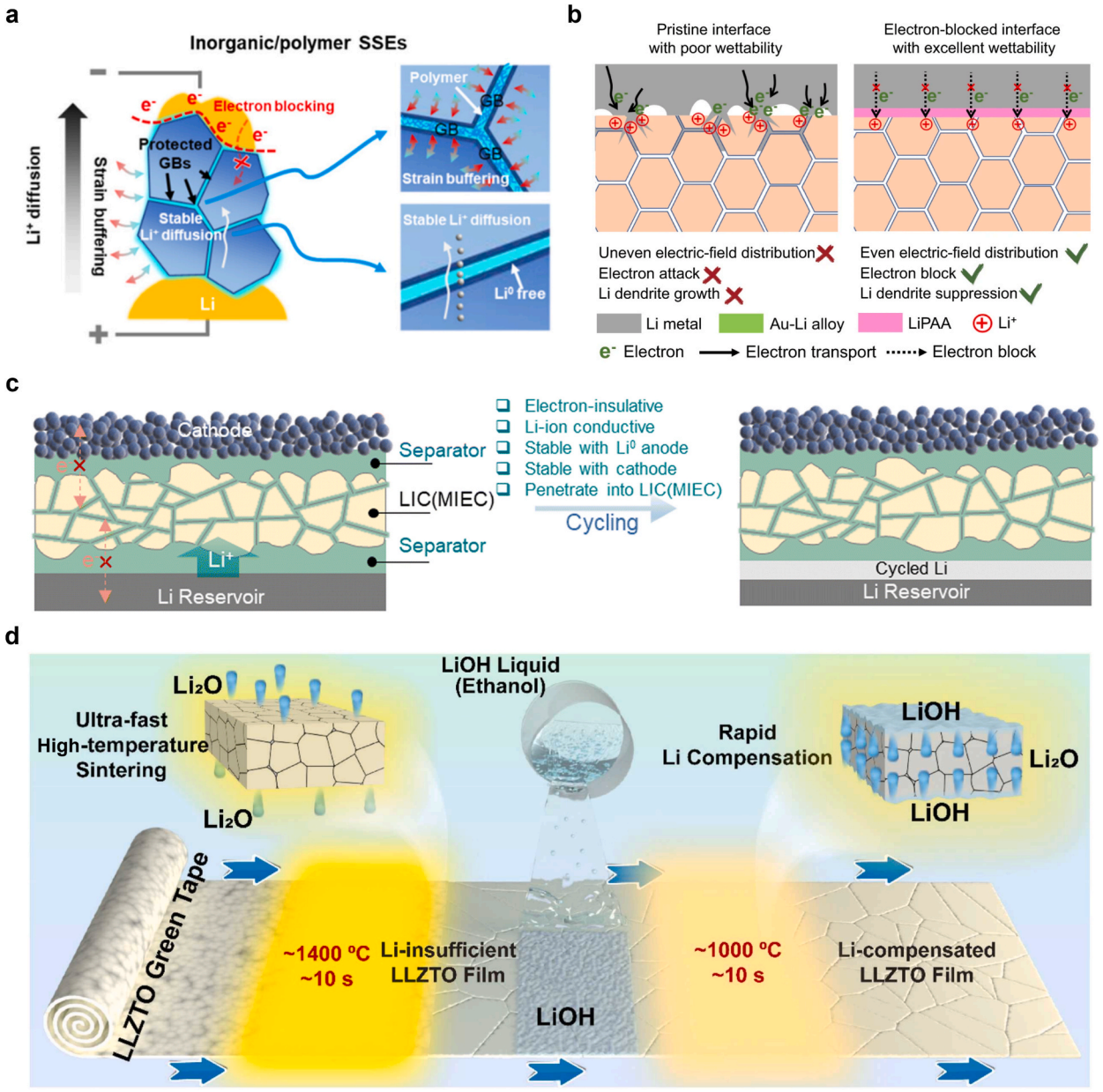

Fig. 6. (a) Stabilization mechanisms in inorganic/polymer SSEs. Reproduced with permission from ref. [149]. Copyright 2025, Journal of the American Chemical Society. (b) Illustrative diagrams showing Li dendrite formation at various interfaces. Reproduced with permission from ref. [151]. Copyright 2021, Nature Communications. (c) Schematic of anode/cathode–SSE interphase evolution in SSBs when using the sandwich-type SSE. Reproduced with permission from ref. [157]. Copyright 2023, Energy & Environmental Science. (d) The preparation of Li-compensated LLZTO films via RLC technique combined with UHS technology and tape casting process. Reproduced with permission from ref. [79]. Copyright 2023, Nano Energy.

migration kinetics and interfacial compatibility. The assembled lean-lithium (2 μm) Li|BNRA–LATP|Li symmetric cell was stably cycled reversibly for 1800 h at 0.05 mA cm^{-2}. Liu et al. [135] developed a SnO_2 gradient buffer layer that formed a low-electronic-conductivity SnO_2/Sn/Li_xSn interface via *in situ* reaction (Fig. 5c), suppressing the interfacial side reactions of Li/LATP. The assembled Li||Li symmetric cell operated stably for 1000 h at 0.1 mA cm^{-2} and 1 mA cm^{-2} without short-circuiting. Alternatively, introducing LEs at the SSE/Li anode interface offers a complementary strategy to improve interfacial stability. Sun's group [136] introduced 2 μL LE at the Li/LATP interface to form a solid–liquid hybrid electrolyte interphase (Fig. 5d), effectively suppressing the reduction of LATP by lithium and ensuring long-term electrochemical durability of LATP within the LE environment. However, LE fails to eliminate grain boundary-mediated dendrite propagation, compromising long-term cyclability. Thirdly, researchers have focused on fabricating inorganic layers to modify NASICON-type SSE surfaces. Ci et al. [146] *in situ* constructed a flexible reduced graphene oxide (rGO) buffer layer with uniformly distributed ZnO at the LAGP–Li interface through Zn/GO reduction, which aids in achieving optimal interfacial contact and inhibits the reduction of LAGP, while ZnO contributes to the homogenization of Li^+ flux. As illustrated in Fig. 5e, Li et al. [137] introduced a multifunctional LiF@Li–Zn alloy interlayer at the Li/LAGP interface by *in situ* conversion reactions between a ZnF_2 thin film and molten Li at 220 °C. This nano-interlayer not only achieves a stable interface with low impedance but also homogenizes the Li^+ flux without lithium dendrites. Li et al. [138] further proposed a mesoporous fluorination interlayer based on high-surface-area AlF_3 (Fig. 5f) to physically block the LATP electrolyte and Li anode as well as alleviate volume changes. Notably, the AlF_3 interlayer induced the formation of a Ti–F transition layer on the LATP surface, which prevented the reduction of Ti^{4+} by Li during electrochemical processes. As shown in Fig. 5g, the engineered Li||Li symmetric cell demonstrated exceptional cycling stability for at least 500 h, while the Li||FeF_3 full cell delivered a remarkable capacity of 696.7 mAh g^{-1} with outstanding cyclability. Concurrently, the electrochemical fusion process integrates the LATP electrolyte, AlF_3 interlayer, and Li anode into a unified whole, reducing interfacial resistance and thereby ensuring rapid Li^+ migration. These strategies demonstrate the effectiveness of alloys or inorganic interlayers in stabilizing NASICON-type SSE/Li interfaces, though practical implementation faces challenges of thickness-dependent ionic conductivity constraints.

In summary, LLZO forms Li_2CO_3 surface layers due to Li^+ Coulombic repulsion, impairing ion transport, while Ti^{4+}/Ge^{4+} reduction in LATP/LAGP causes structural collapse, and LLTO undergoes grain-boundary hydration-induced cracking. Mitigation strategies include atomic-scale doping to suppress Li_2CO_3, moisture-blocking barriers, and sintering-optimized grain boundary stabilization, aiming to achieve ASSLBs with enhanced lithium compatibility and high humidity tolerance.

2.3. Dynamic Li dendrite penetration

The non-negligible electronic conductivity of oxide-based SSEs (ranging between 10^{-5} and 10^{-4} mS cm^{-1}) may accelerate the formation of lithium dendrites at the Li/SSE interface and their propagation along microstructural defects such as grain boundaries or voids, posing a risk of short circuits, particularly under fast charging/discharging or HT operating conditions [147]. Wang's group [148] innovatively applied time-resolved *operando* neutron depth profiling to monitor the dynamic evolution of lithium concentration distribution during lithium deposition, elucidating the origin and growth patterns of dendrite formation on three typical SSEs (LiPON, LLZO, and amorphous Li_3PS_4). High electronic conductivity was regarded as the primary reason for dendrite formation, and identifying and reducing the electron leakage paths rather than further improving ionic conductivity may be a more urgent safety issue to be addressed. Xin's group [149] pioneered nanoscale visualization of the soft-to-hard short-circuit dynamic transition mechanism and associated lithium plating kinetics in inorganic SSEs through *in situ* transmission electron microscopy (TEM). The research revealed that soft short circuits are characterized by dynamically reversible non-Faradaic electronic breakdown, resulting from transient interconnectivity and localized melting of nanoscale Li^0 precipitates, eventually evolving into hard short circuits with intensified electronic leakage (Fig. 6a). It is worth noting that this failure mode is common in garnet-type and NASICON-type SSEs, which prompts researchers to consider how to block the electron permeation path through material composite strategies. For example, incorporating a 3D polymer network with electronic insulation and mechanical flexibility to construct a CSE, which effectively suppressed Li^0 nucleation and interconnection, remarkably improving electrochemical stability. To further analyze the atomic-scale dynamic mechanism of dendrite growth, Mo et al. [150] employed large-scale molecular dynamics simulations to reveal the phase transition pathways and energy barriers during the lithium deposition process. They found that electrodeposited lithium initially forms high-energy disordered-Li or random hexagonal close-packed (rHCP)-Li phases, and then transforms into lower-energy body-centered cubic (BCC)-Li crystals. The interfacial overpotential caused by the phase transition energy barrier directly drives dendrites to expand along SSE pores or grain boundaries. This discovery emphasizes the significance of interfacial engineering in regulating lithium crystallization paths and inspires the development of novel interface design strategies. For example, Sun et al. [151] developed a flexible electron-blocking interface (EBS) shield via *in situ* substitution reactions, which simultaneously impeded electron penetration into LLZTO SSE to suppress dendrite formation and accommodated lithium volume fluctuations during cycling to preserve interface integrity (Fig. 6b). Density functional theory (DFT) calculations revealed a substantial electron tunneling barrier between lithium metal and the EBS, corroborating its exceptional electronic blocking efficiency. Wang et al. [152] demonstrated the *in situ* formation of a LiF-enriched SEI layer at the Li/SSE interface, where the dual electronic insulation and inherent electrochemical stability of LiF synergistically suppressed dendrite infiltration and interfacial parasitic reactions. Im et al. [153] designed an Ag-coated LLZTO integrated with an Ag–C interlayer, simultaneously enhancing lithium transport kinetics and interfacial adhesion. This approach successfully guided lithium deposition to thermodynamically favorable sites, effectively suppressing dendrite penetration, as evidenced by DFT calculations. Furthermore, the bulk–interface synergistic optimization strategy demonstrates unique advantages. Wen et al. [154] innovatively incorporated Li-rich Al_4Li_9 alloy into the bulk LLZO SSE, leveraging the spontaneous wetting behavior of alloy to form an Al-rich interphase. This approach achieved an ultralow interfacial impedance of < 1 Ω cm^2 and enabled dendrite-free

operation at high current densities. SSE architectural designs have also been widely applied to suppress lithium dendrites. For instance, Kang et al. [155] fabricated a layer-by-layer structure incorporating both a lithophilic Ag layer and an electron-blocking layer. The former uniformly distributes the lithium-ion flux and promotes wettability, while the latter passivates electron transport paths at the interface, thereby preventing lithium nucleation caused by internal electron leakage in LLZTO SSEs. This design increased the critical current density (CCD) of Li||Li symmetric cell to 3.1 mA cm^{-2} at 60 °C, demonstrating the effectiveness of the multilayer strategy in solving the multi-source lithium dendrite problem. Wachsman et al. [156] designed a porous single-phase garnet-type mixed ionic–electronic conductor (MIEC) and further constructed a trilayer electrolyte configuration of porous MIEC–dense Ta-doped LLZO–porous MIEC. The porous structure facilitates current distribution to prevent stress concentration hotspots that induce dendrites, helping to significantly increase the CCD to 100 mA cm^{-2} and achieve stable cycling at 60 mA cm^{-2} in Li||Li symmetric cell. To further advance SSE material selection, Xin's group [157] proposed a universal SSE architectural design, in which a lithium-ion conductor (LIC) or MIEC is sandwiched between electron-insulating separators (Fig. 6c). This design enabled stable cycling in ASSLBs even when using ceramic materials with electronic conductivity, lithium reactivity, or high-voltage instability.

The inherent rigidity of oxide-based SSEs results in poor physical point contact with lithium metal, leading to elevated interfacial impedance and reduced CCD. Excessive localized current further induces non-uniform lithium deposition, severely limiting their practical application in LMBs. Addressing this challenge, researchers have pursued dual approaches of material modification and interfacial engineering. Thangadurai et al. [158] reported an alkaline earth metal-doped $Li_7La_{2.75}A_{0.25}Zr_{1.75}M_{0.25}O_{12}$ (A = Ca, Sr, Ba; M = Nb, Ta) garnet-type electrolyte that demonstrated a low interfacial resistance of ~ 33 Ω cm^2 and a CCD of 0.5 mA cm^{-2} at 25 °C without any surface coating. This electrolyte exhibited stable cycling performance across −30 °C to 50 °C for over 50 cycles with negligible voltage fluctuations. Complementing this approach, densification strategies enhance performance through microstructure control. Mukhopadhyay et al. [159] synthesized a Ga-doped LLZO (LLZGO) electrolyte with high relative density (~ 92 %) via the sol–gel method. The porosity-free electrolyte effectively reduced both intergranular ionic resistance and electrode–electrolyte interfacial resistance, while enhancing mechanical strength and suppressing dendrite growth, thereby achieving a CCD of 2.99 mA cm^{-2}. Cyclic voltammetry (CV) tests demonstrated fully reversible electrochemical reactions with no additional interfacial phase formation. Beyond bulk optimization, interfacial engineering proves critical for contact challenges. Liang et al. [160] proposed an innovative *in situ* conversion strategy to construct a Li_2S@C composite layer with high ionic and electronic conductivity on the LLZTO surface through the chemical reaction of CS_2 with lithium. This approach significantly enhanced the wettability between LLZTO SSE and Li anode, enabling Li||Li symmetric cells to achieve a low interfacial resistance of 78.5 Ω cm^2, a CCD of 1.4 mA cm^{-2}, and exceptional long-term stability over 3000 h. He et al. [161] employed magnetron sputtering to deposit an ultrathin ZnO layer on LATP, enabling the *in situ* formation of a low electronic conductivity and multifunctional SEI upon lithium contact. This SEI not only enhanced interfacial adhesion and minimized charge transfer resistance at the Li/LATP interface but also mitigated undesirable chemical interactions, thereby effectively impeding dendrite propagation. Similarly, multifunctional interlayers demonstrate enhanced adaptability. Zhao et al. [162] inserted a low-melting-point metal chloride interlayer between SSE and Li anode, coupled with an *in situ* thermal lithiation strategy to optimize interfacial adhesion. This approach reduced the interfacial resistance of the Li||Li symmetric cell from 948 Ω to 3.5 Ω and increased the CCD from 0.3 mA cm^{-2} to 10.0 mA cm^{-2}. Innovative reactive coatings further advance interfacial stability. Kang et al. [163] coated LLZO SSEs with SnF_2 particles, which chemically transformed into a multifunctional interface composed of LiF and Li–Sn alloy upon lithiation. The conformal LiF layer serves as an electron-insulating buffer with enhanced adhesion to lithium, reducing interfacial resistance and preventing short circuits, while Li–Sn alloys improve Li diffusion kinetics to suppress void formation during cycling. Mechanical stress management has been demonstrated as a pivotal strategy for dendrite suppression, particularly achieved through interfacial stress distribution optimization to inhibit lithium penetration along cracks or voids. Chueh et al. [164] revealed that impurity-induced localized compressive stresses during compaction generate microcracks promoting dendrite nucleation, whereas controlled bulk compressive stresses effectively inhibit crack propagation. Aetukuri et al. [165] identified interfacial void growth as a precursor to dendrite formation, demonstrating that metallic interlayers (W/Al) mitigate void expansion and enhance dendrite tolerance even without high stack pressure. Ultimately, microstructure design requires electrode integration. Chung et al. [166] demonstrated that the implementation of fine LATP particles in composite cathodes effectively reduces porosity while establishing homogeneous Li^+ conduction networks, in contrast to coarse particles which aggravate interfacial side reactions due to compromised interfacial contact.

Lithium dendrite growth in oxide-based SSEs is primarily driven by electronic leakage, interfacial kinetic imbalance, and bulk defect trapping. Mitigation strategies encompass element doping for enhanced intrinsic stability, interfacial engineering (e.g., artificial SEI/sputtering), and hot-pressing densification. Furthermore, integrating advanced *in situ* characterization techniques with stress-field simulation will enable the elucidation of chemo-mechanical coupling mechanisms, advancing highly stable, dendrite-resistant electrolyte systems.

2.4. Thin-film electrolytes

The employment of thick SSEs in current designs presents multiple challenges, including elevated internal resistance, excessive inactive material content, diminished practical energy density, and high manufacturing costs [167]. Therefore, reducing the thickness of SSEs and developing facile and economical preparation technologies are crucial for the commercialization of high-performance thin-film SSEs. The amorphous LiPON thin films exhibit good interfacial compatibility with both high-voltage cathodes and lithium metal anodes due to their wide ESWs, representing the first practical validation of the ceramic thin-film electrolyte concept. The syntheses of LiPON thin films are usually achieved by inserting N atoms or replacing O atoms with N atoms within the amorphous or polycrystalline structure of Li_3PO_4 [168]. The most common preparation methods include RF magnetron sputtering, ALD, pulsed laser deposition

(PLD), and ion beam assisted deposition technologies. Reducing the electrolyte thickness to ≤ 2 μm is expected to alleviate the inherent ionic conductivity limitations of LiPON, enabling excellent rate capability and cycling stability. When the LiPON thin-film electrolyte is paired with the high-voltage cathode $LiMn_{1.5}Ni_{0.5}O_4$, the battery exhibited a capacity retention rate of over 90 % and a coulombic efficiency (CE) of over 99.98 % after 10,000 cycles, indicating an exceptionally stable interface between the LiPON and cathode [169]. Wang et al. [170] deposited an approximately 1.5 μm-thick LiPON layer onto graphene nanosheets–Li_2S (VGs–Li_2S) cathode using RF magnetron sputtering at RT, achieving outstanding long-term cycling stability (over 3000 cycles) and HT tolerance (up to 60 °C). The excellent electrochemical performance could be attributed to the favorable phase capacitance and interfacial stability between VGs–Li_2S and LiPON. Elucidating the interfacial characteristics and associated lithium plating/stripping mechanisms offers pivotal insights for optimizing LiPON electrolytes, thereby advancing lithium metal anode integration. For example, Westover et al. [171] quantified the capacity loss (1.03 ± 0.16 μAh cm^{-2}) of LiPON in contact with lithium metal through electrical analysis, attributing this loss to the formation of a 4.7 nm-thick interfacial layer that consumes 5.0 ± 0.8 nm lithium. Additionally, dynamic electrochemical impedance spectroscopy (EIS) tests indicated a diminishing interfacial resistance during lithium deposition and dissolution, correlating with plated lithium quantity. However, the presence of substrate interference has led to methodological debates in LiPON mechanical characterization. To address this, Meng et al. [172] developed freestanding, substrate-free LiPON thin films and conducted comprehensive characterization utilizing multiple advanced analytical techniques. Typically, solid-state nuclear magnetic resonance (ss-NMR) spectroscopy quantified the chemical composition at the interface between lithium metal and LiPON, differential scanning calorimetry identified the glass transition temperature of LiPON to be approximately 207 °C, and nanoindentation testing indicated a Young's modulus of ~ 33 GPa for LiPON. Despite these advances, the limited capacity confines LiPON thin-film batteries to microelectronics and consumer electronics applications.

Garnet-type SSE films are typically fabricated via vacuum deposition techniques such as RF magnetron sputtering, PLD, and ALD. However, their substrate dependence limits applications in ASSLBs and scalable manufacturing. Additionally, HT sintering of green bodies often causes severe lithium evaporation, which degrades ionic conductivity, relative density, and surface flatness while increasing costs [167]. Although adding excess lithium and reducing annealing temperatures may partially restore conductivity, it remains critical to develop novel processing techniques to fabricate freestanding, dense, flat SSE films with high ionic conductivity. For instance, Laine et al. [173] fabricated 25 μm-thick Ga^{3+}-doped LLZO thin films with a relative density of 95 ± 1 % via liquid-feed flame spray pyrolysis and pressureless sintering method, achieving a high ionic conductivity of 1.3 ± 0.1 mS cm^{-1} and a low ionic area resistivity of 2 Ω cm^2. Kwon et al. [174] innovatively developed a disorder-driven, sintering-free LLZTO electrolyte film, achieving an ionic conductivity of 0.18 mS cm^{-1} at 25 °C with electrochemical performance comparable to conventional HT sintered counterparts. Key to their approach was a single-step mild thermal treatment at 500 °C, the dense amorphous precursor simultaneously undergoes cubic phase transformation (initiating at 350 °C) and achieves interparticle connectivity. To relieve lithium loss, Wang et al. [79] developed a rapid lithium compensation (RLC) technique combined with UHS and tape casting to produce self-supported LLZTO films, as illustrated in Fig. 6d. The lithium-compensated cubic LLZTO film features a thickness of 40 μm, a surface roughness of 5 μm, a relative density of 95 %, and an ionic conductivity up to 0.43 mS cm^{-1}, which is twice that of lithium-deficient films. Further advancing processing speed, Hu et al. [175] employed a printing and radiative heating (PRH) method to fabricate dense polycrystalline LLZTO films via rapidly sintering liquid precursors at 1500 °C for ~ 3 s, achieving an ionic conductivity of 1 mS cm^{-1}. Notably, the PRH process is 10 to 100 times faster than conventional methods, can be extended to various ceramic thin-film electrolytes including LATP, LLTO, β-Al_2O_3, and $LiBO_2$–LLZTO composites, and demonstrates potential for manufacturing multilayer SSBs. Due to the high rigidity, brittleness, and significant interparticle/ electrode–electrolyte interfacial impedance of oxide-based SSEs, compositing with flexible SPEs represents a more prevalent thin-film fabrication strategy. Unlike conventional approaches of directly dispersing ceramic particles in polymer matrices, Guo et al. [176] fabricated a < 10 μm-thick electrolyte membrane by bonding a uniformly conjugated polyacrylonitrile (PAN) nanocoating onto LLZTO particles. This design enables effective Li^+ transport between particles without particle sintering or external pressure. The resulting electrolyte exhibits adequate ionic conductivity of 0.11 mS cm^{-1}, high t_{Li+} of 0.66, and a wide ESW of 4.35 V vs. Li^+/Li, facilitating stable cycling in both Li||Li symmetric cells and ASSLBs.

By comparison, research on alternative oxide-based SSE thin films remains relatively scarce, primarily confined to challenges in ionic conductivity and anode interfacial compatibility. For instance, perovskite-type LLTO thin films fabricated via techniques such as e-beam evaporation [177], PLD [178], and ALD [179] display relatively low ionic conductivity ranging from 0.1 to 10^{-3} mS cm^{-1}. NASICON-type LATP/LAGP thin films synthesized through sol–gel driven spin-coating [180], aerosol deposition [181], and RF sputtering [182] demonstrate reduced ionic conductivity compared to bulk configurations, primarily attributed to challenges in controlling the glass–ceramic phase transition during thin-film processing. Jiang et al. [183] introduced a class of IL-enhanced LATP SSE films with a thickness of 59 μm and ionic conductivity of 1.05 mS cm^{-1}, compatible with fluoride cathodes. The incorporation of IL creates additional ion transport pathways within the SSE, enabling synergistic optimization of flexibility and conductivity in the electrolyte film. This cost-effective dry process eliminates energy losses associated with conventional sintering and is suitable for the large-scale preparation of thin films.

2.5. Summary

Table 1 provides a performance comparison of various oxide-based SSEs studied in recent years. Current research on oxide-based SSEs primarily focuses on garnet-type, perovskite-type, and NASICON-type SSEs. Garnet-type SSEs exhibit optimal comprehensive performance including high ionic conductivity, lithium metal stability, and excellent thermal stability. However, they suffer from poor stability to H_2O and CO_2, relatively high electronic conductivity which may induce lithium dendrites, and the requirement of elevated sintering temperatures resulting in costly production. Perovskite-type SSEs possess the highest crystalline conductivity and structural

Table 1
Comparison of electrochemical performance of various oxide-based SSEs.

Battery	SSE		Performance						Ref.
	σ (mS cm^{-1})	CCD (mA cm^{-2})	Voltage range (V, vs. Li^+/Li)	First discharge capacity (mAh g^{-1})	Cycling number (N)	CE (%)	Capacity retention (%)	T (°C)	
Li|LLZTO@LSO|LFP		1.2	2.8–4.2	127.6 (1.8 mg cm^{-2}, 50 μA cm^{-2})	80	90.8	95	30	[123]
Li|$BiCl_3$–LGLZO–LE|LFP	0.787	10	2.7–4.3	138.8 (2.5–3.5 mg cm^{-2}, 1C)	600	99	100	RT	[162]
Li|LPO@LLZTO|LFP	0.5	2.2	2.8–4.1	122 (2 mg cm^{-2}, 1.5C)	400	99	88	25	[109]
Li|LLZTO–LPO|LCO	1.05	1.2		129.63 (3.2 mg cm^{-2}, 0.1C)	150	99	81	30	[139]
Li|Ta-LLZO + 4 wt% LZO|S	1	0.9	1.5–2.8	1320 (0.266 mg cm^{-2}, 0.2C)	200	100	39.3	25	[184]
LNO10|SN–LLZTO|NCM811	0.63	1.4	2.7–4.3	178.8 (2 mg cm^{-2}, 0.2C)	115		80.0	RT	[130]
Li|LLZTO–HMP|LFP	0.73	1.91	2.5–4.0	138.6 (2 mg cm^{-2}, 0.2C)	500		89.5	RT	[110]
Li|LLZTO@EBS|LFP	1.1	1.2		130.2 (2 mg cm^{-2}, 0.2C)	300		82.8	RT	[151]
Li|LLZTO*|NCA	1.1	3.2	2.8–4.3	164.7 (12 mg cm^{-2}, 0.5C)	400		75.1	60	[124]
Li|LLZTO–RAT|LFP	0.64			142.7 (2 mg cm^{-2}, 0.1C)	150	93.3	82.1	30	[122]
Li|Ag/LiF–LLZTO|LFP	0.45	3.1	2.8–4.2	– (3.5 mg cm^{-2}, 1C)	2400	99.7		60	[155]
Li–In_2O_3|Li_2O@LLZTO|LFP	0.48	2.4	3–3.8	112.38 (1.7 mg cm^{-2}, 1C)	600		84	RT	[185]
Li|$InCl_3$/LLZTO/LE|LFP		0.7	2.8–4.3	127.4 (2 mg cm^{-2}, 0.5C)	475	99.9	97.8	RT	[186]
LSN|LLZTO|LFP	0.695	1.3	2.5–4.2	139.6 (2 mg cm^{-2}, 1C)	200		95.9	RT	[132]
Li|mLLZTO|NCM622	1.1	1.1		154.88 (2.5 mg cm^{-2}, 0.1C)	150	99	82	30	[140]
Li|SnF_2-treated LLZTO|LFP		2.4	2.8–4.3	110 (3–3.5 mg cm^{-2}, 2C)	600	99		RT	[163]
Li|SPE/LATP@SPE–Al|LFP	0.637 (30 °C)			121.3 (0.5C)	500	99.9	88.9	50	[187]
Li|GCMP–LATP|LFP	0.82		3.0–4.6	168 (2.5 mg cm^{-2}, 0.2C)	120	99.9	99.1	25	[96]
Li|AlF_3/IA@LATP|FeF_3	0.121 (30 °C)			696.7	100	99.2	34.4	60	[138]
Li|ZnO@LATP|LFP				167.3 (2.55 mg cm^{-2}, 0.1C)	200	99	88	RT	[161]
Li|IL@SPF–LATP|FeF_3	0.734			524.3 (1 mg cm^{-2}, 0.1C)	100	97	66	60	[133]
Li|BNRA–LATP|LFP	0.169	1	2.5–4.0	150.9 (1.1 mg cm^{-2}, 0.5C)	500	99.5	92.0	RT	[145]
Li|GC–LATP–LE|LFP	0.41		2.5–4.1	120 (1.5–2 mg cm^{-2}, 1C)	100			RT	[136]
Li|LATP|NCM622	0.202			159.1 (2.8 mg cm^{-2}, 0.1C)	80	90		RT	[188]
Li|SSE@KANF–LATP|LFP	0.3	1.4	2.5–4.0	157 (2 mg cm^{-2}, 0.1C)	180	99.8	95	30	[134]
Li|LATP–CP|NCA	0.045 (25 °C)		3.0–4.2	172 (2–3 mg cm^{-2}, 18 mA g^{-1})	100	99	65	60	[166]
Li|Z-LAGP|LFP	0.249	2		154 (2 mg cm^{-2}, 0.1C)	40	99.6	97.4	RT	[137]
Li|GZO@LAGP|LFP	0.323	3	2.8–4.0	131.6 (1.2 mg cm^{-2}, 0.5C)	100	88.6	93.8	25	[146]
Li|UVEA–LATP–UVEA|NCM811	0.773	14	2.0–4.2		400	100	87	RT	[157]
Li|CN@LAGP|LFP	0.238	2		157.0 (0.1C)	340	99.4	82.8	RT	[189]

(*continued on next page*)

Table 1 (*continued*)

Battery	SSE		Performance						Ref.
	σ (mS cm^{-1})	CCD (mA cm^{-2})	Voltage range (V, vs. Li^+/Li)	First discharge capacity (mAh g^{-1})	Cycling number (N)	CE (%)	Capacity retention (%)	T (°C)	
Li|LAGP–EMIM-20|FeF_3	1.05 (RT)		0–4.7	359 (120 mA g^{-1})	50		≈ 58	35	[183]
Li|CPE–LAGP–CPE|LFP	22.5	1	0–6	166.7 (4 mg cm^{-2}, 0.1C)	100	96	100	60	[190]
Li |LAGP|NCM811	0.298		3–4.25	109 (13 mg cm^{-2}, 0.1C)	50	70	100	60	[191]
Li|LE–LAGP–LE|LFP	0.50			130.2 (4 mg cm^{-2}, 1C)	600	99.99	84.7	25	[192]
Li|LAGP–IL|LFP	0.36	2		≈ 140 (5 mg cm^{-2}, 0.3C)	200		48.2	RT	[193]
Li|LAGP|LFP	1			120 (8 mg cm^{-2}, 0.2C)	50		96	80	[194]
Li|l-SN/LAGP|l-SN|LFP	0.209 (RT)	2	2.8–4.0	168.4 (0.5C)	100		93.17	40	[195]

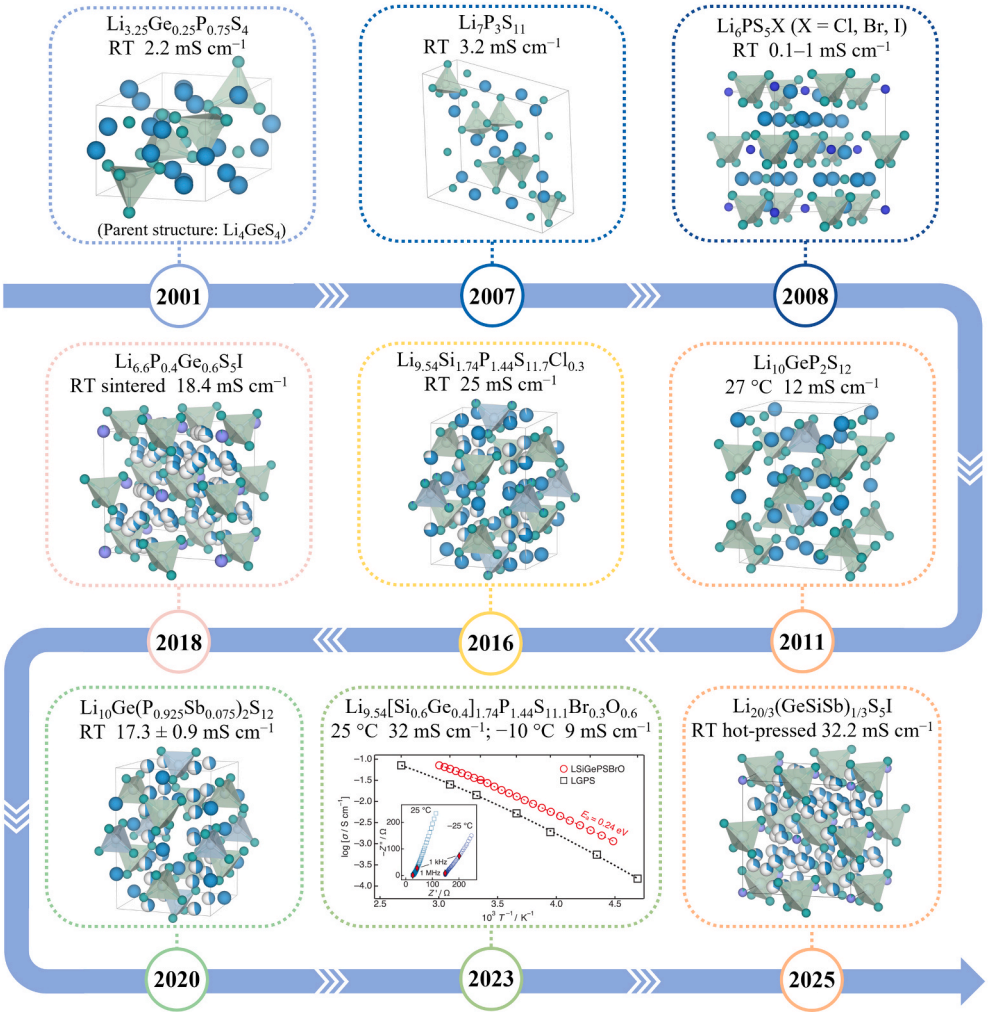

Fig. 7. A brief review of the development of sulfide-based SSEs. Reproduced with permission from ref. [40,41,211,215–220].

stability, but their bulk conductivity is constrained by low grain boundary conductivity, and incompatibility with lithium metal restricts their application. NASICON-type SSEs feature the widest ESWs, exceptional air stability, low sintering temperatures, and cost-effectiveness, showing promise for matching high-voltage cathodes or scalable production in ambient environments. Nevertheless, the presence of high-valent Ti^{4+} ions also compromises their stability against lithium metal anodes.

This chapter summarizes strategies to address the aforementioned issues. Ionic conductivity enhancement primarily relies on cost-effective doping, sintering optimization, and additive engineering, achieving levels up to 1 mS cm^{-1} to support commercialization. To mitigate the high interfacial impedance caused by poor solid–solid contact between rigid oxide-based SSEs and electrodes, particularly

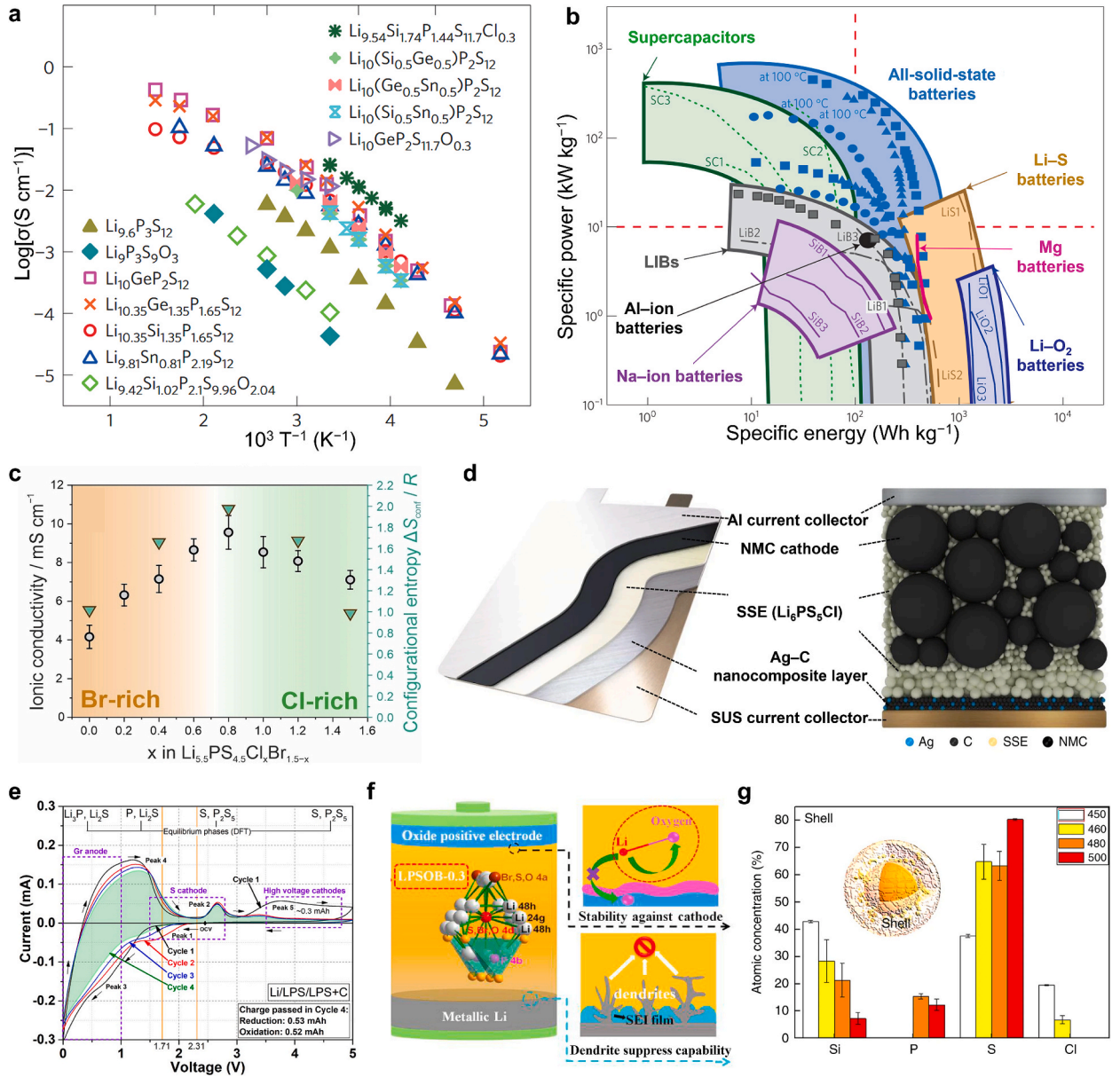

Fig. 8. (a) Arrhenius conductivity plots of LSiPSCl. (b) The Ragone plots showing the energy density versus rate property relationships of various battery system. Reproduced with permission from ref. [216]. Copyright 2016, Nature Energy. (c) Relationship between configurational entropy ΔS_{conf} of the anion sublattice and ionic conductivity. Reproduced with permission from ref. [223]. Copyright 2023, Angewandte Chemie International Edition. (d) Schematic of an ASSLB composed of a NCM cathode with a high areal capacity (> 6.8 mAh cm^{-2}), SSE and an Ag–C nanocomposite anode layer. Reproduced with permission from ref. [224]. Copyright 2020, Nature Energy. (e) CV for the first four cycles of a Li|β-Li_3PS_4|β-Li_3PS_4 + C cell. Reproduced with permission from ref. [230]. Copyright 2019, Chemistry of Materials. (f) Schematic illustration of the superiority of O-doped electrolyte on the both cathode and Li anode side. Reproduced with permission from ref. [231]. Copyright 2019, Journal of Power Sources. (g) STEM EDS analyses showing the opposite trend of Si and S concentration evolution in the shell of LSiPSCl as a function of the annealing temperature. Reproduced with permission from ref. [232]. Copyright 2018, Nature Communications.

the loose contact resulting from cathode volume changes during cycling, effective modification strategies include *in situ* artificial SEI construction, interlayer integration, and polymer compositing. Furthermore, electrode–electrolyte interface incompatibility can also lead to localized excessive current density, causing uneven lithium deposition and dendrite formation. It is crucial to identify electron leakage pathways via *operando* or *in situ* characterization techniques and to sever these paths through implementing electron-insulating layers or improving densification processes. Regarding the reactivity of perovskite-type and NASICON-type SSEs with lithium metal and the air instability of garnet-type SSEs, understanding the chemical and electrochemical degradation mechanisms and employing strategies like doping modification, surface coating, chemical conversion, or introducing interlayers to reduce side reactions is essential. Finally, balancing electrolyte membrane thickness with electrochemical performance remains challenging for large-scale commercialization of oxide-based SSEs. Developing simple, rapid, LT preparation techniques to replace conventional methods like PLD, ALD, and RF magnetron sputtering, or forming flexible polymer composites, will enable high-quality, dense, free-standing thin-film electrolytes. Future research should leverage high-throughput experimental and computational methods to reduce production complexity and cost while maintaining quality, accelerating industrial adoption.

3. Sulfide-based solid-state electrolytes

3.1. Development based on ionic conductivity

Sulfide-based SSEs have emerged as a leading next-generation battery electrolyte technology due to their exceptional ionic conductivity (> 10 mS cm^{-1} at RT), which rivals that of conventional LEs, as well as lithium-ion transference numbers approaching 1 [196–198]. By substituting O^{2-} ions of oxide-based SSEs with larger, more polarizable S^{2-} ions, the resulting sulfide-based SSEs weaken Li^+–anion Coulombic interactions and broaden ionic migration channels, enabling efficient Li^+ transport. Their excellent mechanical flexibility enables densification and intimate electrode contact via cold pressing, while their environmental friendliness and simple processing facilitate scalable manufacturing. Some milestones and achievements in the development of sulfide-based SSEs are shown in Fig. 7, with several types now in production for ASSLBs. Based on their structural features, sulfide-based SSEs are categorized into binary system (Li_2S–M_xS_y, M = Si, P), ternary system ($Li_{10}GeP_2S_{12}$-type), thio-LISICON ($Li_{4-x}M_{1-x}M'_xS_4$, M = Si, Ge and M' = P, Al, Zn, Ga) and argyrodite-type. Binary Li_2S–M_xS_y, as the first type of sulfide-based SSE discovered, has gained intensive research since the 1980s due to the decent conductivity of above 0.1 mS cm^{-1} at RT. The representative binary was Li_2S–P_2S_5, which primarily exists in a glassy state with higher ionic conductivity than crystalline state owing to the absence of grain boundaries [199–204]. Doping strategy further improves the conductivity of binary system [205–207]. Furthermore, it was discovered that the glassy phase with the precipitation of a Li^+-conductive crystalline phase formed the glass–ceramic system, contributing to the improvement of ionic conductivity [203,204,208–210]. The ball-milled $70Li_2S$–$30P_2S_5$ glass–ceramic system precipitated Li^+-conductive crystal $Li_7P_3S_{11}$ with an anionic framework consisting of PS_4^{3-} and $P_2S_7^{4-}$ structural units after heat treatment, exhibiting a high ionic conductivity of 3.2 mS cm^{-1} at RT [211]. It was also found that the heat-treatment temperature determined the amount of synthesized $P_2S_7^{4-}$ and local structure within $Li_7P_3S_{11}$, thus affecting the transport network and ionic conductivity [212–214]. $Li_{3.25}Ge_{0.25}P_{0.75}S_4$, as the first discovered thio-LISICON crystal in 2001 [40], exhibited a 3D framework structure composed of GeS_4 tetrahedra with an ionic conductivity of 2.2 mS cm^{-1} at RT, high electrochemical and thermal stability, and excellent compatibility with lithium metal. The thio-LISICON family follows the general formula, $Li_{4-x}M_{1-y}M'_yS_4$ (M = Si, Ge, and M' = P, Al, Zn, Ga), and adopts the same structure of oxide, γ-Li_3PO_4.

In 2011, Kamaya, et al. [41] synthesized a lithium superionic conductor $Li_{10}GeP_2S_{12}$ (LGPS) through solid-phase reaction method with an unprecedented ionic conductivity of 12 mS cm^{-1} at RT, comparable to or even exceeding many organic LEs. The 3D ionic framework of LGPS consists of PS_4 tetrahedra, $(Ge_{0.5}P_{0.5})S_4$ tetrahedra, LiS_4 tetrahedra and LiS_6 octahedra and one-dimensional (1D) lithium ionic highly-conductive pathways along the *c*-axis. The rapid transport within *ab* plane could be triggered at elevated temperature. LGPS-type ternary system typically possesses superior ionic conductivity above 10 mS cm^{-1} with a distinct structure of 3D anionic framework and efficient lithium-ion transfer channels. Motivated by its ultrahigh ionic conductivity, the family of LGPS obtaines numerous breakthroughs and continues to refresh the record of Li^+ mobility. In 2016, Kanno's group [216] set a new ionic-conductivity record of 25 mS cm^{-1} for another superionic conductor $Li_{9.54}Si_{1.74}P_{1.44}S_{11.7}Cl_{0.3}$ (LSiPSCl) via Cl-substitution in $Li_{10}SiP_2S_{12}$, surpassing all previously reported sulfide-based SSEs (Fig. 8a). This marked the first experimental demonstration of 3D conduction pathways at RT in LMPS family, moving beyond the previously limited 1D transport mechanisms. Based on LSiPSCl and supported by high-entropy principle, Kanno's group [219] further designed $Li_{9.54}[Si_{0.6}Ge_{0.4}]_{1.74}P_{1.44}S_{11.1}Br_{0.3}O_{0.6}$ (LSiGePSBrO) with exceptionally high ionic conductivity of 32 mS cm^{-1} at 25 °C and even 9 mS cm^{-1} at −10 °C, which enabled excellent charge–discharge performance in SSBs consisting of a millimeter-thick LCO cathode at both RT and extreme temperatures. LGPS-type SSEs are well-established for unparallel ionic conductivity, holding a great potential for high areal-capacity, power-density, and energy–density batteries, as shown in the Ragone plots of Fig. 8b. Besides, LGPS family has also brought up the strategy of replacing costly Ge by Si or/and Sn. Kanno et al. [221] synthesized a series of $Li_{10+\delta}Sn_ySi_{1-y1+\delta}P_{2-\delta}S_{12}$ solid solution maintaining the LGPS-type structure. The double substitution by adjusting the Sn^{4+}/Si^{4+} ratio could broaden the ion diffusion channel and elevate the Li^+ concentration, achieving the highest ionic conductivity of 11 mS cm^{-1} for $Li_{10.35}Sn_{0.27}Si_{1.08}P_{1.65}S_{12}$. The cost-effective Ge-free electrolytes provided more feasibility for widespread application. Argyrodite Li_6PS_5X (LPSX, X = Cl, Br, I) originated from Ag^+ superionic conductor Ag_8GeS_6 via substitution of supporting cation Ge^{4+} with P^{5+} and mobile ion Ag^+ with Li^+. To further get the ion conduction improved, halogen elements were incorporated to enhance the anion-site disorder while maintaining the structure intact. In 2008, the first discovered Li_6PS_5X with 3D ion conduction pattern showed a promising Li^+ conductivity from 1 to 10 mS cm^{-1} [215]. The superior ionic conductivity of Li_6PS_5Cl (LPSC) and Li_6PS_5Br (LPSB) compared to Li_6PS_5I (LPSI) could be rationalized by the greater X^-/S^{2-}

disorder for Cl^- and Br^- substitution, while I^- faced a difficulty in replacing S^{2-} in the framework because of the much larger radius. Hence, LPSI possessed a relatively ordered site arrangement along with a lower ionic conductivity. Aliovalent substitution in $Li_{6+x}P_{1-x}Ge_xS_5I$ significantly enhanced the site disorder, decreased the migration barrier, and accomplished 5.4 mS cm^{-1} and 18.4 mS cm^{-1} for cold-pressed and sintered pellets, respectively [217]. With more cations Ge, Si, and Sb substituting for P, the enhanced Li^+ content and anion site disorder considerably pushed the ionic conductivity of iodine-based argyrodite to a record value, 32.2 mS cm^{-1} (after hot-pressing) [220]. Also, the equal effect can be achieved by improving the content and complexity of halogen [222,223]. Dual-doping halogen-rich $Li_{5.5}PS_{4.5}Cl_{0.8}Br_{0.7}$ endowed with augmented Li vacancies and more pronounced anion disorder led to the record highest ionic conductivity of 22.7 mS cm^{-1} at RT [223]. The positive correlation between anion-sublattice configurational entropy (ΔS_{conf}) and Li^+ transport kinetics of ceramic sulfide-based SSEs was clearly revealed by neutron powder diffraction and ^{31}P magic-angle spinning nuclear magnetic resonance (MAS-NMR) spectroscopy, as summarized in Fig. 8c. This relationship has been successfully leveraged to achieve long-term cycling in $Li_{5.5}PS_{4.5}Cl_{0.8}Br_{0.7}$-based ASSLBs, demonstrating that tuning compositional complexity can guide the design of argyrodite-type materials with ultrahigh ionic mobility. Due to the absence of high-valence metal elements such as Ge, LPSC possessing the stability towards Li and cost benefits has been considered as the SSE with the most promising commercial applications. Lee et al. [224] prepared 0.6 Ah all-solid-state pouch cells employing high-Ni cathode and LPSC SSE (Fig. 8d) provided an ultrahigh energy density (942 Wh L^{-1}), broad operation temperature range (−10 ~ 60 °C), and excellent cycling stability (89 % capacity retention after 1000 cycles). The great breakthrough in constructing high-energy long-cycling battery really laid argyrodites a leading position among sulfide-based SSEs and encouraged the further progress of electronic device integration.

Throughout the development of sulfide-based SSEs, substitution strategies including isovalent, aliovalent, single-ion, and multi-ion types have always been considered most effective for improving ionic conductivity [206,207,221,223,225–229]. These substitutions modify the Li^+ sublattice, creating additional Li^+ sites, shortening migration distances, forming favorable conduction channels, and increasing structural disorder. Collectively, these changes significantly lower the activation energy for Li^+ migration. Consequently, years of effort have largely overcome ionic conductivity as a barrier to commercializing sulfide-based ASSLBs. However, intrinsic electrochemical and air instability now pose the major challenge to the widespread adoption of sulfide-based SSEs.

3.2. Electrochemical stability

Apart from high ionic conductivity, wide ESWs are also important for sulfide-based SSEs to match high-voltage cathodes and lithium anode and maximize the energy density of ASSLBs. Sulfide-based SSEs tested with ion-blocking-electrode battery present a high-voltage stability beyond 5 V [207], theoretically compatible with typical oxide cathodes. However, in practical ASSLBs, severe decomposition occurs at the interface between oxide cathodes and sulfide-based SSEs, leading to sluggish ion transport and rapid cell failure [233,234]. First-principles calculations revealed that LGPS stabilized only within 1.71–2.14 V due to the reducibility of P and oxidability of S, highlighting discrepancies between experimental and theoretical ESW values [235]. Fig. 8e displays the electrochemical reaction and corresponding chemical composition variation during cycling within 0–5 V based on Li|β-Li_3PS_4|β-Li_3PS_4 + C cell, demonstrating the irreversible oxidization in the voltage range belonging to high-voltage cathodes with an ion-blocking interphase [230]. The employment of Li|SSE|SSE–carbon cell increases the contact area between the SSE and the electron-conductive part, facilitating more efficient reactions and yielding ESW measurements closer to intrinsic values.

The narrow ESWs of various sulfide-based SSEs give rise to serious interfacial redox reactions with electrodes [236], which makes ion migration less efficient due to interfacial impedance, resulting in poor cycling life. Therefore, great efforts have been made to widen the intrinsic ESWs of sulfide-based SSEs. For instance, oxygen substitution has been widely employed to suppress the interfacial decomposition, as demonstrated in materials such as $Li_6PS_{4.7}O_{0.3}Br$ [231], $Li_{9.42}Si_{1.02}P_{2.1}S_{9.96}O_{2.04}$ [237], $Li_6PS_{4.75}ClO_{0.25}$ [238], $Li_3P_{0.98}Sb_{0.02}S_{3.95}O_{0.05}$ [239]. Fig. 8f depicts that the incorporation of oxygen mitigates the mismatch in chemical/electrochemical potential between oxide cathode and sulfide-based SSE and *in situ* forms a well-contacted interface layer to circumvent further reduction towards Li anode. Apart from chemistry modification, designing specific microstructure for interface stabilization also worked. Interestingly, Wu's group [232] elaborated a core–shell microstructure for LSiPSCl by tuning composition of amorphous shell with higher silicon and lower sulfur content than that of the crystalline core through controlling the annealing temperature, as displayed in Fig. 8g. Owing to the unique core–shell structure, the composite possessed the enlarged ESW to 0.7–3.1 V and quasi-stability window up to 5 V. Besides, the volume constraint imposed on the electrolyte via the unique core–shell morphology hindered the volume expansion of electrolyte and made decomposition thermodynamically unfavorable. The severe electrochemical instability of electrolytes obviously affects the reversible capacity and lifespan of the batteries, and therefore composition modification, structure design or integrated strategies are imperative for the successful operation of sulfide-based ASSLBs.

3.3. Air stability

The intrinsic air/moisture sensitivity of sulfide-based SSEs causes structural degradation, conductivity loss, and toxic H_2S release upon air exposure, necessitating costly dry, inert environments that hinder scalability [203].

The moisture instability can be elucidated by the hard–soft acid–base (HSAB) theory [240]. The central P^{5+} cations in sulfide-based SSE act as strong acids, forming weak P–S bonds with weak bases S^{2-} anions. When exposed to air (containing H_2O or O_2), the unstable P–S bonds in the structure unit PS_4 are easily attacked and broken, converting into more stable P–O bonds with strong bases O^{2-} anions, resulting in the structural damage. Concurrently, liberated S reacts with H to release H_2S. Soft-acid cation (In^{3+}, As^{5+}, Sn^{4+}, Ge^{4+}, Sb^{5+}, etc.) substitution based on the HSAB theory is an effective strategy to enhance the inherent air stability of sulfides through forming stronger bonds [240]. Sun's group [218] utilized Sb^{5+} as a dopant in LGPS, achieving enhanced moisture tolerance and a high

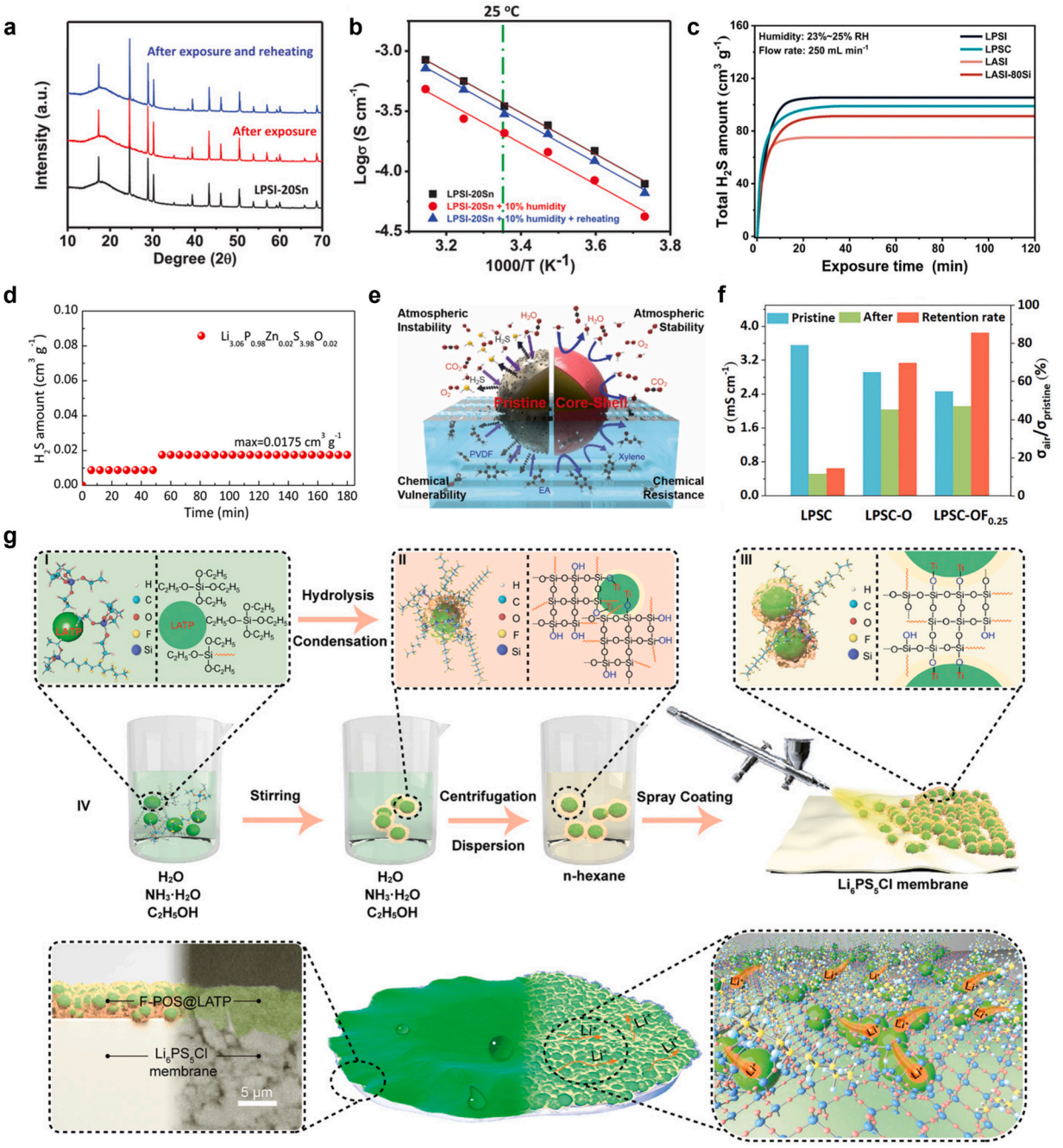

Fig. 9. (a) XRD patterns and (b) Arrhenius plots of the LPSI-20Sn electrolyte before and after exposure to air with 10 % humidity, as well as after reheating. Reproduced with permission from ref. [241]. Copyright 2020, Advanced Energy Materials. (c) The total H_2S amount of LPSI, LPSC, LASI, and LASI-80Si when exposed to flowing air with 23–25 % RH. Reproduced with permission from ref. [242]. Copyright 2023, Nature Communications. (d) The amount of H_2S generated from $Li_{3.06}P_{0.98}Zn_{0.02}S_{3.98}O_{0.02}$ when exposed to the humid air. Reproduced with permission from ref. [243]. Copyright 2019, Energy Storage Materials. (e) Schematic illustration of core–shell microstructure with a LPSC glass–ceramic core coated by hydrophobic oxysulfide nanolayer to resist moisture and organic corrosion. Reproduced with permission from ref. [244]. Copyright 2020, ACS Omega. (f) Ionic conductivity and retention ratio of LPSC-based electrolytes with post annealing (150 °C, 2 h) after exposure to air with 35 ± 2 % RH for 0.5 h. Reproduced with permission from ref. [245]. Copyright 2023, Advanced Science. (g) Schematic illustrations of the preparation process and the design principle of the superhydrophobic Li^+-conducting protective layer on LPSC SE membranes. Reproduced with permission from ref. [246]. Copyright 2022, Advanced Energy Materials.

ionic conductivity of 15.7 mS cm^{-1} after 24 h of exposure to air with 3 % relative humidity (RH). This represents a negligible decrease compared to the pristine value of 17.3 ± 0.9 mS cm^{-1}. The intact structure and almost undetectable H_2S evolution demonstrated by XRD pattern and gas detection confirmed the improved air stability due to Sb^{5+} doping. Sun's group [241] further designed the argyrodite LPSC with 20 mol% of P^{5+} substituted by Sn^{4+} (LPSI-20Sn), which remained stable without any structure degradation in

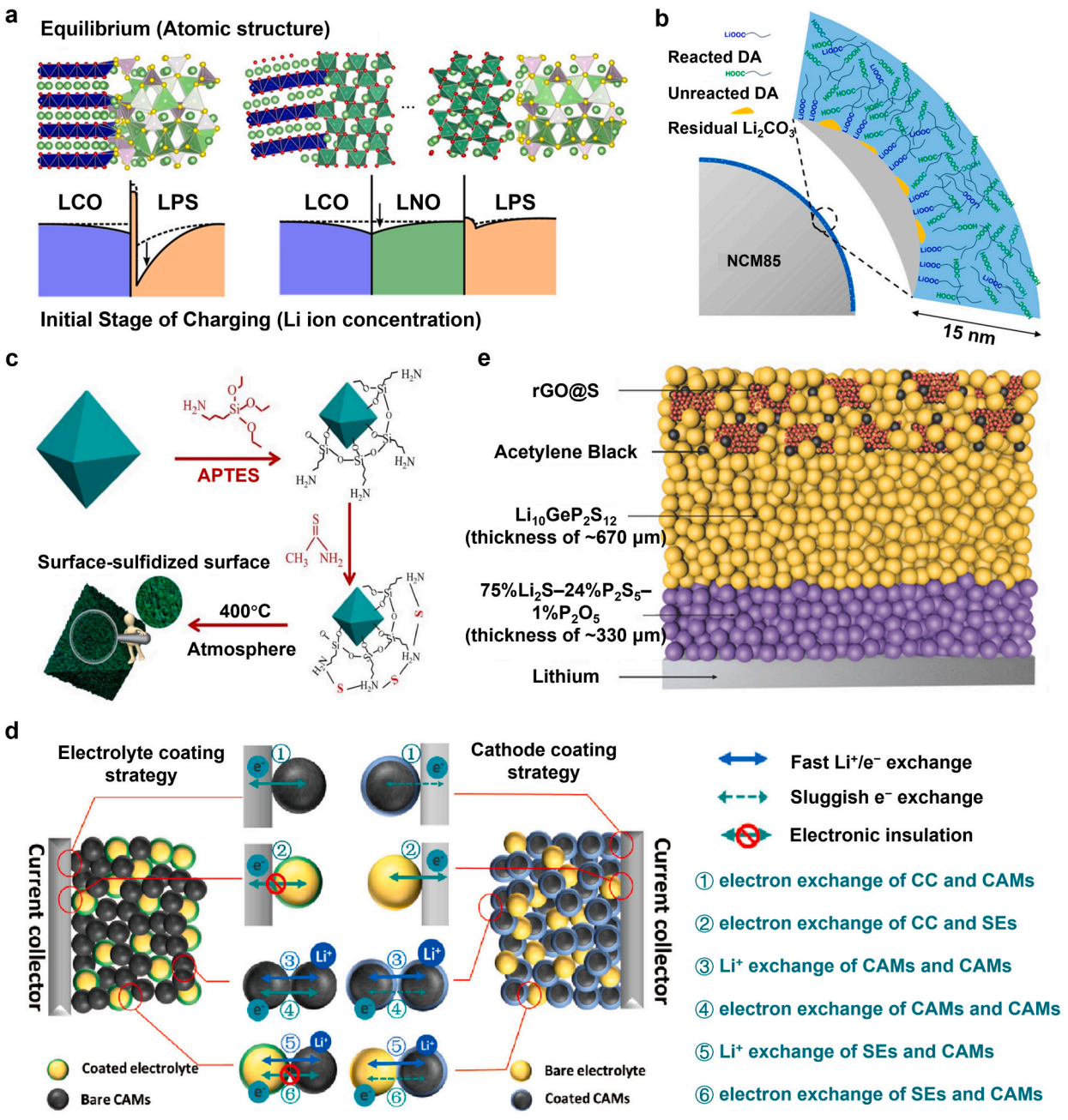

Fig. 10. (a) Optimized interfacial atom structure and expected Li-ion concentration at the initial stage of charge at the LCO/β-Li_3PS_4 interface through modification of $LiNbO_3$. Reproduced with permission from ref. [258]. Copyright 2014, Chemistry of Materials. (b) Schematic illustration of DA coating on the NCM85 surface via acid–base reaction. Reproduced with permission from ref. [269]. Copyright 2023, ACS Energy Letters. (c) Schematic illustration of the preparation for surface-sulfurized $LiNi_{0.5}Mn_{1.5}O_4$ powder. Reproduced with permission from ref. [270]. Copyright 2020, Chemical Engineering Journal. (d) Schematic depiction of advantages of electrolyte coating strategy over conventional electrode coating strategy. Reproduced with permission from ref. [271]. Copyright 2023, ACS Energy Letters. (e) Schematic illustration of a Li–S SSB. Reproduced with permission from ref. [278]. Copyright 2017, Advanced Energy Materials.

pure O_2 and 10 % RH atmosphere, demonstrated by almost complete recovery of the ionic conductivity after post-heat treatment, as presented in Fig. 9a–b. Additionally, the versatile aliovalent substitution with larger ionic radius provided the improved ionic conductivity of LPSI-20Sn more than two orders of magnitude higher than that of pristine one. To maintain structural and performance stability under ambient conditions with higher humidity (> 20 % RH), the concentration of doping could be further increased, even reaching complete substitution. Wu's group [242] reported that with As^{5+} fully replacing P^{5+}, much stronger As–S bonds formed in LASI and resulted in an exceptional moisture stability with the least amount of H_2S gas production exposed to the 25 % RH environment for 2 h (Fig. 9c). With partial silicon substitution, the $Li_{6.8}Si_{0.8}As_{0.2}S_5I$ (LASI-80Si) electrolyte, featuring high ionic conductivity and moisture tolerance, enables Li–In|SSE|TiS_2 ASSLBs to achieve an ultralong cycle life exceeding 62,500 cycles with minimum capacity fluctuation.

Aside from composition tuning based on HSAB theory, incorporation of metal oxides as gas adsorbents into sulfide-based SSEs can thermodynamically inhibit the reaction of the electrolyte with moisture to evolve H_2S. These oxides act as impurity sorbents, reacting with H_2S via highly negative Gibbs free energy changes, thereby reducing the driving force for sulfide hydrolysis. The synthesized $Li_{3.06}P_{0.98}Zn_{0.02}S_{3.98}O_{0.02}$ via doping Li_3PS_4 with 2 mol% ZnO exhibited an elevated ionic conductivity of 1.12 mS cm^{-1} at RT and excellent stability against humid air with only 0.0175 cm^3 g^{-1} H_2S generated after 3 h in ambient environment (Fig. 9d), in stark contrast to pristine Li_3PS_4 with 0.07 cm^3 g^{-1} for after 20 min [243].

Since most soft-acid elements are expensive, some are even heavily poisonous like As^{5+}, and metal oxides cannot resolve atmospheric instability radically, other effective methods to maintain conductive framework integrity and stable electrochemical performance of sulfide-based SSEs are urgently desired. Physical protection layers with strong hydrophobicity and rapid ion mobility have been demonstrated an ideal choice to suppress decomposition of sulfide-based SSEs when exposed to water. Kim et al. [244] designed a core–shell microstructure with a LPSC glass–ceramic core coated by hydrophobic oxysulfide nanolayer (Fig. 9e) via high-energy ball milling under a high oxygen partial pressure. The composite remained quite stable with almost undetectable structure deterioration and slight ionic conductivity variation under 35 % RH condition at 25 °C for over 2 h. Bulk doping of oxygen and fluorine for LPSC reported by Zhou et al. [245] allowed for an enhanced conductivity (2.47 mS cm^{-1}) and improved humid air tolerance (recoverability in 35 ± 2 % RH) compared to unmodified counterparts in Fig. 9f. Encouragingly, Wu's group [246] fabricated an organic/inorganic superhydrophobic composite layer on the surface of LPSC consisting of $Li_{1.4}Al_{0.4}Ti_{1.6}(PO_4)_3$ (LATP) nanoparticles coated by fluorinated polysiloxane (F-POS), as shown in Fig. 9g. The modified electrolyte exhibited a high ionic conductivity due to Li^+ transport channel provided by LATP nanoparticles and superior resistance to an extreme exposure condition at approximate 70 % RH, which was mainly ascribed to micro-toughness from F-POS.

The effectiveness of the protective coating method has been confirmed by many research groups especially in the highly humid environment, seeming more suitable for practical applications than element doping and metal oxide incorporation, which are typically employed in relatively dry conditions (< 30 % RH). The outer insulating nanolayer always consists of oxygen or/and fluorine to realize hydrophobicity and stability of the inner sulfide electrolytes. In many cases, flexible polymers are utilized as main compositions of coating layer to comply with SSEs, but at the expense of interfacial ionic conduction [247,248]. Filler effect and conductive polymer are always implemented to strike a balance between moisture or air stability and ionic conductivity of polymer-ceramics composites [249,250]. Liu et al. [251] demonstrated a long chain alkyl thiol, 1-undecanethiol, as a promising protection layer for sulfide-based SSE, is chemically compatible with electrolyte and has negligible influence on ionic conductivity. Even when exposed to air with 33 % RH, sulfide-based SSE could maintain intact structure and decent ionic conductivity.

To balance ionic conductivity and humidity insensitivity, Wu's group [252] developed a simple one-step gas-phase synthesis approach to fabricate the inherently air-insensitive Li_4SnS_4 without using an Ar-filled glovebox, and the structure degradation and gas evolution under water infiltration could be ignored. Then, the types and concentrations of dopants were screened and adjusted to improve ionic conductivity from below 0.1 mS cm^{-1} for Li_4SnS_4 to 2.34 mS cm^{-1} for $Li_{3.875}Sn_{0.875}As_{0.125}S_4$. The cost-efficient, time-saving, and high-production synthesis method easily conducted in an ambient environment promotes the widespread application of sulfide-based SSBs. However, the toxicity of certain kinds of raw materials (CS_2 and As_2S_3 as sulfurization initiator and dopant, respectively) contradicts the trend towards environment friendliness, and thereby other clean candidates with equal effects should be exploited to optimize the overall performance.

In conclusion, soft-acid ion substitution, oxide incorporation, and water-resistant coating have been demonstrated as effective strategies, and the development of novel sulfides with inherent humidity-insensitivity or hydrolytic reversibility appears to be a fundamental and promising direction to promote the air stability of sulfide-based SSEs.

3.4. Interfacial compatibility towards electrodes

When it comes to battery level, the most prominent challenge is component compatibility, particularly the chemical and electrochemical compatibility between electrodes and electrolytes [253]. As for cathodic interface, oxidative decomposition is frequently observed especially between layered oxide cathodes and sulfide-based SSEs due to the narrow intrinsic ESWs previously discussed. The severe interfacial decomposition blocks the ion conduction and causes reversible capacity decay [254,255]. Notably, the electrochemical decomposition of the sulfide-based SSE is seriously aggravated by carbon conductive agents [256]. Hence, selecting proper cathodes with decent electron conductivity can effectively avoid this problem [257]. The chemical potential discrepancy between the oxide and sulfide displayed in Fig. 10a, originating from stronger bonding strength of oxygen with lithium ions than that of sulfur, drives Li^+ migration from electrolyte to electrode, generating a space-charge layer (SCL) and great interfacial impedance [258].The interfacial side reactions and SCL are major interfacial challenges of ASSLBs composed of oxide active materials and sulfide-based SSEs. Moreover, element mutual diffusion at the contact area resulting from the chemical potential difference also exerts a

negative influence on the interfacial stability, requiring to be inhibited [259].

Composition tuning through O doping is a promising and universal strategy to improve electrochemical stability of sulfide-based SSEs towards oxide cathodes, including systems like $Li_6PS_{4.7}BrO_{0.3}$ [231], $Li_{9.42}Si_{1.02}P_{2.1}S_{9.96}O_{2.04}$ [237], $Li_6PS_{4.75}ClO_{0.25}$ [238]. Although oxygen incorporation enhances cathode compatibility to some extent, it reduces ionic conductivity due to stronger Li^+–O interactions that hinder ion mobility. Coating strategies are widely used to mitigate chemical/electrochemical potential differences,

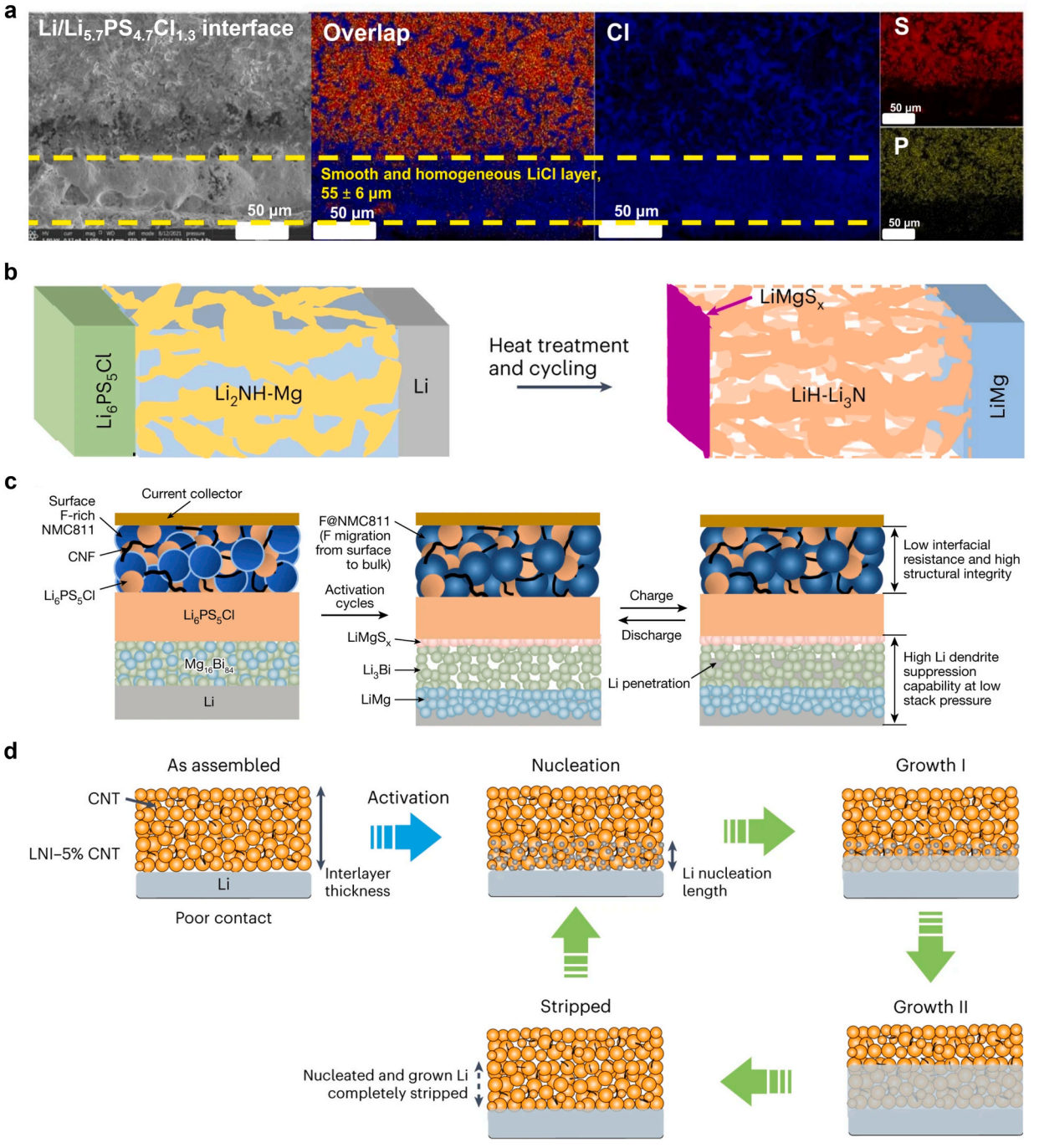

Fig. 11. (a) Cross-sectional SEM and EDS images for $Li/Li_{5.7}PS_{4.7}Cl_{1.3}$ interface. Reproduced with permission from ref. [283] Copyright 2022, Nature Communications. (b) Interphase evolution and element distribution at the Li_2NH–Mg/LPSC interface through heat treatment and Li plating/stripping cycles. Reproduced with permission from ref. [285]. Copyright 2023, Nature Energy. (c) Schematic illustrations of the evolution of $Mg_{16}Bi_{84}$ alloy to $LiMgS_x/Li_3Bi/LiMg$. Reproduced with permission from ref. [286]. Copyright 2023, Nature. (d) The successive evolution of Li/LNI–5 % CNT interface after activation, plating and stripping. Reproduced with permission from ref. [287]. Copyright 2024, Nature Energy.

eliminate the space-charge effect, and suppress undesired side reactions. Typical coatings for high-voltage cathodes include oxides such as $LiNbO_3$ [41,260,261], Li_2CO_3 [262–264], $LiAlO_2$ [265,266], NASICON [267] and garnet [268] et al. Coating methods extend beyond wet chemistry to advanced techniques like ALD, ensuring uniform surface coverage. Organic buffer layers offer deformability to isolate incompatible electrodes/SSEs. Huang et al. [269] constructed an organic fatty acid salt layer on $LiNi_{0.85}Co_{0.1}Mn_{0.05}O_2$ (NCM85) via acid–base reactions (Fig. 10b), extending the ESW of LPSC to 4.3 V while maintaining 90 % capacity retention over 200 cycles. The nanoscale layer minimally impacted ionic conductivity due to precise thickness control. This all-organic coating dominated the inorganic oxide ones in terms of simplicity, flexibility, sustainability. Impressively, Wu et al. [270] demonstrated remarkable stability of LPSC against 5 V spinel cathode through *in situ*-formed –O–S– bonds (Fig. 10c), which could limit oxygen diffusion and suppress interfacial reactivity between cathode and electrolyte. The resulting SSB surpassed coated counterparts in capacity retention during long-term cycling. Yang's group [271] creatively proposed electrolyte coating, which outperforms electrode coating by enabling unrestricted electron exchange between cathode particles and between active particles and current collector, as demonstrated in Fig. 10d. Direct ball-milling argyrodite with lithium difluoro(oxalate)borate (LiDFOB) *in situ* formed a mixing organic–inorganic layer coated on electrolyte particles, which not only stabilized LPSC against LCO at 4.5 V, but blocked carbon-induced decomposition, achieving capacity retention of 91.1 % and 89.3 % after 900 and 1500 cycles, respectively.

Significant progress has been made in stabilizing oxide cathode/sulfide-based SSE interfaces, while novel electrode systems are being explored for optimal matching. Sulfur-based cathodes (e.g., S, Li_2S, TiS_2) are attractive for sulfide-based SSEs owing to their low operating potentials, high theoretical capacities, and inherent chemical compatibility [198,272–274]. However, their insulating nature necessitates conductive composites, and significant volume changes exacerbate interfacial instability [275–277]. To mitigate these problems, Yao et al. [278] assembled a Li–S battery (Fig. 10e) in which the volume accommodation effect of rGO and the uniform distribution of rGO@S in the LGPS-AB mixed conducting matrix effectively reduced the adverse effects of volume fluctuations on structural integrity and electrochemical performance. Wang's group [279] further reported an ASSLB comprising an LPSC SSE and the transition metal sulfide $Co_{0.1}Fe_{0.9}S_2$ cathode without any additional protection showcased a high reversibility over 400 cycles and excellent cycling stability over 800 cycles, demonstrating the stability of this SSE with chalcogenide cathodes.

On the anode side, sulfide-based SSEs exhibit thermodynamic incompatibility with lithium metal anodes due to their narrow intrinsic ESWs [235], leading to inevitable reductive decomposition. The resulting products form interfacial layers between the SSE and anode, which are categorized into two types based on kinetic characteristics. Typically, electrolytes containing high-valence ions (Ge^{4+}, Sn^{4+}, etc.) tend to be reduced to form lithium alloys, producing an MIEC-type interfacial layer. The MIEC type cannot block electron transfer, permitting continuous reductive reactions at the interface and progressive thickening of the interlayer. Conversely, the SEI-type layer exhibits self-limiting passivation by preventing electron penetration, thereby stabilizing the interface. However, uneven lithium deposition caused by ion-blocking interphases leads to dendrite growth, posing a great safety hazard. Hao et al. [280] revealed that the electron-conducting defects (e.g., cracks and grain boundaries) function as initiators and catalysts for lithium dendrite propagation, providing critical insights for bulk and interfacial engineering.

Establishing stable buffer layers is essential for suppressing interfacial side reactions and dendrite growth, whether achieved through *in situ* formation or artificial introduction [281,282]. Zhang et al. [231] reported O-doped Li_6PS_5Br, which exhibited excellent compatibility with the lithium anode and suppressed dendrites. This performance was attributed to oxide-rich interphases, particularly Li_3OBr, which acts as a superionic conductor enabling uniform lithium deposition while enhancing shear modulus to impede the growth of dendrites. Employing a specific cooling approach, Zeng et al. [283] observed that LiCl nanoshells precipitated on $Li_{6.4}PS_{5.4}Cl_{1.3}$ grains and migrated to form an interphase layer during Li plating. The self-limiting LiCl-rich interlayer suppressed parasitic interfacial reactions and dendrite growth due to the electron-insulating properties, high surface energy, and self-healing ability of LiCl (Fig. 11a). The Li||Li symmetric cells with modified electrolytes exhibited steady cycling for over 1000 h at 0.5 mA cm^{-2}. Lim et al. [284] studied the effect of various interlayers including LiF, Mg, and conversion-type MgF_2 on Li compatibility, revealing that only MgF_2 enabled long-term cycling with Li anode (up to 2000 h for Li|LPSC|Li symmetric cell and 800 cycles for full cell). This was attributed to the *in situ*-formed LiF and Li_xMg nanograins stabilizing the interface and homogenizing Li^+ flux. Besides, Wang's group [285] has designed various interlayers at the Li/argyrodite interface in recent years. They introduced a mix-conductive Li_2NH–Mg interlayer at the LPSC/Li–1.0 wt% La interface, and the sandwich structure evolved into LPSC/$LiMgS_x$/LiH–Li_3N/LiMgLa multilayer configuration after initial activation cycles, as shown in Fig. 11b. The lithiophilic alloy enabled uniform Li plating, while porous LiH–Li_3N accommodated reversible Li dendrite penetration. This superior compatibility was quantified by critical interphase overpotential, which is a novel metric for dendrite suppression. Afterwards, Mg–Bi alloys were chosen as interlayer in another work [286], and $Mg_{16}Bi_{84}$ enabled LPSC to achieve a high CCD of 1.9 mA cm^{-2} and ultralong cycling at 1.2 mA cm^{-2} for over 2700 h. It was demonstrated that $Mg_{16}Bi_{84}$ was converted into multifunctional $LiMgS_x$–Li_3Bi–LiMg structure during Li plating/stripping, respectively serving as electronically insulative SEI, dendrite-accommodating porous sublayer, and solid binder along with providing Li nucleation sites (Fig. 11c). Besides, the addition of high-surface-energy O/Cl could further suppress dendrite formation. By finely tuning three key factors of interlayer-lithiophobicity, electronic/ionic conductivities, and porosity, this group fabricated a porous lithiophobic interlayer Li_7N_2I–carbon nanotube (LNI–CNT) [287]. This interlayer enabled Li to plate at the Li/LNI–CNT interface rather than LPSC/LNI–CNT interface and lithium dendrites to reversibly penetrate into and strip from the interlayer (Fig. 11d). The Li symmetric cells achieved a high CCD of over 4.0 mA cm^{-2} at 4.0 mAh cm^{-2} and long-term cyclic stability for more than 600 h. These interlayer engineering principles offer new opportunities for high-energy-density and long-life ASSLBs.

Aside from interfacial engineering between sulfide-based SSE and lithium anode, anode alternatives are expected to mitigate the severe interfacial decomposition and detrimental dendrite penetration. The Li–Si alloy anode has garnered increasing attention because of high specific capacity, moderate lithiation potential, and reduced risks of lithium dendrite growth and side reactions compared to pure lithium anodes. Wu et al. [288] designed a hard-carbon-stabilized Li–Si alloy anode via simple pressure-induced

reaction and established a 3D ionic–electronic transport network with $Li_{15}Si_4$ and LiC_6 phases. Co-doping of Si and hard carbon enhanced the reaction kinetics and chemical stability of pure metal anode, and ASSLBs equipped with this anode delivered excellent electrochemical performance including tolerance to high current density, high mass loading, and prolonged cycle life (30000 cycles at 20C and 0.7 mAh cm^{-2}, 5000 cycles at 1C and 5.86 mAh cm^{-2}). Lee et al. [224] further proposed a Li-free Ag–C anode where lithiophilic Ag with low nucleation barrier regulated uniform Li deposition on the current collector, while carbon functioned as a separator between electrolyte and deposited Li. Li-free anodes offer higher cost-effectiveness than Li metal by eliminating rare raw materials, and further direction should focus on achieving high mass loading of active materials at current densities exceeding 3C.

In summary, sulfide-based SSEs require broader ESW for ASSLB applications. ESW extension comprises intrinsic widening and artificial enhancement. Chemical modifications (e.g., O-doping, halide incorporation) improve inherent oxidation stability and Li compatibility, while interfacial engineering (e.g., artificial or *in situ* interlayers) mitigates SSE–electrode incompatibility. High-

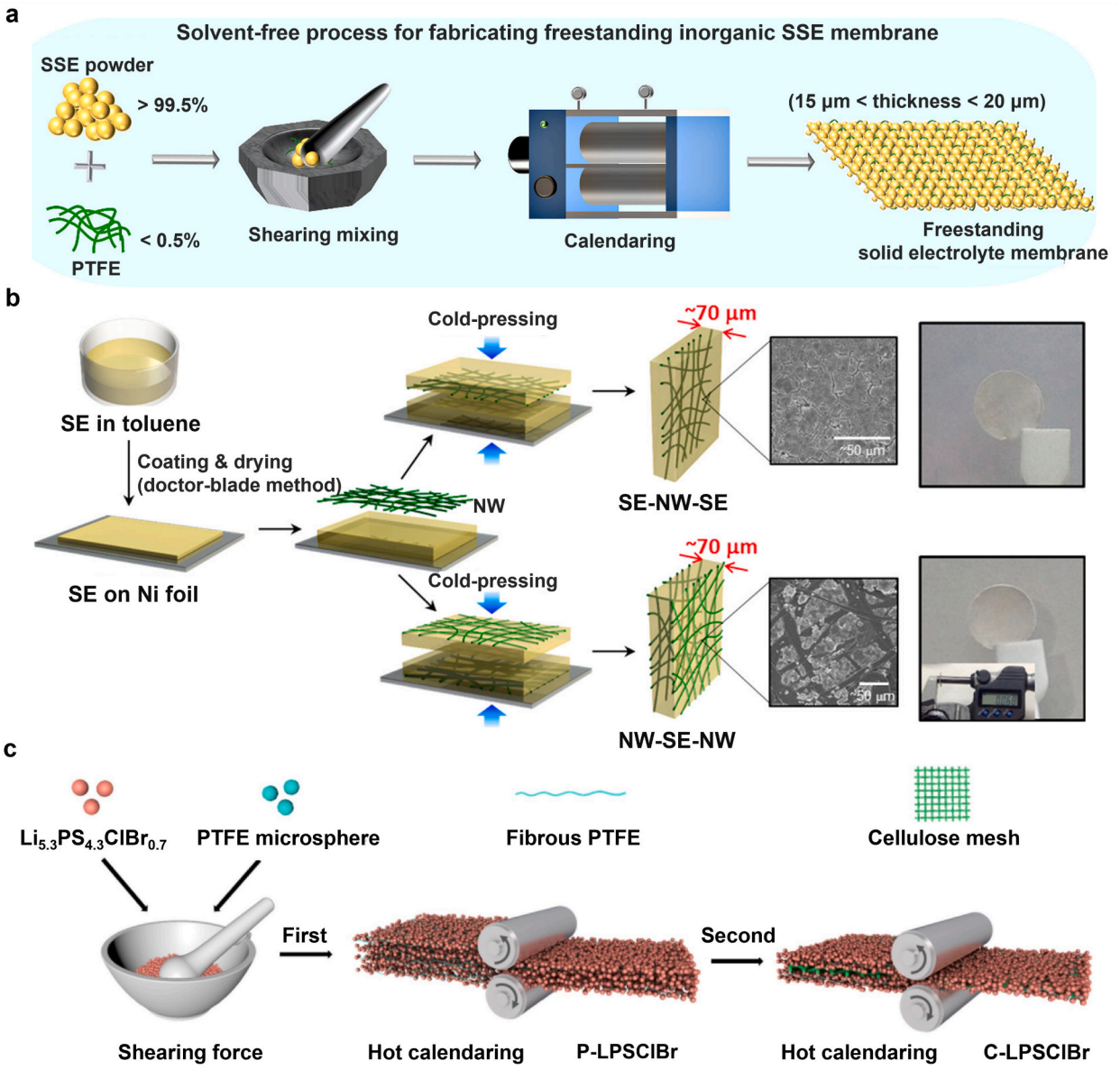

Fig. 12. (a) Schematic illustration of the preparation process for thin LPSC membranes. Reproduced with permission from ref. [291]. Copyright 2021, ACS Energy Letters. (b) Schematic illustration of the fabrication process of bendable sulfide (Li_3PS_4 and $Li_{10}GeP_2S_{12}$) NW-SSE films with two structures (SSE-NW-SSE and NW-SSE-NW), also providing FESEM and photo images. Reproduced with permission from ref. [293]. Copyright 2015, Nano Letters. (c) The fabrication schematics of C-LPSClBr membrane. Reproduced with permission from ref. [294]. Copyright 2022, Journal of Energy Chemistry.

capacity electrodes with moderate potentials (e.g., chalcogenide cathodes, Li-alloy anodes) offer promising alternatives.

3.5. Mechanical properties and compositing modification

Sulfide-based SSEs are flexible enough to form intimate contact with electrodes through direct cold-pressing. However, their volumetric and interfacial integrity degrades under cyclic stresses and strains caused by repeated electrode volume changes during operation. Besides, voids created during cold-pressing act as crack initiation sites. These highly ion-insulating vacancies and cracks disrupt the interconnected ionic pathway, offsetting the high bulk ionic conductivity of sulfide-based SSEs. The resulting solid–solid contact loss between active materials and SSEs in composite cathodes gives rise to rapid capacity decay, which was demonstrated in Ni-rich layered cathode active materials with 80 % Ni content [289]. Some elaborate "zero-strain" electrodes, such as an LCO–NCM composite cathode, which features opposite strain signs of LCO and NCM materials through mechanical blending [290], effectively minimize bulk dimensional changes and pressure fluctuations at the macroscopic level. While this approach enhances mechanical integrity, it inherently restricts the diversity of compatible electrode materials. Although external pressure can suppress electrode volume variations and void formation, low-pressure or pressure-free configurations are preferred for practical applications to simplify system design and improve safety. Furthermore, reducing SSE thickness is critical for energy density, but ultrathin films exhibit greater susceptibility to cracking. To address brittleness, rigid inorganic SSEs are often composited with soft polymers. This hybrid design mitigates mechanical instability by dissipating cyclic stresses and filling interparticle voids but reduces ionic conductivity compared to inorganic counterparts. Consequently, balancing mechanical durability with ionic conductivity remains a critical challenge.

Nan's group [249] synthesized PEO or PVDF-reinforced freestanding $78Li_2S–22P_2S_5$ glass–ceramic electrolyte membranes through a liquid-phase method. The polymer filled the voids and gaps among sulfide particles, reducing the thickness of the composite membrane to 120 μm. Although reducing polymer content and adding lithium salt increased ionic conductivity by orders of magnitude, the composite electrolytes still fell short of commercial ASSLB requirements. Sun's group [291] reported self-supporting LPSC SSE membranes with thicknesses of 15–20 μm, fabricated through polytetrafluoroethylene (PTFE) fibrillation and further roll-to-roll processing, as displayed in Fig. 12a. These ultrathin membranes presented high ionic conductivities (> 1 mS cm^{-1}) due to the trace amount of polymer (< 0.5 wt%) and the absence of solvents. This solvent-free mixing method is universal, scalable, time and cost-efficient, and holds great promise in fabricating various thin-film batteries. Besides, Zhang et al. [292] discovered that the ionic mobility of sulfide-based SSE membrane progressively increased by reducing PTFE amount. Through simple ball-milling and hot-pressing processes, they successfully fabricated a 30 μm-thick electrolyte membrane composed of 99.8 wt% $Li_{5.4}PS_{4.4}Cl_{1.6}$ and 0.2 wt% PTFE, achieving an ionic conductivity of 8.4 mS cm^{-1}, comparable to bulk electrolytes hundreds of micrometers thick. Except for fundamental disordered blending, introducing polymers as flexible scaffolds to construct ordered structures is also a common strategy. Jung's group [293] reported for the first time a bendable sulfide-based SSE membrane reinforced with a flexible poly(paraphenylene terephthalamide) nonwoven (NW) scaffold via cold pressing, forming an SSE-NW-SSE multilayer structure in Fig. 12b. The stackable ASSLB assembled with a 70 μm freestanding composite electrolyte membrane exhibited 3 times higher energy density than the NW-free counterpart and contributed to further enhancing the system-level energy density of solid-state systems. However, this improved mechanical stability came at the expense of relatively low ionic conductivity (< 1 mS cm^{-1}) on account of nonconductive NW scaffold. Tu's group [294] prepared an ultrathin $Li_{5.3}PS_{4.3}ClBr_{0.7}$ (LPSCB) membrane using a trace PTFE binder and reinforced with a cellulose mesh, as shown in Fig. 12c. The 30 μm-thick electrolyte membrane, consisting of a 14 μm-thick cellulose mesh layer sandwiched between two electrolyte layers, showed excellent compatibility with rolling processes, resistance to bending-induced fracture, and a high ionic conductivity of 6.5 mS cm^{-1}. The flexible cellulose mesh scaffold significantly alleviated the brittleness of the LPSCB membrane, while its porous structure facilitated interparticle connections to construct a 3D Li^+ conductive network, thereby minimizing the insulating effect of polymers. Compared to simply blended systems, the polymer framework endowed the membrane with enhanced crack resistance and suppressed pulverization. Similarly, Lee et al. [295] also proposed a mechanically robust frame-based SSE (f-SSE) membrane synthesized by coating LPSC slurry onto a perforated polyethylene separator as a supporting frame. Leveraging its thickness (45 μm) and tensile stress (44.1 MPa) advantages, the ASSLB with f-SSE membrane achieved excellent energy density (314 Wh kg^{-1}) and cycling stability (82.3 % capacity retention after 250 cycles).

3.6. Summary

Sulfide-based SSEs, despite their exceptional ionic conductivity at RT, face critical challenges in electrochemical stability, moisture resistance, and mechanical robustness due to intrinsic thermodynamic instability and narrow ESWs. To address these limitations, strategies such as interfacial engineering, compositional tuning, and nanocomposite design have been developed. Notably, their application requires balancing ionic conductivity and stability to meet the practical needs of ASSLBs. For instance, oxygen doping endows the modified materials with decent ionic conductivity and enhanced electrochemical stability by combining the advantages of both sulfides and oxides, and representative examples are summarized in Table 2. Another often-overlooked aspect, organic solvent stability, is also critical and determines the feasibility of wet chemical synthesis for sulfide-based SSEs. Wet chemistry synthesis offers a sustainable alternative to energy-intensive solid-state reactions and time-consuming ball milling, enabling precise composition homogenization, morphology regulation, and scalable fabrication of sheet-type electrodes. However, it demands chemically compatible solvents and passivation techniques to mitigate sulfide degradation. Certain nonpolar solvents [296] have been verified to be usable, but this comes at the expense of partial ionic conductivity due to the susceptibility of P–S bonds in sulfides. Crucially, effective modifications and next-generation electrolytes depend on understanding atomic-scale ion transport dynamics, phase transformations, and interfacial evolution. Advanced *operando* techniques (*in situ* X-ray photoelectron spectroscopy (XPS), X-ray absorption

Table 2
Comparison of electrochemical performance of various sulfide-based SSEs.

SSE	Ionic conductivity (mS cm^{-1})	CCD (Li||Li, mA cm^{-2})	Operating temperature (°C)	Cathode (mass loading)	Voltage range (V, vs. Li^+/Li)	First discharge capacity (mAh g^{-1})	Capacity retention	Rate performance	Ref.
$Li_3PS_{3.69}O_{0.31}$	1.38	0.58	RT	TiS_2 (1.25 mAh cm^{-2})	1–2.5 V (vs. Li–In/Li^+)	278 (0.1C)		1C	[206]
$70Li_2S{\cdot}29P_2S_5{\cdot}1SeS_2$	5.28 (20 °C)		30	S-rGO	1–3	658.1 (0.1 mA cm^{-2})	84.8 % (100 cycles)		[207]
$Li_{9.54}Si_{0.6}Ge_{0.41.74}P_{1.44}S_{11.1}Br_{0.3}O_{0.6}$	32		25	LCO@LNO (245 mg cm^{-2})	4.25	22.7 (0.587 mA cm^{-2})	> 92 % (100 days)	14 mA cm^{-2}	[219]
$Li_{6.6}P_{0.4}Ge_{0.6}S_5I$	18.4 ± 2.7 (sintering) (25 °C)		60	NCM622 (6.80 mAh cm^{-2})	2.65–4.30	88.8 (0.25C)	no capacity fade (50 cycles)	1C	[217]
$Li_{5.5}PS_{4.5}Cl_{0.8}Br_{0.7}$	22.7		RT	s-NCM90@Li_3BO_3 (8.9 mg cm^{-2})	2.4–3.7	163 (0.1C)	93.66 % (2C, 700 cycles)	2C	[223]
Li_6PS_5Cl	1.8 (RT)		60	$LiNi_{0.9}Co_{0.05}Mn_{0.05}O_2$ (6.80 mAh cm^{-2})	2.5–4.25	146 (0.2C)	89 % (0.5C, 1000 cycles)	2C	[224]
$75Li_2S{\cdot}24P_2S_5{\cdot}1P_2O_5$	0.8	0.1 mA cm^{-2} (100 cycles)	25	LCO (4.6 mg cm^{-2})	3.0–4.2	109 (0.1C)	85.2 % (0.1C, 30 cycles)		[226]
$Li_7P_{2.9}Mn_{0.1}S_{10.7}I_{0.3}$	5.6		RT	S	1.5–3	796 (0.05C)	800 mAh g^{-1} (0.05C, 60 cycles)	0.5C	[227]
$Li_6PS_{4.7}O_{0.3}Br$	1.54 (RT), 11.32 (90 °C)	0.89	RT	NCM811	2–3.7 (vs. Li–In/Li^+)	108.7 (0.1C)		0.8C	[231]
$Li_6PS_{4.75}ClO_{0.25}$	4.7	1.0	25	LCO	2.5–3.7	131 (0.1C)	86 % (0.3C, 250 cycles)		[238]
$Li_3P_{0.98}Sb_{0.02}S_{3.95}O_{0.05}$	1.08	1.0 (> 400 h)	RT	LCO	3.0–4.3	133 (0.1C)	78.6 % (0.1C, 50 cycles)		[239]
$Li_{10}Ge(P_{0.925}Sb_{0.075})_2S_{12}$	17.3 ± 0.9		25	$LiNbO_x$-coated LCO	2.5–4.2	128 (0.1C)	111 mAh g^{-1} (0.1C, 111cycles)	2C	[218]
$Li_{6.2}P_{0.8}Sn_{0.2}S_5I$	0.35	1.26 (> 200 h)	25	$LiNbO_x$-coated LCO	2.8–4.2	123.7 (0.05C)	88.5 % (0.1C, 50 cycles)	1C	[241]
$Li_4P_{0.9}Sb_{0.1}S_4I$	1.6	0.1 (1500 h)	25	LCO	3.0–4.2	109.2 (1C)	83.6 % (1C, 500 cycles)		[298]
$Li_6P_{0.925}Sb_{0.075}S_5Cl$	3.6	1.2	25	$LiNbO_3$-coated NCM523	2.5–4.3	129.9 (0.2C)	82.6 % (0.2C, 60 cycles)	1C	[299]
$Li_{6.12}P_{0.92}In_{0.08}S_{4.88}O_{0.12}Cl$	2.67	1.4	RT	s-NCM811	2.8–4.3	161.6 (0.1C)	82.9 % (100 cycles)	1C	[300]
$Li_{6.8}Si_{0.8}As_{0.2}S_5I$	10.4 (25 °C)		30	TiS_2 (44.56 mg cm^{-2})	0.5–2.4	9.26 (0.53 mA cm^{-2})	≈ 78.9 % (2.44 mA cm^{-2}, 62,500 cycles)	24.45 mA cm^{-2}	[242]
$Li_{3.06}P_{0.98}Zn_{0.02}S_{3.98}O_{0.02}$	1.12	0.5 (1600 h)	RT	$LiNbO_3$-coated LCO	3.0–4.3	139.1 (0.1C)	89.1 % (0.1C, 100 cycles)		[243]
oxysulfide-coated LPSC	3.02		RT	$LiNbO_3$ coated NCM622	2–3.6 V	125.6	64.8 % (0.1C, 200 cycles)		[244]
$Li_6PS_4Cl_{0.75}$-$OF_{0.25}$	2.47	1 (> 1270 h)	25	LCO (25 mg cm^{-2})	2.5–4.3	129 (0.5 mA cm^{-2})	≈ 60 % (2 mA cm^{-2}, 800 cycles)	2C	[245]
F-POS@LATP coated LPSC			35	$LiNbO_3$-coated LCO	0.8–3.0	148.4 (0.1C)	98.5 % (0.1C, 80 cycles)	1C	[246]
$78Li_2S$–$22P_2S_5$–5PEO–LiTFSI	0.7		RT	S	0.6–3.6	778.1 (3rd, 0.176 mA cm^{-2})	93.2 % (0.176 mA cm^{-2}, 100 cycles)		[249]

(*continued on next page*)

Table 2 (*continued*)

SSE	Ionic conductivity (mS cm^{-1})	CCD (Li||Li, mA cm^{-2})	Operating temperature (°C)	Cathode (mass loading)	Voltage range (V, vs. Li^+/Li)	First discharge capacity (mAh g^{-1})	Capacity retention	Rate performance	Ref.
$Li_{3.875}Sn_{0.875}As_{0.125}S_4$	2.45 (25 °C)		30	$LiNbO_3$-coated LCO	0.05–3.25	176.8 (0.1C)	83.43 % (0.1C,100 cycles)	1C	[252]
$Li_{10}GeP_2S_{12}$			60	$LiNbO_3$-coated core–shell $LiNi_{0.8}Co_{0.15}Al_{0.05}O_2$	2.1–3.7	184.1(0.06 C)	89.4 % (0.3C, 400 cycles)	4.2C	[261]
$Li_{10}GeP_2S_{12}$			RT	LCO@ CoO@Li_2CO_3/C	2.6–4.3	144.9 (0.2C)	93.1 % (0.2C, 100 cycles)	1C	[262]
LPSC@Li_2CO_3	1.62		RT	LCO	2.6–4.5	160 (0.1C)	89.4 % (0.5C, > 2100 cycles)	3C	[264]
$Li_{5.5}PS_{4.5}Cl_{1.5}$	4.51	1.0	RT	$LiAlO_2$@NCM811	2.7–4.2	139.46 (0.05C)	82.4 % (0.05C, 60 cycles)		[265]
$Li_{5.5}PS_{4.5}Cl_{1.5}$	3.3		25	LATP@NCM811	2.7–4.2	151.5 (0.1C)	81.6 % (0.1C, 100 cycles)	1C	[267]
LPSC	2.4		RT	DA-coated NCM85	2.8–4.3	190 (0.1C)	90 % (0.2C, 200 cycles)	2C	[269]
LiDFOB coated LPSC	2.0		30	LCO	2.8–4.5	167 (0.1C)	89.3 % (1C, 1500 cycles)	2C	[271]
$Li_{10}GeP_2S_{12}$ (75 % Li_2S–24 % P_2S_5–1 % P_2O_5)	8.27 (RT)		60	rGO@S-40	1.5–2.8	1629 (0.05C)	91.9 % (1C, 750 cycles)	5C	[278]
Li_6PS_5Cl		> 3.0	RT	$Co_{0.1}Fe_{0.9}S_2$	0.5–3.0		1.4 mAh cm^{-2} (150 mA g^{-1}, 854 cycles)		[279]
$Li_{5.7}PS_{4.7}Cl_{1.3}$	5.3	> 1	24	LNO@NCM622	2.4–4.3	≈ 137 (0.1 mA cm^{-2})			[283]
Li_6PS_5Cl		1.4	30	$LiNi_{0.70}Co_{0.15}Mn_{0.15}O_2$	3.0–4.3	157 (0.1C)	82 % (0.1C, 800 cycles)	2C	[284]
Li_6PS_5Cl		6.0	80	F@NCM811	2.8–4.3		157.8 mAh g^{-1} (444 cycles, 5C)	5C	[286]
Li_6PS_5Cl		4.0 (> 600 h)	60	Li_4SiO_4@NCM811	2.7–4.3	191.6 (0.5 C)	82.4 % (350 cycles, 0.5 C)		[287]
Li_6PS_5Cl	3.9 (RT)		55	LCO	2.5–4.2		72.1 % (30000 cycles, 20 C)	50C	[288]
				NCM811	2.5–4.2	≈ 175 (0.l C)	61.5 % (5000 cycles, 1 C)		
Li_6PS_5Cl/Li_3InCl_6 bilayer membrane (PTFE)	> 1		RT	Li_3InCl_6@LCO	2.5–4.2	121.2 (0.1C)	68.6 % (50 cycles, 0.1C)		[291]
$Li_{5.4}PS_{4.4}Cl_{1.6}$ (PTFE)	8.4 (RT)	0.1 (> 400 cycles, 60 °C)	60	NCM523	2.8–4.3	100.1 (0.05C)	80.2 % (150 cycles, 0.05C)		[292]
PE frame based Li_6PS_5Cl	0.51	over 50 h at 0.1 (> 50 h, 25 °C)	25	$LiNi_{0.7}Co_{0.15}Mn_{0.15}O_2$	3.0–4.3	171.1 (0.1C)	82.3 % (> 250 cycles, 0.1C)	2C	[295]
$Li_{9.88}GeP_{1.96}Sb_{0.04}S_{11.88}Cl_{0.12}$ (toluene)	1.9 (25 °C)		60	LCO	3.0–4.3	125.6 (0.1C)	86.3 % (250 cycles, 0.1C)	1C	[296]

*In addition to individual labeling, ionic conductivity data are obtained at operating temperatures.

spectroscopy (XAS), ss-NMR, cryo-electron microscopy (Cryo-EM)) and theoretical simulations are critical for these insights.

Commercialization is constrained not only by inherent properties but also by production costs, which determine scalability. At present, the synthesis costs of sulfide-based SSEs still remain at a relatively high level, especially when lithium sulfide precursors are utilized. However, recent innovations have demonstrated a viable cost-reduction pathway through partially replacing lithium sulfide with low-cost lithium oxides, as evidenced by $Li_7P_3S_{7.5}O_{3.5}$ [297], which slashes raw material costs to \$14.42 kg^{-1}—far below the \$50 kg^{-1} commercialization threshold. This economic breakthrough not only accelerates sulfide-based SSE deployment but also establishes a scalable framework for developing next-generation affordable electrolytes.

4. Halide-based solid-state electrolytes

4.1. Development based on ionic conductivity

Emerging halide-based SSEs are currently a research hotspot relying on the relatively well-rounded properties versus oxide- and sulfide-based SSEs, including decent ionic conductivity of more than 1 mS cm^{-1}, excellent mechanical deformability enabling intimate contact with electrode materials, superior high-voltage oxidation stability up to 6 V vs. Li^+/Li, and compatibility with water/solvent-mediated synthesis [308–311]. Initially, halide-based SSEs failed to develop smoothly and suffered from prolonged obscurity. The earliest halide-based SSEs, binary lithium halides LiX (X = F, Cl, Br, I), were studied in the 1930s but exhibited extremely low ionic conductivity of $< 10^{-4}$ mS cm^{-1} [312]. Afterwards, a series of ternary halides gradually appeared: $LiAlCl_4$ in the 1970s; Li_2MnCl_4, Li_2MgCl_4, Li_2FeCl_4 and Li_3AlF_6 in the 1980s; Li_3InBr_6 in the 1990s; $Li_3InBr_3Cl_3$ in the 2000s et al. [313–318]. Although these electrolytes achieved higher ionic conductivity up to 0.01 mS cm^{-1} through central metallic cation-induced site disorder enhancement, they still failed to meet commercial ASSLB requirements, leading to industrial stagnation. A historic breakthrough pushing halide-

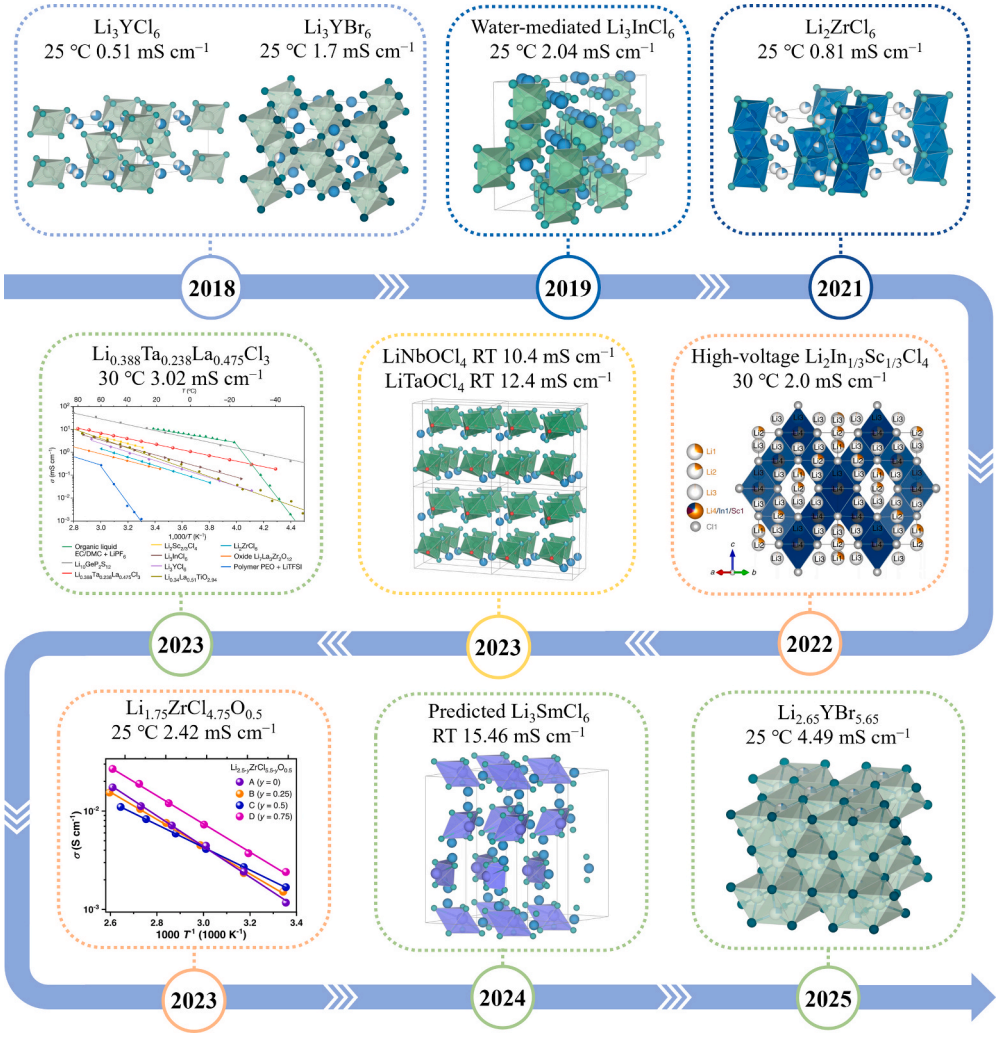

Fig. 13. A brief review of the development of halide-based SSEs. Reproduced with permission from ref. [62,64,301–307].

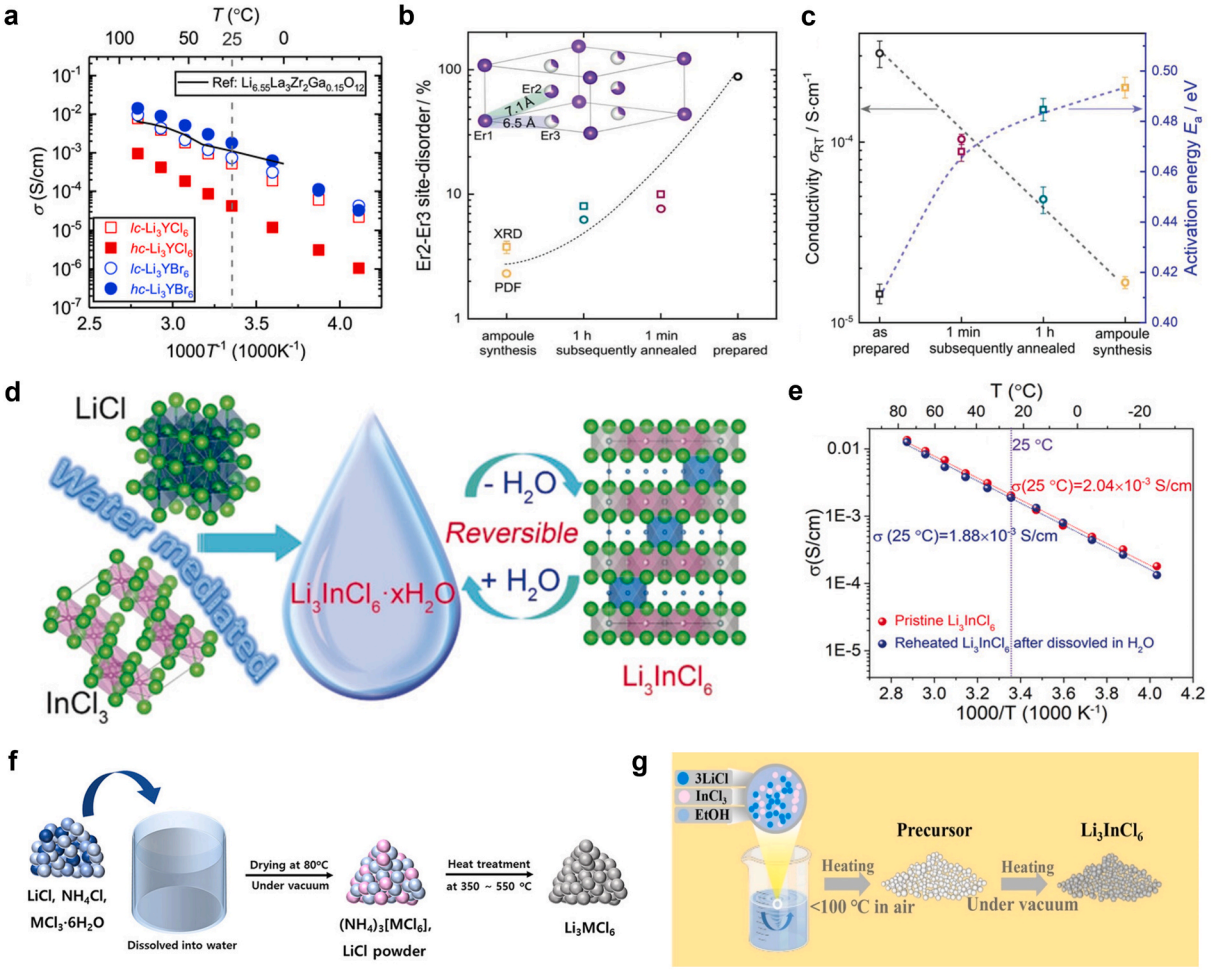

Fig. 14. (a) Arrhenius conductivity plots of Li_3YCl_6 and Li_3YBr_6. Sample labeled *lc* are mechanochemically synthesized without heat treatment and samples labeled *hc* are measured after ball milling and annealing. Reproduced with permission from ref. [62]. Copyright 2018, Advanced Materials. (b) Evolution of the Er2-Er3 site disorder (open circles) and Rietveld refinements (open squares), (c) ionic conductivities and corresponding activation barriers of differently prepared Li_3ErCl_6 samples. Reproduced with permission from ref. [319]. Copyright 2019, Advanced Energy Materials. (d) Schematic illustration of the water-mediated synthesis route for Li_3InCl_6 SSE and the reversible interconversion with the hydrated $Li_3InCl_6{\cdot}xH_2O$. (e) Ionic conductivities of the pristine Li_3InCl_6 SSE and a sample completely dissolved in water and subsequently reheated. Reproduced with permission from ref. [64]. Copyright 2019, Angewandte Chemie International Edition. (f) Schematic illustrating the ammonium-assisted synthesis method of halide-based SSEs. Reproduced with permission from ref. [308]. Copyright 2022, ACS Energy Letters. (g) Schematic diagram of ethanol-mediated synthesis route for halide-based electrolytes. Reproduced with permission from ref. [323]. Copyright 2022, ACS Applied Materials & Interfaces.

based SSEs forward occurred in 2018 as shown in Fig. 13 [62], when Asano et al. successfully synthesized Li_3YCl_6 and Li_3YBr_6 via high-energy ball milling followed by annealing, achieving appreciable ionic conductivities of 0.51 and 1.7 mS cm^{-1} at RT, respectively (Fig. 14a). Zeier's group [319] further revealed the influence of different synthesis methods on the Li^+ mobility mechanism. Mechanochemical synthesis induced significant non-Li metallic cation site disorder even up to complete inversion between Er2 and Er3 sites in Li_3ErCl_6, whereas the conventional solid-state reaction method yields ordered structures. Enhanced disorder facilitated ion transport through Li^+ rearrangement via repulsive force and diffusion channel broadening (Fig. 14b–c). The energy-, time- and cost-efficient liquid-mediated synthesis route enables large-scale production of halide-based SSEs [64,320]. Notably, Sun's group [64] reported a superionic conductor Li_3InCl_6 synthesized via a water-mediated approach, showing a high ionic conductivity of 2.04 mS cm^{-1} at 25 °C along with superior reversibility in a humid environment, as displayed in Fig. 14d–e. yet there are only a few examples. Subsequently, the same group developed a universal ammonium-assisted wet-chemistry synthesis approach for preparing various halide-based SSEs with decent ionic conductivities, including Li_3ScCl_6 (1.25 mS cm^{-1}), Li_3YBr_6 (1.09 mS cm^{-1}), Li_3ErCl_6 (0.407 mS cm^{-1}), and Li_3YCl_6 (0.345 mS cm^{-1}) [321]. The improved moisture tolerance of electrolytes could be attributed to the formation of $(NH_4)_3MCl_6$ (M = trivalent metal elements) intermediates, as shown in Fig. 14f [308], which inhibited the hydrolysis of MCl_3. Recently, they developed a

scalable hydrate-assisted systhesis for aluminum-based oxychloride SSEs, further offering promise for broad applications of halide-based SSEs [322]. Besides, Tu's group [323] proposed a solvent-mediated synthesis to eliminate the detrimental effect of trace water via ethanol dissolution and precursor post-treatment (Fig. 14g). The prepared Li_3InCl_6 exhibited superior thermal stability beyond 300 °C and a high ionic conductivity of 0.79 mS cm^{-1} at 20 °C.

Based on the structure–property correlation, microstructural features including Li vacancies, lattice distortion, interplanar spacing, and stacking faults have been proven to strongly affect the ionic transport properties [324–330]. Crystal structure is closely linked to material composition, especially the non-Li metallic cations in halides. Consequently, extensive research has focused on the composition tuning for improving ionic conductivity and other critical properties. Ternary halide-based SSEs with the formula Li–M–X (where M mainly refers to Sc, Y, In, Er, and X = Cl, Br, I) have drawn much interest due to their ionic conductivities beyond 1 mS cm^{-1}, which are expected to be further enhanced via iso- or aliovalent substitutions or mixed metallic element strategies. The novel mixed-metal spinel $Li_2In_{1/3}Sc_{1/3}Cl_4$ exhibited a high ionic conductivity up to 2.0 mS cm^{-1} due to the disturbed Li^+ distribution [302]. Recent investigations into typical tetravalent Zr doping are particularly encouraging, such as $Li_{2.7}Yb_{0.7}Zr_{0.3}Cl_6$ (1.1 mS cm^{-1}) [326], $Li_{2.6}In_{0.6}Zr_{0.4}Cl_6$ (1.25 mS cm^{-1}) [328], $Li_{2.5}Er_{0.5}Zr_{0.5}Cl_6$ (1.4 mS cm^{-1}) [324], and $Li_{2.375}Sc_{0.375}Zr_{0.625}Cl_6$ (2.2 mS cm^{-1}) [331]. These studies directly reflect the composition–structure–property relationship. Aliovalent substitution creates more Li vacancies and cation disorder to form 3D diffusion channels and distorts the structure to lower the migration energy barrier to facilitate efficient Li^+ transport. In addition, Zr, as a low-cost and resource-rich element, plays a crucial role in constituting more cost-effective halide-based SSEs [301,305]. Yu et al. [330] innovatively elucidated the correlation between cation (M) arrangements (content and ordering) and Li diffusion kinetics in trigonal Li_3MCl_6. In this structure, M serves both as a pillar to enlarge the interplanar spacing and facilitate ion diffusion within planes and as a disruption to the in-plane percolation network. Therefore, there exists an optimal M occupancy range to strike a balance between two inverse effects, as displayed in Fig. 15a. Specially, tetravalent Zr incorporation would induce more M vacancies without Li^+ content variations, and the optimized $Li_3Y_{0.2}Zr_{0.6}Cl_6$ demonstrated a satisfactory conductivity of 1.19 mS cm^{-1}, almost six times higher than Li_3YCl_6 (≈ 0.2 mS cm^{-1}). Moreover, composition alteration also triggered metallic ion rearrangement and structure transition from trigonal to orthorhombic phase, contributing to the improved ionic conductivity of $Li_{2.7}Yb_{0.7}Zr_{0.3}Cl_6$ by reducing the lithium-ion migration activation energy barrier, as evidenced by bond valence site energy calculations [326]. Nazar et al. [332] depicted the phase evolution of $Li_3M_{1-x}Zr_xCl_6$ (M = Er, Y) in depth, uncovering that the key factor determining the crystal structure was the average transition metal ion size. The transition to a new, highly conductive phase upon Zr substitution was accompanied by new Li sites, ion arrangements and migration channels, all of which facilitated the enhanced ionic conductivity [333]. Fig. 15b compares and summarizes the structure features and ionic conductivities of three typical types of close-packed halides [327,334–336]. Among these, monoclinic *ccp*-stacked phase possessing 3D isotropic ion diffusion network ranks highest in ionic conductivity, followed by orthorhombic *hcp*-stacked phase and then trigonal *hcp*-stacked phase. Both latter phases exhibit anisotropic network with fast *c*-axis 1D migration channel. In addition, Sun's group [335] supplemented a concept of cationic and anionic factor τ to describe the relative polarization power between cation and anion sublattice, thereby aiding structural determination. More than ten halide superionic conductors with ionic conductivities of 1 mS cm^{-1} were synthesized via predictive function of τ, indeed guiding the structure design of novel halide-based SSEs through metallic ion regulation (Fig. 15c–d).

Yao et al. [304] designed UCl_3-type halide superionic conductors derived from the $LaCl_3$ lattice with $P6_3/m$ space group. As displayed in Fig. 15e, the abundant large 1D channels in the $LaCl_3$ lattice were interconnected into a 3D Li^+ migration network through Ta-doped La vacancies, achieving an ionic conductivity of 3.02 mS cm^{-1} at 30 °C. Complementary *ab* initio molecular dynamics (AIMD) simulations and experimental measurements confirmed the enhanced ionic conductivity of this non-close-packed framework structure compared to traditional structures, attributable to its greater density of distorted sites and expanded diffusion channels. Furthermore, high-throughput computational screening designated $LiGaCl_3$ as a viable candidate material [337]. Considering the abundance of UCl_3-type halides and their derivatives, Sun et al. [338] proceeded with exploitation of UCl_3-type structure by employing $LaCl_3$ and $CeCl_3$ as skeletons and multiple metal cations as dopants (Fig. 15f). The intrinsic rich large-size 1D channels and highly disordered amorphous phase induced by multiple cations mixing jointly contributed to ionic conductivities beyond 1 mS cm^{-1}. In term of novel electrolytes, Patel et al. [66] also designed 2LiX–GaF_3 (X = Cl, Br, I) electrolytes with high ionic conductivity and mechanical pliability via high-energy mechanochemical mixing. Unique structural units $Ga(F, X)_n$ or GaX_mF_{n-m} polyanions (Fig. 15g) identified by ^7Li, ^{71}Ga, ^{19}F ss-NMR and DFT simulations promoted Li^+ transport to 3.2 mS cm^{-1} by weakening Li^+–X^- binding through charge clustering effects. This mechanism has also proven applicable to multivalent cation conductors such as Ca^{2+} and Mg^{2+}, demonstrating significant potential for electrolyte design. Harnessing structure estimation and first-principles calculations, Li_3SmCl_6 was discovered as a lithium superionic conductor with a high RT ionic conductivity of 15.46 mS cm^{-1} [306]. Apart from chlorides, more bromine lithium-ion conductors have also demonstrated potential as SSEs in high-energy-density ASSLBs. Li-deficient $Li_{3-x}YBr_{6-x}$ (x = 0 to 0.5) achieved 4.49 mS cm^{-1} at 25 °C through the co-melting methods [307].

Throughout the development of halide-based SSEs, mainly referring to progress after 2018, halides have achieved mS cm^{-1}-level ionic conductivity supporting significant research and industrial interest, yet the demand for high energy density and fast charging requires ionic conductivity comparable to LEs. Through composition modification, structure optimization, and novel electrolyte designs, the fast lithium-ion conductivity of halides has been continuously tapped, revealing certain commonalities in ion transport enhancement mechanisms and effective utilization of structure–property relationships. However, most studies focus on the crystalline structures of electrolytes, while amorphous structures, typically obtained by high-energy ball milling, lack systematic understanding. Notably, emerging evidence suggests that amorphous phases significantly influence electrolyte electrochemical performance. For example, amorphous Li–Ta–Cl-based SSE composed of $LiCl_4^{3-}$, $LiCl_5^{4-}$, $LiCl_6^{5-}$ polyhedra with $TaCl_6^-$ octahedra exhibited Li^+ conductivity up to 7.16 mS cm^{-1} [339]. Furthermore, the reaction kinetics can be effectively enhanced by regulating the amorphous formation process [340]. Amorphous oxyhalide-based SSEs have recently been proposed with ionic conductivity exceeding 10 mS cm^{-1},

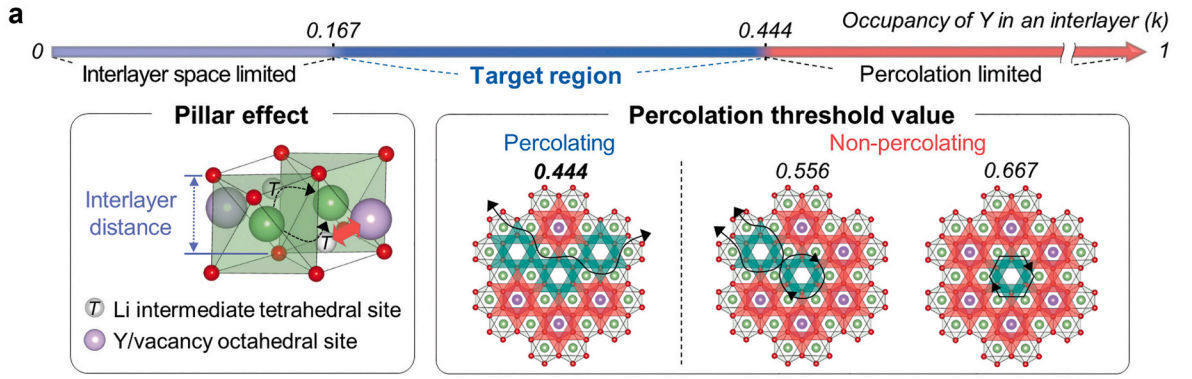

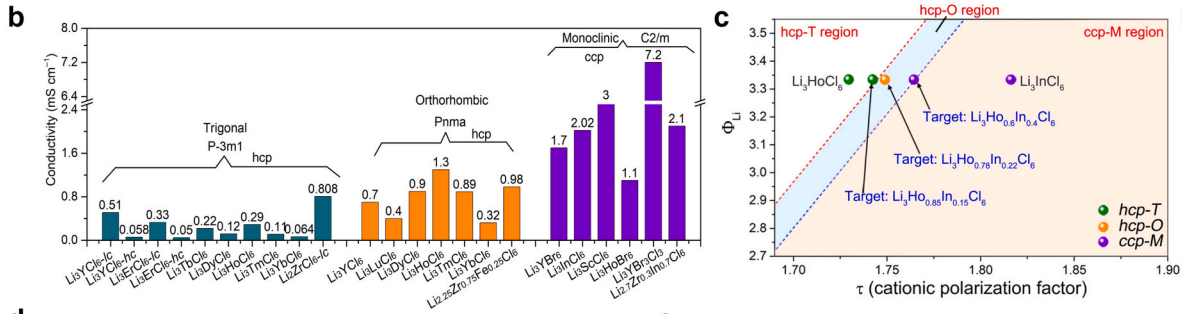

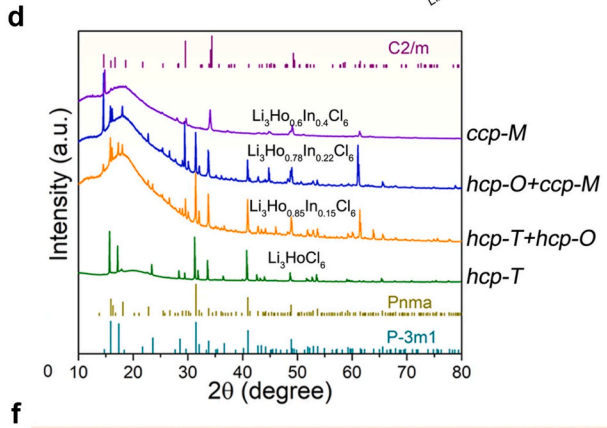

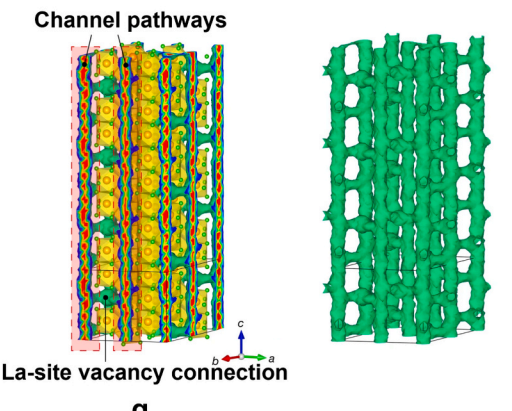

f

	Li content	Prototype composition: UCl_3 skeleton	Prototype composition: Vacancy inducer
Basic recipe	LiCl	$LaCl_3$ or $CeCl_3$, or mixture	
Vacancy involved recipe	LiCl	$LaCl_3$ or $CeCl_3$, or mixture	$ZrCl_4$ or $TaCl_5$, etc.
Multiple-cation mixed recipes	1.5LiCl	$(LaCl_3)_{0.2}$ $(CeCl_3)_{0.2}$	$(ZrCl_4)_{0.2}$ $(HfCl_4)_{0.2}$ $(TaCl_5)_{0.2}$
	LiCl	$(LaCl_3)_{0.2}$ $(CeCl_3)_{0.2}$	$(ZrCl_4)_{0.2}$ $(AlCl_3)_{0.2}$ $(TaCl_5)_{0.2}$
	1.5LiCl	$(LaCl_3)_{0.2}$ $(CeCl_3)_{0.2}$	$(HfCl_4)_{0.2}$ $(AlCl_3)_{0.2}$ $(TaCl_5)_{0.2}$
	1.5LiCl	$(LaCl_3)_{1/6}$ $(CeCl_3)_{1/6}$	$(ZrCl_4)_{1/6}$ $(HfCl_4)_{1/6}$ $(AlCl_3)_{1/6}$ $(TaCl_5)_{1/6}$

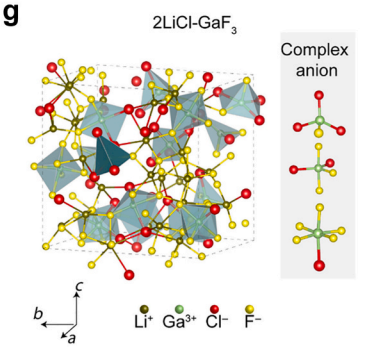

(caption on next page)

Fig. 15. Structure regulation via compositional modification and discoveries of new halide superionic conductors. (a) Design rules of cation arrangements based on two diffusion-determining factors in trigonal halide superionic conductors. Reproduced with permission from ref. [330]. Copyright 2023, Science. (b) RT ionic conductivity summary of halide-based SSEs classified by phase structure. Reproduced with permission from ref. [336]. Copyright 2022, Science Advances. (c) The structure design of $Li_3Ho_{1-x}In_xCl_6$ and $Li_3YCl_{6-x}Br_x$ halides based on τ. (d) XRD patterns of the $Li_3Ho_{1-x}In_xCl_6$ samples and the standard references. Reproduced with permission from ref. [335]. Copyright 2024, Nature Communications. (e) Li^+ probability density in the vacancy-contained $LaCl_3$ lattice, and isolated Li^+ probability density isosurfaces by removing all $LaCl_9$ polyhedra to show 3D interconnection Li^+ migration pathways. Reproduced with permission from ref. [304]. Copyright 2023, Nature. (f) Prototype composition design of different UCl_3-type chloride SSEs. Reproduced with permission from ref. [338]. Copyright 2023, Angewandte Chemie International Edition. (g) Simulated amorphous structure of 2LiCl-GaF_3 featuring polyanions $GaCl_mF_{n-m}$. Reproduced with permission from ref. [66]. Copyright 2023, Science Advances.

including $LiNbOCl_4$ [303,341], $LiTaOCl_4$ [303,342], and $Li_3ZrCl_4O_{1.5}$ [340]. Advanced characterization and comprehensive research are needed to probe local structures and factors governing ionic conduction, guiding both optimization of existing halides and discovery of novel electrolytes.

4.2. Electrochemical stability

To achieve exceptional performance in ASSLBs, SSEs must simultaneously satisfy two fundamental conditions: high Li^+ conductivities and wide ESWs. Halide-based SSEs have been particularly renowned for their high intrinsically electrochemical oxidation stability since their discovery; therefore, no additional protective layers are required between the oxide cathodes and the halide-based SSEs in most cases [62]. Wang et al. [334] studied the intrinsic ESWs of Li–M–X ternary fluorides, chlorides, bromides, iodides through first principles computation, making a comparison with oxides and sulfides in Fig. 16a. Clearly, fluorides possess the widest ESWs and best oxidation stability above 6 V due to the large electronegativity of F^-. However, they are rarely employed in batteries, because F^- with a smaller radius constructs an anionic framework with narrow ion channels, impeding Li^+ transportation (< 0.01 mS cm^{-1}) [343]. Iodides encounter the opposite situation to fluorides, endowed with high conductivity but poor oxidation stability, even worse than notoriously unstable sulfides. Chlorides, conversely, strike a good balance between decent ionic conductivity above 1 mS cm^{-1} and excellent oxidative potential beyond 4 V, capable of matching most oxide cathodes without any protective coating or even of growing *in situ* on cathode with low interfacial impedance [320,344–346]. These advantages rationalize why chlorides are the most popular halide electrolytes and hold promise for replacing sulfides and oxides in future ASSLBs. Bromides are limited by their inferior electrochemical stability, with an upper voltage limit of only 3–4 V. This restricts their compatibility with various cathodes, often necessitating specific electrode selection or interfacial engineering for high-voltage operation. Achieving high operational voltage ($>$ 4.5 V) is a key pursuit for high-energy-density storage devices. Nevertheless, even typically stable chlorides struggle to reach this limit, as Cl^- tends to oxidize above approximately 4.3 V, requiring specialized modification on composition or interface.

Incorporation of highly oxidative F into halide-based SSEs has proven effective in extending electrochemical stability at the cathode side [66,330,343,347]. For example, Sun et al. [348] designed a dual-halogen lithium-ion conductor $Li_3InCl_{4.8}F_{1.2}$ by ball milling and subsequent annealing to address the electrochemical instability issue. The inclusion of F resulted in a dense, crack-free morphology, ensuring intimate contact with cathode. More importantly, F atoms selectively occupied specific lattice sites in Li_3InCl_6, contributing to the formation of fluorination interphases (LiF, $LiInF_4$ and InF_3). These interphases featur broad ESWs with ultrahigh upper limits above 6 V, effectively suppressing interfacial reactions at the cathode side [347]. Full cells employing dual-halogen electrolytes charged steadily at 4.8 V (vs. Li^+/Li), confirming their high-voltage stability. Mixed-metal-cation electrolytes reap the benefits of both superior ionic conduction and enhanced oxidative decomposition resistance via local structure distortion caused by the discrepancy in ionic radii. For instance, $Li_2In_{1/3}Sc_{1/3}Cl_4$ formed stable interfaces with bare-LCO, bare-NCM622 or NCM85 and operated impressively steadily at 4.8 V (vs. Li^+/Li) [302]. Similarly, Zr^{4+} substitution in Li_3YCl_6 and Li_3ErCl_6 enabled uncoated-LCO ASSLBs with good cycling performance up to 4.5 V (vs. Li^+/Li) [332]. Recently, Luo and Hang's group [349] designed a multi-cation mixed chloride $Li_{2.75}Y_{0.16}Er_{0.16}Yb_{0.16}In_{0.25}Zr_{0.25}Cl_6$ based on high entropy stability effect. The severe structure distortion within this high-entropy material effectively regulated ion kinetics and distribution. Cl^- exhibited a confined vibration range and reduced kinetic oxidation, improving the intrinsic oxidative resistance of electrolyte beyond 4.6 V. Furthermore, interfacial engineering seems universally applicable to SSEs and demands consideration of interfacial ion conduction. One strategy involves preemptively introducing artificial protective and conductive interlayers to counteract the resistive interphases formed by electrolyte decomposition at the cathode side. Lee et al. [350] employed this approach by solution-coating a Li_3PO_4 protective layer between high-voltage, cobalt-free, Fe^{3+}-doped $LiNi_{0.5}Mn_{1.5}O_4$ (Fe-LNMO) and Li_3InCl_6. This ASSLB displayed exceptional cycling performance with a stabilized interphase at a high voltage ($\approx$ 4.7 V). Exploration of the interface chemistry revealed that synergistic proper doping and selective coating reduced interfacial resistance. Crucially, the protective layer extended the ESW beyond the intrinsic limit of electrolyte, inhibiting parasitic reactions involving Li_3InCl_6 and enabling full utilization of the capacity of Fe-LNMO cathode. Further, Zhang et al. [351] highlighted the disadvantages of artificial interlayers, such as nonuniformity, unsustainability, and complexity, and proposed a surface lattice doping strategy to address the interfacial instability challenge. Specifically, they prepared LCO@$AlPO_4$ precursors and calcined at 800 °C to transform these into LCO cored with Al/Co/Li disordered shells, accompanied by Li^+-conductive Li_3PO_4 particles on the surface of active material (Fig. 16b). During sintering, Al^{3+} diffused homogeneously into surface lattice of oxide with a controlled manner, primarily enabled by the precise manipulation of $AlPO_4$ thickness. This reconstructed surface flattened Li chemical potential difference and mitigated chemical/electrochemical instability in halides at high voltage. Consequently, the ASSLBs exhibited excellent rate and cycle performance (88.5 % capacity retention over 2000 cycles at 3C at RT) and a high areal capacity (9.1 mAh cm^{-2}) at 4.5 V.

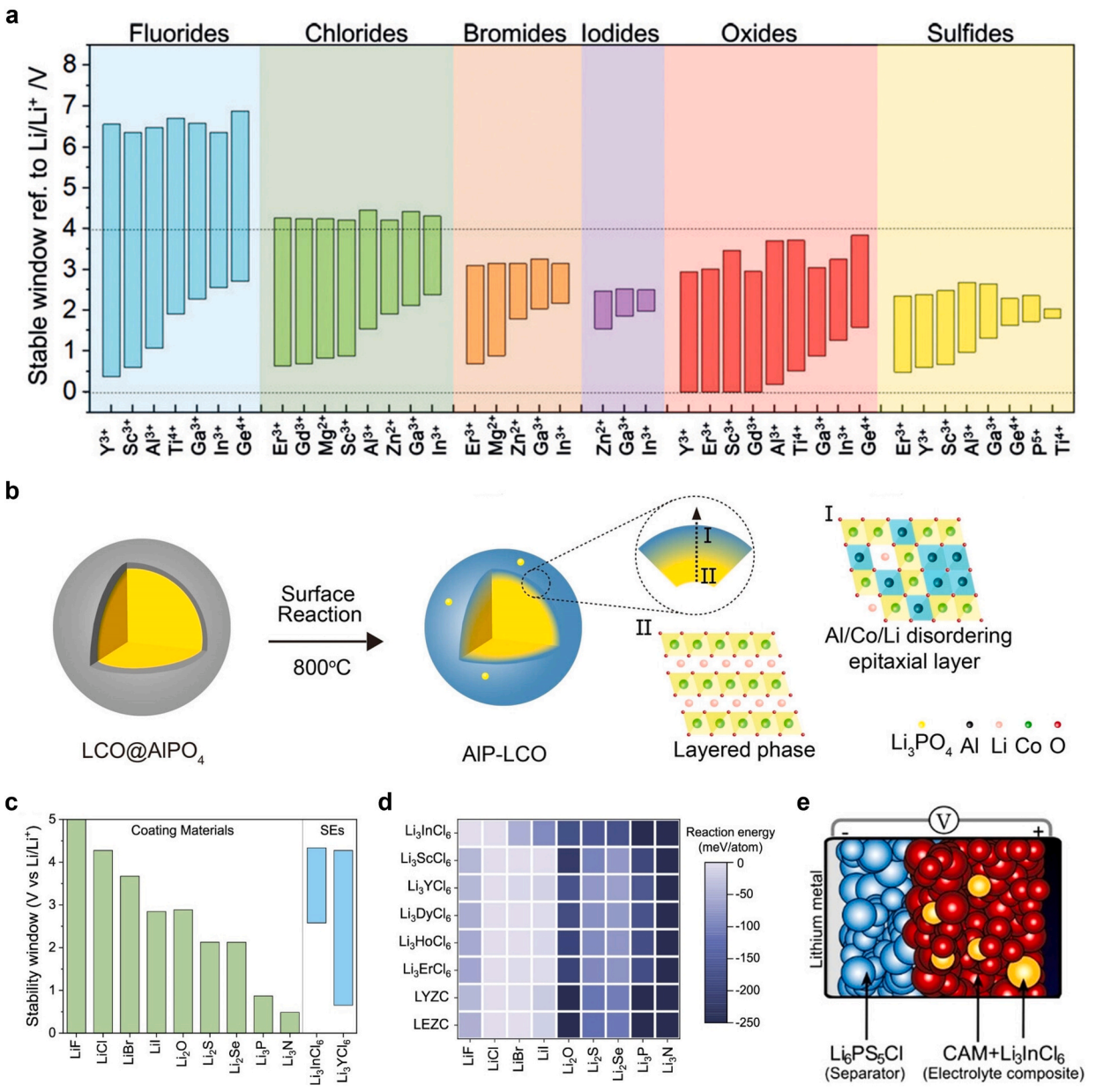

Fig. 16. (a) Calculated thermodynamics intrinsic electrochemical windows of Li–M–X ternary fluorides, chlorides, bromides, iodides, oxides, and sulfides. Reproduced with permission from ref. [334]. Copyright 2019, Angewandte Chemie International Edition. (b) Schematic illustration of the surface modification of $LiCO_2$. Reproduced with permission from ref. [351]. Copyright 2021, Advanced Energy Materials. (c) ESWs of binary coating materials for the interface between the Li metal anode and chloride SSEs. (d) Heatmap of the reaction energy between binary coating materials and chloride SSEs. Reproduced with permission from ref. [354]. Copyright 2021, ACS Applied Materials & Interfaces. (e) Schematic ASSLB bilayer structure with Li_3InCl_6 as cathode electrolyte and LPSC as separator towards Li anode. Reproduced with permission from ref. [353]. Copyright 2021, Angewandte Chemie International Edition.

Using fluorides as electrolyte is the most direct and effective approach to mitigating the interfacial issue. The successful synthesis of β-Li_3AlF_6 by mechanical milling previously reported with 0.01 mS cm^{-1} at 100 °C shed light on the potential of fluorides as stable SSEs, and continued efforts are required for efficient ion conduction [343].

In most cases, halide (especially chloride)-based ASSLBs possess apparent advantages of unobstructed Li^+/e^- transfer at uncoated cathodes and broader operational voltage range over sulfide-based counterparts, showcasing strong market competitiveness. Nevertheless, the interfacial compatibility of halides with lithium metal is problematic [352]. Riegger et al. [353] studied the formation of a reaction layer between Li_3InCl_6 (Li_3YCl_6) and lithium through *in situ* XPS and EIS characterization. The interface was identified as

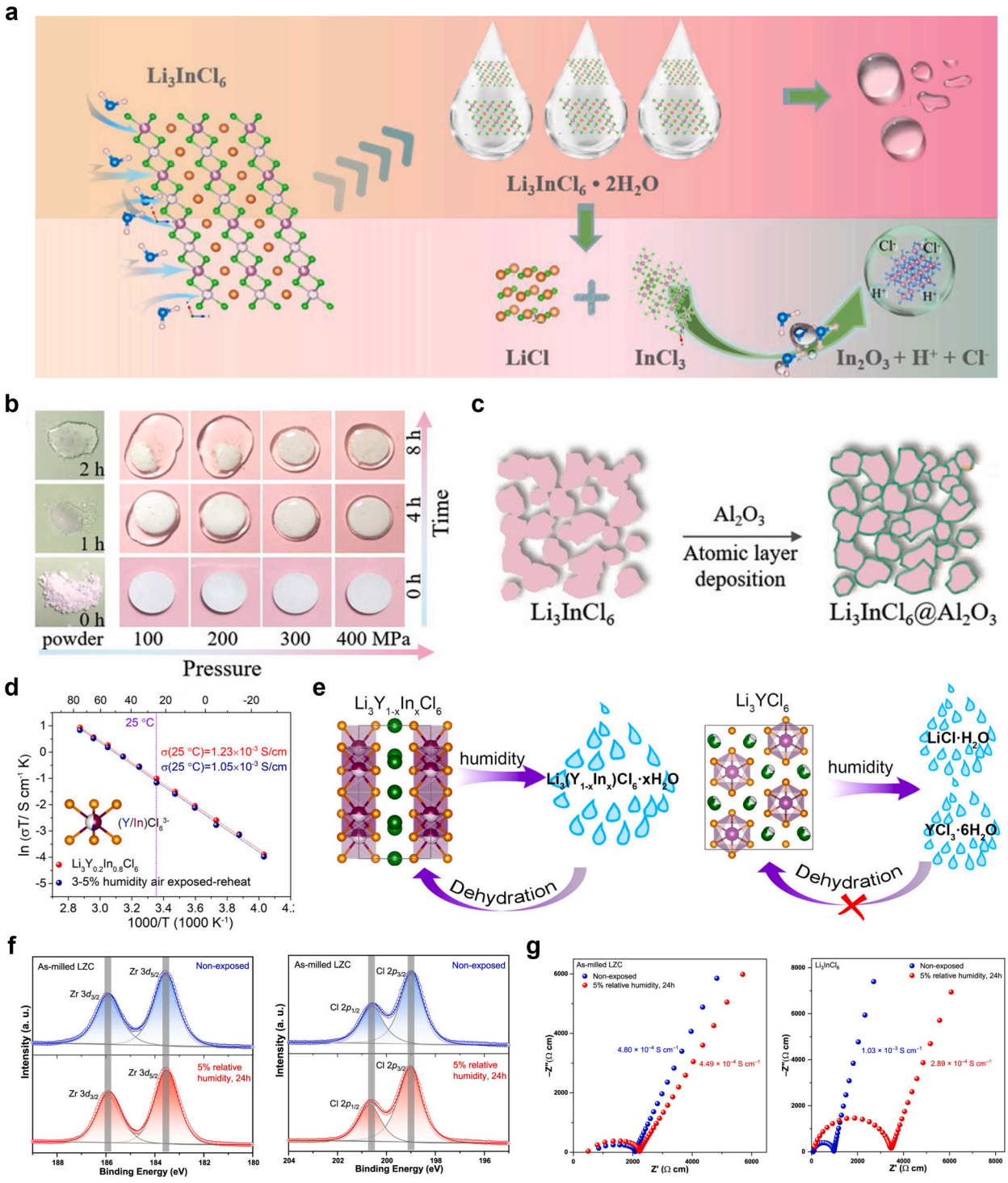

Fig. 17. (a) Schematic diagram of Li_3InCl_6 reaction mechanism in air. (b) Digital photos of the macroscopic morphology changes of Li_3InCl_6 powder and Li_3InCl_6 pellets (fabricated under different pressures) over time upon exposure to air (25 °C, 35 ± 5 % RH). (c) Schematic diagram of coating Li_3InCl_6 with Al_2O_3 by ALD. Reproduced with permission from ref. [359]. Copyright 2021, Advanced Functional Materials. (d) Arrhenius plots of $Li_3Y_{0.2}In_{0.8}Cl_6$ before and after exposure to air with 3–5 % humidity for 12 h and reheated. (e) Schematic illustration of the humidity stabilities of $Li_3Y_{1-x}In_xCl_6$ and Li_3YCl_6. Reproduced with permission from ref. [361]. Copyright 2020, Nano Letters. (f) Zr-3d and Cl-2p XPS of the as-milled LZC, and (g) Nyquist plots of the as-milled LZC and Li_3InCl_6 before and after exposure to an atmosphere with 5 % RH. Reproduced with permission from ref. [301]. Copyright 2021, Nature Communications.

thermodynamically unstable with reduced In^0 and continuously increasing interfacial impedance, which suggested the infeasibility of halide-based ASSLBs. Yu et al. [354] unveiled the thermodynamic instability of representative chlorides due to relatively high reduction potentials (usually > 0.6 V) derived from the reactive central metal ions. The reducible metallic ions tend to turn into elemental metals and then readily form MIEC interphases, leading to continuous decomposition and performance degradation of SSEs and ultimately battery short circuit. They also proposed artificial coating as an effective strategy and demonstrated that binary halides are appropriate coating materials between the metallic Li anode and lithium chloride SSEs based on the electrochemical and chemical compatibility studies in Fig. 16c–d. In order to improve the intrinsic instability against Li anode, Sun's group [348] designed a F-doped $Li_3YBr_{5.7}F_{0.3}$, where a robust F-rich interphase spontaneously formed on the Li metal surface during plating/stripping process. Li|$Li_3YBr_{5.7}F_{0.3}$|Li symmetric cell delivered an exceptional cycle life exceeding 1000 h with almost constant potential at 0.1 mA cm^{-2} and the capacity of 1 mAh cm^{-2}. Importantly, this spontaneously formed interphase outperformed artificial fluorinated passivation layers over time in both symmetric and full cells, which attributed to a more uniform fluoride distribution and intimate solid contact at the anode interface.

Bilayer configuration combining halide as cathode electrolyte and lithium-stable materials as the anode electrolyte is often adopted to improve the electrode compatibility, as shown in Fig. 16e. The halide–LPSC bilayer electrolyte offers opportunity for stable operation of halide-based ASSLBs due to the negligible impedance between halides and LPSC. However, the bilayer configuration concept has been severely questioned. Tarascon et al. [355] unraveled that a pronounced chemical/electrochemical incompatibility of Li_3InCl_6 toward LPSC and β-Li_3PS_4, leading to the poor performance reversibility and increasing interfacial resistance upon cycling, which turned worse at higher temperature due to the intensified reaction [356]. Subsequent characterization using in-depth time-of-flight secondary ion mass spectrometry (ToF-SIMS) and focused ion beam scanning electron microscopy (FIB-SEM) detected an In-S species-rich region at the Li_3InCl_6/LPSC contact area after several cycles [357]. This observation provided direct evidence for the interfacial degradation drawback due to the chemical incompatibility between chlorides and sulfides. To address this issue, Tarascon et al. [356] further introduced a highly conformal, uniform, and dense Li_3PO_4 protective layer between Li_3InCl_6 and LPSC via ALD technology. The cell containing a 2 nm-thick Li_3PO_4 layer realized both higher charge/discharge capacity (172/150 mAh g^{-1}) and extraordinary long-term cycling performance (92.3 % retention after 400 cycles). Moreover, the buffer layer in the heterostructure is not limited to sulfides, and can extend to other materials possessing fast Li^+ conduction along with stability towards Li and halides. For example, Deng et al. [358] adopted an antiperovskite-type halide Li_2OHCl in bilayer structure to overcome the aforementioned interfacial problem. The cold-pressing ASSLB combined the high ionic conductivity and oxidative stability of Li_3InCl_6 with the high Li compatibility of Li_2OHCl, presenting excellent rate performance and long-term cycle stability even over 3000 h at an elevated temperature. Developing new electrolytes intrinsically compatible with lithium metal is another vital strategy for building a stable interface. Ta-doped $Li_{0.388}Ta_{0.238}La_{0.475}Cl_3$ featuring a unique UCl_3-type lattice enabled stable cycling for over 5000 h without any protection in LMB. This stability was attributed to a low electronegativity of central metallic element (Ta and La) and *in situ* formation of an electrically insulated LiCl passivation layer for gradient reduction [304]. This work opens vast possibilities for enriching this family by substituting La with other lanthanides or selecting dopants with low electronegativity, clearly pointing out a promising new research direction. Aside from composition modification and structure design of electrolytes, utilizing alloy anodes such as $Li_{0.5}In$, $Li_{15}Si_4$, and $Li_{11}Sn_6$ is an effective approach in suppressing reductive reaction of halides at the interface. However, this approach comes at the expense of a reduced cell voltage range and energy density to some degree [332,355–357].

In conclusion, state-of-the-art halide-based SSEs enable high-voltage operation (> 4.5 V) with oxide cathodes through protective layers or compositional modifications, yet their application is hindered by Li-driven reduction of central metal cations. While introducing interlayers mitigates interfacial degradation, the chemical/electrochemical compatibility at both halide/interlayer and Li/interlayer interfaces critically governs overall battery stability and lifespan due to bilayer architectures. Given the manufacturing complexity of bilayer structures, future breakthroughs necessitate identifying redox-robust central cations to achieve intrinsically stable monolithic halide-based SSEs.

4.3. Air stability

Consistent with sulfide-based SSEs, halide-based SSEs suffer significant structure and performance degradation upon moisture exposure, necessitating strict handling protocols during preparation and transportation. However, the hydrolysis mechanism of halides apparently varies from that of sulfides (based on HSAB theory). Wang et al. [359] investigated the degradation mechanism of Li_3InCl_6 and Li_3YCl_6, finding that the moisture tolerance was correlated with the central metal, as evidenced by the higher water absorption of Li_3YCl_6 than Li_3InCl_6. When exposed to water, Li_3InCl_6 converts into crystalline hydrate $Li_3InCl_6{\cdot}2H_2O$, a small fraction of which decomposes into LiCl and $InCl_3$, and the $InCl_3$ further hydrolyzes to form corrosive acid and In_2O_3 (Fig. 17a). These degradation products characterized by XRD, Raman spectroscopy, and pH measurements represented irreversible electrolyte loss. Most of the hydrate, however, remained intact and could fully recover to Li_3InCl_6 upon heat treatment, explaining why Li_3InCl_6 could be synthesized through a water-mediated method. Besides, the contact area with air also affected the hydrolysis process that highly pressurized Li_3InCl_6 pellets exhibited higher air stability than powder (Fig. 17b). Additionally, coating on the surface of Li_3InCl_6, such as Li_3InCl_6@Al_2O_3 via ALD in Fig. 17c, performed effectively in ambient environment (35 ± 5 % RH) by reducing water absorption and extending liquifying time severalfold.

To date, Li_3InCl_6 exhibits the excellent resistance to irreversible hydrolysis among halide-based SSEs [63,359]. Doping with indium (In^{3+}) at the central metal site is an effective strategy to improve air instability by forming almost completely recoverable hydrate and inhibiting further degradation [360,361]. Sun et al. [361] prepared a series of $Li_3Y_{1-x}In_xCl_6$ ($0 \le x < 1$) and verified that the humidity stability was greatly improved when adding sufficient In^{3+} content (x > 0.5). The hydrated intermediates follow reversible hydration/

dehydration routes, retaining conductivity above 80 % after moisture exposure for 12 h (Fig. 17d–e). Besides, engineering new intrinsically moisture-stable electrolytes is important for advancing halide family. Impressively, Li_2ZrCl_6 displayed no sign of either moisture uptake or conductivity degradation after exposure to 5 % RH atmosphere. This performance even outperformed the reported

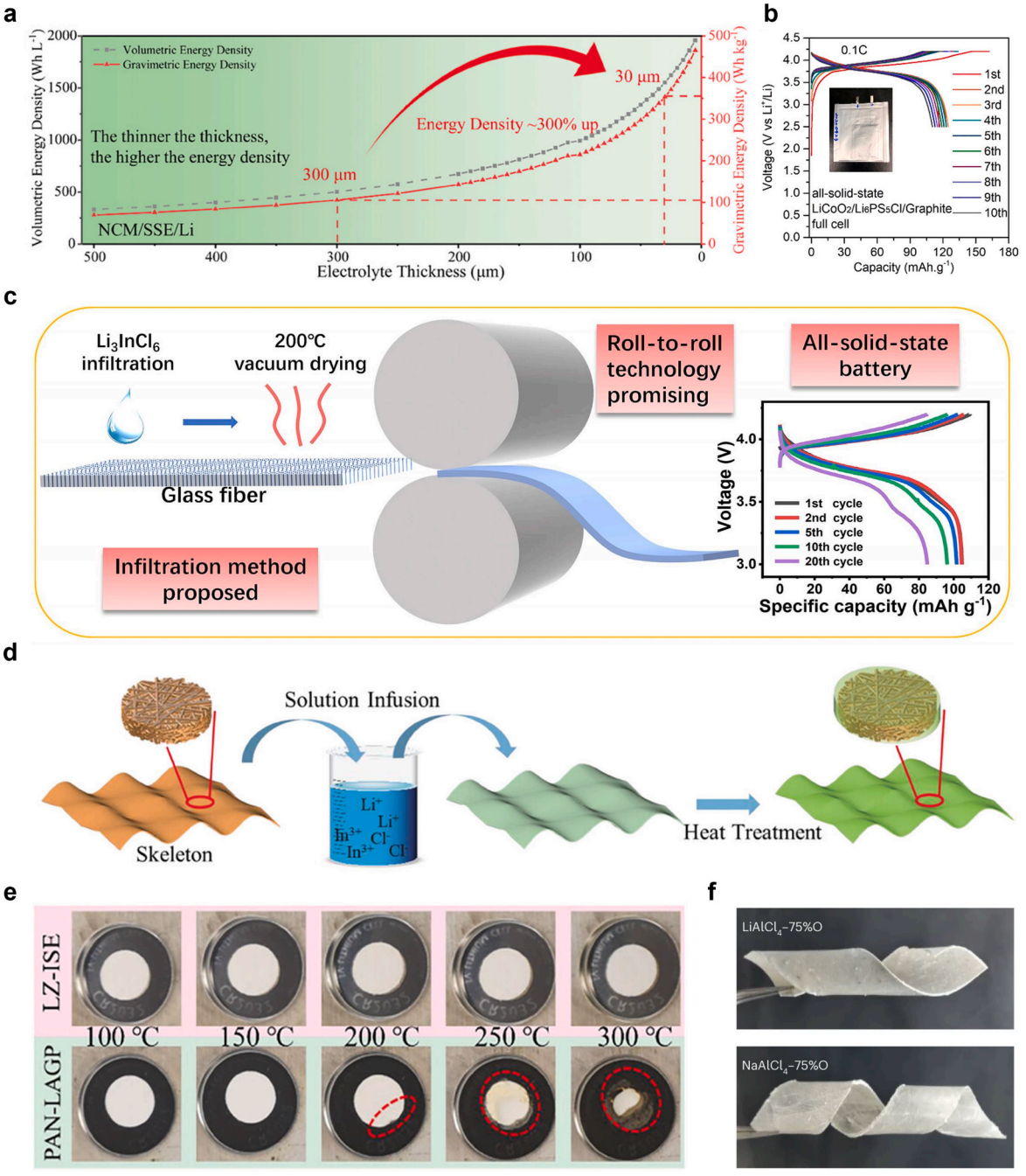

Fig. 18. (a) Energy density as a function of electrolyte thickness. (d) Schematic illustration of the preparation of the Li_3InCl_6/ZrO_2 ISE membrane (LZ-ISE). (e) Photographs of LZ-ISE membranes and PAN-LAGP films at different temperatures. Reproduced with permission from ref. [363]. Copyright 2023, Advanced Energy Materials. (b) Initial 10 charge–discharge curves of ASSLBs with a configuration of Li_3InCl_6@LCO/Li_3InCl_6 + LPSC/Graphite@LPSC. Reproduced with permission from ref. [291]. Copyright 2021, ACS Energy Letters. (c) Schematic of preparation of Li_3InCl/glass-fiber CSEs and charge–discharge performance in ASSLBs. Reproduced with permission from ref. [364]. Copyright 2022, Materials Letters. (f) Winding membranes of $LiAlCl_4$-75 %O (LACO75) and $NaAlCl_4$-75 %O (NACO75) obtained by the rolling process. Reproduced with permission from ref. [366]. Copyright 2023, Nature Energy.

Table 3
Comparison of electrochemical performance of various halide-based SSEs.

SSE	Ionic conductivity (mS cm^{-1})	Operating temperature (°C)	Cathode	Voltage range (V, vs. Li^+/Li)	First discharge capacity (mAh g^{-1})	Capacity retention	Rate performance	Ref.
$Li_{2.73}Ho_{1.09}Cl_6$	1.3	25	NCM811	1.9–3.7 (vs. Li^+/LiIn)	172 (0.1C)	73 % (0.1C, 180 cycles)	1C	[327]
Li_3InCl_6	1.49	25	LCO	2.5–4.2	127 (0.1C)	74.8 % (0.1C, 100 cycles)	1C	[63]
Li_3InCl_6	2.04	25	NCM811	1.9–3.8 (vs. LiIn/Li^+)	154 (0.13 mA cm^{-2})	97.4 % (0.1 mA, 70 cycles)	1 mA	[64]
Li_3InCl_6	1.5	25	LCO	3.1–4.2	131.7 (0.1C)	93.8 mAh g^{-1} (0.1C, 200 cycles)	4C	[320]
Li_3YCl_6	0.345	25	LCO	2.6–4.2	139.1 (0.1C)	85.2 % (0.1C, > 50 cycles)	1C	[321]
Li_3InCl_6	0.79	RT	NCM811	2.5–4.4	150.3 (0.05C)	165.7 mAh g^{-1}, 94.8 % (0.1C, 200 cycles)	1C	[323]
$Li_{2.6}Er_{0.6}Zr_{0.4}Cl_6$	1.13	27	LCO	3.0–4.2	147.5 (0.1C)	77 % (0.1C, 500 cycles)	3C	[324]
$Li_{2.7}In_{0.7}Hf_{0.3}Cl_6$	1.28	RT	LCO	3.0–4.2	108.1 (0.1C)	76.3 mAh g^{-1}, 70.8 % (0.1C, 50 cycles)		[325]
$Li_{2.8}Yb_{0.8}Zr_{0.2}Cl_6$	1.1	30	NCM622	2.8–4.3	170 (0.2C)	≈ 80 % (0.2C, > 150 cycles)	1C	[326]
$Li_{2.375}Sc_{0.375}Zr_{0.625}Cl_6$	2.2	25	NCM90,	2.8–4.3	219.4 (0.1C)	≈ 78.1 % (0.5C, > 200 cycles)	3C	[331]
$Li_{2.5}Er_{0.5}Zr_{0.5}Cl_6$	1.4	RT	LCO	3–4.3	> 110 (0.11 mA cm^{-2})	≈ 77 % (0.55 mA cm^{-2}, 200 cycles)		[332]
$Li_{0.388}Ta_{0.238}La_{0.475}Cl_3$	3.02 (30 °C)	30	NCM523	2.2–4.35	163 (0.44C)	81.6 % (0.44C, over 100 cycles)		[304]
1.5LiCl–$(LaCl_3{\cdot}CeCl_3{\cdot}ZrCl_4{\cdot}HfCl_4{\cdot}TaCl_5)_{0.2}$	1.8 (25 °C)	25	LCO	2.5–4.3	217.2 (0.1C)	80 % (4C, 3000 cycles)	5C	[338]
amorphous $LiTaCl_6{\cdot}LiCl$	7.16 (30 °C)	30, −10	$LiNi_{0.88}Co_{0.07}Mn_{0.05}O_2$	2.8–4.3	≈ 205.6 (≈ 0.2C)	99 % (3C, 800 cycles), 77 % (3.4C, 9800 cycles, −10 °C)	4C	[339]
$Li_3ZrCl_4O_{1.5}$	1.35	RT	NCM83	2.5–4.3	185.7 (0.1C)	90.1 % (1C, 300 cycles)	3C	[340]
$Li_{5/3}Cr_{1/3}Zr_{1/3}Cl_4$	0.313	25	LCO	2.6–4.3	108.2 (0.2C)	86 % (1C, 410 cycles)	2C	[344]
$Li_2Sc_{2/3}Cl_4$	1.5	RT	LCO	2.8–4.3	135 (0.5C)	≈ 93 % (0.1C, 110 cycles)	3C	[346]
$Li_3InCl_{4.8}F_{1.2}$	0.51	RT	LCO	2.6–4.47	160.6 (0.063 mA cm^{-2})	102 mAh g^{-1} (0.125 mA cm^{-2}, 70 cycles)		[347]
$Li_3YBr_{5.7}F_{0.3}$	1.8	RT	LCO	2.5–4.2	121.6 (0.14 mA cm^{-2})	70 % (0.14 mA cm^{-2}, 70 cycles)		[348]
$Li_2In_{1/3}Sc_{1/3}Cl_4$	2.0	RT	NCM85	2.8–4.8		> 80 % (3C, 3000 cycles), > 94 % (2C, > 1800 cycles)	3C	[302]
$Li_{2.75}Y_{0.16}Er_{0.16}Yb_{0.16}In_{0.25}Zr_{0.25}Cl_6$	1.171	RT	LCO	2.5–4.2/4.6	185 (0.2C)	88.9 % (0.5C, 500 cycles, 4.2 V), 91.6 % (0.2C, 50 cycles, 4.6 V)	1C	[349]
Li_3InCl_6	1.07	25	$LCO@AlPO_4$	3–4.5	189.8 (0.1C)	94 % (0.2C, 100 cycles), 88.5 % (3C, > 2000 cycles)	1C	[351]
Li_3InCl_6/Li_3PO_4/LPSC		RT	NCM622	2.7–4.3	143 (0.05C)	92.3 % (0.05C, 400 cycles)		[356]
Li_3InCl_6/Li_2OHCl	0.1 (80 °C)	80	LFP	2.7–3.9	148.8 (0.1C)	86.7 % (0.1C, 100 cycles),		[358]
$Li_{2.8}Zr_{0.2}In_{0.8}Cl_6$	1.4	25	NCM811	2.82–4.42	169 (0.2C)	71 % (0.1C, 500 cycles)	2C	[360]

(*continued on next page*)

Table 3 (*continued*)

SSE	Ionic conductivity (mS cm^{-1})	Operating temperature (°C)	Cathode	Voltage range (V, vs. Li^+/Li)	First discharge capacity (mAh g^{-1})	Capacity retention	Rate performance	Ref.
Li_2ZrCl_6	0.81	RT	LCO	2.5–4.2	137 (0.1 C)	91.9 % (0.5C, 100 cycles)	2C	[301]
			NCM811	2.8–4.4	181 (0.1 C)	≈ 93 % (1C, 200 cycles)	2C	
Li_3InCl_6/ZrO_2	0.5	25	LCO	3–4.2	126.6 (0.1C)	80 % (0.1C, 100 cycles)	1C	[363]
			NCM811	3–4.3	140.5 (0.1C)	80 % (0.2C, 200 cycles)		
Li_3InCl_6 (PTFE)	> 1	25	LCO	2.5–4.2	124.3 (0.1C)	83.1 (0.1C, 50 cycles)		[291]
viscoelastic inorganic glass $LiAlCl_{2.5}O_{0.75}$	≈ 1 (30 °C)	60	NCM622	2.8–4.3	173 (1C)	125 (1C, 600 cycles)		[366]
$LiMOCl_4$ (Nb, Ta)	10.4 (M = Nb), 12.4 (M = Ta)	RT	Bare LCO	3.1–4.2	125 (0.1C)	/	5C	[303]

*In addition to individual labeling, ionic conductivity data are obtained at operating temperatures.

Li_3InCl_6, as confirmed by XPS and EIS characterization (Fig. 17f–g) [301]. Building on this concept, Fan's group [362] further enhanced the moisture insensitivity of Zr-based halides through strategic Zn^{2+} doping.

It should be recognized that scientific investigation on air stability of halide-based SSEs remains conspicuously insufficient, with no universal degradation mechanism established for humidity exposure to date. Currently, only two systems, the benchmark Li_3InCl_6 and the emerging Li_2ZrCl_6, exhibit ambient-air stability, yet only under low-humidity conditions to maintain near-pristine structure and performance. Effective measures against moisture at relatively high humidity conditions concentrate on oxide coating, though invariably at the expense of ionic conductivity. Future directions toward air-stable halide-based SSEs must prioritize elucidating reaction mechanisms and influencing factors governing air stability across diverse halides using advanced *operando* characterization, then leveraging these insights to overcome hydrolysis limitations and design intrinsically humidity-tolerant materials.

4.4. Mechanical properties and processing

Halide-based SSEs exhibit cold-pressing compressibility comparable to sulfide-based SSEs, yet face persistent challenges in maintaining interfacial contact and fabricating tens μm-level films, both of which are critical for achieving long-cycle-life and high-energy-density ASSLBs. As shown in Fig. 18a, reducing electrolyte thickness from 300 μm to 30 μm can increase the energy density of cell by up to 300 % [363]. The mainstream solution for mechano-electrochemical decoupling involves compositing with soft polymers. For instance, incorporating merely 0.5 wt% PTFE fibers enabled fabrication of a bendable Li_3InCl_6 sheet via shear mixing, and this sheet was subsequently pressed into a freestanding 15–20 μm membrane using roll-to-roll technology [291]. Solid-state pouch cells with bilayer Li_3InCl_6 and LPSC membranes delivered high capacity (124.3 mAh g^{-1} at 0.1C) and initial CE (89.4 %), as presented in Fig. 18b. Fig. 18c further demonstrated that Li_3InCl_6 dissolved in water/alcohol mixed solvent could infiltrate glass fiber separators, enabling thickness reduction via roll-pressing [364]. Li et al. [363] fabricated an ultrathin self-standing all-inorganic halide membrane with a minimum thickness of 25 μm. Benefiting from water-mediated synthesis, Li_3InCl_6 spontaneously precipitated onto an electrospun ZrO_2 nanowire skeleton immersed in LiCl/$InCl_3$ solution, as clearly depicted in Fig. 18d. Li_3InCl_6/ZrO_2 composite exhibited the ionic conductivity comparable to Li_3InCl_6 powder. Reduced electrolyte thickness decreased the resistance to 1/11 of the original value, contributing to superior rate performance and power density of the battery. Moreover, exceptional thermal stability maintained composite film integrity beyond 300 °C, surpassing oxide/polymer films due to the absence of organic components (Fig. 18e). Alternatively, Li_3InCl_6 films can be directly fabricated via wet-slurry method using compatible binders and solvents, analogous to sheet-type electrode production [364,365]. Dai et al. [366] improved the inferior mechanical stability of inorganic electrolyte by developing a class of viscoelastic inorganic glass $MAlCl_{4-2x}O_x$ (MACO, M = Li, Na). Oxygen doping in tetrachloroaluminates lowered the glass transition temperature, yielding polymer-like flexibility at RT (Fig. 18f). This enabled tight curling, scalable thin-film roll production, and intimate electrode contact. The resulting pressure-less Li- and Na-based SSBs (< 0.1 MPa) achieved high capacity, CE, and stable cycling performance, eliminating the need for high stack pressure while boosting energy density. The versatile, cost-effective, and oxidatively stable MACO system have established a new research paradigm: vitrifying inorganic SSEs to achieve polymer-like viscoelasticity at RT, thereby resolving interfacial mechanical issues.

4.5. Cost

Cost is the primary consideration for large-scale SSE production and remains a conspicuous obstacle hindering the transition of halide-based SSEs from laboratory to practical application [13,336]. Costs mainly comprise two categories: raw materials and processing cost, and the dominated factor varies among different electrolytes based on their chemistry and processability. Oxide-based SSEs require energy-consuming HT fabrication and assembly process for densification and sufficient electrode infiltration [118,367–369], while sulfide-based SSEs face high costs from irreplaceable Li_2S precursors ($653.87 kg^{-1}) [370,371]. For halide-based SSEs, the central metal halides rather than lithium-containing compounds (e.g., LiCl at $5.88 kg^{-1}) constitute the primary cost driver, as their rare-earth metal elements exhibit low crustal abundance and high expense, thereby limiting mainstream adoption [310,336].

The crustal abundance of Zr element is 165 ppm, 660 times greater than that of commonly utilized In. This abundance disparity enables the precursor $ZrCl_4$ to be priced nearly two or three orders of magnitude lower than other metal halide precursors. Previously reported $ZrCl_4$ as dopant yields high-ion-conduction and cost-effective electrolytes, such as $Li_{2.7}Yb_{0.7}Zr_{0.3}Cl_6$, $Li_{2.6}In_{0.6}Zr_{0.4}Cl_6$, $Li_{2.5}Er_{0.5}Zr_{0.5}Cl_6$, $Li_{2.375}Sc_{0.375}Zr_{0.625}Cl_6$ [324,326,328,331] discussed above. Recently, Li–Zr–Cl (LZC)-based materials have gained prominence due to cost–performance advantages. Ma et al. [301] synthesized LZC via mechanochemical method using a stoichiometric LiCl:$ZrCl_4$ mixture (molar ratio of 2:1), and the considerably low-cost system enables cost-competitive ASSLBs production. LZC also demonstrated high ionic conductivity (0.81 mS cm^{-1} at 25 °C), good deformability, excellent compatibility with oxide cathodes, and exceptional moisture stability. Oxygen-doped $Li_{1.75}ZrCl_{4.75}O_{0.5}$ further elevated conductivity to 2.42 mS cm^{-1} at 25 °C while enhancing electrochemical stability, with raw material costs as low as $11.60 kg^{-1} [305]. Moreover, Sun's group [340] developed a rarely reported amorphous LZC system, using oxygen to mediate amorphization and achieve high ionic conduction through corner-sharing Zr–O/Cl polyhedra that lower ion-transport activation energy. Above all, Li_2ZrCl_6 and derivatives benefiting from the cost-effective and abundant metal halide demonstrated strong potential to accelerate halide-based SSE industrialization.

4.6. Summary

Although ion-conducting halides were identified many years ago, halide-based SSEs with suitable electrochemical properties have

only emerged in recent years, and the relative development in ASSLBs was summarized in Table 3, offering significant room for further optimization. Some major limitations hinder their production, storage, and implementation: lithium anode instability, moisture sensitivity, and high raw material costs. To address the instability against lithium, advanced strategies include screening compatible interlayers with both halides and Li anodes to prevent direct contact and maintain the stability of battery systems [372], incorporating redox-inactive dopants (Ta^{5+}) to elevate reduction potential thresholds [304], and *in situ* construction of electronically insulating and mechanically robust LiF layers to suppress SSE reduction and dendrite penetration [348]. For moisture sensitivity, more water-resistant halides are required to support wet-synthesis methods (e.g., water-, ammonium-, or ethanol-mediated synthesis) for scalable production. Regarding cost, leveraging experimental characterizations and computational simulations to understand ion mobility mechanisms, particularly in systems employing precursors such as $ZrCl_4$, will accelerate the exploration of highly conductive and cost-effective SSEs. Beyond these intrinsic challenges, processability can be improved by compositing with polymers or producing viscoelastic chloride glasses to achieve free-standing halide-based SSE membranes, contributing to high energy density and low stacking pressure for cell operation. While chlorides and bromides dominate, fluorides have been overlooked due to poor ion conduction. However, their ultra-wide ESW and high oxidation limit—critical for pairing with ultrahigh-voltage cathodes—merit more attention. Promising approaches to enhance fluoride utilization include mixing with chlorides/bromides and designing highly conductive interface phases. Unlike sulfides, halides release no toxic gases, facilitating environmental certification. Though currently experimental, industrialization of halide-based SSEs will accelerate with technical advances and policy support.

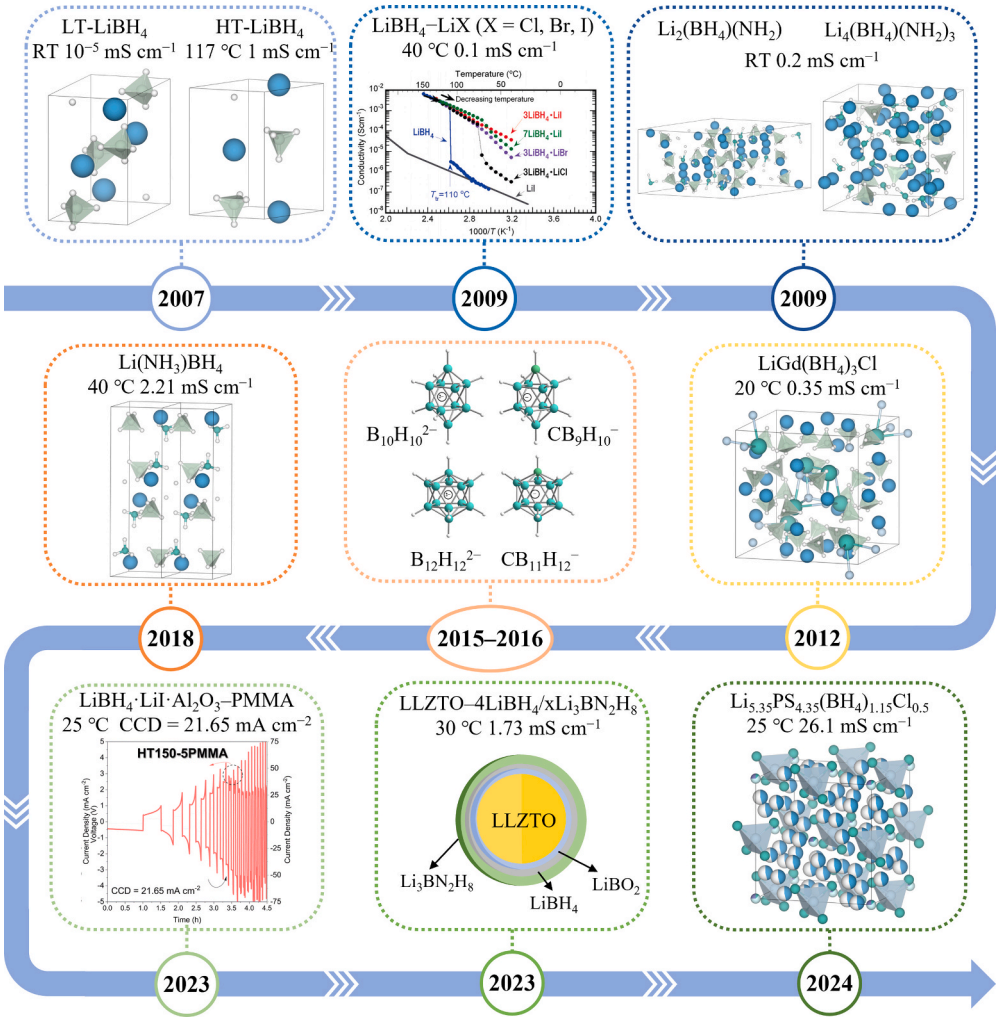

Fig. 19. A brief review of the development of hydride-based SSEs. Reproduced with permission from ref. [42,47,52,54,382,394–398].

Table 4
Comparison of electrochemical properties of various hydride-based SSEs.

Electrolyte(thickness)	t_{Li+}	σ (mS cm^{-1})	ESW vs. Li^+/Li (V)	Li||Li symmetric cells Current–Capacity (mA cm^{-2}–mAh cm^{-2}	Cycling life (h)	CCD (mA cm^{-2})	Full cells Cathode	Cycling number (N)	CE (%)	Capacity retention (%)	Ref.
$LiBH_4$–LiBr–LiCl (0.2–0.6 mm)		0.013 (30 °C)	4.04								[406]
$Li_4(BH_4)_3I$	0.7 (100 °C)	3.8×10^{-3} (30 °C)		0.2–0.2 (100 °C)	250	1.1	NS–SPAN (100 °C)	150	99	64.8 (0.1C)	[458]
$Li_2[B_{10}I_{10}]$ (1.0–1.7 mm)	0.999 (100 °C)	3.12×10^{-3} (25 °C)	3.3	0.4–0.2	66	0.9					[407]
$Li_4(BH_4)_4B_{10}H_{14}$ (0.7 mm)		0.021 (30 °C)									[408]
0.7Li(CB_9H_{10})–0.3 ($CB_{11}H_{12}$) (1.0 mm)		6.7 (25 °C)	5	0.2–0.1	300		S (60 °C)	100	≈ 100	62.85 (5C)	[409]
$Li_3(B_{11}H_{14})(CB_9H_{10})_2$ (0.6–1.0 mm)		1.1 (25 °C)	2.6	0.05–0.5	620	0.16 (60 °C)	TiS_2	150	99.5	82 (0.2C)	[410]
$Li_2B_{10}H_{10-y}$ (0.5–1.4 mm)		7.6×10^{-3} (30 °C)	6								[412]
$Li_3(CB_{11}H_{12})_2(CB_9H_{10})$ (0.85 mm)		1.5 (25 °C)	3.9 (60 °C)				NCM811	2000	> 99	54 (0.5C)	[411]
$Li_3(BH_4)(NH_2)_2$ (1.6 mm)		6.4 (40 °C)					$Li_4Ti_5O_{12}$		≈ 100	101 (5C)	[419]
$LiBH_4$·AB (2 mm)	0.9993 (40 °C)	0.404 (25 °C)	2	0.2–0.03	40	3.0					[44]
$LiBH_4$· CH_3NH_2 (1.6 mm)	0.9983	1.24 (25 °C)	2.1				TiS_2	9	98	30 (0.05C)	[45]
HP-$LiBH_{2.4}$ (1 mm)	0.97	0.27 (35 °C)	5	1–	1000		TiS_2	50	≈ 100	83.7 (0.1C)	[434]
$LiBH_4$·xNH_3–Li_2O (1–1.5 mm)		0.54 (20 °C)	3.8	0.1–0.05	30						[437]
LiF-decorated $Li_2B_{12}H_{12}$ (2 mm)	0.95	0.50 (75 °C)	5			3.6	$LiFeO_4$	30	≈ 100	84	[435]
H400-AlBH		1.38 (25 °C)	6	7.56–	2700	15.12	$LiCoO_2$	400	99.82	89.8 (0.5C)	[46]
$LiBH_4$·1/2NH_3–Al_2O_3 (1 mm)		1.1 (30 °C)	3.6	0.1–0.05	24						[438]
$LiBH_4$·1/2NH_3–MgO (1 mm)		4.0 (25 °C)	4.0	0.1–0.625	40						[439]
$Li_4(BH_4)_3I$ @SBA-15 (3 mm)	0.97	0.25 (35 °C)	5	0.5–	350	2.6 (55 °C)	$Li_4Ti_5O_{12}$ (55 °C) S (55 °C) $LiCoO_2$ (55 °C)	3	≈ 100	90 (0.05C) 83 (0.05C) 87 (0.05C)	[442]
$LiBH_4$–$LiNH_2$@Al-SBA-15		0.5 (30 °C)									[446]
$Li_{16}(BH_4)_{13}I_3$@g-C_3N_4 (1 mm)		0.315 (30 °C)	5 (60 °C)	0.3–	250		$Li_4Ti_5O_{12}$ (60 °C)	200		91.1	[443]

(*continued on next page*)

Table 4 (*continued*)

Electrolyte(thickness)	t_{Li+}	σ (mS cm^{-1})	ESW vs. Li^+/Li (V)	Li||Li symmetric cells Current–Capacity (mA cm^{-2}–mAh cm^{-2}	Cycling life (h)	CCD (mA cm^{-2})	Full cells Cathode	Cycling number (N)	CE (%)	Capacity retention (%)	Ref.
$LiBH_4$/2 (h-BN) (0.5–2.0 mm)	0.97 (25 °C)	0.115 (40 °C)	5	0.5– (70 °C)	>500	4.6	TiS_2	30	98	83 (0.1C)	[444]
							NCM811	20		85 (0.1C)	
LLP20 (1 mm)	0.9999	0.377 (30 °C)	5	0.5–0.5	1000	1.6	$Li_4Ti_5O_{12}$ (100 °C)	20	≈ 100	89.1 (0.5C)	[43]
							SPAN (100 °C)	100 (0.05C)			
$L_{2.46}(PS_4)_{0.46}(BH_4)_{1.08}$		11 (25 °C)	5				$LiNi_{0.7}Mn_{0.15}Co_{0.15}O_2$	100 (0.5C)	≈ 100		[450]
$Li_5PS_4(BH_4)_2$ (0.9–1.1 mm)		3.9 (25 °C)					NCM811	20 (0.2C)	≈ 100		[452]
$Li_{5.35}PS_{4.35}(BH_4)_{1.15}Cl_{0.5}$		26.1 (25 °C)	5	1–1	2000	2.1	NCM811	100		72.6 (0.5C)	[398]
Li_3PS_4·1.8$LiBH_4$·0.7LiBr		14.4 (25 °C)	5			2.3	$LiNi_{0.7}Mn_{0.15}Co_{0.15}O_2$	300	84	92 (0.5C)	[451]
LLZTO–4$LiBH_4$ (1–2 mm)	0.9999	0.0802 (30 °C)	6	0.15–0.075	1000 (60 °C)	0.7	$LiCoO_2$	21	95	91	[49]
LLZTO–4$LiBH_4$/ x$Li_3BN_2H_8$ (0.75–1.5 mm)	0.9999	1.73 (30 °C)	3.7	0.15–	1600	1.3	TiS_2	80	≈ 100	98.5 (0.1C)	[397]
LLZTO–x$Li_4(BH_4)_3I$ (0.7 mm)		0.0135 (40 °C)	5	0.1–	2200	0.7					[51]
25($Li_4(BH_4)_3I$)@75LLZTO	0.9999	0.108 (40 °C)	2.5	4.0–	200	4.0	SPAN	100	≈ 100	91 (0.2C)	[48]
PEO–$Li_4(BH_4)_3I$	0.45	0.409 (70 °C)	3.6	0.05–0.05	> 360		SPAN	75	> 99	62.2 (0.12C)	[50]
HT150-5PMMA	0.99999	0.51 (25 °C)	10	10.83–	6000	21.65	$LiCoO_2$	300		94.2 (0.5C)	[47]
AOLiBHI–xPMMA		0.447 (25 °C)	5.0	5.10–	5000	11.43	$LiCoO_2$	200		86.62 (0.5C)	[454]

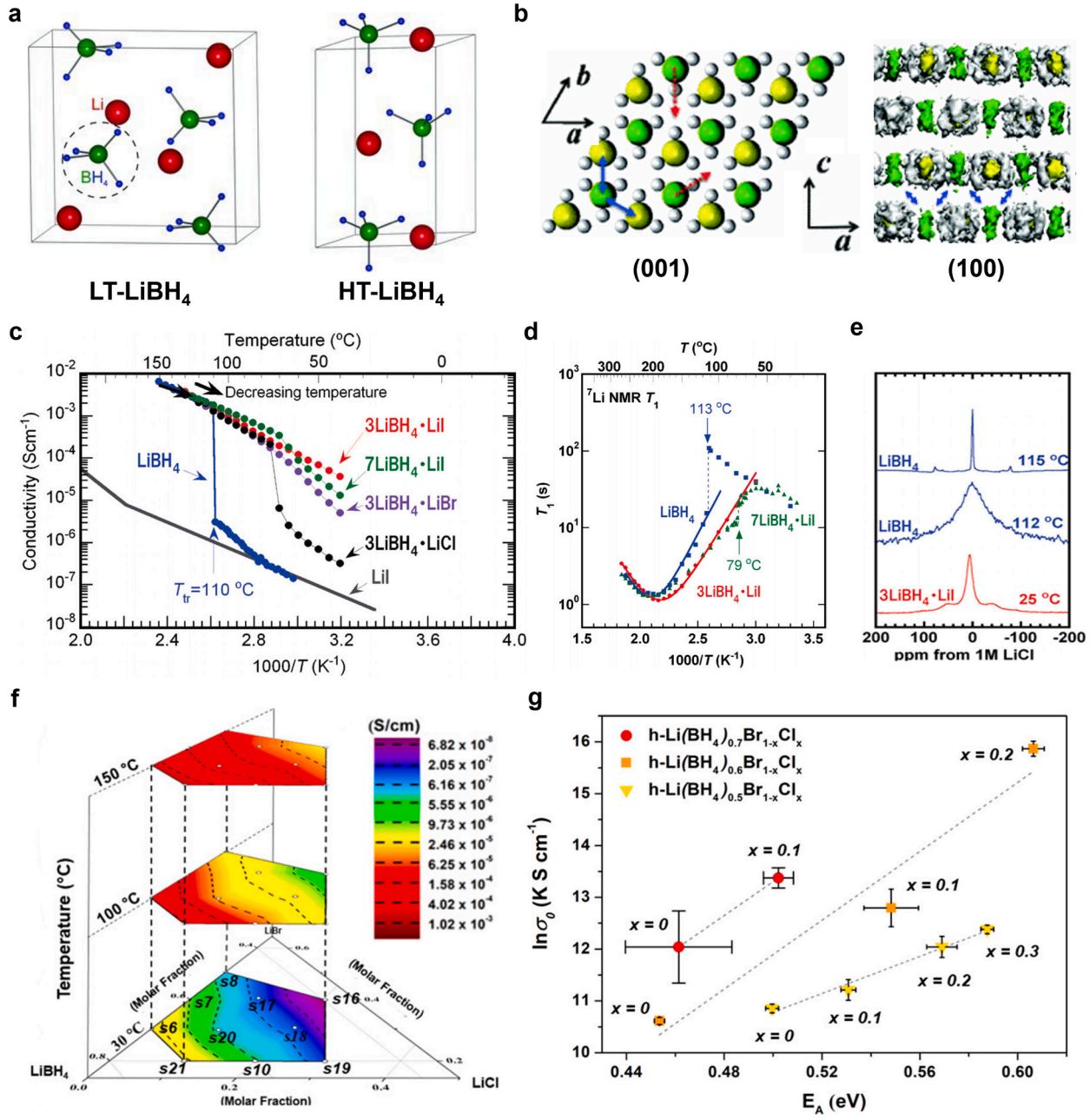

Fig. 20. (a) Crystal structures of the LT and HT phases of $LiBH_4$. Reproduced with permission from ref. [402]. Copyright 2011, Advanced Energy Materials. (b) HT hexagonal phase structures of $LiBH_4$. Reproduced with permission from ref. [403]. Copyright 2011, Physical Review B. (c) DC electrical conductivities of $LiBH_4$–LiX composites (X = Cl, Br, and I). (d) Temperature dependence of ^{7}Li NMR spin–lattice relaxation times (Γ_1's) for $LiBH_4$, $7LiBH_4$·LiI, and $3LiBH_4$·LiI, respectively. (e) Temperature variation of ^{7}Li NMR spectra for $LiBH_4$ and $3LiBH_4$·LiI. Reproduced with permission from ref. [52]. Copyright 2009, Journal of the American Chemical Society. (f) Contour map of Li^+ conductivity as a function of composition for three selected temperatures. (g) Plot of the logarithm of the pre-exponential factor ($\ln \sigma_0$) as a function of activation energy (E_A) for samples in the hexagonal solid solution for the $LiBH_4$–LiBr–LiCl system. Reproduced with permission from ref. [406]. Copyright 2019, Chemistry of Materials.

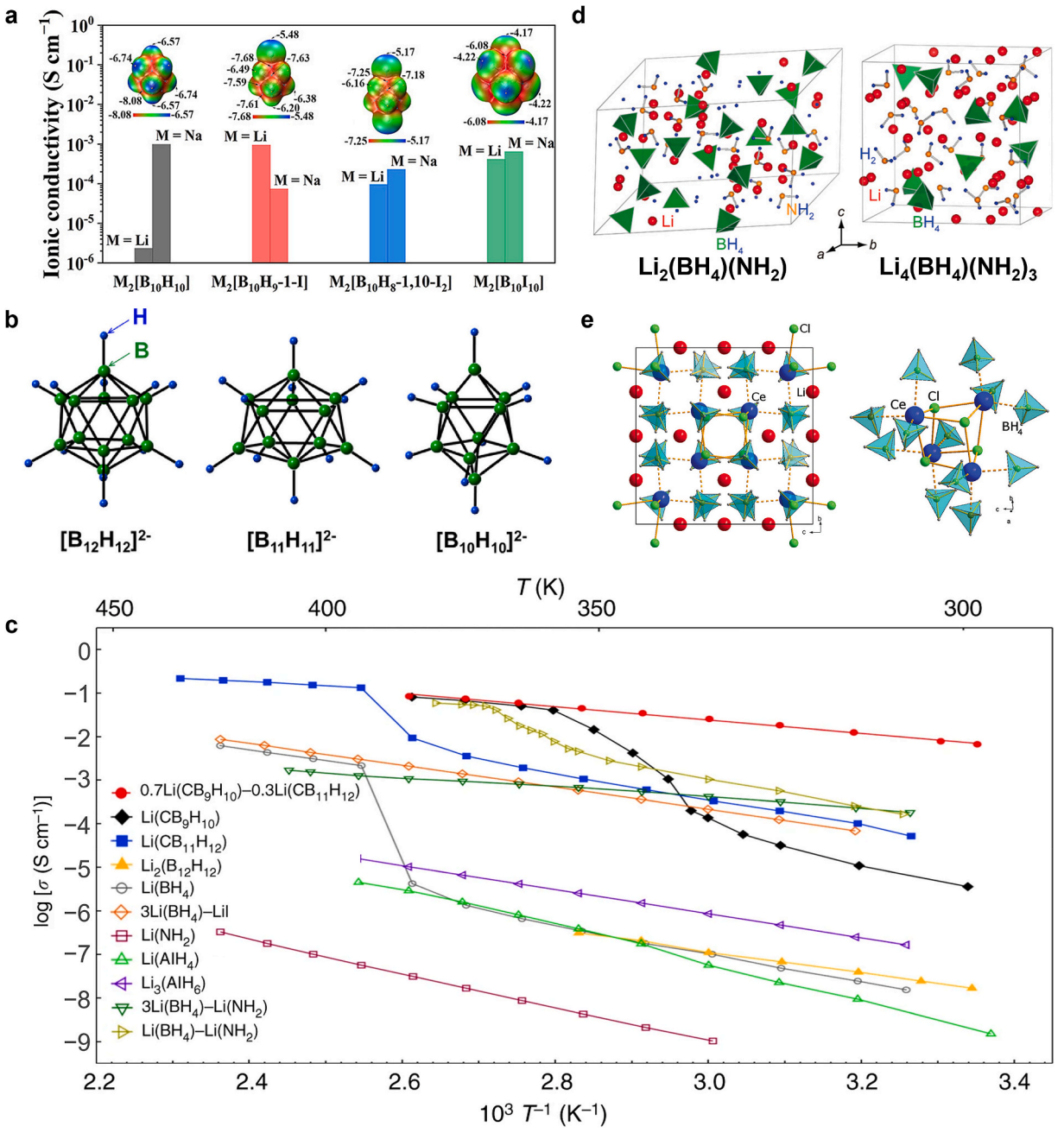

Fig. 21. (a) Geometries, approximate relative sizes, ionic conductivity and ESPs of $[B_{10}H_{10}]^{2-}$, $[B_{10}H_9$-1-I$]^{2-}$, $[B_{10}H_8$-1,10-$I_2]^{2-}$, and $[B_{10}I_{10}]^{2-}$. Reproduced with permission from ref. [407]. Copyright 2021, ACS Applied Materials & Interfaces. (b) Related geometries of $[B_{12}H_{12}]^{2-}$, $[B_{11}H_{11}]^{2-}$, and $[B_{10}H_{10}]^{2-}$ complex anions. Reproduced with permission from ref. [408]. Copyright 2019, Journal of Energy Chemistry. (c) Arrhenius plots of the conductivities of 0.7Li(CB_9H_{10})–0.3Li($CB_{11}H_{12}$). Reproduced with permission from ref. [409]. Copyright 2019, Nature Communications. (d) Crystal structures of $Li_2(BH_4)(NH_2)$ and $Li_4(BH_4)(NH_2)_3$. Reproduced with permission from ref. [382]. Copyright 2009, Journal of the American Chemical Society. (e) Crystal structure of the novel compound $LiCe(BH_4)_3Cl$ and $[Ce_4Cl_4(BH_4)_{12}]^{4-}$. Reproduced with permission from ref. [429]. Copyright 2012, Chemistry of Materials.

5. Hydride-based solid-state electrolytes

5.1. Development of hydride-based solid-state electrolytes

Recently, hydrides have been reported as emerging SSEs for SSBs, with preeminent properties like low grain-boundary resistance, good reduction stability, and high mechanical flexibility. Hydrides, notably borohydrides, show promise for achieving ionic conductivity on the order of 10 mS cm^{-1} [373]. The high reducibility of $H^{\delta-}$ endows hydrides with higher compatibility and more stable interfaces with metal anodes [374]. Other excellent properties include high ion selectivity, high cation mobility, and easy device integration, which have spurred hydride-based SSEs to receive extensive attention and present bright development prospects [7,373,375].

The discovery of hydride-based SSEs is closely related to the unique lattice transition, and the development route with important breakthroughs over the past two decades is shown in Fig. 19. Hydrides were initially investigated as hydrogen storage materials in 1953 [375,376], gaining prominence for their higher thermal stability, safer handling, and absence of fuel loss during storage [377]. The first report of a fast Li-ion conductor among hydrides dates back to 1979, when Boukamp and Huggins [378] discovered Li_2NH with an ionic conductivity of 0.377 mS cm^{-1} at 25 °C. Subsequently, research on fast ionic conduction in borohydrides remained scarce for an extended period. In 1997, Bogdanović and Schwickardi [379] reported the catalyzed release of hydrogen from $NaAlH_4$. Following this, a study in 2003 investigated $LiBH_4$ [380], a reversible hydrogen storage material, and this pioneering work immediately stimulated extensive research on borohydrides and complex hydrides. Despite numerous studies, attention focused primarily on the hydrogen storage properties of $LiBH_4$, while its potential as an ionic conductor remained overlooked. A turning point occurred in 2007 when Orimo, Matsuo, and Nakamori [42] reported that the ionic conductivity of $LiBH_4$ surged to 1 mS cm^{-1} after the HT phase transition at 117 °C due to anion disorientation. This elucidated fast Li^+ conduction in the hexagonal $P6_3mc$ phase versus low Li^+ conduction in the orthorhombic *Pnma* phase [381]. Though this work was extremely inspiring, the high temperature of transition posed significant challenges. Shortly afterward, Orimo et al. further proposed incorporating halide [52] and azanide ions [382] into $LiBH_4$ to stabilize the superionic phase at RT. Concurrently, another class of fast Li^+ conductors was discovered during the decomposition experiments of borohydrides, and these were intermediate species with the *closo*-hydroborate anion $[B_{12}H_{12}]^{2-}$ [383,384]. Subsequent studies characterized the phase transition and ionic conductivity of $Li_2B_{12}H_{12}$ [385,386]. Researchers expanded to other *closo*-structures via carbon atom substitution, synthesizing $Li_2B_{10}H_{10}$, $LiCB_{11}H_{12}$, and $LiCB_9H_{10}$ [53,387–390]. Compared with $[BH_4]^-$, the larger $[B_nH_n]^{2-}$ and $[CB_nH_{n+1}]^-$ exhibit weaker Li^+ affinity, enhancing cation mobility and ionic conductivity. As the hydride family expanded, the exploration of hydride-based SSEs continued unabated. Given the dual role of hydrides in hydrogen storage and ionic conduction, hydrogen storage modification strategies (e.g., ion substitution, ligand complexation, nanoconfinement) were successfully adapted to SSEs, yielding substantial performance enhancements. Recently, CSEs combining hydrides with sulfides or polymers have achieved high RT ionic conductivity and wide ESWs. Meanwhile, with the rapid development of machine learning, relevant algorithms have been gradually applied to the evaluation and screening of electrolyte materials while yielding promising results [391–393]. These advancements underscore the immense potential of hydride-based SSEs.

To date, the hydride-based SSEs primarily includes MBH_4, MB_3H_8, $M_2B_nH_n$/MB_nH_n (n = 10, 12), MCB_nH_{n+1}/MCB_nH_{n+1} (n = 9, 11), $MB_{11}H_{14}$, M-7-$CB_{10}H_{13}$, M-7,8-$C_2B_9H_{12}$-based SSEs, and related compounds [399]. Although high ionic conductivity after HT phase transition is a key advantage of hydrides, their extremely low RT conductivity hinders practical application. Additionally, hydrides typically exhibit low oxidative stability, leading to incompatibility with high-potential cathodes such as NCM and $LiFePO_4$ (LFP) [374]. This section reviews recent research on hydride-based SSEs, with a focus on borohydride-based SSEs, and highlights modification strategies, performance improvement, and industrial indicators. The ionic conductivities of these modified hydride-based SSEs and their electrochemical performance assembled with different cathodes are summarized in Table 4.

5.2. Ionic conductivity

The limited ionic conductivity remains the primary challenge hindering the commercialization of hydride-based SSEs. Generally, modification routes to lower diffusion barriers at RT can be categorized into bulk phase modification and phase boundary engineering, and specific strategies include ion substitution, ligand complexation, interfacial engineering, nanoconfinement and composite design [374].

5.2.1. Ion substitution

For bulk phase modification, ion substitution is an effective strategy extensively explored in terms of material selection and technique conditions. In the field of hydrogen storage materials, based on the first-principles calculation, ion substitution, such as F^- and Cl^-, is used to improve the thermodynamics of dehydrogenation [400,401]. Fig. 20a–b present the crystal structures of the LT orthorhombic phase and HT hexagonal phase $LiBH_4$ [402], as well as the Li^+-conduction path in the HT phase [403]. When the temperature of $LiBH_4$ increases to 117 °C, a metastable Li^+ state forms in the *a-b* plane at interstitial site surrounded by three Li^+ and three $[BH_4]^-$. Subsequently, thermally excited Li^+ hops from the original sites to these interstitial sites, creating vacancies that enable rapid Li^+ diffusion. This mechanism implies that it is feasible to enhance the ionic conductivity through ion substitution. Inspired by Wang et al. [400,401], early modifications of hydride-based SSEs focused on halogen substitution [404]. For example, brominated borohydrides exhibit significant static/dynamic disorder that induces rotational disorder of the $[BH_4]^-$ anions [405]. Orimo et al. [52] demonstrated that doping $LiBH_4$ with lithium halides (LiCl, LiBr, LiI) could stabilize the HT phase at low temperatures. The $3LiBH_4$·LiI composite showed no apparent transition from HT to below RT (Fig. 20c–d), and the ^7Li NMR revealed that the Li^+-conduction path

was similar to that in hexagonal $LiBH_4$ (Fig. 20e), confirming RT stable superionic conduction. Additionally, the activation energy of the LiI-doped sample was lower than those of LiBr-doped and LiCl-doped counterparts. The incorporation of highly polarizable I^- anion modified the electronic structure, weakening Coulombic interactions between anions and cations and facilitating Li^+ conduction. Baricco et al. [406] further stabilized the hexagonal structure at RT by co-incorporating Br^- and Cl^- into $LiBH_4$. EIS and CV data

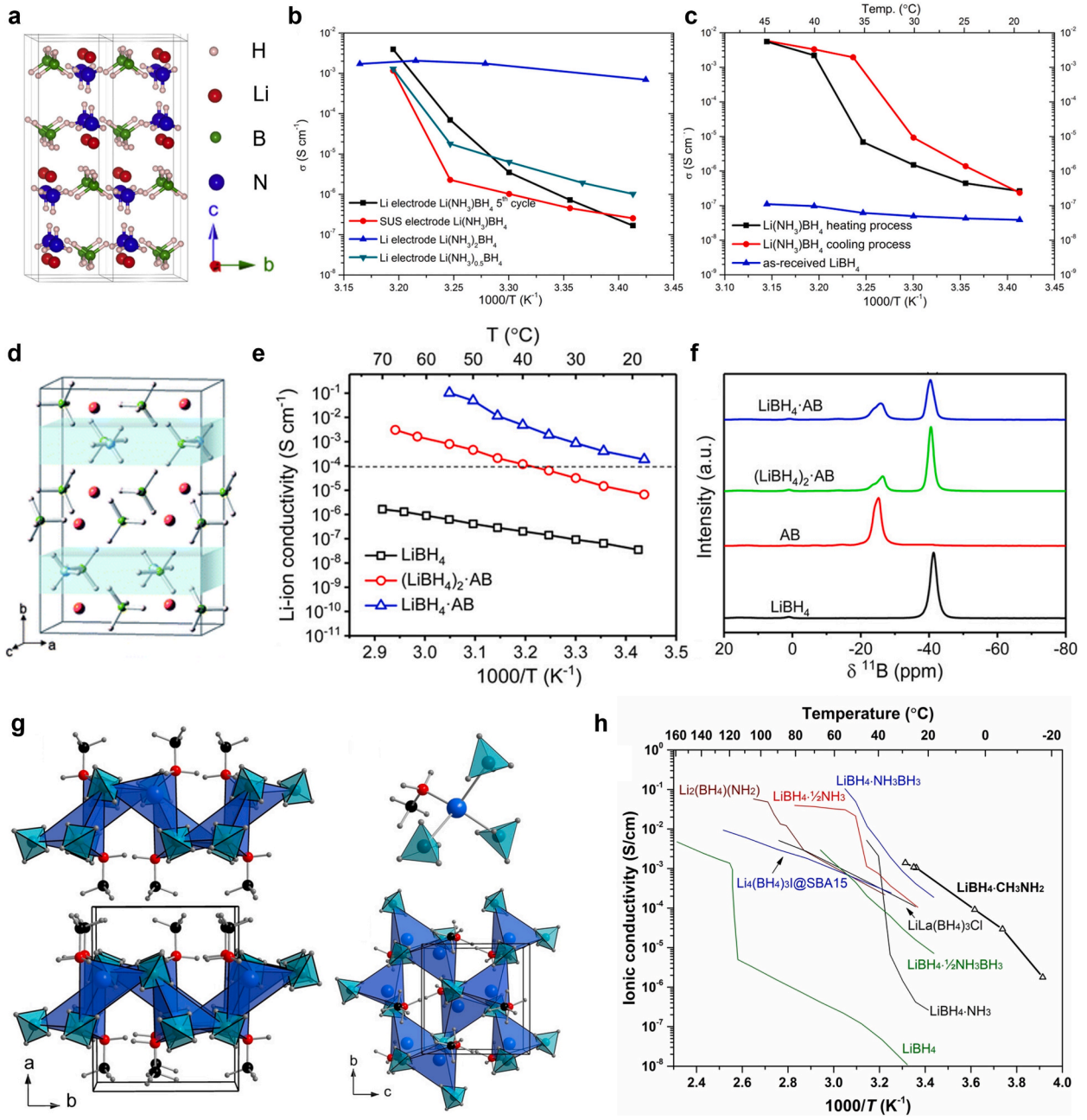

Fig. 22. (a) Crystal Structures of Mono-ammoniate. (b) Lithium ionic conductivity of four samples, $Li(NH_3)BH_4$ for the fifth cycle (black), SUS electrode $Li(NH_3)BH_4$ (red), $Li(NH_3)_2BH_4$ (blue), and $Li(NH_3)_{0.5}BH_4$ (dark cyan). (c) The lithium ionic conductivity of $Li(NH_3)BH_4$ obtained in heating process, cooling process and as-received $LiBH_4$. Reproduced with permission from ref. [54]. Copyright 2018, Joule. (d) Crystal structure of $LiBH_4$·AB. Li, B, N, and H atoms are represented by pink, green, blue, and white spheres, respectively. (e) Arrhenius ionic conductivity plots of $LiBH_4$, $(LiBH_4)_2$·AB, and $LiBH_4$·AB. (f) ^{11}B ss-NMR spectra for $LiBH_4$, AB, $(LiBH_4)_2$·AB, and $LiBH_4$·AB. Reproduced with permission from ref. [44]. Copyright 2020, Chemistry of Materials. (g) The crystal structure of $LiBH_4{\cdot}CH_3NH_2$ from the view of *ab*-plane and *bc*-plane withthe local lithium coordination. Color scheme: Li^+ (blue), $[BH_4]^-$ (light blue tetrahedra), N (red), C (black) and H (grey). (h) Temperature-dependence of the Li^+ conductivity of $LiBH_4{\cdot}CH_3NH_2$ compared to other selected hydrides. Reproduced with permission from ref. [45]. Copyright 2022, Angewandte Chemie International Edition.

revealed that the halogenation enhanced the ionic conductivity (reaching up to 1.3×10^{-2} mS cm^{-1} at 30 °C for ternary samples, Fig. 20f), electrochemical stability, thermal stability, and energy density. However, the Br/Cl ratio did not affect the lattice structure, and Cl^- increased the activation energy (Fig. 20g).

From the relatively simple $[BH_4]^-$ tetrahedron to complex borohydrides, ion substitution still remains effective for modifying hydride-based SSEs. Chen et al. [407] synthesized a series of pure alkali metal-iodinated *closo*-decaborates, $M_2[B_{10}H_{10-n}I_n]$ (M = Li, Na; n = 1, 2, 10), achieving a slight conductivity increase to 3.12×10^{-3} mS cm^{-1} at 30 °C (Fig. 21a). Building on halogen substitution strategies, Orimo et al. [408] adopted complex anion substitution, synthesizing *closo*-type hydrides from $LiBH_4$ and $B_{10}H_{14}$ at varying molar ratios. The resulting complex hydrides contained three *closo*-type borohydride anions: $[B_{12}H_{12}]^{2-}$, $[B_{11}H_{11}]^{2-}$ and $[B_{10}H_{10}]^{2-}$ (Fig. 21b), and the ionic conductivity rose from 1.4×10^{-3} mS cm^{-1} to 2.1×10^{-2} mS cm^{-1} with increasing $LiBH_4$ proportion. To address residual byproducts from incomplete anion mixing, Orimo's group [409] formed a solid solution from two hydrides, $0.7Li(CB_9H_{10})$–$0.3Li(CB_{11}H_{12})$. This complex hydride achieved 6.7 mS cm^{-1}, attributed to $LiCB_{11}H_{12}$ partially stabilizing $LiCB_9H_{10}$. Fig. 21c compares ionic conductivities of several hydride-based SSEs, highlighting the superiority of this work. For cost reduction, Remhof et al. [410] developed a high-purity synthesis of $LiB_{11}H_{14}$, a cost-efficient precursor, enabling $Li_3(B_{11}H_{14})(CB_9H_{10})_2$ to reach 1.1 mS cm^{-1}. They further demonstrated its compatibility with NCM811 cathodes, delivering 54 % of the initial discharge capacities at C/2 after 2000 cycles, making a breakthrough for ion-substituted hydride-based SSEs [411]. Finally, Jensen et al. [412] investigated the polymorphism, thermal stability, and electrochemical properties of $LiB_{10}H_{10}$, $Li_2B_{12}H_{12}$ and their γ-$Li_2B_{10}H_{10-y}$ composites, expanding research in this field.

Research on Li_2NH as a lithium-ion conductor has spurred significant interest in amino groups, which were extensively studied for hydrogen storage [413–416]. Studies reveal a relationship between Li^+ conductivity and catalytic dehydrogenation. For instance, $LiTi_2O_4$ facilitated rapid Li^+ migration between LiH and $LiNH_2$, demonstrating the potential of the Li–N–H system in LIB materials [417]. Orimo et al. [382] synthesized $Li_2(BH_4)(NH_2)$ and $Li_4(BH_4)(NH_2)_3$ by combining $[BH_4]^-$ and $[NH_2]^-$ anions, both exhibiting an ionic conductivity of 0.2 mS cm^{-1} at RT (crystal structures in Fig. 21d). This work demonstrated that complex anion combinations created new Li^+ occupation sites and facilitated mobility, offering a novel direction for the development of fast lithium-ion conductors. Subsequently, the same team reported $Li_3(NH_2)_2I$ with a conductivity of 0.017 mS cm^{-1} at 300 K [418]. Based on this, Remhof et al. [419] optimized the $LiBH_4$–$LiNH_2$ molar ratio, achieving 6.4 mS cm^{-1} at 40 °C. XRD and DSC analyses indicated enhanced anion dynamics and strong Li^+–anion coupling, which drove the high ionic conductivity. Further NMR studies elucidated the reorientation motion and Li^+ diffusion mechanism in this system [420]. Additionally, Soboyejo et al. [421] revealed that ionic transport induced spatiotemporal multi-axial strain distributions in $LiBH_4$–$LiNH_2$–LiI SSEs.

Beyond the substitution of $[BH_4]^-$, cationic substitution of Li^+ has also received extensive attention. Fang et al. [422] suggested that ball-milled $LiBH_4$–$Ca(BH_4)_2$ composites formed double-cation borohydrides $Li_xCa_y(BH_4)_{x+2y}$, whereas Lee et al. [423] and Vegge et al. [424] argued that these composites remained physical mixtures. The $0.75LiBH_4$–$0.25Ca(BH_4)_2$ mixture exhibited ionic conductivities of 8.8×10^{-3} mS cm^{-1} at 40 °C and 1 mS cm^{-1} at 100 °C [424]. Inspired by hydrogen storage studies, divalent-cation SSEs including the $LiBH_4$–$NaBH_4$ system [425], $LiBH_4$–MgH_2 system [426,427], and ternary system $LiBH_4$–$NaBH_4$–MgH_2 [428] were developed. Notably, $NaBH_4$–MgH_2 stabilized the *P6₃mc* phase of $LiBH_4$, enabling the $4LiBH_4$–$NaBH_4$–30 %MgH_2 composite to reach 11.2 mS cm^{-1} at 110 °C with an extended ESW of −1–4 V vs. Li^+/Li [428]. Rare earth cations can also promote $LiBH_4$ modification. These borohydrides exhibit dual functionalities (e.g., Li^+ conduction and luminescence), with extensive research on binary alkali/lanthanide systems. For example, $LiM(BH_4)_3Cl$ (M = Ce, La, Gd) [394,429] showed similar crystal structures and improved Li^+ conduction, delivering conductivities of 0.103 mS cm^{-1}, 0.23 mS cm^{-1}, and 0.35 mS cm^{-1} at 20 °C, respectively. Fig. 21e illustrates the representative structure of $LiCe(BH_4)_3Cl$.

Ion substitution has emerged as a primary modification strategy for hydride-based SSEs, driven by straightforward synthesis (typically involving ball milling and annealing) and yielding substantial RT ionic conductivity enhancement. Research has focused on optimizing substitution ratios, elucidating phase and structural transformations, modifying anion/cation interactions, introducing dynamic disorder, and exploring complex *closo*-type anions derived from borohydride frameworks. Collectively, these advances demonstrate that rational ion substitution enables ambient-temperature stabilization of HT superionic phases. This establishes rapid Li^+ migration pathways, significantly boosting ionic conductivity.

5.2.2. *Ligand complexation*

Beyond ion substitution, ligand complexation represents an efficient strategy to boost RT ionic conductivity in hydride-based SSEs. Inspired by the ammonia absorption properties of $LiBH_4$ [430–432], Zhang et al. [54] introduced NH_3 to dynamically modify its crystalline structure (Fig. 22a), synthesizing lithium borohydride ammoniates $Li(NH_3)_nBH_4$ ($0 < n \leq 2$) with high ionic conductivity (≈ 1 mS cm^{-1}) near RT (Fig. 22b–c). Ammonia partial desorption induced structural changes, generating defects, altering atomic arrangements, and reducing Li^+ volumetric density—thereby lowering Li^+ migration activation energy with reversible behavior. First-principles calculations revealed a stable ESW of about 4 V and LFP compatibility for $Li(NH_3)BH_4$. Complementarily, Jensen's group [433] established that $[BH_4]^-$ reorientation depended on the local environment in $LiBH_4{\cdot}NH_3$.

However, gaseous ligands compromise morphological stability. For instance, $Li(NH_3)_xBH_4$ transforms from solid to liquid upon heating [54]. To address this issue, Liu et al. [44] integrated solid-state ammonia borane (AB) into $LiBH_4$, creating ultrafast RT conductors $(LiBH_4)_x{\cdot}AB$ (Fig. 22d). Experimental and theoretical analyses demonstrated fast Li^+ conduction, attributed to expanded unit cells and reduced Li^+ density (Fig. 22e). NMR verified structural integrity during heating–cooling cycles (18–55 °C) (Fig. 22f). AIMD simulations further revealed ratio-dependent diffusion modes. Similarly, Jensen et al. [45] incorporated mono-methylamine into $LiBH_4$ (Fig. 22g), where hydrophobic $-CH_3$ layers created interlayer voids, enabling 1.24 mS cm^{-1} at RT (Fig. 22h). Unfortunately, CV and GV results revealed that parasitic reactions occurred between TiS_2 and the $LiBH_4{\cdot}CH_3NH_2$ electrolyte, causing

detrimental interfaces and uncontrolled oxidation that hindered the development of SSBs.

In summary, ligand complexation enhances conductivity by expanding lattices, reducing Li^+ density, and introducing defects. Key challenges include ligand volume constraints, phase instability, and electrode compatibility—as evidenced by CH_3NH_2/TiS_2 reactions—necessitating systematic ligand screening.

5.2.3. *Interfacial engineering*

As established, bulk modification strategies, such as ion substitution and ligand complexation, effectively enhance Li^+ conductivity in hydride-based SSEs. Concurrently, interfacial engineering has evolved as a pivotal approach for further optimization. Zheng et al.

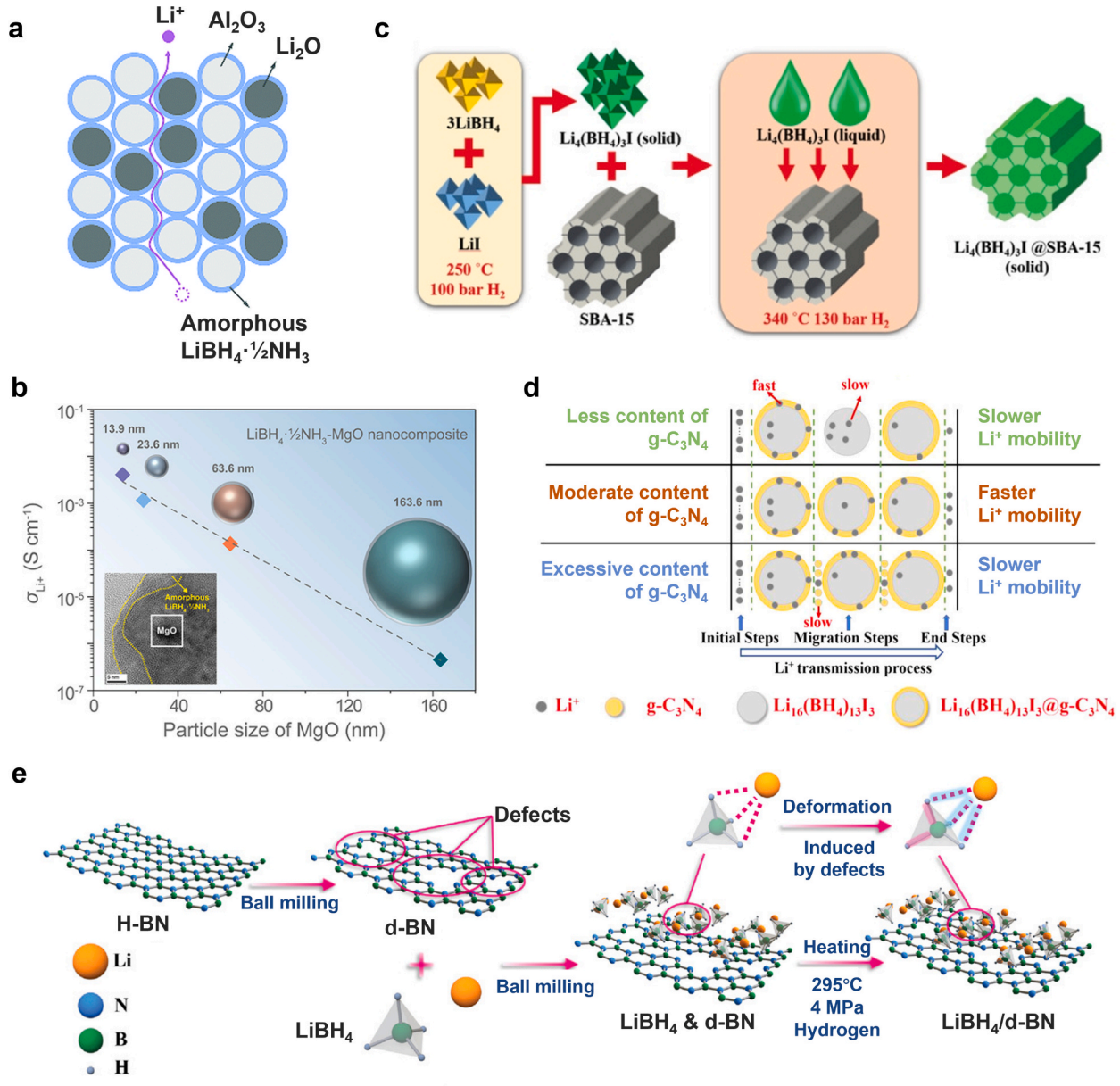

Fig. 23. (a) Schematic diagram of Li^+ migration in the $LiBH_4{\cdot}1/2NH_3$–Al_2O_3 composite. Reproduced with permission from ref. [438]. Copyright 2021, Chemical Communications. (b) Lithium ionic conductivity at RT as a function of the size of MgO nanoparticles for the LBN–MgO nanocomposites. Reproduced with permission from ref. [439]. Copyright 2022, ACS Applied Materials & Interfaces. (c) Schematic diagram of preparing process of $Li_4(BH_4)_3I$ in SBA-15. Reproduced with permission from ref. [442]. Copyright 2019, Advanced Functional Materials. (d) Schematic diagram of Li^+ migration in the $Li_{16}(BH_4)_{13}I_3$@g-C_3N_4. Reproduced with permission from ref. [443]. Copyright 2022, ACS Applied Materials & Interfaces. (e) Schematic illustration of the synthesis of $LiBH_4$/d-BN composites. Reproduced with permission from ref. [444]. Copyright 2022, Advanced Functional Materials.

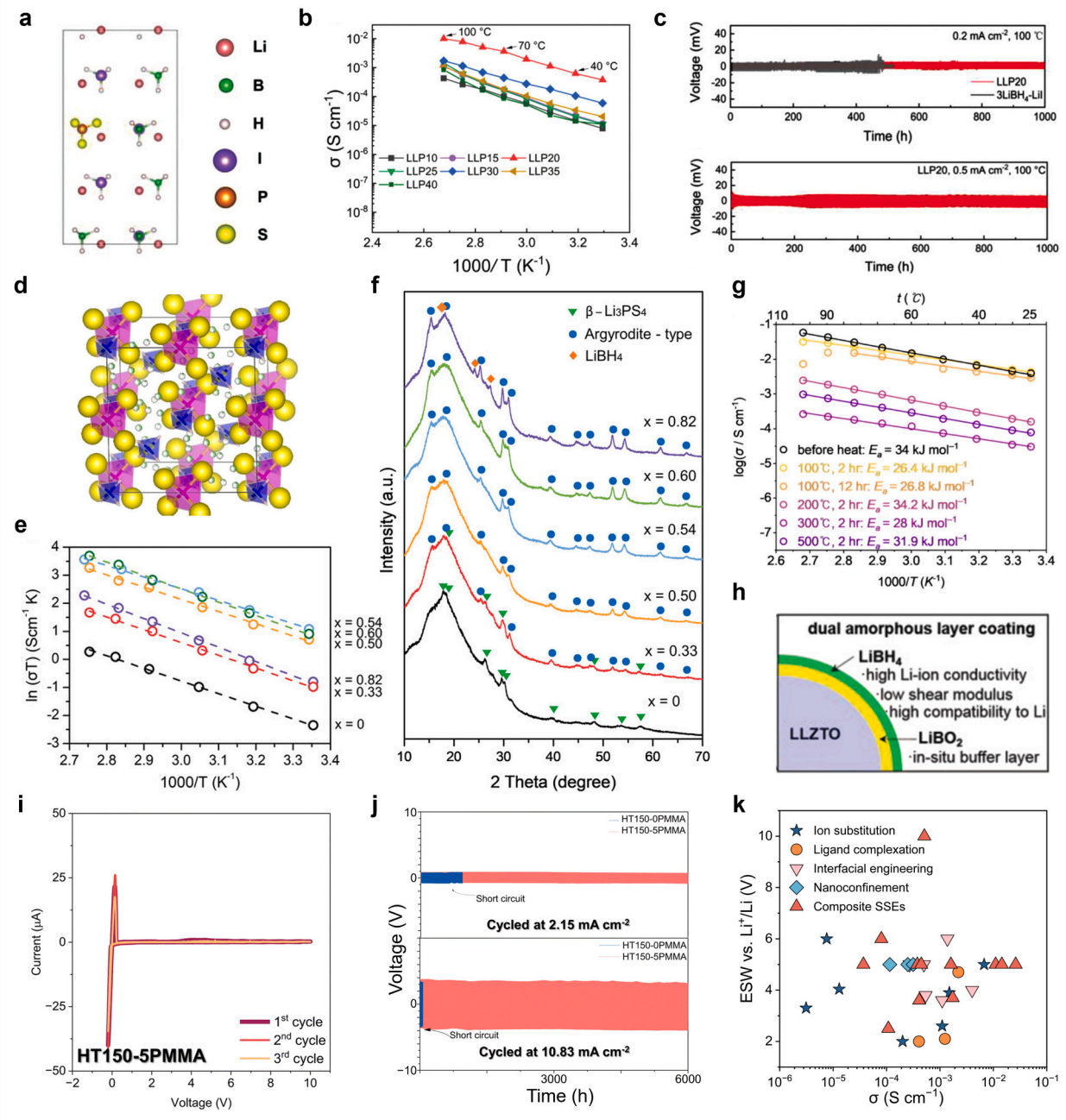

Fig. 24. (a) Schematic calculation models of LLP20 from *a*-axis. (b) Arrhenius ionic conductivity plots of LLPx. (c) Voltage transients during Li plating/stripping with different current densities at 0.2 mA cm^{-2} and 0.5 mA cm^{-2}. Reproduced with permission from ref. [43]. Copyright 2021, Small Methods. (d) The structure of crystalline argyrodite-type $Li_6PS_5(BH_4)$. Reproduced with permission from ref. [449]. Copyright 2018, ACS Omega. (e) Temperature dependence of ionic conductivities and (f) XRD patterns of the prepared SSE samples with the composition of (1−x) Li_3PS_4·2x$LiBH_4$. Reproduced with permission from ref. [450]. Copyright 2023, Advanced Science. (g) Nyquist plots for synthesized $Li_5PS_4(BH_4)_2$ using a ZrO_2 pot. Reproduced with permission from ref. [452]. Copyright 2024, Korean Journal of Chemical Engineering. (h) Schematic of the structure of $LiBH_4$-modified LLZTO. Reproduced with permission from ref. [49]. Copyright 2021, Advanced Functional Materials. (i) CV data over three continuous cycles of HT150-5PMMA. (j) Li plating and striping cycles at 2.15 mA cm^{-2} and 10.83 mA cm^{-2} at 25 °C. Reproduced with permission from ref. [47]. Copyright 2023, Energy & Environmental Science. (k) Comparison of RT ionic conductivity and ESW vs. Li^+/Li of different modified hydride-based SSEs.

[434] synthesized Li–B–H complexes via partial $LiBH_4$ dehydrogenation, achieving 0.27 mS cm^{-1} at 35 °C. This enhancement originated from conductive interfaces between dehydrogenation-derived $[Li_2B_{12}H_{11+1/n}]_n$ and $LiBH_4$. Similarly, Pan's group [46] constructed an *in situ*-LiH-dispersed electron-blocking layer on $LiBH_4$. Synergistic rotation of $[BH_4]^-$ and $[B_{12}H_{12}]^{2-}$ anions enabled LiH-modified $LiBH_4$ to reach 1.38 mS cm^{-1} at 25 °C. Shi et al. [435] utilized the solid-state reaction between $LiBH_4$ and $LiBF_4$ to *in situ* generate LiF-decorated $Li_2B_{12}H_{12}$. Here, a defect-rich amorphous $Li_2B_{12}H_{12}$ matrix facilitated Li^+ transport, while ultrafine LiF nanoparticles reduced interfacial resistance and enhanced electrode compatibility. These *in situ*-formed amorphous *closo*-borate interfaces demonstrated high conductivity [436].

Oxide nanoparticles enhance conductivity through strong interfacial interactions. Yan et al. [437] reported that *in situ*-formed Li_2O during ball-milling of $LiBH_4/LiNH_2/LiOH$ boosted $LiBH_4{\cdot}xNH_3$ conductivity to 0.54 mS cm^{-1} at 20 °C, while expanding the ESW from 0.5 V to 3.8 V. Chen et al. [438] designed $LiBH_4{\cdot}1/2NH_3$–Al_2O_3 composite where B–O bonds induced amorphous hydride formation on Al_2O_3 (Fig. 23a). At γ-Al_2O_3 loadings $\geq$ 60 wt%, the ionic conductivity increased from 0.2 to 1.1 mS cm^{-1} at 30 °C with a 3.6 V ESW, though excessive loading degraded conductivity. Subsequently, Chen et al. [439] further investigated how MgO nanoparticle size critically influenced $LiBH_4{\cdot}1/2NH_3$ conductivity. Smaller particles (e.g., 13.9 nm) significantly enhanced interfacial effects, leading to simultaneous improvement in ionic conductivity (4 mS cm^{-1} at RT) and electrochemical stability (4.0 V) (Fig. 23b). Further extending this concept, Zettle et al. [440] studied the structural and dynamic features of nanoconfined $LiBH_4$-LiI/Al_2O_3. Scheiber et al. [441] incorporated ZrO_2, MgO, and $MgAl_2O_4$ as insulator phases into the $LiBH_4$ conductor phase, where conductor–insulator heterocontacts stabilized interfacial defects and enabled high ionic conductivity.

In summary, interfacial engineering leverages *in situ* layered structures and tailored electrolyte–nanoparticle interactions to optimize SSEs. Notably, innovations adapted from hydrogen storage research—particularly hydrogenation/dehydrogenation—enable framework engineering. However, current studies predominantly target conductivity gains, with insufficient focus on critical interfacial challenges. Key issues such as lithium dendrite suppression at anodes and compatibility with high-voltage cathodes (> 4 V) remain understudied. Advancing ASSLB applications necessitates prioritizing interfacial chemical stability and mechanical compatibility in future work.

5.2.4. Nanoconfinement

Recent studies have confirmed that the nanoconfinement of borohydride-based SSEs within nanoporous scaffolds improves electrochemical performance, leveraging interface effects and size reduction [445]. Originally developed for hydrogen storage materials to mitigate particle agglomeration and shorten hydrogen diffusion paths, this strategy enhances Li^+ diffusion in SSEs by enabling uniform electrolyte dispersion, thereby boosting ionic conductivity. Blanchard et al. [445] confined $LiBH_4$ within the pores of ordered mesoporous silica scaffolds via melting infiltration under high hydrogen pressure, achieving high ionic conductivity up to 0.1 mS cm^{-1} at RT. Extending this, Lu et al. [442] confined the LiI-doped $LiBH_4$ in mesoporous silica SBA-15, primarily attributing the high Li^+ conductivity (0.25 mS cm^{-1} at 35 °C) to enhanced Li^+ mobility within the 1.2-nm interface layer (Fig. 23c). More importantly, $Li_4(BH_4)_3I$@SBA-15 exhibited a wide ESW of 0–5 V, compatibility with S/oxide cathodes, and stable cycling. Similarly, Laura M. et al. [446] incorporated $[NH_2]^-$-partially substituted $LiBH_4$ into mesoporous oxide scaffolds, including mesoporous silica (MCM-41 and SBA-15) and aluminated silica (Al-SBA-15), achieving ionic conductivity up to 0.5 mS cm^{-1} at 30 °C. Distinct from pure $LiBH_4$ systems, the ionic conductivity achieved in this work correlated with scaffold pore volume, indicating stabilization of conductive phases rather than hydride/oxide interfacial effects. Focusing on the mesoporous silica, Yu's group [447] demonstrated that Li^+ transport dynamics in the interfacial regions surpassed crystalline domains by orders of magnitude.

Innovatively, Hu et al. [443] embedded a two-dimensional (2D) one-atom-thick planar sheet material, graphitic carbon nitride (g-C_3N_4), into $Li_{16}(BH_4)_{13}I_3$ to synthesize a fast lithium-ion conductor (Fig. 23d). The sample exhibited a high ionic conductivity of 0.315 mS cm^{-1} at 30 °C and a wide ESW of 0–5 V. Wu et al. [444] chose another 2D lamellar-structure material, hexagonal BN (h-BN), as the scaffold and introduced defects to induce ion migration by ball milling (Fig. 23e). The $LiBH_4$/h-BN sample delivered an ionic conductivity of 0.115 mS cm^{-1} at 40 °C, a wide ESW of 0–5 V, and good electrochemical compatibility.

Extensive studies have documented that the interfacial effects brought by nanoconfinement with porous or sheet structures can significantly improve the ionic conduction of hydride-based SSEs. In contrast to interfacial engineering, nanoconfinement imposes stricter limitations on scaffold material selection, where the structural and dimensional parameters profoundly influence the performance of hydride-based SSEs. The divergent physicochemical characteristics between nanoconfined and bulk-phase electrolytes necessitate mechanistic insights into Li^+ transport. However, many studies prioritize ionic conductivity enhancements over mechanistic investigations, leaving critical questions unresolved—such as how pore geometry modulates Li^+ diffusion barriers or whether interfacial bonding between scaffolds and hydrides dictates ion migration pathways. Future efforts should prioritize atomic-scale interfacial dynamics and scaffold-chemistry optimization to advance high-voltage compatible SSEs for ASSLBs.

5.2.5. Composite solid-state electrolytes

By integrating hydride-based SSEs with other SSEs, CSEs leverage synergistic properties to overcome individual limitations while amplifying complementary advantages. For example, sulfide-based SSEs offer near-LE-level conductivity, flexibility, and wide ESWs but suffer from severe instability against lithium metal, which is expected to be alleviated by compositing with hydride-based SSE. Yu et al. [43] developed a series of CSEs, $(100-x)(3LiBH_4{\cdot}LiI)$–$xP_2S_5$ (LLPx, $0 \leq x \leq 50$), composed of hydrides and sulfides through a dual-anion substitution strategy. Remarkably, LLP20 (Fig. 24a) demonstrated the highest ionic conductivity of 0.377 mS cm^{-1} at 30 °C (Fig. 24b), an ESW of 5.0 V, flexibility, and excellent lithium dendrite inhibition performance (Fig. 24c). The enhanced conductivity was attributed to the larger radii of I^- and $[PS_4]^{3-}$ groups compared to $[BH_4]^-$, which led to larger lattice volumes and lower Li^+ diffusion barriers, as evidenced by first-principles calculations. The composition ratios of sulfide-based and hydride-based electrolytes

could affect the crystallization state of CSEs. Tatsumisago et al. [448] initially prepared $(100-x)(0.75Li_2S{\cdot}0.25P_2S_5){\cdot}xLiBH_4$ ($0 \leq x$ (mol%) ≤ 33) glass electrolytes via mechanical ball milling. At $x = 33$, the electrolyte exhibited a peak ionic conductivity of 1.6 mS cm^{-1} and a broad ESW of 5 V vs. Li^+/Li. Subsequently, they increased x to ≥ 43, obtaining a crystalline argyrodite $Li_6PS_5(BH_4)$ phase where $[BH_4]^-$ occupies halide sites in Li_6PS_6X (X = Cl, Br, I) (Fig. 24d) [449]. For $x = 50$, the argyrodite-type SSE demonstrated Li^+ conductivity of 1.8 mS cm^{-1} at 25 °C with an activation energy of 16 kJ mol^{-1}. Inspired by this, Cho et al. [450] developed $(1-x)Li_3PS_4{\cdot}2xLiBH_4$ CSE with an ultrahigh ionic conductivity of 11 mS cm^{-1} at RT (Fig. 24e), surpassing most borohydride-based SSEs and even common LEs. Similarly, the final samples presented a strong relation between the phase structure and the exact composition. As illustrated in Fig. 24f, XRD results revealed the coexistence of β-Li_3PS_4 phase and argyrodite phase at $x = 0.33$, pure argyrodite phase at $0.50 \leq x \leq 0.60$, and unreacted $LiBH_4$ at $x = 0.82$, which was verified by Raman spectra. Notably, the argyrodite-type phase with partial substitution of $[PS_4]^{3-}$ by $[BH_4]^-$ played a crucial role in improving ionic conduction. Conversely, the formation of non-stoichiometric $P_2S_7^{2-}$ and $P_2S_6^{2-}$ caused by inappropriate ball milling conditions harmed the ionic conduction. Further advancing this approach, Cho et al. [398] synthesized a system of borohydride/halide dual-substituted argyrodite-type electrolytes via two-step ball milling, where cold-pressed $Li_{5.35}PS_{4.35}(BH_4)_{1.15}Cl_{0.5}$ achieved the highest ionic conductivity of 16.4 mS cm^{-1} at RT. The excellent conductivity stemmed from increased Li vacancies, driven by greater disordered occupancy of $[BH_4]^-$ and halide at the 4a/4d sites within the argyrodite structure, as evidenced by XRD and ss-NMR analyses. LT sintering (120 °C) and subsequent annealing reduced grain boundary resistance, leading to a further increase in conductivity up to 26.1 mS cm^{-1}. Similarly, this team achieved significant success in Br^- substitution efforts, with the ionic conductivity of the resulting samples reaching 14.4 mS cm^{-1} [451]. Another hydrosulfide SSE $Li_5PS_4(BH_4)_2$ also presented good ionic conductivity of 3.9 mS cm^{-1} at 25 °C (Fig. 24g) and excellent deformability [452]. Taking a step further, Kim's group [453] discussed the influence of different anionic species on the ionic conductivity of hydrosulfide electrolytes. They revealed that compounds with two anions exhibited superior conductivity and lower ionic migration barriers compared to those with three anions. This finding contradicts some existing reports [219], underscoring the substantial variability inherent in multicomponent effects and their intricate linkage to the structure of the anions employed.

Apart from sulfide-based SSEs, garnet-type oxide LLZTO has been incorporated into hydride-based CSEs. However, its high ionic conductivity typically requires HT sintering, while inherent brittleness and poor electrode contact remain unresolved challenges. Pan et al. [49] synthesized a CSE via ball milling of $LiBH_4$ and LLZTO without sintering, featuring a dual amorphous coating with $LiBO_2$ as the inner layer and $LiBH_4$ as the outer layer (Fig. 24h). In this system, $LiBH_4$ and $LiBO_2$ filled the pores of LLZTO and enhanced interparticle contacts, constructing a continuous ion-conductive network. The cold-pressed pellet exhibited ionic conductivity four orders of magnitude higher than that of unsintered LLZTO (8.02×10^{-2} mS cm^{-1} at 30 °C), along with extremely low electronic conductivity, a high t_{Li+} of 0.9999, a wide ESW of 0–6 V, and excellent stability against lithium metal. To further enhance conductivity, Pan's group [397] introduced $Li_3BN_2H_8$ into the LLZTO–$LiBH_4$ system, and obtained an ultrafast ionic conductivity at RT (≈ 1.73 mS cm^{-1} at 30 °C) together with long stable cycles of Li symmetric cells (1600 h at 30 °C). The outstanding performance was attributed to the compactness of the electrolyte pellets, the high intrinsic ionic conductivity, and the easy deformation of $Li_3BN_2H_8$. To improve the contact between the electrolyte and electrodes, this group demonstrated a novel LLZTO–$Li_4(BH_4)I_3$ CSE, which presented ultra-stable Li||Li symmetric battery performance and strong inhibition of lithium dendrites [51]. Focusing on the same system, Yu's group [48] identified the optimal composition ratio for LLZTO and $Li_4(BH_4)I_3$ as $25(Li_4(BH_4)I_3)$@75LLZTO. This CSE exhibited a high interfacial ionic conductivity of 11 mS cm^{-1} and could be stably cycled for 200 h at 4 mA cm^{-2} in a Li||Li symmetric battery.

Compared with inorganic fillers, organic polymers offer superior mechanical flexibility, interfacial compatibility, and electronic insulation. These properties enable them to form effective composites with hydride-based SSEs, resulting in enhanced oxidation stability and suppression of lithium dendrite growth in CSEs. For instance, Zhang et al. [50] developed PEO–$Li_4(BH_4)_3I$ CSE with ionic conductivity of 0.409 mS cm^{-1} at 70 °C, incorporating nano-SiO_2 fillers as dendrite-blocking agents. Unlike the Li^+ transport mechanism in $LiBH_4$, which depends on defects or local Li sites in the crystal phase, $LiBH_4$ in PEO–$LiBH_4$ CSE serves as a lithium source to provide Li^+ coordinating with O atoms from ether groups to achieve Li^+ migration. Advancing this approach, Pan et al. [47] adopted an *in situ* melting reaction of $LiBH_4$ with polymethyl methacrylate (PMMA) to generate covalently bonded coordination $(OCH_3)_xBH_{4-x}$ on the surfaces of SSE particles. This coordination thermodynamically suppressed anion oxidative decomposition and kinetically blocked electron penetration, while simultaneously acting as a binder to enhance the mechanical strength of the CSE. Consequently, the synthesized HT150-5PMMA CSE demonstrated an unprecedented ESW of 0–10 V (Fig. 24i), a record-high CCD of 21.65 mA cm^{-2} at 25 °C, and a broad operating temperature range (−30 to 150 °C), enabling lithium symmetric cell with stable cycling for over 6000 h at 2.15 mA cm^{-2} or 10.83 mA cm^{-2} (Fig. 24j). Further innovating, Pan's group [454] fabricated a flexible polymeric electronic shielding layer (PESL) on $LiBH_4$ particles, yielding a high CCD of 11.43 mA cm^{-2} and long cycling stability of 5000 h at 5.70 mA cm^{-2} (25 °C). Notably, the PESL also ensured fast ionic conduction in CSEs (0.447 mS cm^{-1} achieved by AOLiBHI-5PMMA), attributed to the fast $[BH_4]^-$ rotational dynamics and surface Li^+ enrichment. Moreover, the flexibility of the PESL guaranteed structural integrity during lithium plating/stripping, resulting in long cycling stability.

Recent advances have validated composite strategies for overcoming inherent hydride-based SSE limitations while preserving advantages. Integrating hydrides with sulfides, oxides, or polymers has yielded unprecedented improvements in ionic conductivity and electrochemical stability. These composites also demonstrate adaptive Li^+ transport mechanisms, where hydrides act as Li^+ reservoirs or facilitate coordination with polymer matrices. Notably, synergistic effects in multi-phase systems—such as argyrodite-type structures with dual-anion substitution—enable balanced ionic/electronic conductivity and thermal stability. Despite these advancements, challenges persist in exploring the rate and cycling performance of ASSLBs. With substantial advancements in ionic conductivity and ESWs of composite hydride-based electrolytes, the next critical frontier lies in developing compatible high-voltage cathodes and establishing robust high-current–density and long-cycling battery systems.

5.3. Interfacial compatibility towards electrodes

While hydride-based SSEs have largely met the practical ionic conductivity requirements using the methods mentioned above, challenges remain regarding electrode compatibility for the configuration and commercial applications of SSBs.

5.3.1. The anode compatibility

The inherent reducibility of $H^{\delta-}$ enables thermodynamic stability of hydride-based SSEs toward anodes, evaluated through electrochemical stability and electrode compatibility. Standard CV measurements of Li|SSE|stainless steel cells serve as the characterization method for electrochemical stability. Wu et al. [444] employed CV to demonstrate a significantly wider ESW of 0–5 V vs. Li^+/Li for $LiBH_4$/h-BN compared to oxide- or sulfide-based SSEs, which was corroborated by multiple studies [409,410,434,435]. Given the dominance of lithium metals as anodes, anode compatibility specifically denotes lithium dendrite suppression capability, as benchmarked by long-term cycling and CCD in Li|SSE|Li symmetric cells. Notably, ionic conductivity enhancement strategies mentioned above concurrently optimize anode compatibility, as exemplified by CCD of 11.43 mA cm^{-2} for AOLiBHI–5PMMA CSE [454], 15.12 mA cm^{-2} for H400-AIBH SSE [46], and a record 21.65 mA cm^{-2} for HT150-5PMMA CSE [47]. These ultrahigh values confer universal commercial viability through superior dendrite inhibition.

Furthermore, selecting metal hydrides with high theoretical lithium storage capacity as anodes for hydride-based SSEs significantly enhances interfacial stability during lithium deposition/stripping cycles. For instance, Zheng et al. [455] leveraged an *in situ* solid-state short-circuit electrochemical reaction between $LiAlH_4$ and Li, utilizing fast electron/lithium-ion conductors (C and *P6₃mc* $LiBH_4$) to synthesize Li_3AlH_6-Al nanocomposites comprising dispersed Al nanoparticles within an amorphous Li_3AlH_6 matrix. The Li|$LiBH_4$|Li_3AlH_6–Al half-cell delivered specific capacity of 2266 mAh g^{-1}, CE of 88 %, capacity retention of 71 % after 100 cycles, and rate capability of 1429 mAh g^{-1} at 1 A g^{-1}. Yu et al. [55] fabricated *in situ* MgH_2 and Mg_2NiH_4 nanocrystals uniformly confined in an electrochemically inert Nd_2H_5 framework via hydrogenation of single-phase $Nd_4Mg_{80}Ni_8$ alloy. This structure shortened Li^+/electron diffusion paths while mitigating volume-change-induced stress, ensuring electrode integrity. The resulting Li|$LiBH_4$|$Nd_4Mg_{80}Ni_8H_x$ half-cell maintained 997 mAh g^{-1} after 100 cycles at 1C rate (2038 mA g^{-1}).

5.3.2. The cathode compatibility

Although hydride-based SSEs demonstrate excellent stability against lithium metal anodes, their propensity for oxidation at elevated potentials poses compatibility challenges with certain cathode materials. Here, several compatible cathode materials applicable to hydride-based SSEs are discussed.

Sulfur cathodes demonstrate applicability in hydride-based ASSLBs with a high theoretical capacity of 1675 mAh g^{-1} and an acceptable potential around 2.1 V. Orimo's group [409] blended S–C composite with $0.7Li(CB_9H_{10})$–$0.3Li(CB_{11}H_{12})$ SSE to prepare a composite cathode, which achieved initial discharge and charge capacities of 2013 and 1557 mAh g^{-1} at 0.03C and 1.0–2.5 V vs. Li^+/Li. The excess discharge capacity was attributed to SSE contribution, subsequently keeping stable near theoretical values. This Li–S battery configuration demonstrated potential for achieving 2500 Wh kg^{-1} reversible energy density at high current densities of 1–3C. Through analyzing microstructural evolution of cathodes during cycling, Kisu et al. [456] investigated the capacity degradation mechanisms in Li–S batteries employing $Li_4(BH_4)_3I$ SSE. Cross-sectional SEM and Raman spectroscopy revealed that discharge-triggered reactions between sulfur active species and Li^+ induced cathode thickening due to volume expansion, while subsequent lithium extraction during charging caused contraction. This repeated stress fluctuation generated cracks within the $Li_4(BH_4)_3I$ of the cathode region, progressively degrading ionic pathways, elevating interfacial resistance, and partially deactivating the S–C composite, ultimately resulting in capacity fading. Increasing $Li_4(BH_4)_3I$ content in cathodes effectively mitigates this degradation mode. Replacing sulfur cathodes with sulfide polyacrylonitrile (SPAN) alleviates shuttle effects and volume expansion while enhancing conductivity and stability, thereby enabling extended cycling and high CE. This stems from sulfur molecules or atoms in SPAN cyclizing with polar –CN groups to form heterocyclic structures that successfully confine sulfur [457]. Zhang et al. [458] further designed nanospherical SPAN (NS-SPAN) cathodes coupled with $Li_4(BH_4)_3I$ SSE, improving cathode/electrolyte interfacial compatibility and lithium-ion diffusion kinetics. The resulting Li|$Li_4(BH_4)_3I$|NS-SPAN ASSLB delivered discharge capacity of 878.5 mAh g^{-1} after 150 cycles with CE of 99 % at 0.1C. The 2D layered TiS_2 cathode possesses a stable host structure and excellent electronic conductivity, with a relatively low operating potential of only about 2 V. Unemoto et al. [459] investigated the interface between TiS_2 and $LiBH_4$ during oxidation, discovering that $Li_2B_{12}H_{12}$ formed *in situ* as a stable interfacial phase. Furthermore, they assembled a Li|$Li_4(BH_4)_3I$|TiS_2 SSB and observed that I^- doping reduced interfacial stability, leading to capacity degradation [443]. The spinel-structured $Li_4Ti_5O_{12}$ is known as a "zero-strain" material due to its negligible volume change during lithium-ion insertion/extraction. With a lithiation potential around 1.55 V, this value is sufficiently low to prevent significant decomposition of hydride-based SSE. The Li|$Li_{16}(BH_4)_{13}I_3$@g-C_3N_4|$Li_4Ti_5O_{12}$ cell demonstrated stable cycling with low polarization at 60 °C. However, further research is constrained by the high cost and insufficient electrical conductivity of $Li_4Ti_5O_{12}$.

However, these aforementioned cathode materials compatible with hydride-based SSEs generally operate at low voltages, potentially leading to lower energy density. Notably, recent studies have successfully integrated hydride-based SSEs with high-voltage cathodes like LFP, LCO, and NCM811 into full-cell configurations, enabled by advancements in electrolytes with broad ESWs and high CCD. For instance, the borohydride/halide dual-substituted argyrodite-type SSE, $Li_{5.35}PS_{4.35}(BH_4)_{1.15}Cl_{0.5}$, demonstrated high-voltage tolerance (< 4.6 V vs. Li^+/Li) and excellent rate capability (5C) when paired with an $LiNbO_3$-coated NCM811cathode [398]. The full cell exhibited a discharge specific capacity of 121.46 mAh g^{-1} with retention of 72.6 % after 100 cycles at 0.5C within the voltage range of 2.1–3.7 V vs. Li^+/Li–In. The *in situ*-formed ultrafine LiF nanoparticles facilitated the construction of a stable Li^+-conductive cathode–electrolyte interphase (CEI) layer, thereby enhancing the electrode compatibility of $Li_2B_{12}H_{12}$ [435]. The Li|LiF-decorated

$Li_2B_{12}H_{12}$|LFP ASSLB delivered a specific capacity of 108 mAh g^{-1} with 84 % capacity retention after 30 cycles at 75 °C within the range of 2.0–4.0 V vs. Li^+/Li. Similarly featuring electronic insulation properties, the LiH layer modified on $LiBH_4$ surface via partial dehydrogenation strategy significantly enhanced oxidative stability, extending the ESW of SSE to 6.0 V [46]. This was achieved through strong electron localization from $B_{12}H_{12}^{2-}$. When matched with a LCO cathode, the full cell demonstrated a capacity retention of 83.6 % and an average CE of 99.13 % after 50 cycles within an operating voltage range of 3.0–5.0 V vs. Li^+/Li at 0.1C. These developments pave the way for future exploration of diverse cathodes to further enhance the energy density and cycling stability of hydride-based ASSLBs.

5.4. Summary

Hydrides are emerging as promising SSEs for ASSLBs, exhibiting prominent properties including low grain-boundary resistance, superior reduction stability, and high ion selectivity. Following the identification of $LiBH_4$ as a fast Li^+ conductor at elevated temperatures in 2007, extensive exploration of novel hydride-based SSEs and comprehensive characterization have accelerated. Practical deployment of hydride-based SSEs necessitates overcoming ionic conductivity limitations, particularly at RT. Diverse modification strategies, including ion substitution, ligand complexation, interfacial engineering, nanoconfinement, and composite design, have successfully modified crystal lattices and established Li^+ diffusion pathways. As summarized in Table 4 and Fig. 24k, the RT ionic conductivities of hydride-based SSEs have increased from 10^{-5} to 0.1 mS cm^{-1} or even 10 mS cm^{-1}. Concurrent improvements include higher CCDs, wider ESWs, and enhanced compatibility with high-voltage cathodes. Seminal contributions from research groups, such as Yu and Pan's pioneering ligand complexation studies and Kim and Cho's hydride–sulfide composite systems, demonstrate significant progress. Nevertheless, the field remains emergent, with persistent barriers to practical implementation and commercialization.

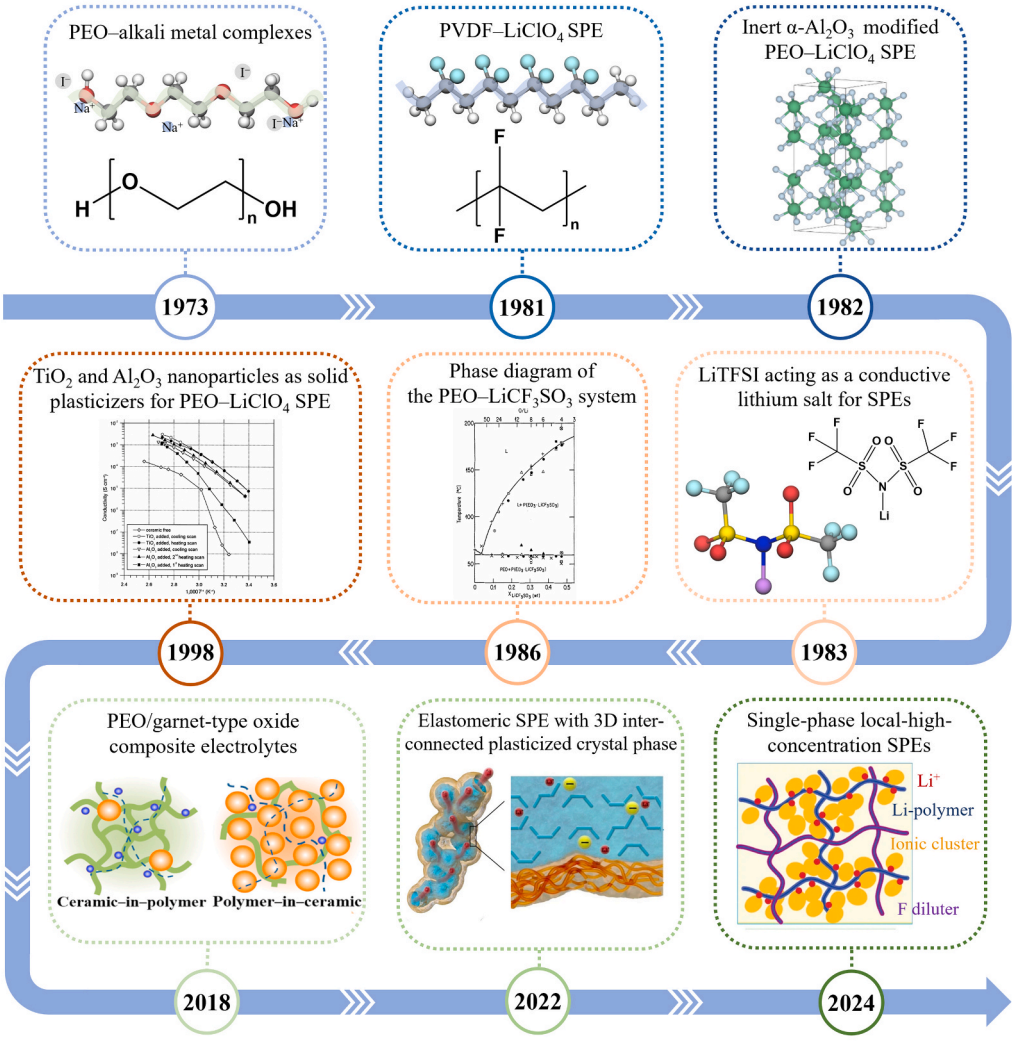

Fig. 25. A brief review of the development of SPEs. Reproduced with permission from ref. [26,462–469].

To advance research on hydride-based SSEs, three key priorities merit emphasis. First, elucidating the Li^+ diffusion mechanisms is imperative. Although existing studies focus on ionic conductivity and electrochemical performance, the fundamental diffusion pathways remain incompletely resolved. Deeper mechanistic insights are crucial for unlocking the full potential of hydride-based SSEs and guiding targeted optimization. Second, achieving a balance between high ionic conductivity and electrode compatibility is essential. While certain hydride-based SSEs demonstrate superior conductivity, most systems exhibit limited electrode pairing options. Beyond successful integration with sulfides, oxides, or polymers to expand ESWs, exploring novel electrode combinations is critical for enhancing practical viability through improved operating voltage, capacity, interfacial stability, and lithium dendrite suppression. Third, pioneering innovative modification strategies is paramount. Unlike other SSEs, current hydride-based SSE research remains primarily inspired by hydrogen storage studies. Future work should leverage the intrinsic composition and physicochemical properties of hydrides, guided by fundamental insights into their ion conduction mechanisms, to develop tailored modification approaches.

6. Solid-state polymer electrolytes

6.1. Development of solid-state polymer electrolyte

In contrast to the previously mentioned inorganic electrolytes, SPEs present characteristic advantages, such as exceptional flexibility, tunable processability, and excellent interfacial contact with various electrodes [460]. Their cost-effectiveness, wide operational temperature range (−40–100 °C), and compatibility for hybrid integration with inorganic/organic components further establish their status as promising candidates for next-generation energy storage systems. However, the practical application of SPEs also faces severe limitations. For instance, SPEs exhibit insufficient ionic conductivity ($\sigma = 10^{-7}$–10^{-5} S cm^{-1}) and lithium-ion transference number ($t_{Li+} = 0.2$–0.4) at RT, primarily due to sluggish lithium-salt dissociation kinetics and restricted segmental motion of polymer chains. Additional challenges include thermal degradation at elevated temperatures (> 100 °C) affecting safety, insufficient mechanical modulus (< 0.1 GPa) failing to suppress lithium dendrite propagation [461], narrow ESWs (< 4.0 V vs. Li^+/Li) limiting high-voltage compatibility, and interfacial polarization accelerating capacity fade. Addressing these interrelated issues through strategies such as innovative molecular design, advanced composite architectures, and interface optimization is crucial for bridging laboratory research and industrial applications.

The ion transport mechanisms in SPEs vary depending on the crystallinity of polymer. In amorphous polymers or amorphous regions of semi-crystalline polymers, lithium ions dissociate from lithium salts by coordinating with electron–donors (e.g., –O–, –S–, –C≡N) within the polymer matrix. These ions are subsequently transported through the segmental motion of polymer chains and inter-/intra-chain hopping between coordination sites [470]. Conversely, in crystalline polymers or crystalline regions, Li^+ ion transport occurs primarily through hopping within the helical channels [471]. Typical SPE systems incorporate lithium salts such as LiTFSI, lithium trifluoromethanesulfonate (LiOTF), lithium perchlorate ($LiClO_4$), and lithium hexafluoroarsenate ($LiAsF_6$) dissolved in polymer matrices such as PEO, PAN, PVDF, poly(vinylidene fluoride-co-hexafluoropropylene) (PVDF-HFP), PMMA, and polycarbonate (PC). Fig. 25 chronologically outlines the pivotal milestones in the early development of SPEs, along with representative advances in the field of lithium batteries in recent years. Here the structural and functional characteristics of representative SPEs are briefly introduced. In 1973, Wright et al. [26] first discovered PEO–lithium salt complexes, opening the curtain on polymer-based electrolytes. Although PEO-based electrolytes demonstrate excellent interfacial adhesion, mechanical flexibility, Li^+ coordination ability, and low cost, their high crystallinity (75 %–80 %) limits the segmental motion, yielding low RT ionic conductivity ($\sigma = 10^{-5}$–10^{-3} mS cm^{-1}) [472]. Heat treatment can reduce the crystallinity, but it comes at the expense of mechanical strength and thermal stability. Notably, reactive terminal –OH groups (oxidation threshold: 4.05 V vs Li^+/Li) cause high-voltage cathode incompatibility and lithium anode instability [473]. PAN, pioneered by Perche et al. [474] in 1975 for electrolyte applications, is enriched with strong electron-withdrawing –C≡N groups ($\varepsilon = 5.5$) and features robust mechanical strength, exceptional thermal/electrochemical stability, and compatibility with high-voltage cathodes [475]. Nevertheless, its inherent chain rigidity and –C≡N/Li reactivity necessitate composite modification strategies such as blending, co-polymerization, or incorporation of nanofillers to enhance flexibility and ionic transport [476].

PVDF-based electrolytes, characterized by ordered chain arrangement and high crystallinity, exhibit robust mechanical strength, thermal stability, and wide ESWs (4.5 V vs. Li^+/Li), but suffer from low ionic conductivity and limited ion-coordinating groups. The seminal work of Watanabe et al. [462] in 1981 demonstrated PC-modified PVDF–$LiClO_4$ electrolytes achieving RT ionic conductivity of 0.01 mS cm^{-1}. The ion-conducting capability of PVDF-based electrolytes relies on residual solvents that solvate Li^+ into $[Li(solvent)_x]^+$ clusters, which are transported along PVDF chains via interactions with electronegative fluorine atoms [477,478]. However, these solvents, with high highest occupied molecular orbital (HOMO) energy levels, narrow the ESW, decompose at high voltages, and form resistive SEIs on lithium anodes, thereby degrading compatibility with high-voltage cathodes and lithium metal anodes. The PVDF-HFP copolymer synergistically combines the crystalline properties of PVDF with the amorphous nature of HFP, offering high dielectric constants ($\varepsilon_r = 8$–12), lithium salt solubility, mechanical strength, electrochemical stability, thermal stability, and RT ionic conductivity exceeding 0.1 mS cm^{-1}. However, unlike PEO and PAN, which can form dense thin films, the PVDF-HFP matrix comprises micrometer-sized spherical particles. Interparticle voids weaken mechanical strength and induce uneven distribution of lithium-ion flux, promoting uncontrolled lithium dendrite growth [479]. Furthermore, alkaline radicals on the lithium metal surface rapidly trigger defluorination of PVDF-HFP, which leads to the formation of an unstable and porous SEI. PMMA, a lightweight and transparent polymer with abundant ester groups, is predominantly amorphous (96 %) at 25 °C, which is conducive to lithium-ion conduction [480]. In 1985, PMMA was first applied as a polymer matrix for gel polymer electrolytes (GPEs) [481]. PMMA demonstrates cost-effectiveness, excellent lithium-salt solvation capability, high plasticizer absorption, and favorable interface stability with lithium

metal anodes, although high brittleness and poor compatibility with high-voltage cathodes limit the application of PMMA-based SPEs. PC, with strongly polar carbonate groups, effectively dissolves lithium salts and suppresses ion aggregation [482]. Similar properties are observed in other aliphatic and cyclic polyester-based electrolytes. Aliphatic PC exhibits a low glass transition temperature, satisfactory thermal stability, and excellent oxidation resistance, making it a promising candidate for high-voltage lithium batteries. Nevertheless, its practical application faces challenges including complex preparation process, poor interfacial compatibility with lithium anodes and inadequate ionic conductivity.

Based on the above discussion, the primary challenges currently restricting the development of SPEs include low RT ionic conductivity, narrow ESWs, insufficient thermal/chemical stability, weak mechanical strength, and possible interfacial side reactions with electrodes. To address these constraints, substantial research efforts have been dedicated to modifying SPEs. This section comprehensively summarizes recent advancements, with focused analysis on five key strategies: structural modification of polymer matrices, electrode–electrolyte interfacial engineering, precise regulation of lithium salt concentration or composition, innovative fabrication processes for ultra-thin SPE films, and incorporation of functional fillers. These approaches leverage distinct mechanisms to deliver multifunctional performance enhancements in SPEs, thereby establishing viable technological pathways for their implementation in advanced energy storage architectures.

6.2. Structural modification

The structural modification of SPEs primarily falls into two categories: macro-structural modification (e.g., co-blending) and micro-structural modification (e.g., co-polymerization, cross-linking, fluorination). These strategies aim to reduce the crystallinity of polymers, promote lithium salt dissociation and ion transport, homogenize Li^+ deposition, and widen ESWs. Co-blending technology physically combines polymers without altering their chemical structures, thereby leveraging their complementary properties to improve mechanical strength, ionic conductivity, and interfacial stability. A representative example is Li et al. [483], who blended an amorphous bio-polyamide featuring a rigid N-substituted pyrrolidone ring (IBD) with PEO/LiTFSI, fabricating an ultrathin (35 μm), low-crystallinity, and high-strength-modulus co-blended SPE via electrospinning (Fig. 26a). Mechanistically, IBD enhanced the dipole moments of PEO chains, broadened the ion transport channels, and promoted LiTFSI dissociation through carbonyl–Li^+ coordination. The resulting SPE achieved ionic conductivity of 0.426 mS cm^{-1} at 50 °C and an ESW of 4.8 V. However, the thermodynamic immiscibility of polymers often causes phase separation, hindering ion transport at the interface. Compatibilizers can improve the compatibility and stability of blended systems by mitigating the interfacial tension between different phases and enhancing interfacial adhesion. Zhi et al. [484] utilized an inorganic compatibilizer, polyacrylonitrile-grafted MXene (MXene–g-PAN), to improve the miscibility and ion transport at the phase interface of PVDF-HFP/PAN blend. The obtained SPE, as shown in Fig. 26b, enabled Li||$LiCoMnO_4$ SSB with a discharge voltage of 5.1 V and a decent capacity of 131 mAh g^{-1}. In micro-structural approaches, regulating polymer permittivity and conformation offers precise control. Huang et al. [478] exemplified this by introducing an all-trans conformation random copolymer into a highly dielectric terpolymer to interfere with crystallization. The significantly increased relative dielectric constant and an all-trans conformation where all fluorine atoms are on the same side of the carbon chain (Fig. 26c) collaboratively facilitated the dissociation of lithium salts and the rapid hopping of $[Li(DMF)_x]^+$ complexes.

In situ polymerization strategies demonstrate significant potential in enhancing the ionic transport kinetics of SPEs and electrode/electrolyte interfacial compatibility [485]. The mechanism is that the liquid precursors can infiltrate the pores and interstices of electrodes, followed by polymerization-induced pore filling. Furthermore, *in situ* co-polymerization with other polymers can construct 3D crosslinked networks, enriching ion transport pathways. 1,3-dioxolane (DOL), a widely used monomer for *in situ* polymerization, is prone to undergo ring-opening polymerization (ROP) reactions triggered by $Al(OTf)_3$, LiFSI, $LiBF_4$, $LiPF_6$, and other Lewis acid salts under mild conditions [486]. For instance, Deng et al. [487] successfully synthesized ultrathin crosslinked SPE films (4 μm–22 μm) via $LiBF_4$-initiated cationic ROP of DOL and trimethylolpropane triglycidyl ether (TTE) in mesoporous PVDF-HFP matrix, achieving good RT ionic conductivity (0.3 mS cm^{-1}), oxidative stability, and mechanical flexibility. To address the limitations of linear polyether in thermal/electrochemical/interface stability, Zhu et al. [488] developed a hybrid crosslinked polymer electrolyte (HCPE) through $LiPF_6$-initiated *in situ* polymerization of DOL and polyhedral silsesquioxane (PS). The *in situ*-formed hybrid network enhanced HCPE's electrochemical/interface stability (ESW of 5.2 V) and Li^+ transport kinetics ($\sigma = 2.22$ mS cm^{-1} at 30 °C, t_{Li+} of 0.88), as evidenced by stable lithium stripping/plating for 1000 h at 1 mA cm^{-2}. To further optimize the copolymerization strategy, Ren et al. [486] employed LiDFOB-catalyzed *in situ* copolymerization of DOL and 1,3,5-trioxane (TXE) combined with succinonitrile (SN) plasticization. This approach synergistically reduced the crystallinity of copolymer electrolyte and weakened Li^+–EO coordination, resulting in a high t_{Li+} of 0.881, an ionic conductivity of 0.406 mS cm^{-1} at RT, and a wide ESW of 5.1 V, while enabling stable cycling exceeding 1500 h in Li|| Li symmetric cells. Beyond DOL-based systems, Xia et al. [489] designed a dual-crosslinked SPE fabricated via *in situ* thermally initiated polymerization of poly(ethylene glycol diacrylate) (PEGDA) and 2-(3-(6-methyl4-oxo-1,4-dihydropyrimidin-2-yl)ureido) ethyl methacrylate (UPyMA) within a LiTFSI/N-methylurea deep eutectic solvent (DES). The resulting network encapsulated the DES, achieving fast ionic conduction, high modulus, and a wide ESW (5.2 V vs. Li^+/Li). Notably, the assembled Li|SPE|LCO soft-pack battery exhibited an initial specific energy of 428.63 Wh kg^{-1} at 0.1C. Critically, *in situ* co-polymerization strategies can also integrate polymer segments with different chain motility or Li^+ coordination capabilities to effectively balance and optimize the overall performance of the SPE. A representative case is Xue et al. [490], who pioneered a one-step *in situ* synthesis of block copolymer electrolytes (BCPEs) in

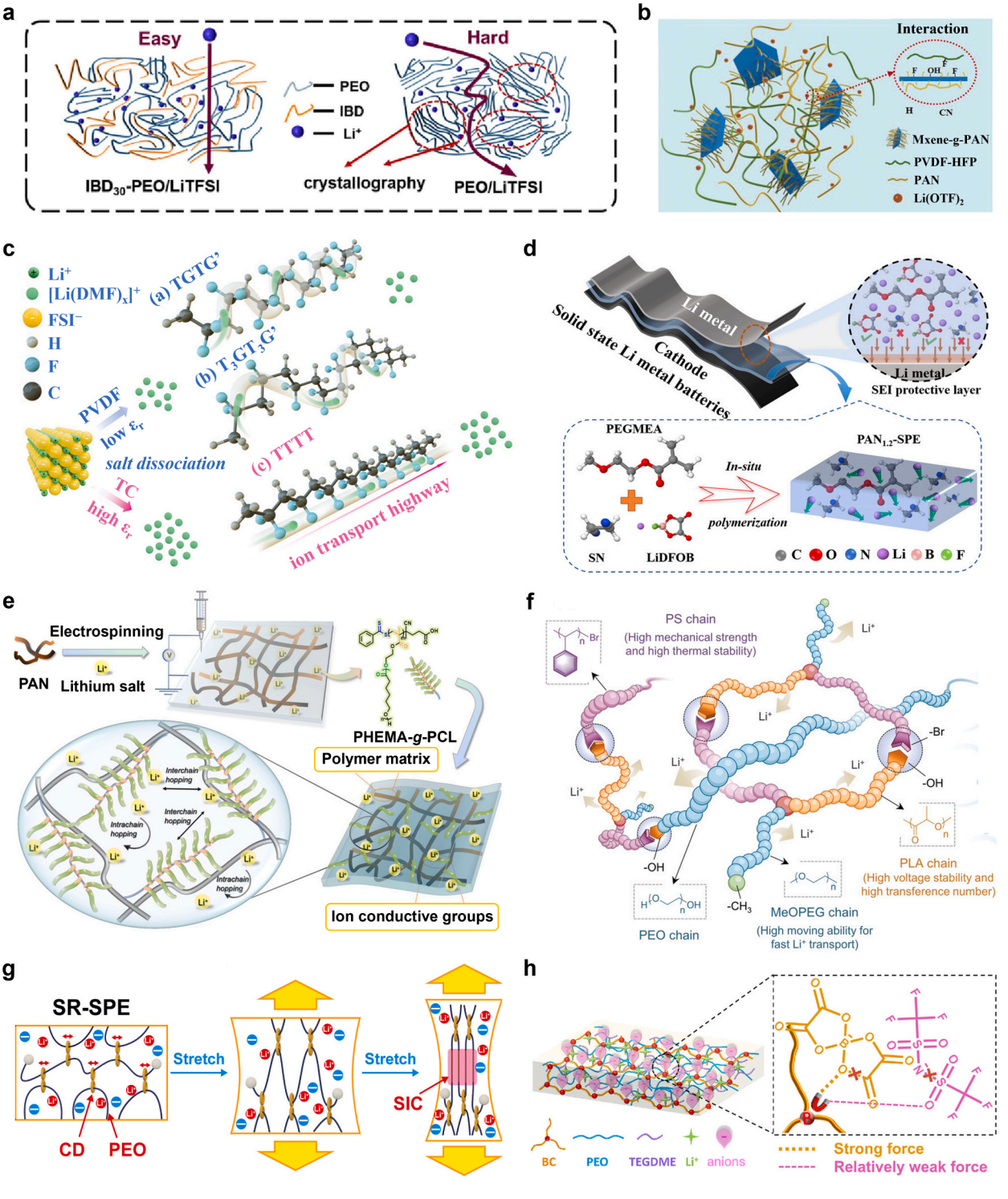

(caption on next page)

LMBs by integrating reversible addition-fragmentation chain transfer (RAFT) polymerization of poly(ethylene glycol) methyl ether acrylate (PEGMEA) with carboxylic acid-catalyzed ROP of ε-caprolactone (ε-CL). This design balances polyether/polyester Li^+ coordination, enabling rapid ion migration while ensuring seamless cathode infiltration and interfacial transport.

Polymerization-induced phase separation (PIPS) is an advanced strategy that induces phase separation of homogeneous precursors

Fig. 26. (a) Schematic of crystallization behavior of IBD_{30}–PEO/LiTFSI electrolyte. Reproduced with permission from ref. [483]. Copyright 2023, Chemical Engineering Journal. (b) Schematic of component and interaction of MXene–g-PAN based SPE. Reproduced with permission from ref. [484]. Copyright 2023, Advanced Functional Materials. (c) Schematic of the lithium salts dissociation and ion transport processes facilitated by SPE with different permittivity and conformation. Reproduced with permission from ref. [478]. Copyright 2023, Advanced Energy Materials. (d) Schematic of the structure for the $PEGMEA_1$-SN_x-SPE. Reproduced with permission from ref. [492]. Copyright 2023, Angewandte Chemie International Edition. (e) Schematic of the preparation route of brushshaped polyester-based graft copolymers. Reproduced with permission from ref. [495]. Copyright 2023, Chinese Chemical Society Chemistry. (f) Schematic of the interactions in the HEMI-ASPE–Li membrane. Reproduced with permission from ref. [497]. Copyright 2022, Advanced Materials. (g) Schematic of the strain-induced crystallization procedure of SR-SPE. Reproduced with permission from ref. [498]. Copyright 2023, Science Advances. (h) Schematic diagram of BSPE + 10 % LiBOB membrane. Reproduced with permission from ref. [504]. Copyright 2023, Energy Environment Materials.

to form multi-scale topological structures by regulating the kinetic parameters of polymerization reactions. It has been extensively employed to resolve the inherent trade-off between high ionic conductivity and high mechanical strength in SSBs. SN, as a prototypical organic plastic crystal, exhibits an elevated acceptor number and high oxidation potential. Its unique molecular architecture can restructure the polymer chain dynamics via molecular-level interactions, thereby synergistically facilitating the lithium salt dissociation and ion transport processes. For example, Lee et al. [466] employed PIPS between the polymer and SN to *in situ* fabricate an elastomeric SSE featuring 3D interconnected plastic crystal phases on copper foil. The optimized electrolyte exhibited exceptional mechanical robustness, high ionic conductivity (1.1 mS cm^{-1} at 20 °C), low interfacial impedance, and an elevated t_{Li+} of 0.75. Similarly, Liu et al. [491] fabricated a shape-memory biphasic SPE via *in situ* thermal induced cross-linking of PEGMEA, ethyl cyanoacrylate (CA), and plasticizer SN. The SN-based plastic crystalline electrolyte established continuous 3D channels within the CA–PEGMEA polymer matrix, enabling efficient lithium-ion transport. Due to the phase separation phenomenon and interfacial lithium-ion conduction, the RT ionic conductivity of biphasic CA–PEGMEA–SN SSE reached 1.9 mS cm^{-1}. In contrast to co-polymerization, which is a chemical reaction process that links multiple monomers into macromolecular compounds under certain conditions, co-crystallization is a physical phenomenon where various components are mixed in certain proportions and solidify simultaneously to form intertwined crystalline structures, collectively establishing a eutectic system. Poly(ethylene glycol) methyl ether methacrylate (PEGMEMA) displays good compatibility with lithium metal, but its ionic conductivity and oxidative stability are not satisfactory. As illustrated in Fig. 26d, Zhang et al. [492] introduced electrophilic SN into PEGMEMA to enhance LiDFOB salt dissociation and free Li^+ concentration. The optimized eutectic-based $PAN_{1.2}$-SPE (PEGMEMA:SN = 1:1.2 mass ratio) exhibited a high ionic conductivity of 1.30 mS cm^{-1} at 30 °C as well as excellent interfacial stability with lithium anode.

Nonlinear polymer electrolytes with high branching topological structures (e.g., hyperbranched, star-shaped, comb-shaped, or brush-shaped) exhibit more modifiable functional groups, lower crystallinity and better lithium salt dissolution ability compared to linear analogs, contributing to accelerating ion transport and potentially enhancing mechanical or chemical or electrochemical properties [493]. Xue's group [494] designed a multilayer bottlebrush-shaped electrolyte (PH-PCL) via ROP of ε-CL using poly2-(hydroxymethyl)acrylic acid (PHMA) as a dual-functional initiator/catalyst. Critically, PCL and carboxylic acid groups constituted the short-range structure of PH-PCL, endowing SPE with increased t_{Li+} of 0.82 at 60 °C and dendrite-free properties, whilst the long-range brush-shaped structure was more conducive to lithium-ion conduction. Subsequently, they synthesized brush-shaped polyester-based graft copolymers via one-pot RAFT–ROP synergy, injecting them into PAN films for high-performance SPEs (Fig. 26e) [495]. Trifluoroethyl methacrylate (TFEMA) can serve to modulate the molecular structure due to its high thermal stability, chemical resistance, low HOMO energy level, and abundance of Li^+ coordination groups (C=O, C–O, and C–F). Capitalizing on these attributes, Hu et al. [496] engineered a 21-arm fluoropolymer through atom transfer radical polymerization (ATRP), integrating it into PEO-based SPE. Notably, supramolecular interactions arising from C=O, C–O, C–F, O–H, and C–H bonds, together with the multi-arm topology structures, significantly improve the high-voltage stability (ESW ≈ 4.7 V vs. Li^+/Li) and t_{Li+} (0.88) of the SPE, as well as physical properties such as toughness and thermal stability. Further innovating, they combined ATRP, ROP, and click chemistry to fabricate multifunctional ABC miktoarm star-shaped terpolymers (ABCTP, Fig. 26f), which were introduced into PEO to prepare high-entropy micro domain interlocked SPEs (HEMI-ASPEs) [497]. The self-assembled dynamic interpenetrating network in HEMI-ASPE delivered excellent toughness (6.72×10^4 kJ m^{-3}), considerable ionic conductivity (0.456 mS cm^{-1} at 70 °C), appreciable t_{Li+} of 0.63 and desirable thermal stability (T_d > 400 °C). Interestingly, Hashimoto et al. [498] redefined mechanical-electrochemical balance via a slip-ring SPE (Fig. 26g), where strain-induced PEO ordered orientation formed planar zigzag crystals under large deformation, coupled with slidable crosslinks to prevent stress concentration. The dual mechanisms enhanced toughness and stiffness without compromising ionic transport, exemplifying topology-engineered solutions for next-generation batteries.

The strategic incorporation of highly electronegative fluorine atoms into SPEs can improve the performance through multifaceted mechanisms. Fluorination reduces polymer crystallinity to facilitate Li^+ transport, promotes the formation of inorganic SEI layers for homogeneous Li^+ deposition, and lowers the HOMO energy level to enhance oxidation resistance and broaden ESW. Yan et al. [499] demonstrated this by synthesizing a flame-retardant SPE via ROP of fluorinated ethylene carbonate (FEC) with LiDFOB, achieving an extended voltage of 5.5 V and stable cycling in 4.9 V-class $LiNi_{0.5}Mn_{1.5}O_4$ battery. Notably, fluorine atoms effectively suppressed the propagation of oxygen radicals during combustion, ensuring the safety of batteries under HT operation. Advancing functional design, Lin et al. [500] designed a fluorinated dual-functional SPE via visible light photo-controlled radical polymerization (PCRP). In this system, fluorinated hydrocarbon chains stabilized the SEI via Li–F interactions, while polyether segments mitigated phase separation between fluorophilic and hydrophilic groups, thereby avoiding localized electric field and uneven ion transport. Further innovations include ultraviolet (UV) light-initiated copolymerized polyfluorinated crosslinked SPEs [501]. The crosslinked network mediated electron-withdrawing effects from fluorinated segments, improving the oxidative resistance (ESW = 5.08 V vs. Li^+/Li) while

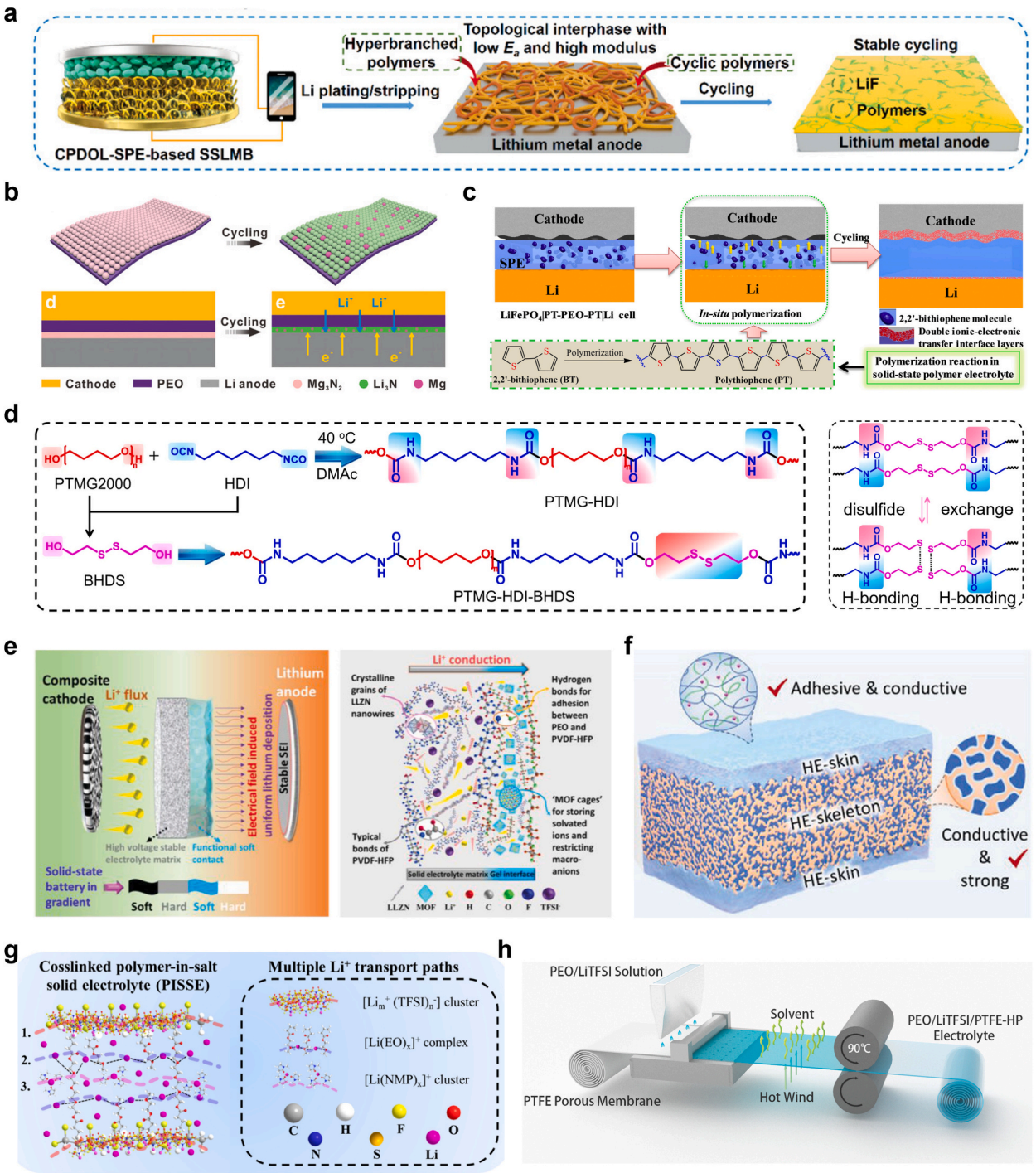

Fig. 27. (a) Schematic of the interface behavior of topologically cross-linked PDOL-based SPEs. Reproduced with permission from ref. [511]. Copyright 2023, Advanced Energy Materials. (b) Schematic of the interface behavior of PEO–Mg_3N_2 electrolyte during cycling. Reproduced with permission from ref. [512]. Copyright 2019, Advanced Functional Materials. (c) Schematic of the formation of a double ion–electron transfer interface layer in LFP|PT–PEO–PT|Li cell. Reproduce with permission from ref. [513]. Copyright 2021, Angewandte Chemie International Edition. (d) Schematic of chemical structures, dynamic covalent disulfide bonds and hydrogen bonds of PTMG-HDI-BHDS. Reproduced with permission from ref. [520]. Copyright 2024, Nature Communications. (e) Schematic of internal construction of PMLSE and possible Li^+ transport pathways. Reproduced with permission from ref. [522]. Copyright 2020, Advanced Energy Materials. (f) Schematic of HETE with sandwiched structure. Reproduced with permission from ref. [525]. Copyright 2023, Advanced Materials. (g) Schematic of Li^+ transport pathways in cross-link PISSE. Reproduced with permission from ref. [526]. Copyright 2024, Energy Storage Materials. (h) Schematic of the preparation processes for ultrathin PEO/LiTFSI/PTFE electrolyte. Reproduced with permission from ref. [527]. Copyright 2023, Energy Storage Materials.

enhancing the mechanical modulus to suppress lithium dendrite growth. Considering that excessive fluorination is prone to slower kinetics and lower polymerization degree, Yang et al. [502] prepared partially fluorinated meltblown cloth reinforced SPEs (PFMC-SPE) by *in situ* UV-light PCRP of acrylate monomers. The PFMC-SPE possesses remarkable RT ionic conductivity (1.0 mS cm^{-1}), a wide ESW (5 V vs. Li^+/Li), enhanced mechanical strength, and effective lithium dendrite suppression. In parallel, researchers have explored fluorinated lithium salts to regulate solvation structures and interfacial chemistry. Liu et al. [503] developed selectively fluorinated aromatic lithium salts (SFALS), which weakened the Li^+–polyether coupling while enhancing Li^+–anion coordination. Hydrogen bonding between SFALS and polymer matrix induced a unique "triad-type" solvation structure, facilitating a robust Li_2O-rich SEI layer. SFALS-based batteries with high-loading LFP (6 mg cm^{-2}) and ultrathin lithium foil (40 μm) demonstrated 97.4 % capacity retention after 582 cycles at 60 °C and 0.2C, highlighting excellent cycling stability and practical viability. Beyond fluorine-specific strategies, functional anions like NO_3^- and bis(oxalato)borate anion (BOB^-) have proven effective in optimizing t_{Li+} and SEI stability. As illustrated in Fig. 26h, Xie et al. [504] synthesized boron-rich hexagonal-structured SPE (BSPE + 10 % LiBOB) by introducing a three-armed boron-rich crosslinker (BC). The sp^2 hybrid boron atom with an empty p-orbital enables BC to immobilize $TFSI^-$ anions via Lewis acid–base interactions, achieving high t_{Li+} of 0.83. Crucially, the stronger interaction between BOB^- and BC moderately attenuated the $TFSI^-$-trapping effect of BSPE, resulting in a uniform and stable LiF, Li_3N-rich $TFSI^-$-derived SEI on lithium anode.

Conventional SPEs exhibit dual-ion transport (Li^+ ions and anions), inducing concentration polarization, degraded ionic conductivity, and lithium dendrite growth. In contrast, single lithium-ion conducting polymer electrolytes (SLICPEs), where anions are covalently anchored to polymer backbones to force Li^+-only migration, theoretically achieve t_{Li+} approaching 1 [505]. However, their complex synthesis and uncontrolled charge distribution often lead to polyanion-cation clustering, exacerbating Li^+–anion interactions and impeding ion dissociation. Addressing these challenges, Feng et al. [506] designed an alternating copolymer P(SSPSILi-alt-MA) via simple radical co-polymerization of maleic anhydride and lithium 4-styrenesulfonyl (phenylsulfonyl) imide, which was blended with PEO to achieve SLICPE with high t_{Li+} (0.97, 80 °C) and ionic conductivity (1.84 mS cm^{-1}, 80 °C). The anhydride groups with high dielectric constants accelerated the dissociation of lithium ions, while the alternating structure allowed molecular-scale ionization and uniform distribution of Li^+, thus suppressing dendrite formation. Topological innovations further advance SLICPE design. A lithium-rich imidazole anionic porous aromatic skeleton (PAF-220-Li) was prepared via Sonogashira–Hagihara coupling reaction and further lithiation [507]. The conjugation of benzene rings and imidazole anions that were immobilized on the skeleton could delocalize negative charges, thereby reducing the binding energy to Li^+. Consequently, only Li^+ transported in interconnected pores, suppressing polarization and achieving t_{Li+} of 0.93 and an ionic conductivity of 0.501 mS cm^{-1}. Through precisely engineered alternating sequences, Chen et al. [508] developed a solid-state fluorinated SLICPE that enabled uniform Li^+ distribution, decoupled Li^+–anion solvation, and enhanced Li^+–anion dissociation within the SPE matrix, synergistically facilitating sequence-assisted PEO–Li^+–anion migration (t_{Li+} = 0.93). These topological strategies and molecular engineering resolve the inherent trade-off between charge localization and dissociation in SLICPEs, establishing novel paradigms for high-safety SSBs.

Overall, structural modification of SPEs commonly focuses on reducing crystallinity and broadening ion-transport pathways via topological regulation (e.g., branching, crosslinking, fluorination), while optimizing electrode contact through *in situ* polymerization or compatibilizers to achieve high t_{Li+}, wide ESWs, and high mechanical strength. However, strategy selection requires trade-off considerations. For instance, enhancing mechanical strength often compromises ionic conductivity, while achieving high t_{Li+} entails complex synthesis processes. Therefore, future efforts should prioritize multi-level synergistic designs with intrinsic compatibility, such as dynamically adaptive interfaces and reversible chemical bonds.

6.3. *Interfacial engineering*

Interfacial engineering strategies for SPEs aim to improve electrode–electrolyte contact intimacy, suppress parasitic side reactions, facilitate directional Li^+ transport, and achieve high-voltage cathode compatibility through additive optimization, constructing ordered ionic highways, fabricating conformal interfaces, or designing multilayer structures. Additives optimize the interfacial compatibility between the electrolyte and the electrode by assisting in constructing the SEI. Lin et al. [509] employed cryo-EM to reveal that incorporating FEC additives into SN-incorporated polyacrylate (SN–PEA) successfully eliminated corrosive side reactions between Li metal and both SN plasticizer and PEA polymer backbone, thereby forming a LiF-rich, conformal, and stable SEI with a mosaic structure. The symmetric Li||Li cell delivered exceptional cycling stability for 1800 h at 0.5 mA cm^{-2}, 1 mAh cm^{-2}, with a CE of 99 %. However, the additive strategy faces several limitations, including incompatibility with specific SPE matrices, long-term interface instability, and environmental pollution concerns. ALD, a thin-film fabrication technique characterized by self-limiting reactions and precisely controlled layer-by-layer growth, has been extensively utilized to engineer conformal electrode–electrolyte solid–solid interfaces in SSBs. Yamauchi et al. [510] demonstrated the ALD of amorphous Al_2O_3 on the surface of PEO–LiTFSI SPE effectively suppressed lithium dendrite propagation and polysulfide shuttle effects.

The stability of electrode–electrolyte interfaces is governed by ion migration dynamics, electron transfer kinetics, and interfacial chemical reactivity. As shown in Fig. 27a, Mai et al. [511] *in situ* constructed topological interphase layers with cyclic and hyperbranched structures by leveraging the redox reactions between topologically cross-linked PDOL-based SPE and lithium metal anode. The interlayer guided dendrite-free, homogeneous, and reversible lithium deposition behaviors, coupled with enhanced mechanochemical stability and fast Li^+ diffusion kinetics. Constructing a mixed ionic–electronic conducting interlayer (MIECI) is an effective approach to homogenize the ion distribution and current density, as validated by *COMSOL Multiphysics* simulation [512]. Wan et al. [512] discovered that the Mg_3N_2 layer decorated on a PEO electrolyte *in situ* converted into an MIECI composed of fast ionic conductor Li_3N ($\sigma \approx 1$ mS cm^{-1} at RT) and benign electronic conductor Mg metal during cycling (Fig. 27b). This regulates ion/electron distribution, enhancing interfacial stability and kinetics of the Li anode. Extending this paradigm, Li et al. [513] constructed an MIECI at the

cathode–electrolyte interface via *in situ* electrochemical polymerization of 2,2′-bithiophene in a PEO electrolyte, as illustrated in Fig. 27c. The *in situ*-formed double conductive polythiophene (PT) layer significantly reduces the interfacial resistance, promotes Li^+ migration, resists oxidative decomposition, and maintains compatibility with the Li anode. The assembled Li|PT–PEO–PT|LFP battery exhibits a capacity retention rate of 94 % after 1000 cycles at 40 °C and 2C. Rational high-entropy topology design can simultaneously improve mechanical strength and ionic conductivity of SPEs, with applicability extendable to SEI. Inspired by the above, Hu et al. [514] constructed PEO–TiN SPEs with mixed ionic/electronic conductivity for modifying the PEO–$LiYF_4$ interlayer. PEO–TiN not only facilitates the formation of Li_3N layer on the lithium metal surface but also serves as a protective barrier to suppress lithium dendrite growth, synergistically enhancing the electrode–electrolyte interface stability. When paired with high-voltage $Li_3V_2(PO_4)_3$ or NCM523 cathodes, the sandwich-structure SPE demonstrates remarkable long-term cycling stability and capacity retention.

Self-healing SPEs have garnered significant interest for their ability to autonomously repair mechanical/chemical-induced interface damage, ensuring battery stability and safety. Common self-healing mechanisms include polymer interchain diffusion, capsule-based self-healing, vascular-based self-healing, reversible covalent chemistry, and supramolecular dynamic chemistry [515]. The external self-healing mechanisms achieve rapid response to environmental anomalies by incorporating microcapsules and nanofibers containing healing agents, though often at the cost of size mismatch, complex preparation processes, and undesirable electrochemical performance [516,517]. The design of bio-inspired materials is expected to break through these limitations and is a major research direction in the future [518]. On the contrary, the chemical self-healing mechanism can provide SPEs with higher compatibility and faster chemical reaction kinetics. Representing this approach, Guo et al. [519] developed a self-healing SPE by *in situ* co-polymerization of UPyMA and ethylene glycol methyl ether acrylate (EGMEA). Reversible hydrogen bonding between –C=O and $–NH_2$ groups in UPyMA spontaneously heals dendrite-induced interfacial defects, endowing the SPE with exceptional ionic conductivity (2.2 mS cm^{-1}), oxidation resistance (5.9 V vs. Li^+/Li), interfacial stability, and compatibility with high-voltage cathodes. Advancing beyond hydrogen bonding, dynamic covalent chemistry provides stronger interfacial restoration. Huang et al. [520] designed self-healing poly(ether-carbamate)-based SPEs through polymerization of polyol and polyisocyanate monomers and introduction of 2-hydroxyethyl disulphide (BHDS) chain extender (Fig. 27d). The synergistic effect of dynamic covalent disulfide and hydrogen bonding between carbamate groups enabled exceptional interfacial healing, achieving low interfacial contact resistance and stable cycling in Li–S batteries.

Ideal SPEs should exhibit good interfacial compatibility with both lithium metal anodes and high-voltage cathodes to ensure the cycling stability of full cells. Consequently, multilayer or multifunctional SPEs customized for the distinct interfacial requirements of cathodes and anodes have become the preferred configuration. The flexible bilayer SPE developed by Goodenough's group [521] exemplifies this approach: poly(N-methylmalonamide) (PMA)–LiTFSI adjacent to the cathode resists oxidative degradation at 4 V, whereas PEO–LiTFSI near the lithium anode ensures dendrite-free, low-impedance Li deposition. Wang et al. [522] further supplemented this paradigm through a bilayer heterostructured SPE combining a PVDF-HFP/garnet nanowire ($Li_{6.75}La_3Zr_{1.75}Nb_{0.25}O_{12}$) matrix for flexibility and high-voltage stability with a HkUST-1/PEO/PVDF-HFP interfacial gel for enhanced anode contact and inhibited side reactions (Fig. 27e). To match high-capacity and high-voltage nickel-rich ternary cathodes, Du et al. [523] constructed a fluorinated and nitrided polymer electrolyte (F&NPE) with dual-reinforced stable interface by co-polymerizing hexafluorobutyl acrylate (HFBA) and N,N'-methylene bisacrylamide (MBAM). The antioxidant fluorinated and nitrided groups promote the construction of robust CEI and favorable SEI, effectively mitigating interfacial parasitic reaction and structural degradation at the NCM cathode and dendrite propagation at the lithium anode. Li|F&NPE|NCM622 battery featured a capacity retention of 85 % after 500 cycles with CE above 99.8 % at 0.5C and 4.5 V. Similarly, Guo et al. [524] fabricated bidirectional functional polymer electrolytes (BDFPE) via direct UV solidification of carbonate-based precursors containing the functional additives FEC and triethyl phosphate (TEP) on the surface of anode and cathode, respectively. The intimate contact between BDFPE and electrodes reduced the interfacial impedance and achieved rapid and efficient Li^+ flux. The Li|NCM622|BDFPE battery exhibited 84 % capacity retention after 150 cycles at 0.5C and a discharge capacity of 104 mAh g^{-1} at a high rate of 5C. Interestingly, Wang et al. [525] engineered a sandwich-structure high-entropy tape electrolyte (HETE, Fig. 27f) leveraging strong polymer chain-ion interactions. The amorphous high-entropy PEO electrolyte serves as the skin layer to facilitate ion transport and surface adhesion, while the high-entropy PEO/PVDF alloy electrolyte acts as the middle layer to improve mechanical properties. The HETE enables pressure-free assembly of flexible SSBs while maintaining stable electrode–electrolyte interfaces, offering novel strategies for scalable integration in next-generation energy storage systems.

The core mechanism of interfacial engineering modification strategies lies in constructing stable, highly conductive, and conformal interface layers. Chemical/electrochemical regulation (additives, *in situ* constructed interlayers or MIECIs) enhances rapid interfacial ion transport while suppressing dendrite growth and parasitic reactions. Multifunctional structural designs simultaneously achieve compatibility with high-voltage cathodes and lithium metal anodes, while *in situ* polymerization, self-healing chemistry, and bio-inspired strategies facilitate real-time damage repair and dynamic equilibrium of interfacial chemistry. Collectively, these strategies ensure uniform Li deposition, rapid ion transport, and extended cycling stability.

6.4. Concentration regulation

While conventional strategies like cross-linking, co-polymerization, and filler/IL incorporation aim to construct multiple Li^+ transport highways in SPEs, they often suffer from phase incompatibility, filler agglomeration, and discontinuous conduction paths. A paradigm-shifting approach involves formulating polymer-in-salt solid electrolytes (PISSEs) by exceeding the critical lithium salt concentration (> 50 wt% in SSEs), where enhanced polymer-salt interactions expand amorphous domains. PISSEs establish dual Li^+ transport mechanisms, including segmental dynamics in amorphous polymer region, and rapid ion hopping through connected ionic cluster networks. Liu et al. [528] prepared PISSE with PVDF-HFP:LiTFSI = 1.1 via solution casting method, and entirely infiltrated

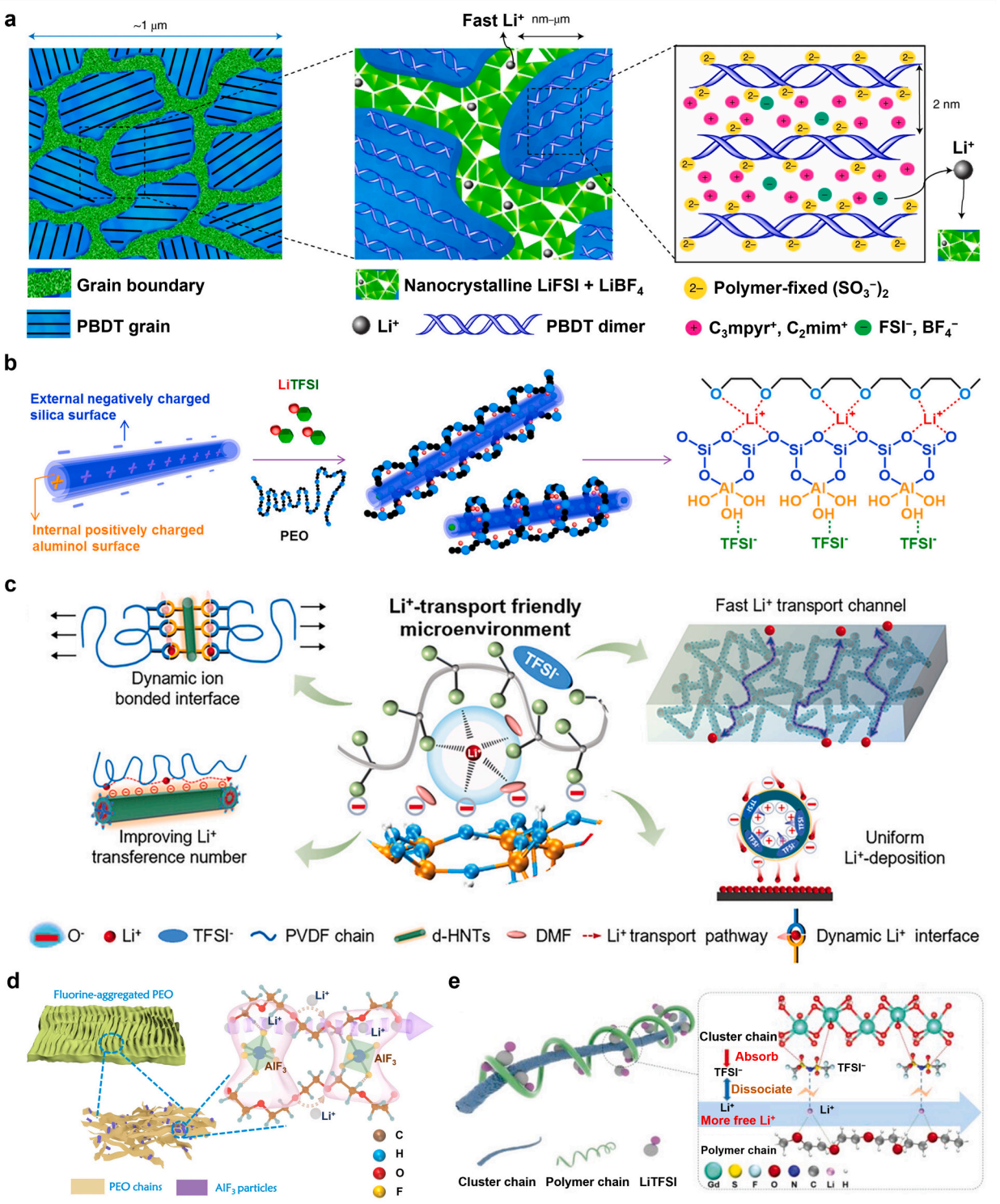

Fig. 28. (a) Schematic of the morphology and Li^+ conduction mechanism of MIC. Reproduced with permission from ref. [544]. Copyright 2021, Nature Materials. (b) Schematic of the preparation and structure of HNT-modified flexible electrolytes. Reproduced with permission from ref. [554]. Copyright 2017, Nano Energy. (c) Schematic of the friendly Li^+ transport microenvironment of d-HNT-doped SPE. Reproduced with permission from ref. [556]. Copyright 2023, Advanced Energy Materials. (d) Schematic of the internal interactions in fluorinated PEO-based electrolyte. Reproduced with permission from ref. [563]. Copyright 2022, Nature Communications. (e) Schematic of the organic–inorganic interface of CPCSE. Reproduced with permission from ref. [564]. Copyright 2023, Advanced Materials.

PISSE into 3D TiO_2 electrode to construct integrated ASSLB with maximum interface contact, electrochemical and mechanical stability. The HFP component facilitated LiTFSI dissolution and all the $TFSI^-$ ions existed as aggregated ion pairs (AGGs), thus enhancing cation/anion association and constructing fast ion transport channels in PISSE. Pu et al. [526] further engineered triple ionic transport pathways via EO-modified PVDF networks: $[Li_m^+TFSI_n^-]$ (m > n) clusters, $[Li(EO)_x]^+$ complexes and $[Li(NMP)_x]^+$ clusters, as illustrated in Fig. 27g. The optimized PISSE featured σ of 0.303 mS cm^{-1} at 25 °C, mechanical strength of 0.811 MPa, and compatibility with 4.3 V high-voltage cathode $LiFe_{0.2}Mn_{0.8}PO_4$. Further innovating filler synergy, Wang et al. [529] synergistically integrated LiFSI/LLZTO garnet into PVDF-HFP (polymer:salt = 0.75), enabling triple Li^+-transport routes. Specifically, Li^+ transport occurred along the PVDF-HFP (via $Li(DMF)_x^+$ clusters), along the LLZTO interfaces, and through high-concentration LiFSI-enabled hopping network. Ultimately, the PISSE achieved an ionic conductivity of 1.67 mS cm^{-1} at 25 °C and an ESW of 4.8 V. To expand the application of unconventional active components in high-performance electrolytes, Li et al. [530] proposed a general solidified localized high-concentration electrolyte (S-LHCE) strategy with the decoupling of ion pairing and ion conduction. By decoupling the electrolyte from a non-solvating PVDF-HFP framework and tailoring solvation structures under ultra-high salt concentrations, improved interfacial compatibility, enhanced ionic conductivity, homogeneous lithium deposition and wide temperature range (−10–100 °C) applications have been achieved. Extending this paradigm of concentration engineering, Wang's group [467] mixed Li–polymer (PIS, salt = 63 wt%) and F diluter (PVDF-HFP) to prepare a locally high-concentration single-phase SPE (LPIFD). The Li–polymer and the high-concentration salt ensured continuous Li^+-conduction channels and contributed forming LiF-rich SEIs that efficiently inhibited the lithium dendrites, while the F diluent increased the mechanical strength. The high miscibility of Li–polymer with F diluent eliminated phase boundaries and further eradicated lithium dendrites, achieving a CCD of 3.7 mA cm^{-2}. Collectively, these PISSE innovations have achieved a balance between ionic conductivity and stability through coordinated manipulation of polymer–salt coordination chemistry and microstructure engineering, offering guidelines for the design of safe high-performance SSBs.

6.5. *Ultra-thinning design*

In ASSLBs, the thickness of SSE affects the energy density by influencing bulk resistance, interfacial transport, and the proportion of inactive substances [531,532]. Janek et al. [533] highlighted that achieving commercial-grade energy densities exceeding 500 Wh kg^{-1} in ASSLBs requires electrolytes with sub-50 μm thickness. Nevertheless, conventional thickness reduction strategies often induce structural defects and mechanical modulus degradation, heightening short-circuit risks through compromised electrode isolation. Therefore, the development of appropriate preparation processes is essential to balance the minimum thickness and mechanical strength of SPEs.

Commercial polyethylene (PE) separators are widely employed as electrolyte frameworks due to their high porosity, excellent mechanical strength, chemical stability, and scalability for mass production. For instance, Huang et al. [534] prepared an ultrathin composite polymer electrolyte (CPE) with a thickness of 7.5 μm by infiltrating PEO/LiTFSI into a PE separator network using a one-step solvent evaporation method. Ultra-thin CPE facilitates sufficient Li^+ conductance, and the robust and flexible PE provided mechanical support, allowing the energy densities of 216 Wh kg_{cell}^{-1} and 317 Wh L_{cell}^{-1} (excluding packaging). Similarly, Han et al. [535] utilized PE as a support framework to fabricate a cross-linked long-chain backbone CPE (16 μm) through *in situ* UV polymerization of PEGDA, LiTFSI and SN. The resulting LMBs, prepared via roll-to-roll process and loaded with 4 mg cm^{-2} LCO, delivered an impressive energy density of 317.68 Wh kg^{-1}. In another innovation, Yao's group [536] modified PE separator by tightly attaching porous poly (methyl methacrylate)–polystyrene (PMMA–PS) interfacial layers on both sides using a phase inversion method. The modified PE was then filled with PEGMEA and lithium salts, resulting in a 10 μm-thick CPE with an ultra-high RT ionic conductivity of 34.84 mS cm^{-1}, remarkable mechanical properties of 103.0 MPa, high elongation of 142.3 %, and CCD of 0.45 mA cm^{-2}. Beyond PE, other porous framework materials such as PTFE, PAN, polyamide (PI), and polyamide (PA) are also increasingly used in ultra-thin SPEs, offering new opportunities for safe and high-energy-density next-generation SSBs. Among these, PTFE stands out for its exceptional thermal, chemical, and mechanical stability. As depicted in Fig. 27h, Wang et al. [527] developed an ultra-thin (6 μm) and highly dense CPE by impregnating PEO/LiTFSI electrolyte into porous PTFE matrix via scraping and hot-pressing processes. The PTFE framework not only provided structural integrity but also contributed to reducing the crystallinity of electrolyte and shortening ionic transport path, substantially lowering ionic transport impedance. Similarly, PAN-based frameworks have gained attention due to their excellent mechanical properties and ability to form stable interfaces with lithium metal anodes. Liu et al. [537] successfully fabricated a 10 μm self-supporting and scalable CPE through infiltrating the PEGDA-based electrolyte into porous electrospun PAN fiber membranes via *in situ* thermal curing. The PAN fiber membrane offered robust mechanical strength and was conducive to the formation of Li_3N-rich SEI, effectively stabilizing lithium metal anode. The pouch cell assembled with ultra-thin CPE and high-loading NCM811 cathode achieved energy densities of 380 Wh kg^{-1} and 936 Wh L^{-1}. Inorganic materials can be strategically incorporated to augment both mechanical integrity and thermal stability in ultra-thin electrolyte systems. Luo et al. [538] synthesized refractory and hard 3D porous vermiculite ceramic films via electrostatic spinning and heat treatment. These films were embedded in a PEO–LiTFSI electrolyte, and subsequently PAN was cast to prepare ultrathin (4.2 μm) and lightweight (1.29 g cm^{-3}) bilayer SPEs. The bilayer structure stabilized both the lithium metal anode and high-voltage cathode, enabling the full cell assembled with NCM811 (N/P = 1.1) to achieve a stable cycling life of over 3000 h and remarkable energy densities of 506 Wh kg^{-1} and 1514 Wh L^{-1}. PI frameworks have the advantages of high modulus, thermal stability, and flame retardancy. Cui's group [539] designed an ultra-thin SPE with a thickness of 8.6 μm and an energy density of 246 Wh kg^{-1} by infiltrating PEO/LiTFSI into a nanoporous PI film. The PI film endowed the CPE with a tensile modulus of 850 MPa, effectively inhibiting dendrite growth to prevent battery short circuits while withstanding abuse tests such as bending, cutting, and piercing. Similarly, for enhanced flame retardancy, Hu et al. [540] prepared an ultra-thin (7 μm), nonflammable SPE by infiltrating a PEO electrolyte solution containing 3 wt% ammonium hexafluorophosphate (NH_4PF_6) flame retardant into a PA-6

nanofiber membrane and drying it, resulting in lower ionic transport impedance, higher energy density, and an ESW of 5 V. These advancements underscore the versatility of various porous framework materials in developing ultra-thin SPEs with enhanced mechanical properties, ionic conductivity, and safety features.

6.6. Functional additives

Functional additives employed in SPEs are divided into liquid additives and solid additives, and each system functions through different mechanisms. Liquid additives, primarily act as plasticizers, significantly improve ionic conductivity by synergistically reducing the crystallinity of polymers and fostering the dissociation of lithium salts. However, high loading of plasticizer required to achieve an ionic conductivity comparable to that of ILs may lead to mechanical performance degradation and gelation risks. In terms of this issue, Xie et al. [541] prepared a polymer-in-plasticizer SSE with Al–O nanoclusters as nodes based on a water-initiated polymer cross-linking strategy, exhibiting a tensile rate of 4640 % and a toughness of 3.87×10^4 kJ m^{-3}. A high-concentration (> 75 wt%) SN-solvated lithium salt established an ionic transport highway, achieving an excellent ionic conductivity of 1.41 mS cm^{-1} at 30 °C. In addition to playing a plasticizing role, various liquid additives have been introduced into SPEs as flame retardants, broadening the application temperature range of ASSLBs. For example, chitosan polycation IL tailored PEO-based SPE enabled Li||LFP cells with excellent electrochemical stability and cycling performance at 150 °C [542]. The SPEs based on polymerized ILs and IL plasticizers exhibited thermal stability up to 300 °C, excellent non-flammability, high oxidative stability (> 5.0 V vs. Li^+/Li), and excellent compatibility with lithium metal [543]. As shown in Fig. 28a, Madsen's group [544] described a solid-state molecular ionic composite electrolyte based on an extremely rigid oriented liquid crystal polymer combined with IL and concentrated lithium salt. This innovative electrolyte featured high strength (200 MPa), non-flammability, dendrite resistance, outstanding Li^+ conductivity (1 mS cm^{-1} at 25 °C), and electrochemical stability (5.6 V vs. Li^+/Li). Furthermore, incorporating liquid additives into polymer matrix can effectively reduce viscosity and surface tension, which enhances interfacial contact and ion transport kinetics between electrolytes and electrodes, and improves high voltage stability of batteries. However, it is crucial to recognize that under certain conditions, the incorporation of liquid additives may induce the formation of GPEs rather than true SPEs, thereby failing to eliminate inherent risks associated with thermal runaway and fire hazards [545–547]. Solid additives share functional parallels with liquid additives while providing superior attributes in intrinsic safety, mechanical stability, ionic transport pathways, and cost-effectiveness, albeit sometimes with increased process complexity. Current research focuses on four primary solid additive classifications: inert inorganic fillers for mechanical reinforcement, active inorganic fillers enabling multiple ion transport and electrochemical stability, nanostructured organic fillers optimizing Li^+ flux through molecular-scale channels, and composite fillers synergistically combining the merits of multiple material systems.

6.6.1. Inert inorganic fillers

The inorganic fillers employed in SPEs are classified into inert fillers and active fillers based on their ionic conductivity. Inert fillers, predominantly oxide ceramics such as TiO_2 [548], Al_2O_3 [549], SiO_2 [550] and ZrO_2 [551], usually do not directly participate in the construction of lithium-ion conduction pathways. Instead, their surface functional groups (e.g., ether bonds, oxygen-containing groups, and fluorine-containing groups) function as Lewis acid sites to effectively anchor anions and facilitate the dissociation of lithium salt, reducing the crystallinity of polymer matrix, thereby enhancing both ionic conductivity and mechanical strength of SPEs. For instance, Sun's group [552] designed a glass fiber reinforced CPE (PEO@GF) via a solution impregnation approach, improving mechanical properties and ionic conductivity while suppressing lithium dendrite growth, thereby effectively preventing short circuits. Asbestos (ASB), a 1D fibrous silicate mineral, offers advantages over metal oxides in cost, abundance, and ease of synthesis. Its abundant surface active sites act as heterogeneous nucleation seeds for Li^+ adsorption, optimizing the uniform distribution, effective diffusion and dendrite-free deposition of Li^+ [553]. Halloysite nanotubes (HNTs), 1D aluminosilicate clays, feature a negatively charged outer surface containing –Si–O–Si– tetrahedral sheets and a positively charged inner surface containing –Al–OH groups, as illustrated in Fig. 28b [554]. This unique structure effectively promotes the dissociation of lithium salts and the transport of free lithium ions, enhancing the electrochemical and mechanical stability of the electrolyte [555]. To further unlock the potential of HNTs in CPE applications, Wang et al. [556] developed monodisperse dipole-like HNT (d-HNT) through treating natural HNT with sodium hexametaphosphate solution, as depicted in Fig. 28c. The incorporation of d-HNT into PVDF matrix could form a quasi-solid-state electrolyte membrane with a Li^+ migration-friendly microenvironment, mechanical properties (toughness, mechanical strength, and puncture resistance) comparable to commercial membranes, and enhanced stability against lithium metal anode.

In contrast to 1D fillers, 2D fillers exhibit significantly enhanced geometric anisotropy and larger surface area, which are critical for optimizing interfacial interactions in CPEs. Aiming at the porous structures and restricted ionic transport of PVDF-based SPEs, Lu et al. [557] proposed a phase-regulation strategy by incorporating 2D $MoSe_2$ nanosheets into PVDF to fabricate a densified CPE. Beyond inducing the all-trans (β-phase) transition of PVDF and optimizing solvation structures to elevate ionic conductivity, $MoSe_2$ could also react *in situ* with lithium anodes to generate Li_2Se fast ionic conductors within SEI, significantly improving interfacial kinetics and CE. Zheng's group [558] reported positively charged 2D monolayer layered double hydroxide nanosheets (SLNs) enhanced PVDF-HFP-based CPE. The incorporation of SLNs not only accelerated the dissociation of LiTFSI and the immobilization of $TFSI^-$ anions but also homogenized Li^+ flux, substantially ameliorating the electrolyte/anode interface compatibility. MXene, a family of 2D transition metal carbide/nitride/carbon-nitride ($M_{n+1}X_nT_x$, n = 1–3), offers a vast surface area, abundant active functional groups, hydrophilicity, and mechanical robustness. In 2019, MXene was first dispersed into PEO–LiTFSI SPE to suppress PEO crystallization and enhance chain segment movement [559]. However, the high electronic conductivity and agglomeration tendency limit the usage dosage of MXene. Regarding this issue, Yang et al. [560] engineered monodisperse MXene mesoporous SiO_2 (MXene–mSiO_2)

nanosheets with a sandwich structure via cationic surfactants-assisted hydrolysis of tetraethyl orthosilicate on the surface of MXene-Ti_3C_2. The abundant hydroxyl and fluorine termini of MXene–$mSiO_2$ nanosheets established hydrogen bonds and Lewis acid-base interactions with anions in the polymer matrix, improving the flexibility and stability of SPE, and accelerating Li^+ migration at the mesopore nanosheet–polymer interface. Xu et al. [561] further fabricated 3D MXene-confined SPEs through coaxially infiltrating MXene nanosheets into PAN fibers via two-stage directional induction with fluid air flow and electric field. This approach constructed continuous Li^+-migration highways while preventing MXene agglomeration. Surface functional groups on MXene mediated electrostatic and hydrogen-bonding interactions with cations in the PAN, boosting Li^+ diffusion ($t_{Li+} = 0.72$).

Fluorine-containing inorganic fillers are widely used in CPE because of the multifunctional role of F^- ions. F^- ions expand the amorphous region of polymer matrices and interact with lithium salts to increase mobile Li^+ concentration, thereby improving the ionic conductivity of CPEs. Furthermore, F^- ions chemically react with lithium metal to form a compact and stable artificial interface layer, which acts as an effective barrier to prevent undesirable side reactions between electrode and electrolyte. Gong et al. [479] dispersed 2D fluorinated graphene in PVDF-HFP, reinforcing mechanical properties via fine-grain strengthening while stabilizing SEI and facilitated interfacial ion transport without thickness increase (45 μm). Advancing catalytic integration, Archer's group [562] developed a fluorinated SPE through *in situ* ROP of DOL initiated $Al(OTf)_3$ and aluminium fluoride (AlF_3), achieving compatible interphases on both cathode and anode sides. The AlF_3 served dual roles as a Lewis acid catalyst and a degradation inhibitor for the electrolyte and Al current collector under high voltage, enhancing the practical cycling performance of Li||NCM622 batteries. Further

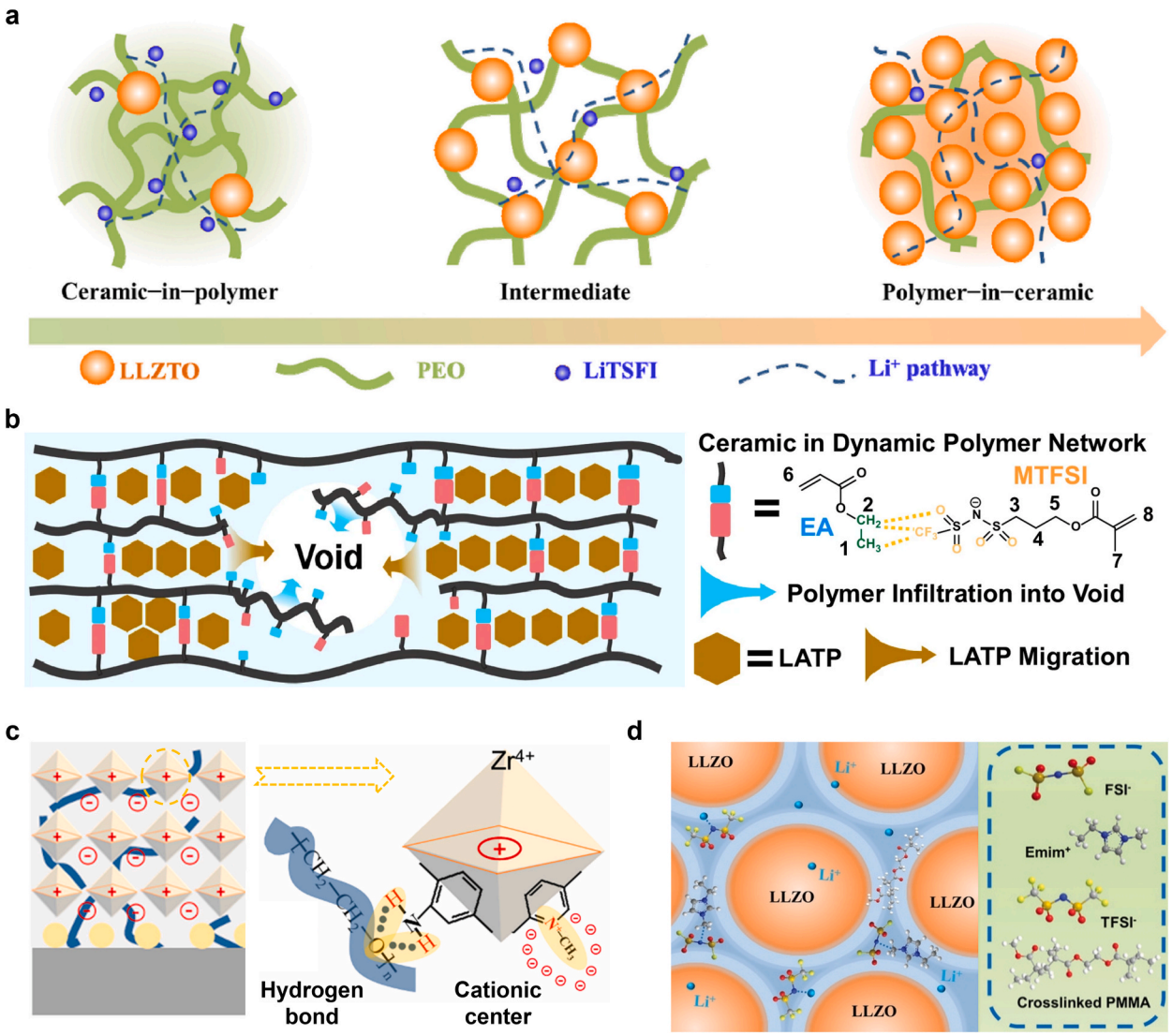

Fig. 29. (a) Schematic of Li^+ transport pathways within PEO-LLZTO CSEs. Reproduced with permission from ref. [469]. Copyright 2018, Nano Energy. (b) Schematic of the structure of PCE. Reproduced with permission from ref. [575]. Copyright 2024, Nature Communication. (c) Schematic of the Li deposition behavior of anion-immobilized PEO@CMOF electrolyte. Reproduced with permission from ref. [585]. Copyright 2019, Energy Storage Materials. (d) Schematic of the SIC electrolyte. Reproduced with permission from ref. [588]. Copyright 2022, Advanced Materials.

advancing this concept, Fig. 28d illustrates the strategic incorporation of self-assembled mesoporous α-AlF_3 nanoparticles with strong Lewis acidity and high specific surface area into the PEO matrix to construct fluorinated SPE [563]. The homogeneously dispersed α-AlF_3 created a fluorine-rich smooth interface to compensate for the fluorine loss during anode conversion reaction, while forming Li_2O-rich SEI to inhibit the growth of lithium dendrites. The resulting Li||FeF_3 all-solid-state pouch battery maintained a reversible discharge capacity of 600 mAh g^{-1} after 200 cycles at 153 mA g^{-1}.

To address the challenge of non-conductive inert fillers obstructing ion transport pathways in CPEs, Mai et al. [564] implemented a mixed-solvent strategy to uniformly monodisperse sub-1 nm inorganic cluster chains within a polymer matrix and combined them to form a homogeneous and continuous organic–inorganic interface. As exhibited in Fig. 28e, these monodisperse cluster chains interconnect to establish a fully active 3D Li^+ conductive network, improving Li^+ transport efficiency ($\sigma = 0.52$ mS cm^{-1}, $t_{Li+} = 0.62$). Concurrently, recognizing the insufficient mechanical reinforcement of SPEs by low-concentration inert fillers, Lu's group [565] uniformly dispersed LM-adsorbed molecular sieves (MSs) into PEO, yielding stable LM-MS–PEO composites as protection layers against lithium dendrites. In addition, MSs could reduce the crystallinity of PEO, regulate the Li^+ transport, and lower the operating temperature. Diverging from conventional approaches that utilize fillers to promote lithium salt dissolution to increase ionic conductivity, Zhou et al. [566] innovatively introduced 3Å zeolite MSs into the PVDF matrix to sequester residual solvents and weaken Li^+-solvent interactions. This strategy induced an anion-rich solvated structure, substantially improving the interfacial stability of the electrolyte with both lithium metal anode and high-voltage cathode.

6.6.2. *Active inorganic fillers*

Compared to inert fillers, active fillers can not only reduce polymer crystallinity and enhance mechanical strength, but also provide mobile Li^+ and supplementary Li^+ transport paths [533]. Common active fillers primarily include oxide-based SSEs such as garnet-type LLZO [567], perovskite-type LLTO [568], NASICON-type LAGP [569], LISICON-type LGPS [570] and so on, while sulfide-based SSEs [571], halide-based SSEs [572] and hydride-based SSEs [50] have been explored. In turn, polymer matrices also impart good interfacial compatibility and processability to these inorganic ceramic electrolyte fillers. To elucidate the ion transport mechanisms of active filler-doped CPE, Goodenough et al. [469] proposed "permeation threshold" concept. By modulating the relative content of PEO and LLZTO, three polymerization systems were prepared, namely "ceramic-in-polymer (CIP)", "intermediate", and "polymer-in-ceramic (PIC)", as shown in Fig. 29a. Below the permeation threshold of LLZTO, Li^+ conduction mainly relies on polymer chain segment motion, whereas at or above this threshold, Li^+ migration occurs through a dual mechanism combining polymer chain dynamics and ion channels constructed by LLZTO ceramic particles, with the latter predominating. Hu et al. [573] further investigated the Li^+ migration path in PEO–LiTFSI–LLZO CSE via ss-NMR technique, revealing a progressive shift from polymer-phase to ceramic-phase conduction with increasing LLZO content, accompanied by reduced ion mobility and elevated reactive ion concentration. When the ceramic/polymer interface was improved by liquid plasticizers, Li^+ was mainly conducted through the modified polymer phase. Lee et al. [567] employed CF_4 reactive ion etching to eliminate the inactive Li_2CO_3 layer from powdered LLZO fillers, simultaneously increasing the mobile Li^+ concentration and interfacial ion transport, ultimately boosting the ionic conductivity of PVDF-based CSE (0.405 mS cm^{-1}). Garnet particles of various sizes and contents can play different roles in polymer matrices. Sun's group [574] discovered that the CIP electrolyte with 20 vol% 200 nm LLZTO particles (CIP-200 nm) exhibited satisfactory ionic conductivity and flexibility, while the PIC electrolyte with 80 vol% 5 μm LLZTO (PIC-5 μm) displayed excellent mechanical strength. Sandwich-type CSE combining PIC-5 μm middle layer and CIP-200 nm outer layers collectively achieved dendrite suppression and favorable interfacial compatibility with lithium anode. Moreover, in order to enhance the interfacial contact and air stability of ASSLB, an integrated hierarchical structure system could be prepared by *in situ* co-polymerization of organic–inorganic CSEs onto lithium foils [569], which was also expected to advance high safety and high energy density. Advancing beyond static CSEs, dynamic CSEs have also been actively explored. Xin et al. [575] developed a cold-milling self-healing plastic–ceramic electrolyte (PCE) by compositing a dynamically cross-linked aprotic polymer containing non-covalent –CH_3···CF_3 bonds with LATP (Fig. 29b). *Operando* X-ray fluorescence and cryogenic TEM characterizations revealed that the PCE achieves self-healing functionality through a two-step dynamic defect-removal mechanism, effectively suppressing lithium dendrite penetration and chemomechanical degradation. This granted Li||Li symmetric cells exceptional 2000 h cyclability at 1 mA cm^{-2}.

The aforementioned zero-dimensional spherical particle fillers characterized by high specific surface area and low aspect ratio tend to agglomerate, leading to discontinuous ion transport channels and elevated interfacial impedance for Li^+ migration. In contrast, 1D nanofibrous fillers with high aspect ratio enable continuous Li^+ transport pathways. He et al. [477] demonstrated this advantage by integrating LATP nanowires tightly anchored with DMF into PVDF polymer matrices, fabricating multiple collaborative ceramic–polymer–liquid Li^+ transport highways that homogenized Li^+ flux distribution, suppressed electrode–electrolyte interfacial side reactions, and enabled dendrite-free lithium deposition. By further extending structural dimensionality, 2D nanosheets featuring ultrathin structures, high anisotropy, and satisfactory polymer compatibility improve the physicochemical properties of CSEs when incorporated into polymers. Song et al. [576] pioneered the dispersion of garnet nanosheets synthesized via co-deposition with graphene oxide templates into a PEO–$LiClO_4$–EmimFSI matrix to furnish interconnected Li^+ transport channels. Beyond channel construction, 2D materials enable functional SEI engineering. Huang's group [577] employed 2D $Li_{0.46}Mn_{0.77}PS_3$ (LiMPS) nanosheets with strong adsorption and high Li^+ conductivity to homogenize the Li^+ flux, forming a dense and stable SEI layer enriched with inorganic substances that physically blocked Li dendrites. Building on the universality of 2D physical shielding, precision structural regulation enables transformative performance leaps. Zhang et al. [578] engineered a self-supporting intercalated CSE through inserting poly(ethylene carbonate)-based electrolyte into the interlayer of single-ion conductor lithium montmorillonite with charge distribution difference, achieving the orderly arrangement of Li^+ into the intercalation space. The developed CSE demonstrated a high t_{Li+} of 0.83 and synergistically suppressed lithium dendrites when paired with a 3D lithium anode.

To achieve fully conductive inorganic ceramic phases, 3D fillers are essential for constructing continuous Li^+-conductive nanoceramic networks. These 3D ceramic frameworks simultaneously enhance mechanical robustness, thermal and electrochemical stability, and mitigate filler agglomeration while suppressing heterogeneous lithium deposition/stripping. Wachsman et al. [579] employed a flexible garnet fiber textile with unique structure as 3D framework offering continuous Li^+ conduction route and high surface area/volume ratio, immersed in PEO–Li^+ mixture to prepare a flexible self-supporting CSE. Li^+ primarily migrated through garnet fibers rather than the polymer matrices or inorganic/organic interfaces, with a substantial improvement in migration efficiency. Analogously, Fan et al. [143] fabricated 3D interconnected porous LATP conductive framework using NaCl powder as sacrificial template, which was repeatedly immersed into PEO–LiTFSI solution in vacuum and dried to prepare CSEs. The uniform filling of PEO in the 3D LATP framework enabled stable interfaces and long-range continuous Li^+ transport channels, yielding CSE with excellent ionic conductivity (0.747 mS cm^{-1} at 60 °C) and mechanical properties. However, in the aforementioned studies, functional fillers were randomly distributed or exhibited disordered structures within the polymer matrix, ultimately yielding isotropic electrolytes. In contrast, Wang et al. [580] pioneered an anisotropic SPE with an oriented support structure by embedding LLZTO-loaded aligned PAN fiber network into PEGDA–SN–LiTFSI composite matrix. The directional fibers homogenized ion flux and physically suppressed dendrites, while LLZTO particles established additional Li^+ transport pathways and reduced SN–lithium anode reactivity, achieving an ionic conductivity of 1.46 mS cm^{-1} at RT and exceptional cycling performance.

6.6.3. Organic fillers

Recent advancements in SPEs have witnessed expanding applications of organic fillers, primarily categorized as low-molecular-weight polymers and porous organic frameworks. For instance, Wang et al. [581] introduced a few low-molecular-weight hydrolytic polymaleic anhydride (HPMA) into PEO, which remarkably restrained the crystallization of PEO, thereby improving the ionic conductivity, flexibility, and stability towards lithium of the SPE. Common organic porous fillers include metal–organic frameworks (MOFs) and covalent organic frameworks (COFs) [582], leveraging their large surface areas and dense Li^+-coordinating sites to construct interconnected ion transport networks within CPEs. MOFs are crystalline porous materials with periodic network structure formed by self-assembly of transition metal ions and organic ligands, featuring high specific surface area, ultra-high porosity, abundant active centers and tunable structure [583]. In 2013 [584], MOF was introduced for the first time as a filler in PEO matrix, providing highly conductive ionic pathways along the interface, and related research has flourished since then. Guo et al. [585] synthesized a novel cationic MOF (CMOF) with a specific surface area up to 1082 m^2 g^{-1} based on UiO-66 (ZrBDC MOF) via the nucleophilic substitutions of grafting pyridine N. As illustrated in Fig. 29c, the CMOF immobilized anions via electrostatic carrier interactions, accelerating the diffusion of Li^+ in the PEO matrix ($t_{Li+} \approx 0.72$) and guiding the uniform deposition of Li^+ to construct dendrite-free ASSLB. To mitigate the agglomeration of MOF particles and maximize spatial confinement effects, Wang et al. [586] engineered sandwich-structure CPEs by intercalating a MOF electrospun fiber membrane between dual PEO–LiTFSI electrolyte layers via hot-pressing. The multiphase sandwich structure and the thermally assisted fabrication method suppressed the crystallinity of PEO, which endowed the CPE with high ionic conductivity (0.49 mS cm^{-1}, 25 °C) and mechanical strength. The grafted $–NH_2$ groups in the above two systems could protect the ether oxygen of PEO through hydrogen bonding, which had higher electrochemical stability and extended the ESW (5 V vs. Li^+/Li) of electrolytes. Alternatively, directionally aligned and unilaterally deposited Zeolite imidazolate framework-67 (ZIF-67) fillers served to promote *in situ* ROP of DOL to form long-chain PDOL with elevated oxidative potential of 5.9 V vs. Li^+/Li, as well as to modulate interfacial Li^+ fluxes and optimize the SEI compositions [587].

COFs are crystalline porous polymeric materials with periodicity in which organic structural units are connected by strong covalent bonds (e.g., B–O, C=N, C–N, C=C). COFs are characterized by low density, high crystallinity, tunable pore structure, large specific surface area, ease of surface modification, and high chemical and thermal stability. Manthiram et al. [589] developed a single lithium-ion conductive COF electrolyte mediated by DMA@LiTFSI. The electronegative C=O functional group of the flexible DMA chain decoupled Li^+ from the rigid COF and polymer segments, increasing the carrier concentration within COF channels and accelerating the directional movement of Li^+ ($t_{Li+} = 0.85$). Building on the ion-regulation capabilities of COFs, their functional versatility extends to interfacial stabilization under high-voltage operation. Qian et al. [590] designed an antioxidant cationic COF with ultra-low HOMO energy level (−12.55 eV), integrating it as a reinforcing scaffold into solid polycarbonate electrolyte. This design successfully constructed a robust and stable CEI, effectively suppressed the decomposition of polycarbonate and interfacial side reactions under high voltage. The 4.5 V-class Li||LCO cell exhibited initial capacity of 160.3 mAh g^{-1} at 0.1C with capacity retention of 83.9 % at 1C after 200 cycles.

6.6.4. Composite fillers

In many situations, single filler cannot meet the modification requirements of SPEs, necessitating the introduction of multiple fillers to achieve synergistic effects. Common combinations include liquid additives–solid fillers and active fillers–inert fillers. Song et al. [591] modified PEO/PVDF-HFP polymer blend matrix by introducing conductive ceramic filler LAGP and solvent ionic liquid (SIL, LiFSI in tetra ethylene glycol dimethyl ether, 1:1 in molar ratio) plasticizer. Both additives improved the ionic conductivity, in particular, with the SIL additionally enhancing the stability of the electrolyte–lithium anode interface while inhibiting the lithium dendrite and side reactions. Zhai et al. [588] developed an innovative single-ion conducting material termed “superconcentrated ionogel-in-ceramic (SIC)” by immobilizing a concentrated IL electrolyte (comprising 3 M LiTFSI dissolved in EmimFSI) within a cross-linked PMMA scaffold. As illustrated in Fig. 29d, the immobilization process achieved through *in situ* thermal initiated radical polymerization, while the resulting superconcentrated ionogel was anchored to LLZTO particles, yielding remarkable RT ionic conductivity (1.33 mS cm^{-1}) and an exceptional t_{Li+} of 0.89. Although SN plasticizers in SPEs promote lithium salt dissociation and enhance electrochemical oxidation resistance, excessive SN compromises mechanical integrity and induces interfacial side reactions. Aiming at

Table 5
Comparison of electrochemical properties of various SPEs.

Electrolyte(thickness)	t_{Li+}	σ (mS cm^{-1})	ESW vs. Li^+/Li (V)	Li||Li symmetric cells			Full cells				Ref.
				Current–Capacity (mA cm^{-2}–mAh cm^{-2})	Cycling life (h)	CCD (mA cm^{-2})	Cathodes	Cycling number (N)	Capacity retention (%)	CE (%)	
BA/PEGDA–SN/LiTFSI PCEE	0.75	1.1 (20 °C)	4.5	10–10	1500		NCM83 > 10 mg cm^{-2}	100 (0.5 mA cm^{-2})	88	94	[466]
PTFEP–LPIFD	0.64	0.30(RT)		0.5–0.5	1000	3.7	NCM811	> 400 (0.5C)	80	99.95	[467]
PVLN-15	0.58	0.6 (RT)		0.5–0.5	700	2.2	NCM811	1500 (2C)	61.4	99.7	[477]
P(VDF-TrFE-CTFE)–P(VDF-TrFE)	0.61	0.237 (25 °C)	4.5	0.05–0.025	> 4500		NCM811	600 (2C)	82.6	≈ 100	[478]
FPH–Li (46 μm, 1.227 g cm^{-3})	0.472	0.132 (30 °C)		0.1–0.1	900		NCM622	300 (1C)	81.5	99.5	[479]
IBD_{30}–PEO–LiTFSI (35 μm)	0.43	0.426 (50 °C)	4.8	0.2–0.05	> 750		LFP	580 (0.5C)	80.2	> 99.5	[483]
PVDF-HFP/$PAN^{0.3}$/MXene–g-$PAN^{0.1}$ (25.7 μm)	0.16	0.217 (25 °C)	5.46	0.5–0.5	1000		LCMO	500 (1C)	83.5		[484]
SN–P(DOL-TXE)	0.881	0.406 (25 °C)	5.1	0.2–0.2	600		LFP	900 (0.5C)	84.1	≈ 100	[486]
Poly(DOL-TTE)–LP (4–22 μm)	0.35	0.3 (RT)	4.9	0.5–0.5 1.0–1.0	2000 1000		LFP	200 (0.2C)	≈ 80	99.85	[487]
PDOL–5 % PS	0.88	2.22 (30 °C)	5.2	1–0.5	1000		LFP (25 °C)	600 (2C)	92.1	≈ 100	[488]
PEGDA–UpyMA–DES		0.342 (25 °C)	5.2	0.2–0.2	2250		LCO	1000 (0.5C)	80	99.6	[489]
CA–PEGMEA–SN (11 μm)	0.56	1.90 (25 °C)	4.9	0.1–0.1	1600	0.5	NCM622 3 mg cm^{-2}	250 (0.1C)	92		[491]
$PEGMEMA_1$–$SN_{1.2}$ SPE	0.55	1.30 (30 °C)	4.8	0.3–	> 500	0.5	LFP	1500 (0.5C)	80.3	> 99.5	[492]
$0.6PH_{115}$–PCL	0.82 (60 °C)	0.0553 (30 °C)	4.6	0.05–0.15	> 800		LFP (25 °C)	150 (0.1C)	81.7	≈ 100	[494]
(21-β-CD-g-PTFEMA)–PEO–Li	0.88	0.642 (60 °C)	≈ 4.7	0.1–0.1	> 3800		LFP (70 °C)	400 (70 mA g^{-1})	98	> 99	[496]
HEMI-ASPE–Li	0.63	0.456 (70 °C)		0.1–0.1	> 4000	2.4	LFP	300 (70 mA g^{-1})	96	≈ 100	[497]
$PEGMEA_{950}$–HFBMA	0.25	0.145 (70 °C)	5.0	0.2–0.6	1500		LFP	50 (0.1C)	96	99	[500]
P(IL-OFHDODA-VEC)	0.40	1.37 (25 °C)	5.08	0.1–0.1	2500		NCM523 (30 °C)	200 (0.5C)	90		[501]
PFMC-SPE	0.57	1.0 (25 °C)	5	0.1–0.05	800		LFP (30 °C)	750 (1C)	84.7	99.94	[502]
							NCM622 (30 °C)	100 (1C)	66.7	99	
BSPE–10 % LiBOB	0.83	1.22 (30 °C)	4.94	0.1–0.1	1000		LFP	450 (0.5C)	≈ 100	≈ 100	[504]
20 wt% P(SSPSILi-alt-MA)–PEO	0.97 (80 °C)	0.308 (25 °C)	5	0.01–0.02	1200		LFP (80 °C)	350 (0.1C)	≈ 90	≈ 100	[506]

(*continued on next page*)

Table 5 (*continued*)

Electrolyte(thickness)	t_{Li+}	σ (mS cm^{-1})	ESW vs. Li^+/Li (V)	Li||Li symmetric cells			Full cells				Ref.
				Current–Capacity (mA cm^{-2}–mAh cm^{-2})	Cycling life (h)	CCD (mA cm^{-2})	Cathodes	Cycling number (N)	Capacity retention (%)	CE (%)	
PAF-220-ASPE	0.93	0.501 (20 °C)	5	0.25–	2400		LFP	180 (0.2C)	90	≈ 100	[507]
alter-SLICPE P8	0.93	0.042 (30 °C)		0.05–0.15	1500		LFP	> 40 (0.05C)	92	99.3	[508]
FEC–SN–PEA	0.57	1.01 (30 °C)	4.6	0.2–1	1800	3.2	LFP (22 °C)	2000 (0.5C)	83		[509]
CPDOL	0.46	0.101 (RT)	5.1	0.1–0.1	3000		LFP	500 (0.5C)	95.1	99.78	[511]
PEO–Mg_3N_2		0.173 (60 °C)	4.4	0.2–0.2	1500		LFP	200 (0.5C)	86.3		[512]
PT–PEO–PT	0.54	0.106 (40 °C)	4.9	0.05–	1100		LFP	1000 (2C)	94.6	99.1	[513]
PEO–TiN/PEO–$LiYF_4$/PEO–TiN	0.38	0.17 (30 °C)	> 5	0.2–0.1	3000		NCM523 (45 °C)	300 (0.2C)	71.4		[514]
P(EGMEA-UPyMA)	0.75	2.20 (25 °C)	5.9	0.5–0.5	> 650	>3	NCM811 3 mg cm^{-2}	500 (0.5C)	80.4	≈ 100	[519]
PTMG-HDI-BHDS/LiFSI	0.81	0.24 (30 °C)	> 5	0.2–0.2	6000		SPAN	700 (0.3C)	93	99	[520]
PEO–LiTFSI/PMA–LiTFSI	0.37	0.205 (65 °C)		0.1–0.1	336		LCO	100 (0.2C)	91.2	99.9	[521]
PVDF-HFP/LLZN/ LiTFSI + HKUST-1 /PEO/PVDF	0.62	0.2 (RT)	4.92	0.25–0.0125	1700		LFP	200 (1C)	85.5		[522]
F&NPE	0.50	1.01 (RT)		0.5–0.5	700		NCM622	500 (0.5C)	85	> 99.8	[523]
BDFPE	0.69	0.584 (RT)		1–1	1800		NCM622	150 (0.5C)	84.3	≈ 100	[524]
HETE	0.62 ± 0.02	0.35 ± 0.053 (RT)		0.1–0.1	1100		LFP	210 (0.1C)	92	98.5	[525]
cross-linked $PISSE_{60\%}$	0.546	0.303 (25 °C)	5.44	0.1–0.1	500	3.2	$PISSE_{60\%}$@LFP	800 (0.5C)	71		[526]
PVDF-HFP:LiTFSI = 1.1 PISSE	0.53	0.124 (RT)	4.7	0.3–0.15	400	0.5	NCM811	200 (1C)	93.2		[528]
PVDF-HFP/LiFSI/LLZTO (90 μm)	0.56	1.67 (25 °C)	4.8	0.3–0.3	240	3.2	LFP	300 (0.5C)	97.2	99.75	[529]
S-LHCE	0.72	0.27 (20 °C)		0.1–0.1	4100		LFP (100 °C)	200 (8C)	> 90	> 99	[530]
							NCM811 (25 °C)	110 (0.2C)	≈ 93	> 99	
PE/PEO/LiTFSI (7.5 μm)		0.154 (60 °C)		0.1–0.1	1500		LFP	200 (0.2C)	99.4	> 99.8	[534]
PE + PEGDA–SN–LiTFSI (≈ 16 μm)	0.71	0.111 (RT)	4.7	0.1–0.1	1000		LCO	385 (0.2C)	76.1	≈ 100	[535]
m-PPL (10 μm)	0.227	34.84 (RT)	5.2	0.1–0.1 (60 °C)	1500		LFP (pouch, 60 °C)	1000 (1C)	76.4	≈ 100	[536]

(*continued on next page*)

Table 5 (*continued*)

Electrolyte(thickness)	t_{Li+}	σ (mS cm^{-1})	ESW vs. Li^+/Li (V)	Li||Li symmetric cells			Full cells				Ref.
				Current–Capacity (mA cm^{-2}–mAh cm^{-2})	Cycling life (h)	CCD (mA cm^{-2})	Cathodes	Cycling number (N)	Capacity retention (%)	CE (%)	
UFF/PEO/PAN/ LiTFSI (4.2 μm)	0.50	0.068 (25 °C)	4.9	1–0.5 0.4–4	> 1100 200		NCM811 (N/P = 1.1, 50 °C)	150 (0.1C)	67		[538]
PI/PEO/LiTFSI (8.6 μm)		0.23 (30 °C)		0.1–0.05 (60 °C)	1000		LFP (60 °C)	200 (0.5C)		≈ 100	[539]
PEO/LiTFSI/3% NH_4PF_6@PA6 (7 μm)			5.5	0.1– (60 °C)	> 2000		LFP (60 °C)	300 (1C)	≈ 100	99.3	[540]
ACCE		1 (30 °C)		0.25–0.5	2000	3.6	LFP	1000 (1C)	98.6	≈ 100	[541]
PEO–10 %HACC–TFSI	0.34	0.501 (60 °C)	5.26	0.25–0.125	2700		LFP (60 °C)	100 (0.2C)	≈ 97		[542]
40PIL–IL (85 ± 2 μm)	0.44	0.8 (25 °C)	> 5	0.1–0.1	> 1700		NCM811	600	72	99.9	[543]
LiMIC-15	0.60	1 (25 °C, σ_{Li+})	5.6	0.2–0.2	2000						[544]
PEO@GF		0.19 (60 °C)	4.9	0.2–0.2 0.42–0.4	2000 1000		VL-LFP (10.5 mg cm^{-2}, 80 °C)	50 (0.1C)			[552]
PVDF-HFP/LiTFSI/ASB (60 μm)	0.63	0.77 (30 °C)	4.7	0.5–0.5	1000		LFP	300 (1C)	69.5		[553]
							NCM811	80 (0.5C)			
PVDF + 5 % d-HNT NDCPE	0.75 ± 0.04	0.29 ± 0.04 (RT)	5.0	0.5–0.5	400		LFP	300 (1C)	80	≈ 100	[556]
							NCM811	200 (0.5C)	70	≈ 100	
PVDF-HFP/SLN (1 %)	0.78	0.22 (25 °C)	≈ 4.9	0.1–0.05	900		NCM811	85 (0.2C)	84.3		[558]
MXene–$mSiO_2$		0.46 (RT)	4.3	0.2–0.2	500		LFP	250 (0.5C)	> 90	≈ 100	[560]
C-MX PAN	0.72	3.07 (25 °C)		1–0.5	2000	1	LFP	500 (1C)	85.18	99.9	[561]
LiTFSI–PEO–0.2AlF_3	0.67	0.278 (60 °C)	≈ 5	0.1–0.1	1200		FeF_3	900 (0.7 A g^{-1})	≈ 33.3		[563]
CPCSE	0.62	0.52 (RT)	5.1	0.1–0.1	1500		LFP	700 (1C)	80.2	≈ 100	[564]
							NCM811	250 (0.5C)	93.7	≈ 100	
PEO–3D LATP		0.747 (60 °C)	5.1	0.1–0.1 0.2–0.2	2000 1000		LFP	200 (1C)	80		[143]
PV–MS20	0.47	0.45 (28 °C)	4.6	0.5–0.5	200	1.3	NCM811	1130 (1C)	68.7	99.7	[566]
PEGMA–LAGP–Li (8.5 μm)	0.87	0.237 (RT)	5.4	0.1–0.1 0.2–0.2	3500 2100	0.5	LFP	300 (0.5C)	93	> 99	[569]
CIP-200 nm/PIC-5 μm/CIP-200 nm		0.023 (30 °C)	5.03	0.2–0.1	400		LFP	200 (0.1C)	82.4		[574]

(*continued on next page*)

Table 5 (*continued*)

Electrolyte(thickness)	t_{Li+}	σ (mS cm^{-1})	ESW vs. Li^+/Li (V)	Li||Li symmetric cells			Full cells				Ref.
				Current–Capacity (mA cm^{-2}–mAh cm^{-2})	Cycling life (h)	CCD (mA cm^{-2})	Cathodes	Cycling number (N)	Capacity retention (%)	CE (%)	
PCE	0.74	0.75 (30 °C)		1–0.5	2000		$LiNi_{0.8}Mn_{0.13}Ti_{0.02}Mg_{0.02}Nb_{0.01}Mo_{0.02}O_2$ (50 °C)	3600 (1C)	> 60	≈ 100	[575]
PEO–$LiClO_4$–EmimFSI + 2D LLZNO		0.36 (RT)		0.1–0.1	200		LFP (40 °C)	30 (0.05C)	97.5	> 96	[576]
PEO–5LiMPS		0.21 (30 °C)	4.8	0.2–0.1	600	1.6	NCM811	200 (0.2C)	> 80	> 99	[577]
30PEC–70LiMNT–80LiFSI–15FEC–5PTFE	0.83	0.35 (25 °C)	4.6	0.5–0.5	600		LFP	200 (0.5C)	91.9		[578]
PAN–PEGDA LASE	0.55	1.46 (RT)		0.5–0.25	1500		NCM811 (2.8 mg cm^{-2})	300 (100 mA g^{-1})	84		[580]
PEO–1 % HPMA	0.22	0.113 (35 °C)	5.1	0.1–0.1	1000		LFP	1255 (1C)	99.5		[581]
PEO@CMOF	0.72	0.031 (25 °C)	4.97	0.1–0.1	400		LFP (60 °C)	300 (1C)	85.4		[585]
PEO–LiTFSI/PEO + UiO-66-NH_2/ PEO–LiTFSI	0.72	0.49 (25 °C)	5	1–1	1800		LFP	110 (0.2C)	≈ 100	≈ 100	[586]
ZIF-67/PDOL	0.68	0.18 (RT)	2–5.8	0.1–0.1	> 2300		LFP	570 (2C)	92.5	99	[587]
SIC	0.89	1.33 (25 °C)	5.5	0.5–0.5	600		LFP	300 (1C)	90.4	≈ 100	[588]
							NCM523	200 (1C)	72.7		
DMA@LiTFSI–COF	0.85	0.17 (23 °C)		0.3–0.075	450		LFP (pouch, 65 °C)	130 (0.5C)	90.2		[589]
COF–PC	0.62	0.13 (25 °C)	5.2	1–1	900		LCO	200 (0.1C)	83.9		[590]
PPLS90	0.34	3.27 (RT)	4.9	0.1–	800	0.32	LFP	100 (0.1C)		≈ 100	[591]
PEO–60 % SN–15 % LLZTO		0.766 (RT)	4.7	0.1–0.05	> 1000		LFP	240 (0.5C)	92.6	≈ 100	[592]
ATS–PEO–LLZAO		0.39 (50 °C)	> 5.2	0.2–	250		LFP	280 (0.3C)	94.4		[593]
PVDF-HFP + 5 % LLZTO + 1 % SiO_2	0.42	1.01 (25 °C)	≈ 5	0.25–0.25	1500		NCM811	200 (1C)		99	[594]
ANF–PEO–20LLZO	0.5 (60 °C)	1.36 (30 °C)		0.2–0.2	400		LFP	400 (0.5C)	88	99	[595]

*The test temperatures of symmetric batteries and full batteries were consistent with that of ionic conductivity, except for special marks.

this problem, Huo et al. [592] incorporated 15 wt% LLZTO into PEO-based CPE containing 60 % SN. The La^{3+} in LLZTO would interact with the N atoms in SN through cation-assistance, locking SN in electrolyte layer to prevent the corrosion of the lithium anode. To mitigate organic/inorganic interfacial incompatibility in CSEs, silane coupling agents with alkoxy and alkyl chains have proven effective. Hou et al. [593] introduced aminopropyltriethoxysilane into PEO–LLZAO CSE, which features a unique amine effect in addition to the conventional chemical bridging effect. This is manifested by the formation of hydrogen bonds between $–NH_2$ and PEO to enhance the interface, while the lone pair electrons of N atom could not only react with the solvent acetonitrile to promote the homogeneous dispersion of LLZAO, but also complex with Li^+ to promote lithium salt dissociation and uniform Li^+ diffusion.

The harmonious integration of inert and active fillers not only skillfully addresses specific challenges, but also synergistically transcends the simple addition of individual effects, significantly boosting the overall performance and durability of the system. Zhang et al. [594] incorporated nanosized SiO_2 aerogel with excellent thermal stability and high specific surface area along with activated ceramic LLZTO into PVDF-HFP matrix. The –OH groups of SiO_2 aerogel interacted with the –F groups of PVDF-HFP to form a strong hydrogen bond network, while LLZTO established additional ion transport path. These synergistic effects accelerated the dissociation of lithium salts and Li^+ transport by expanding the amorphous region of polymer matrix, yielding high-voltage-resistant CSEs with high ionic conductivity, flame retardancy, stability and mechanical strength. Gao et al. [595] fabricated a 3D flexible framework through electrostatic interactions between aramid nanofibers and PEO, and introduced Li^+-conducting LLZO particles into the polymer backbone. This dual modification collaboratively reduced the crystallinity, created continuous ion transport pathways, and significantly enhanced the toughness and hardness of CSE. To enhance nanofiller dispersion quality and precisely control polymer-ion interactions, Zhong et al. [548] proposed a surface modification strategy to fabricate protein–ceramic hybrid nanofillers through combining the ion-conductive soy protein and pre-treated TiO_2 nanoparticle. The interaction between denatured soy protein and TiO_2 improved the mechanical strength, ionic conductivity, electrochemical stability, and adhesion properties of the PEO–$LiClO_4$ CSE.

Functional additives are designed to enhance ionic conductivity and lithium-ion transference number by reducing polymer crystallinity, promoting lithium salt dissociation, and constructing continuous ion-transport channels, while simultaneously broadening ESW and inhibiting dendrites. Although liquid additives (e.g., plasticizers, ILs) rapidly increase ionic conductivity, they typically compromise mechanical strength. Among solid fillers, inert fillers (TiO_2, ASB, HNT, etc.) anchor anions via surface Lewis acid sites; active fillers (LLZO, LATP, etc.) provide additional Li^+-conduction pathways; organic porous fillers (MOFs, COFs, etc.) with high surface areas regulate Li^+ flux; and composite fillers leverage synergistic effects to surpass intrinsic performance limits.

6.7. Summary

In summary, SPEs offer critical advantages including interfacial compatibility, mechanical flexibility, and enhanced safety, enabling applications in flexible batteries and wearable electronics. However, their commercialization faces barriers including low RT ionic conductivity, narrow ESWs, thermal instability, and scalability limitations. To overcome these barriers and accelerate the deployment of SPEs in ASSLBs, the following approaches are summarized. Firstly, polar group introduction, co-polymerization, and cross-linking strategies can increase the proportion of amorphous regions in the polymer matrix, enhance segmental mobility, and promote lithium salt dissociation, thereby significantly improving ionic conductivity. Secondly, designing SEI layers enriched with inorganic components (e.g., LiF, Li_3N) or constructing multilayer SPEs with sandwich structures can enhance interfacial compatibility and stability between SPEs and electrodes while mitigating electrode corrosion and dendrite formation. Thirdly, incorporating plasticizers or inorganic nanofillers can suppress polymer recrystallization, improve chain mobility, and provide Lewis acidic/basic sites to immobilize anions and facilitate Li^+ transport. Notably, achieving enhanced mechanical strength without compromising ionic conductivity by modulating additive composition or ratios is particularly desirable. Fourthly, regulating lithium salt concentration, integrating nanoscale conductive ceramic fillers, or embedding porous organic frameworks can establish continuous and rapid Li^+-transport pathways, further boosting ionic conductivity and electrochemical performance. Finally, the selection of appropriate framework materials coupled with the development of novel preparation processes is essential for fabricating high-performance SPE thin-films suitable for commercialization. Table 5 comparatively summarizes the key electrochemical properties of diverse SPEs fabricated through the aforementioned optimization strategies.

Concurrently with material innovation, advanced characterization techniques are essential to elucidate atomic-scale ion transport mechanisms and capture *operando* structural or interfacial evolution during cycling. Industrial deployment requires prioritizing scalable production technologies for SPEs, particularly roll-to-roll manufacturing and precision coating techniques, while implementing cost-competitive solutions. Cross-sector collaboration between academia and industry becomes imperative to translate laboratory breakthroughs into industrial-scale implementations. The integration of computational chemistry, artificial intelligence (AI), and machine learning into material design and process optimization presents opportunities to accelerate the discovery of novel SPE formulations and enhance production efficiency [596].

7. Industrialization of all-solid-state lithium batteries

Building upon the foundational understanding and recent breakthroughs in SSEs reviewed in previous sections, the next critical step lies in bridging the gap between laboratory-scale innovations and commercially viable ASSLBs. While significant progress has been made in optimizing ionic conductivity, electrochemical stability, and interfacial compatibility of SSEs, their practical deployment demands a holistic evaluation of scalability, cost, and system-level integration. Currently, ASSLBs are at a pivotal juncture of technological transformation, with academic insights progressively transitioning to industrial-scale manufacturing [597]. In 2018, Japan's *Basic Policy and Concrete Measures for Electrification of Automobiles* first established all-solid-state batteries and innovative batteries as

core next-generation battery technologies. In October 2020, China's *State Council released the New Energy Automobile Industry Development Plan (2021–2035)*, which explicitly emphasized the strategic importance of advancing research and industrialization of SSBs technology. In 2021, the USA department of energy (DOE) released *the National Blueprint for Lithium Batteries 2021–2030*, aiming to achieve large-scale production of SSBs by 2030. Subsequently, South Korea's *K-Battery Development Strategy* set an ambitious target for SSBs commercialization by 2027. That same year, the European Union formally incorporated SSBs into its *Battery Innovation Roadmap 2030* as a key development direction. On this policy basis, Germany's Fraunhofer Institute released the detailed *Solid-State Battery Roadmap 2035+* in May 2022, outlining a comprehensive technical pathway from laboratory breakthroughs to full commercialization. In conclusion, governments and funding agencies worldwide, including Japan, the USA, South Korea, China, and the European Union have established ambitious roadmaps targeting ASSLB commercialization by 2030–2035. However, the realization of these goals hinges on addressing multifaceted challenges spanning materials engineering, device architecture, process technologies, and application-specific requirements. This section systematically analyzes the prevailing challenges and emerging research directions for ASSLBs across materials design, device engineering, manufacturing processes, and characterization techniques, delineating the critical pathway toward technological maturity.

7.1. Materials

The core materials for ASSLBs include SSE materials, cathode materials, anode materials, and associated auxiliary materials, all of

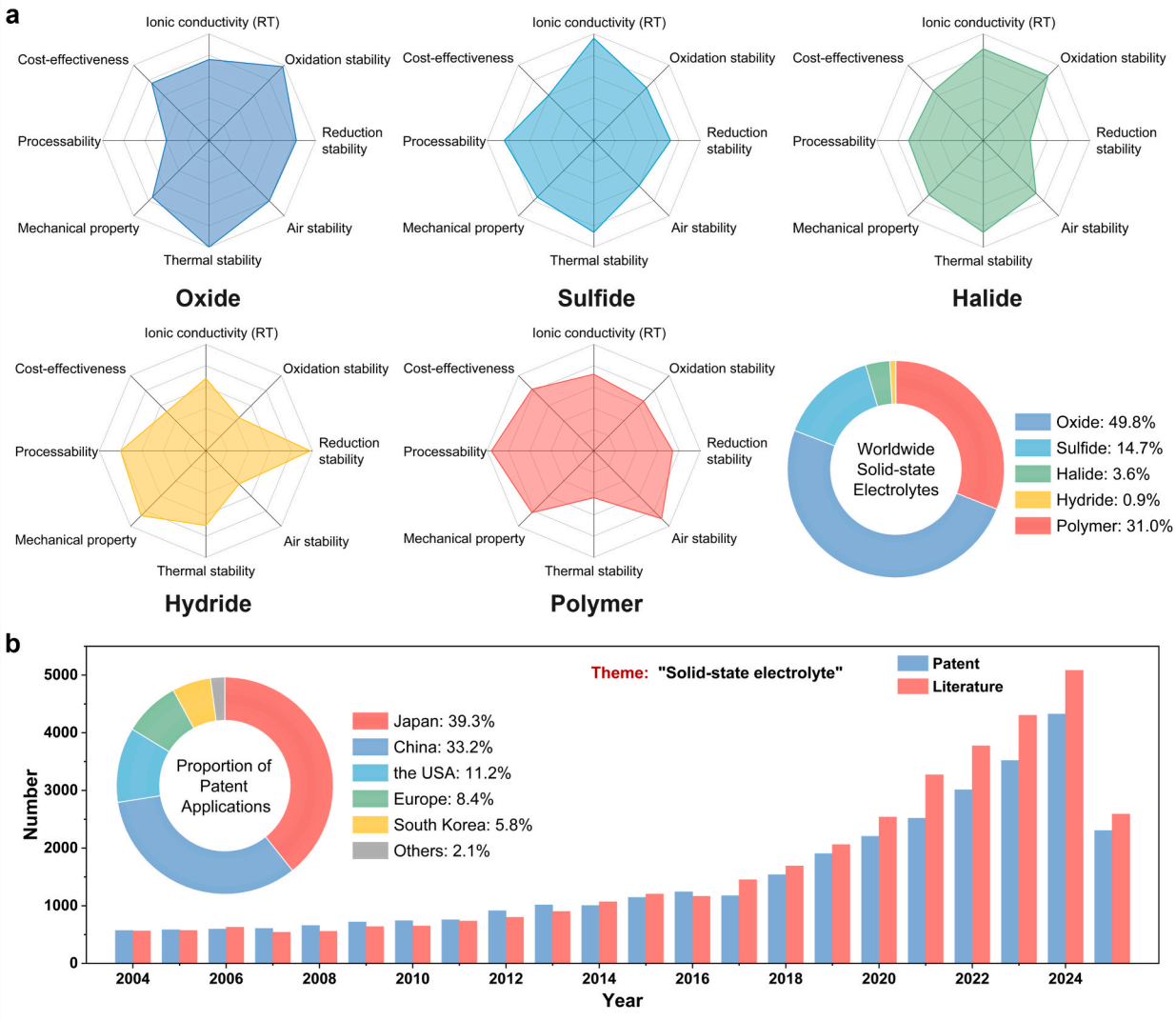

Fig. 30. (a) Comparison of the performance and worldwide popularity of various SSEs. (b) Number of publications and patent applications in the field of SSEs between 2004 and June 2025, data sourced from SciFinder. The illustration shows the publication of patents across various countries and regions in the field of SSEs.

which play crucial roles in determining the overall performance, stability, and energy efficiency of the battery. Scalable ASSLB production faces three critical materials challenges: underperforming SSEs, unstable solid–solid interfaces, and suboptimized electrodes in cycling stability, safety, and cost. Leveraging their early technological advancements and expertise in LIBs, the USA, Japan, and China currently lead the majority of original innovations and technological systems pertaining to commercial electrolytes, cathodes, and anodes. The advancement of SSB technology is thus expected to significantly transform the global battery technology landscape. This section primarily focuses on the research progress, industrial applications, and characteristic analysis of key ASSLBs materials, including electrolytes, cathodes, and anodes.

7.1.1. Solid-state electrolytes

The advantages, existing deficiencies, and modification methods of various SSEs have been discussed from an academic perspective in previous chapters, and a systematic summary is provided here. Fig. 30a compares the properties of each electrolyte. Currently, the development and industrialization of ASSLBs primarily revolve around three electrolyte systems: oxide-based SSEs, sulfide-based SSEs, and SPEs. Oxide-based SSEs exhibit wide ESWs (typically $>$ 5 V), excellent thermal stability, and high mechanical strength [598]. However, their high hardness and brittleness impede intimate interfacial contact with electrodes, which is commonly ameliorated by compositing with polymer [567,599]. HT sintering requirements and limited ionic conductivity at RT (0.1–1 mS cm^{-1}) necessitate further optimization, typically through process refinement, element doping, and grain boundary modification, to advance widespread applications [600–602]. Commercialization efforts center on crystalline oxide-based SSEs, such as garnet-type, perovskite-type, and NASICON-type [603]. QuantumScape in the USA has developed dual material systems, primarily featuring the LLZO garnet-type oxide system, with LGPS sulfide system as a secondary option. In China, the oxide-based SSE supply chain has reached a stage of maturity, with several startups nearing mass production. Leveraging the advantages of both oxide-based SSEs and SPEs, Welion New Energy has successfully industrialized hybrid solid–liquid batteries, while SAIC Group is actively developing oxide-based ASSLBs. Sulfide-based SSEs display high RT ionic conductivity comparable to LEs, good ductility and processability [35]. Nevertheless, they face challenges such as poor compatibility with cathode materials, instability with lithium metal, sensitivity to oxygen and moisture, potential contamination issues, and stringent production requirements [604–607]. Various strategies such as doping, coating, and combining with other SSEs can broaden the compatibility of sulfide-based SSEs to electrode materials [218,608]. Japan and South Korea have the earliest R&D layouts in the sulfide route, and their technology and patents lead the world, representative companies such as Toyota, Nissan, Honda, Panasonic, LG Energy Solution, Samsung SDI, and SK ON. While the European Union, the USA, and China are also accelerating their deployments in this field. Halide-based SSEs have made significant breakthroughs in recent years, combining high oxidation stability, wide ESW, and high ionic conductivity [62,609]. Technical approaches including chemical doping, surface coating, and bilayer electrolyte construction have proven effective in mitigating poor reduction stability and high moisture sensitivity. Wet chemical synthesis methods and $ZrCl_4$ precursors have reduced the production complexity and cost of halide-based SSEs. Regarding global development efforts in halide-based SSEs, Panasonic leads internationally, while enterprises in China like CATL, BYD, EVE Energy, and SAIC Qingtao are accelerating R&D progress. Hydride-based SSEs, as emerging materials, are characterized by low grain boundary resistance, good compressibility, high reduction stability, and compatibility with lithium metal [399]. To address their limitations such as insufficient RT ionic conductivity, poor oxidation stability, and low CCD, modification strategies including ion substitution, ligand complexation, interfacial engineering, nanoconfinement, and composite materials have been proposed. Although commercialization remains unrealized in the near term. In contrast to ISEs, SPEs have achieved earlier commercial applications due to their excellent interfacial compatibility, flexibility, processability, and low cost. Unfortunately, LMP® batteries mass-produced by Bolloré exhibited no driving range advantage over liquid-state LIBs at equivalent capacity, primarily due to inadequate RT ionic conductivity and relatively narrow ESWs. Structural modification strategies, such as cross-linking [491], blending [483] and grafting [495], as well as the incorporation of plasticizers, inert fillers [548] and active fillers [573], are being actively explored to overcome these limitations. Presently, some manufacturers are adopting GPE-based semi-solid-state batteries as a transitional strategy, while the prevailing approach in China centers on polymer–oxide CSE technology. Fig. 30b tracks the growth trajectory of SSE-related publications and patents (SciFinder, 2004–June 2025), demonstrating a nearly tenfold increase that solidifies SSEs as a pivotal battery research frontier.

7.1.2. Cathodes

In commercial LIBs, cathode materials act as the primary lithium source, comprising over 30 % of total material costs. Its intrinsic properties critically dictate three pivotal metrics of batteries: operating voltage, gravimetric energy density, and cycling stability [610–613]. High-voltage cathode materials such as LFP, LCO and ternary materials (NCM, NCA) are already commercialized in LIBs [614,615]. In recent years, they have also been widely used in ASSLBs to achieve excellent energy density performance. The expanded ESWs of SSEs further broadens viable cathode options for next-generation designs. In the short term, semi-solid-state batteries and ASSLBs are anticipated to still employ ternary high-nickel systems, with voltage enhancement achieved through methods such as single crystallization, oxide encapsulation, and metal doping to further increase battery energy density. As SSE and metallic lithium anode technologies mature, cathode materials are projected to further iterate towards novel systems like ultra-high-nickel, lithium-rich manganese-based oxides (LRMOs), and high-voltage spinel. Notably, spinel nickel manganese lithium oxides combine high specific energy, cost efficiency, and intrinsic safety but requires interface stabilization solutions for high-voltage operation ($>$ 4.7 V). LRMOs exhibit exceptional specific capacities and voltage advantages, though practical implementation will likely rely on composite designs to mitigate oxygen release and voltage decay. Pan et al. [616] pioneered the incorporation of redox mediators into conventional LRMO cathodes, effectively mitigating oxygen evolution and thereby enhancing cycling stability. Sulfur-based cathodes present compelling advantages for next-generation energy storage, including environmental benignity, natural abundance, and exceptional theoretical

energy density (2600 Wh kg^{-1}). SSEs address their key limitation by suppressing polysulfide shuttling, enabling practical high-energy storage [617–621]. Pang et al. [622] resolved the all-solid three-phase boundary challenge in Li–S batteries by designing a redox-active electrolyte, triggering rapid solid–solid sulfur redox reaction reactions and fast-charging capabilities, a pivotal breakthrough that places Li–S technology at the cutting edge of sustainable energy innovation.

Easpring, the company has established a comprehensive portfolio of proprietary cathode materials spanning NCM, NCA, LFP, LFMP, LCO, and SSBs components et al. As the global market leader in high-nickel ternary cathodes, it has pioneered 9-series ultra-high-nickel formulations and developed a low-impedance cathode–electrolyte composite system through strategic collaborations, making it an important supplier of cathode materials for SSBs. At InterBattery 2025, LG Chem announced its pioneering achievement as South Korea's first manufacturer to achieve mass production of LFP cathode material precursors, marketed under the "LG Precursor-Free" brand. Its products include ultra-high nickel cathodes with nickel content exceeding 95 %, medium-nickel cathodes for high voltage, high-density LFP, and LFP materials mixed with NCM.

7.1.3. Anodes

In SSB architectures, the primary anode configurations include carbon-based materials, Silicon-based materials, Si–C composites, and lithium metal. Despite decades of research, commercial large-format batteries have witnessed only incremental progress in anode innovation—graphite remains the dominant choice due to its balanced electrical conductivity and structural stability, despite operating near its theoretical capacity limit (372 mAh g^{-1}). Emerging strategies, such as Si–C composites (5–10 % Si content), are being implemented at industrial scale to enhance capacity [623]. Lithium metal anodes, offering an ultralow redox potential (−3.04 V vs. SHE) and exceptional theoretical capacity (3860 mAh g^{-1}) [624–627], represent the ultimate anode candidate for SSBs, yet face persistent challenges including dendrite propagation and interfacial degradation. The current challenges associated with the commercialization of lithium metal include its high reactivity, which results in limited stability when in contact with other battery components, such as SSEs, as well as the difficulties involved in handling lithium metal during the production process. Recently, Pasta et al. [628] discussed the feasibility of achieving ultra-thin lithium technology that can be used in practical production. They identified thermal evaporation as the most promising technology for producing lithium films with a thickness of approximately 17 μm. The technical and economic assessment shown that such lithium metal anodes could achieve a cost of \$24.2 kWh^{-1}, roughly double that of conventional graphite anodes at \$12 kWh^{-1}. Although lithium anodes are already available in polymer-based SSBs, their technological maturity remains relatively low compared to other anode materials. Silicon-based anodes boast a higher theoretical specific capacity (4200 mAh g^{-1}) but face challenges including volumetric expansion (380 %), poor conductivity, and unstable SEI film, often mitigated through graphite doping, porosity and alloying applications. For example, Chen et al. [629] developed the $Li_{21}Si_5$/Si-$Li_{21}Si_5$ double-layer alloy anode for ASSLBs without external pressure. Alloy anode materials, such as Si, tin, and aluminum, possess a significantly higher charge storage capacity compared to traditional graphite anodes, enabling their application various novel batteries to achieve excellent energy densities [630–632]. From a processing perspective, Silicon-based anodes have driven demand for materials like silane, PAA, single-walled carbon nanotubes, and lithiation additives. From a market perspective, Si anodes can thus be considered more promising in the short to medium term for certain SSBs.

At present, among the industrialized companies of anode electrodes, Amprius has developed high-energy-density prototype LIBs utilizing pure Si nanowire technology. In this approach, densely packed Si nanowires are directly grown on copper foil substrates. The inter-wire spacing accommodates volume expansion during cycling, while the structure recovers to its initial state following the first discharge cycle. BTR (China) has maintained its position as the global leader in anode materials for fifteen consecutive years, commanding a 21 % market share in 2024. The company has achieved commercial-scale production of Silicon-based anodes and recently developed an advanced fast-charging Si–C composite anode demonstrating simultaneous high-voltage tolerance and low-volume expansion.

7.2. Device performance

To accelerate commercialization, ASSLBs need to outperform conventional LIBs in parameters such as energy density, lifetime, fast charging and pressure.

7.2.1. Long-term stability

In academia, Cui et al. [633] developed a cathode homogenization approach employing $Li_{1.75}Ti_2(Ge_{0.25}P_{0.75}S_{3.8}Se_{0.2})_3$ as the cathode material. This strategy yields a uniform interfacial structure and minimal mechanical strain, enabling ASSLBs to achieve exceptional cycling stability—over 20,000 cycles at 2.5C under RT conditions while maintaining $>$ 70 % capacity retention. Taking pouch-type cells as a representative system, Kang et al. [634] recently developed a homogeneous SPE featuring attenuated dipole–dipole interactions. In practical applications using Li||NCM811 pouch cell configuration, it exhibited remarkable cycling stability, retaining 78.1 % capacity after 450 cycles at 25 °C with a current density of 54 mA g^{-1}. Yao et al. [635] fabricated a 14-μm ultrathin $Li_{5.4}P_{0.95}Sb_{0.05}S_{4.325}Se_{0.075}Cl_{1.6}$ sulfide-based SSE membrane via wet processing. When implemented in Li||$LiNbO_3$ pouch cell, this SSE enabled stable cycling performance, demonstrating 82.6 % capacity retention after 500 cycles at 60 °C, 0.1C.

In industry, QuantumScape's SSB retained $>$ 95 % capacity after more than 1000 charge and discharge cycles. Furthermore, Powerco, Volkswagen Group's battery subsidiary, conducted rigorous durability testing on QuantumScape's 24-layer SSBs. These SSBs demonstrated exceptional capacity retention of 95 % after 1000 cycles (equivalent to 480000 km of operation), marking a significant advancement in SSB longevity. In December 2024, Factorial announced that its first batch of Solstice™ ASSLBs achieved a capacity of 40 Ah, with smaller prototypes exceeding 2000 cycles. Guangzhou Automobile Group Co., Ltd. (GAC)' ASSLBs target a capacity

retention of 80 % over 1000 cycles, supporting an operational lifespan exceeding millions of kilometers. Further optimization efforts remain ongoing to enhance their performance. Narada Power's SSBs can undergo 500 cycles with a capacity retention rate of 93.4 %. After 2000 cycles, the capacity retention rate remains above 80 %. Ampcera's ASSLBs technology achieves more than 5000 cycles with a capacity retention above the industry standard of 80 %. Solid Power's innovative ASSLB design, combining a NMC cathode with a high-content silicon composite anode, delivers an extended cycle life surpassing 1000 cycles. In February 2025, ION Storage Systems (ION) demonstrated a significant breakthrough with its cell demonstrating a 25-fold capacity increase while surpassing 1000 cycles.

The achievement of extended cycling stability (> 1000 cycles with > 80 % capacity retention) represents a critical milestone for the

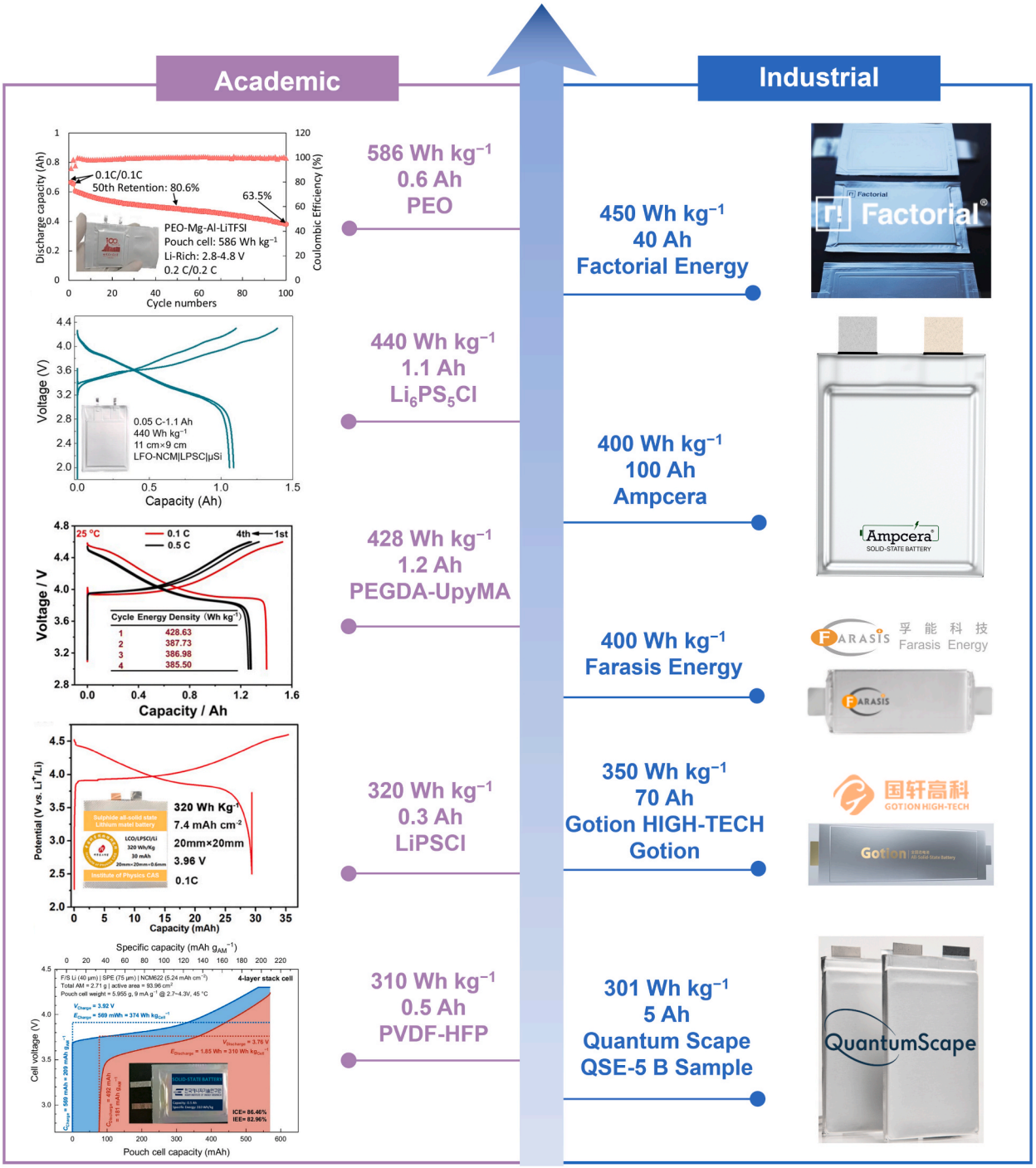

Fig. 31. Schematic of advances in energy density of ASSLBs in academia and industry. Reproduced with permission from ref. [489,636–639].

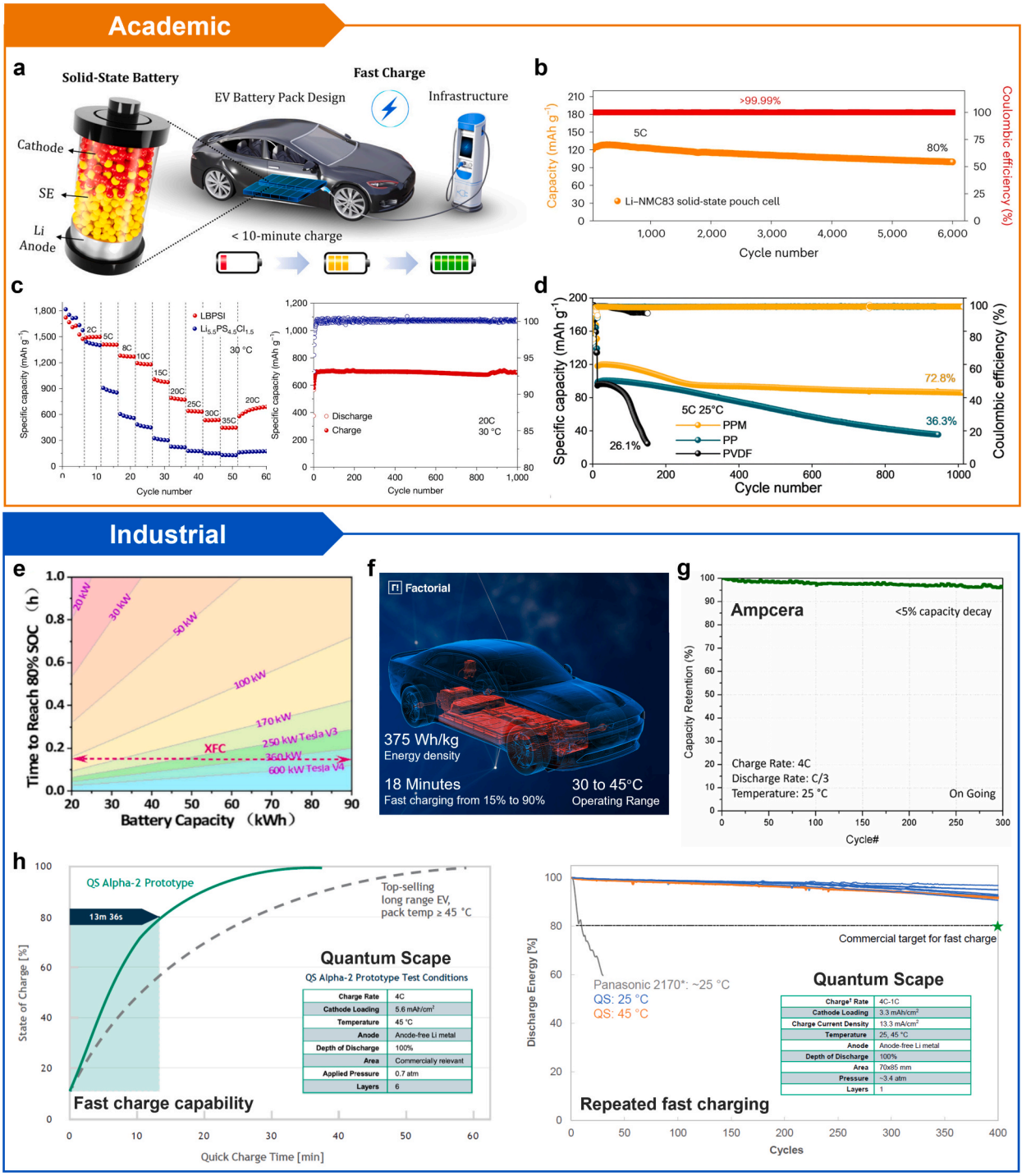

Fig. 32. (a) The practical application of fast charging for SSBs. Reproduced with permission from ref. [640]. Copyright 2021, ACS Energy Letters. (b) The solid-state pouch cell cycling at 5C charge and discharge. Reproduced with permission from ref. [642]. Copyright 2024, Nature Materials. (c) Fast-charging rate and 20C cycle performance chart of Li–S SSB. Reproduced with permission from ref. [622]. Copyright 2025, Nature. (d) Long-term cycling stability at 5C of Li||NCM811 cells. Reproduced with permission from ref. [644]. Copyright 2024, Energy Environmental Science. (e) Theoretical chart charging time to 80 % SOC as a function of power and capacity. Reproduced with permission from ref. [645]. Copyright 2024, Progress in Materials Science. (f) Information on fast charging of SSBs in automotive dimensions at FEST. (g) Ampcera's ASSLBs achieved 4C ultra-fast charging. (h) QuantumScape's SSB successfully completed 400 consecutive 13-min fast charging cycles (10 %–80 % SOC at 4C).

commercialization of ASSLBs, as it directly correlates with vehicle lifespan and total cost of ownership. Current research demonstrates that promising progress has been made, with academic breakthroughs achieving 20,000 cycles and industrial prototypes reaching 1000–5000 cycles. While cathode homogenization, interfacial engineering, and polymer electrolyte optimization have driven the recent advances in ASSLBs, two critical challenges persist. First, interfacial degradation causes performance losses during scale-up from lab cells to practical pouch configurations. Second, unrealistic test conditions and absent standardization protocols distort the true performance metrics under operational stresses. Future efforts must bridge these gaps while balancing energy density and cycle life through integrated material-cell design.

7.2.2. Energy density

SSBs overcome fundamental limitations of conventional LIBs, enabling significant improvements in energy density, which is a critical parameter in battery technology advancement. This enhancement is primarily achieved through two strategies: developing high-capacity electrode materials featuring wider ESWs alongside increased active material ratios, and optimizing structure via reduced current collector thickness and scaled cell dimensions. However, as the field matures, marginal gains from packaging and weight reductions have diminished, while excessive cell upscaling faces inherent thermal management and engineering constraints. Boasting high ESWs, excellent mechanical properties, and thermal resistance, SSEs enable compatibility with high-voltage cathodes and lithium metal anodes while permitting simplified pack design. Consequently, individual cells can be stacked in series and packed more densely, thereby enhancing manufacturing efficiency, reducing packaging size, and increasing volumetric energy density.

Fig. 31 shows the energy densities of SSBs in academic research and industrial implementations. In academic, Jung et al. [636] developed a microstructure-driven parametric battery design incorporating electrode/electrolyte construction parameters. The model incorporated electrode composition, density, loading, dimensions, and stacking configurations, as well as SSE membrane properties, achieving initial specific energies of 280 Wh kg^{-1} for a 1 Ah pouch cell and 310 Wh kg^{-1} for a 0.5 Ah one. Institute of Physics, Chinese Academy of Sciences, CASOL Energy Co Ltd Wu'team [637] assembled an SC–Si_3N_4–Li|LPSC|LCO soft-pack ASSLB to achieve a high energy density (> 320 Wh kg^{-1}), confirming practical viability. As referenced earlier, a 1.2 Ah soft-pack LMB employing a strong-complexation and high-voltage-resistant SPE achieved an energy density of 428 Wh kg^{-1} [489]. Zhou et al. [638] developed an all-solid-state pouch cell with a lithium-free silicon-based anode and Li_5FO_4–NCM cathode, achieving a discharge capacity of 1.1 Ah and a high energy density of up to 440 Wh kg^{-1}, which was based on the total mass of electrodes and electrolyte. Separately, Wang et al. [639] designed a novel PEO–Mg–Al–LiTFSI electrolyte, enabling batteries to operate stably over 300 cycles at 4.8 V and energy density exceeding 586 Wh kg^{-1}.

In industrial, QSE-5 as the first commercial product of the QuantumScape program delivered an energy density of 301 Wh kg^{-1}, 80 % fast charging in less than 15 min, high power, and superior safety compared to traditional LIBs. At CIES2025, Narada Power showcased 30 Ah ASSLB, which featured an ultra-high nickel ternary cathode and a confined-growth silicon–carbon anode. With an energy density of up to 350 Wh kg^{-1}, it could maintain a capacity retention rate of over 92 % after 500 charge and discharge cycles. Subsequently, Gotion High-Tech unveiled the Gotion ASSLBs, which boasted a capacity of 70 Ah and an energy density of 350 Wh kg^{-1}. Significantly, the prototype SSBs have entered on-road vehicle testing, demonstrating critical progress toward mass production. Farasis Energy has introduced high-conductivity SSEs, surface solid-state technology for ultra-high nickel cathode and anode materials, and anode expansion suppression technology, with an energy density of up to 400 Wh kg^{-1}. GAC adopted the third-generation sponge silicon anodes and high-surface-capacity solid-state cathodes to achieve energy density of more than 400 Wh kg^{-1} in ASSLBs. Further, Ampcera's ASSLBs technology can reach energy densities of up to 400 Wh kg^{-1} in cell capacities of up to 100 Ah at full-scale. Factorial Energy, a developer of ASSLBs for electric vehicles, is currently advancing the automotive-grade certification and industrialization of its technology. The company has successfully scaled up its initial Solstice cell to a 40 Ah capacity, marking a critical milestone toward commercialization. With an impressive energy density of up to 450 Wh kg^{-1}, this breakthrough could enable electric vehicles to achieve driving ranges exceeding 600 miles per charge, far surpassing the capabilities of traditional LIBs. In academic discussions of energy density, significant attention is often devoted to the battery's constituent layers, where the fundamental electrochemical processes occur, while overlooking the mass contributions from current collectors and external packaging components. However, the overall energy density of a cell extends beyond stack-level considerations. Commercial batteries are not marketed as bare electrode stacks but as fully encapsulated systems, where packaging design critically influences the net energy density.

7.2.3. Fast charging

Fast-charging capability has become a crucial performance metric for commercial battery systems, particularly in electric vehicles and portable electronics (Fig. 32a) [640]. Enabling rapid charging in SSB systems requires careful optimization of interfacial kinetics and ion transport pathways, typically resulting in compromised energy density. Furthermore, not all SSBs are suitable for fast charging, because the low ionic conductivities of some SSEs limit charging rates. While current-generation SSBs typically exhibit inferior fast-charging performance versus commercial LIBs, advanced architectures leveraging novel materials and structural innovations show strong potential, particularly due to inherent advantages like wide ESW, thermal stability, and operational temperature range [641].

The C-rate serves as a normalized metric for charge/discharge rates, yet critical battery behaviors such as dendrite formation are determined by absolute current density. This parameter, defined as total current divided by electrode geometric area, varies inversely with cathode loading at a fixed C-rate. Since cathode loading directly correlates with electrode thickness, meaningful C-rate comparisons require industry-relevant loadings. For electric vehicle applications, this typically corresponds to 2.5–5 mAh cm^{-2} to ensure practical significance. In systems with Li anode, high discharge currents lead to the formation of cavities and voids in the anode, which locally increase the current densities. Silicon-based anodes, on the other hand, suffer primarily from the strong volume change and the fact that interface surfaces are not stable. On the cathode side, high amounts of conductive material must be introduced due to the poor

intrinsic conductivity of cathode material. Li's group [642] designed a solid-state soft-pack battery using NCM83, lithium metal and Si/Graphene anode protection, achieving a capacity retention rate of about 92 % after 2000 cycles at 5C (Fig. 32b). Subsequently, Li's group [643] further achieved a breakthrough in full-battery kinetics under high cathode load and high area capacity by designing a layered electrode structure. The designed NCM cathode with a high area capacity exceeding 3 mAh cm^{-2} achieved stable cycling at high current densities of 13–40 mA cm^{-2} (5C–10C). Pang et al. [622] designed a redox-active LBPSI electrolyte that enables efficient S/Li_2S redox kinetics in Li–S SSBs. The resulting battery achieved a high specific capacity of 447 mAh g^{-1} at an ultrahigh rate of 35C (59 mA cm^{-2}) and exhibited exceptional cycling stability with 1000 cycles at 20C (Fig. 32c). Ma et al. [644] designed a CSE with h-PAN@MOF network and assembled a Li||NCM811 battery that achieved 1000 cycles at 5C (Fig. 32 d).

Industrial research is intensely focused on optimizing battery designs for fast charging without compromising energy density, safety, or cost. Song et al. [645] highlighted the critical link between electric vehicle battery capacity, charger power, charging time, and the potential advantage of SSBs for future energy density needs (Fig. 32e). Stellantis and Factorial Energy have successfully validated an automotive-grade solid-state cell with an energy density of 375 Wh kg^{-1}, marking a critical step toward commercialization. The breakthrough FEST® technology enabled ultra-fast charging from 15 % to 90 % state of charge (SOC) in just 18 min. The cell demonstrates robust operation from −30 °C to 45 °C, while delivering a high discharge rate of up to 4C (Fig. 32f). Ampcera reported a significant advancement in ASSLB technology, demonstrating rapid charging capability from 0 % to 80 % SOC in less than 15 min, achieving a peak C-rate of 4C (Fig. 32g). QuantumScape's white paper demonstrated fast-charging performance of 10–80 % SOC in under 14 min at 45 °C, maintaining over 80 % capacity retention after 400 cycles with an oxide-based SSE under 4C charging and 1C discharging conditions (Fig. 32h). Solid Power's SSB featuring a silicon anode and sulfide-based SSE demonstrates exceptional cycling stability, retaining 81 % of its initial capacity after 650 cycles with periodic fast charging. However, it should be noted that most of the aforementioned data were obtained from laboratory-scale cells under controlled conditions. When scaling up to automotive battery systems, various practical factors including environmental variations and real-world operating conditions may lead to substantial performance degradation. Consequently, the extent to which these reported values can be replicated in commercial battery cells remains uncertain and requires further investigation.

7.2.4. Pressure

Unlike the fluidity and wettability of LEs, SSEs conduct ions only through limited solid–solid contact, thus requiring external pressure for stable battery operation [646,647]. High pressure renders SSEs with fewer defects, greater strength, wider voltage windows, and more conformal SSE–electrode contact [648]. Consequently, SSBs manufactured under appropriate pressures generally exhibit lower interfacial impedance and enhanced electrochemical performance [649]. In the preparation and operation of SSEs and electrodes, two types of external pressure are involved. The external pressures during electrode/electrolyte preparation and roll pressing range from tens to hundreds of MPa, or even several GPa, and are termed manufacturing pressure (MP) and assembly pressure (AP). Meanwhile, cells often require molds or pressure devices to exert continuous operational pressure (OP) to maintain stable charge–discharge cycling [650]. MP directly affects the porosity and ionic conductivity of electrodes and electrolytes, while appropriate AP ensures effective contact between electrodes and SSEs during assembly. Doux et al. [651] demonstrated that MP significantly influences the porosity of SSE pellets, as evidenced by focused ion beam 3D reconstruction analysis (Fig. 33a). Furthermore, Zhou et al. [652] demonstrated that MP critically controls the relative density and surface morphology of SSEs. The resulting electrolyte flatness, which is a key determinant of ionic conductivity, depends ultimately on the applied pressure (Fig. 33b). During the electrode and SSEs assembling process, AP is applied to enhance solid–solid contact between powder particles, which involves the plastic deformation within the composite electrode. Elastic SSEs can compensate for electrode volume changes during cycling, thereby mitigating high charge-transfer resistance from cracks and voids that would otherwise cause electrochemical isolation of active material. Zhang et al. [653] reported that AP improves interfacial contact between lithium metal and SSEs. Over time, creep promotes conformal Li–SSE contact and homogeneous stress distribution, effects that are further enhanced by increasing AP (Fig. 33c). Sakka et al. [654] established a quantitative correlation between cathode 3D architecture and AP, with direct observations revealing pressure-dependent anisotropic contact characteristics between active materials and SSEs. Increased pressure reduces porosity, improves active material–SSE contact area, and enhances apparent conductivity (Fig. 33d). Thus, identifying an optimal AP range is critical for stable electrochemical performance. During operation, SSBs undergo dynamic volume changes. The external OP not only mitigates electrode structural fracture and interfacial contact degradation caused by cyclic volume expansion, but also suppresses inhomogeneous lithium deposition, thereby reducing dendrite penetration risk [655]. Properly controlled OP therefore substantially improves SSBs' performance and cycling stability. Gao et al. [656] investigated factors enabling high-capacity solid-state cathodes that sustain performance under relatively low pressure of 1 to 2 MPa and at a current density of 1 mA cm^{-2}. As demonstrated in Fig. 33e, Lee et al. [657] integrated compression springs into conventional SSB architectures and employed laser displacement and force sensors to elucidate the mechanical interplay between OP evolution and compression spring dynamics. Their findings underscored the critical role of pressure management in mitigating volume fluctuations during charge–discharge cycles and preserving low interfacial charge-transfer resistance. Aurbach et al. [658] systematically reviewed the coupling between external pressure and electrochemical behaviors in ASSLBs, correlating pressure effects on components (electrodes and interfaces) with thermodynamic/kinetic principles to elucidate performance and safety under pressure.

Although high OP (even exceeding 100 MPa) is commonly employed in lab-scale research to achieve optimal performance, such parameters lack consistency and far exceed industrial requirements (< 1 MPa). This disparity impedes objective SSB evaluation under practical conditions and overlooks scale-up challenges. Critically, the application of such high pressures in SSB assembly introduces multiple technical obstacles, further hindering their commercial viability. Primarily, it necessitates battery casings with enhanced mechanical strength, increasing both component complexity and system weight. Subsequently, manufacturing processes require

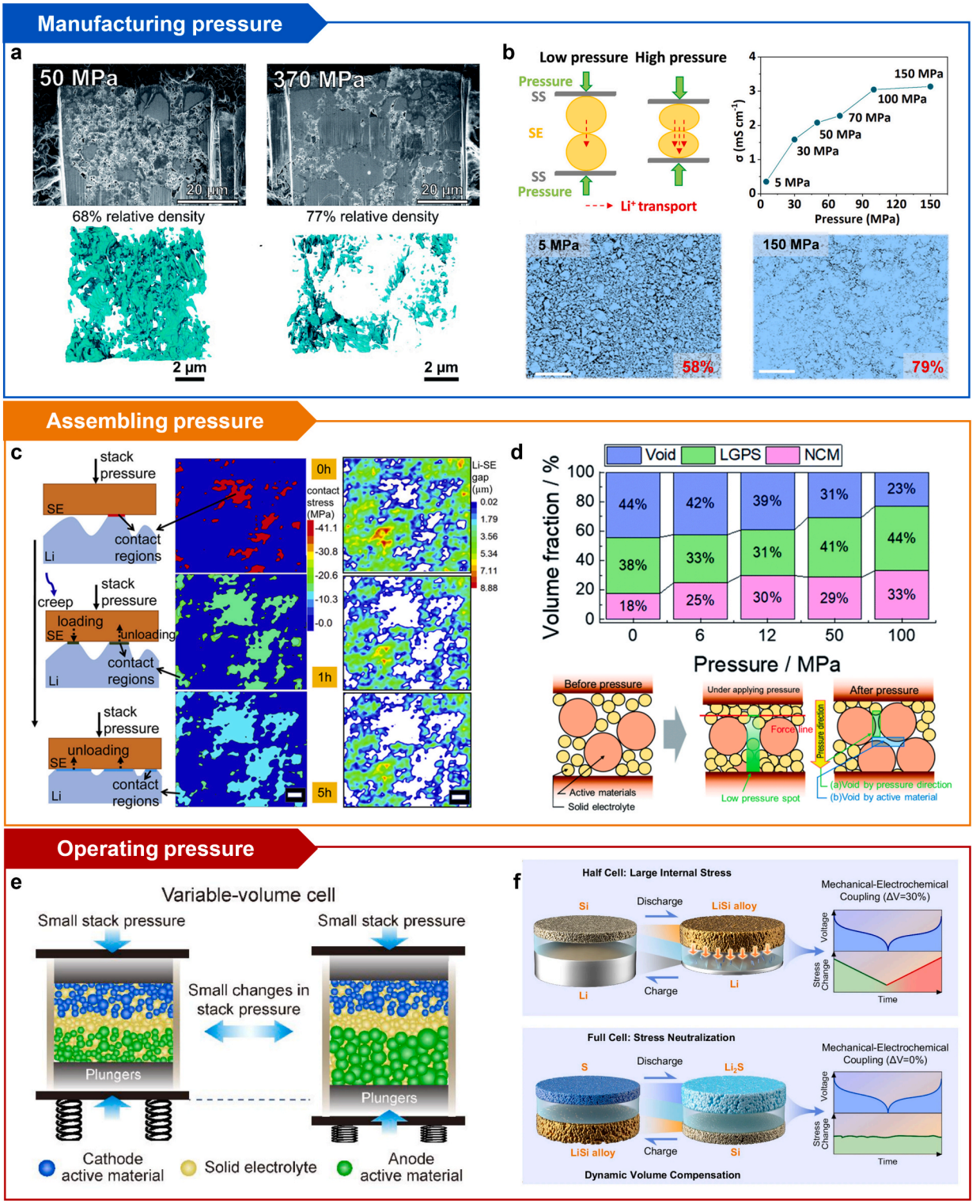

(caption on next page)

Fig. 33. (a) FIB-SEM cross-sectional images of LPSC electrolyte pellets prepared under MP of 50 and 370 MPa, with estimated relative densities indicated. Reproduced with permission from ref. [651]. Copyright 2020, Journal of Material Chemistry A. (b) Effect of stacking pressure on transport behavior of Li^+ in SSEs. Reproduced with permission from ref. [652]. Copyright 2023, Energy Environmental Materials. (c) Evolution of Li–SSE interface creep and interfacial gap formation under AP. Reproduced with permission from ref. [653]. Copyright 2020, Cell Reports Physical Science. (d) Illustration of pressure-induced changes in volume fraction and structure for different components in the composite electrode. Reproduced with permission from ref. [654]. Copyright 2022, Journal of Material Chemistry A. (e) Schematic of a compressible spring-loaded battery mold with tunable volume. Reproduced with permission from ref. [657]. Copyright 2024, Energy Storage Materials. (f) Dynamic volume compensation strategy to design a Si–S full cell in a state of stress-neutralization. Reproduced with permission from ref. [659]. Copyright 2025, Nature Communications.

specialized high-pressure equipment, elevating production costs while compromising yield rates. Furthermore, pressure inhomogeneity may induce interfacial contact loss between cell components, accelerating performance decay and raising safety concerns, all of which hinder commercial viability.

To address these limitations, developing low-pressure operable SSBs has emerged as a critical prerequisite for industrialization.

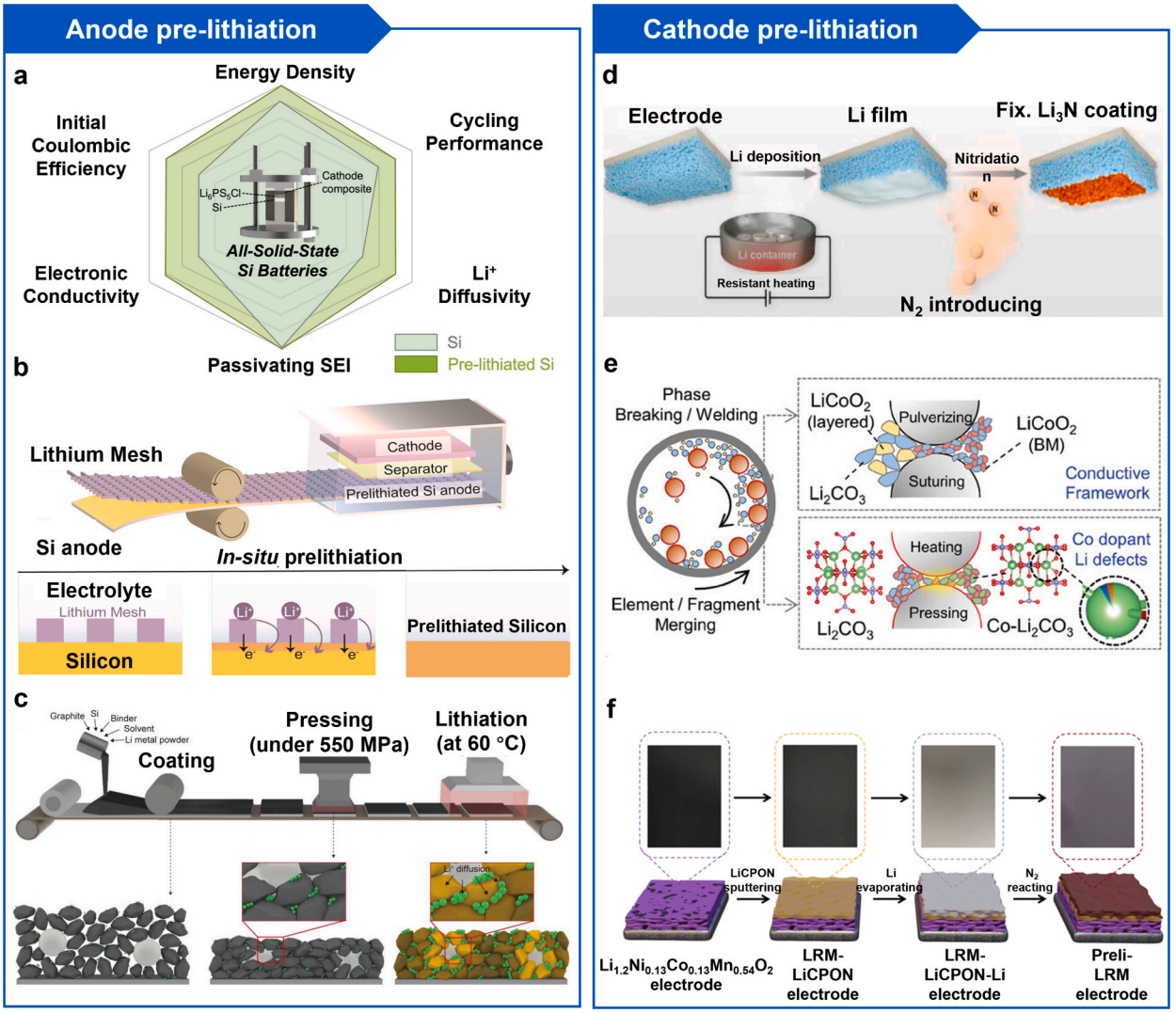

Fig. 34. Pre-lithiation technology of anodes and cathodes. (a) Comparison of Si and pre-lithiated Si for ASSLBs. Reproduced with permission from ref. [664]. Copyright 2024, Nature Communications. (b) *In situ* pre-lithiation design via a lithium network for silicon anodes. Reproduced with permission from ref. [665]. Copyright 2023, Nano Letters. (c) Schematic illustrations of the PL-DDE fabrication process, including the slurry coating, pressing, and dry pre-lithiation process, and the structural and lithiation state changes in each fabrication step. Reproduced with permission from ref. [666]. Copyright 2023, Advanced Energy Materials. (d) Diagram of the fixation process of lithium metal on the electrode surface. Reproduced with permission from ref. [667]. Copyright 2020, Journal of Power Sources. (e) Co-Li_2CO_3@LCO Effect and route of ball mill structure design. Reproduced with permission from ref. [668]. Copyright 2024, Advanced Materials. (f) The entire pre-lithiation process of the $Li_{1.2}Ni_{0.13}Co_{0.13}Mn_{0.54}O_2$ cathode. Reproduced with permission from ref. [669]. Copyright 2024, Energy Storage Materials.

Recent studies propose strategies to maintain high performance at reduced pressures. Silicon anode volume expansion generates significant internal stresses during cycling. This stress compromises SSE structural integrity, destabilizes interfaces, and potentially accelerates lithium dendrite formation, ultimately causing battery failure. Yu et al. [659] resolved this through mechano-electrochemical dynamic volume compensation (Fig. 33f), leveraging opposing volume changes in silicon and sulfur electrodes to neutralize stresses, thereby addressing stress heterogeneity, electrode integrity, and interface stability challenges. Furthermore,

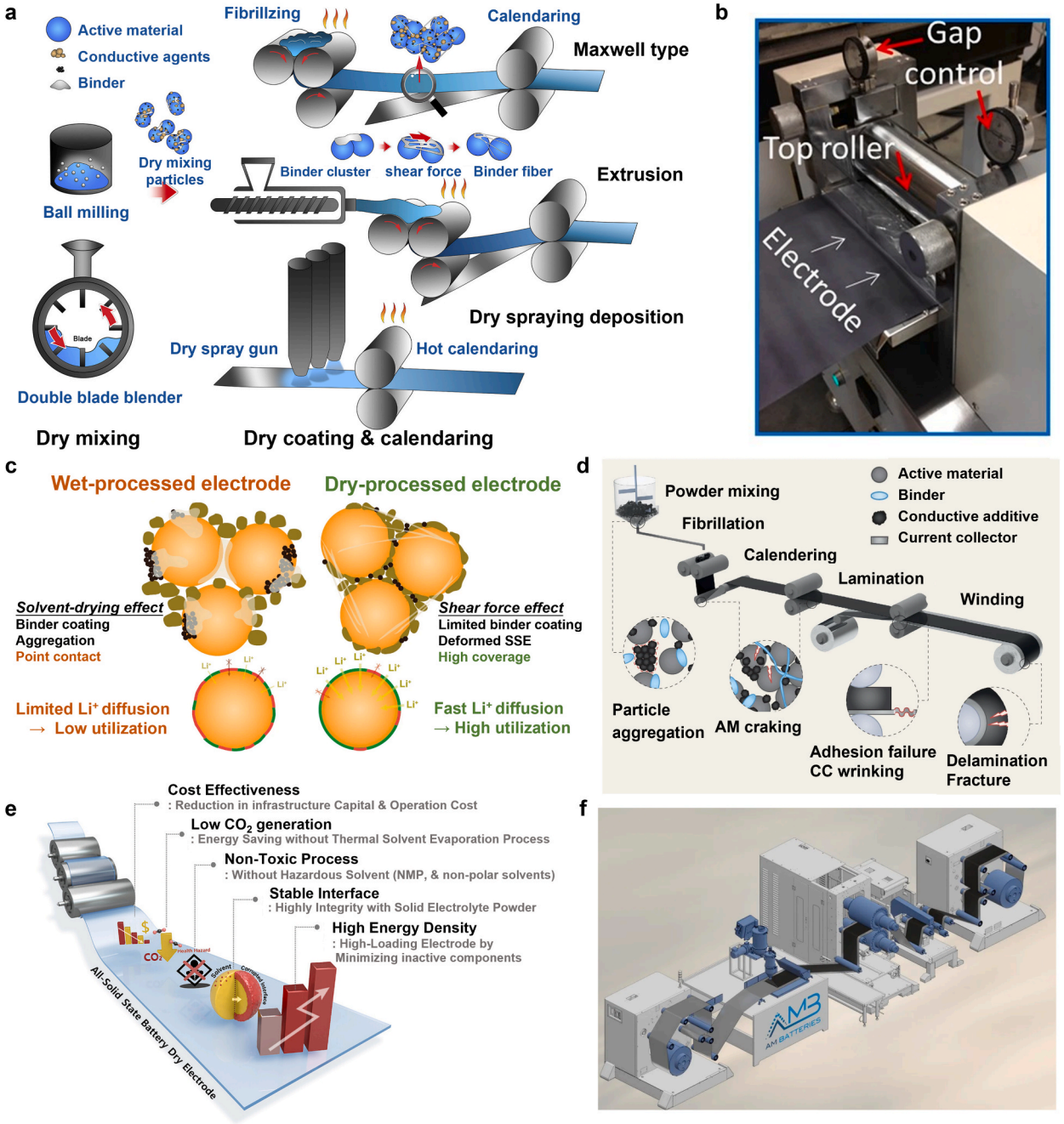

Fig. 35. (a) Typical procedures for applying dry method for electrode preparation. Reproduced with permission from ref. [674]. Copyright 2023, Matter. (b) Physical drawing of the hot-rolled structure. Reproduced with permission from ref. [675]. Copyright 2016, Scientific Reports. (c) The differences and characteristics between wet and dry electrodes. Reproduced with permission from ref. [676].Copyright 2024, Nature Communications. (d) Dry process flow and challenges of roll-to-roll high loading electrode. Reproduced with permission from ref. [677]. Copyright 2025, Nature Energy. (e) The advantages of dry electrodes in ASSLBs. Reproduced with permission from ref. [678]. Copyright 2025, Advanced Materials. (f) Schematic diagram of the powder-to-electrode film process production line of AM Battery Company.

McDowell et al. [660] added soft sodium to lithium to achieve low-pressure operation of SSBs and developed a dynamic interface with adaptive deformation. Wang et al. [661] proposed a protective strategy for solid-state reducing electrophilic interfaces, while Chen et al. [629] designed a $Li_{21}Si_5$/Si-$Li_{21}Si_5$ anode. To homogenize the electric field, Wu et al. [662] developed a low-voltage sulfide-based ASSLB pouch cell using a self-limiting electrolyte. All these results demonstrate that innovative stress-management strategies through mechano-electrochemical compensation and adaptive interface design can effectively decouple solid-state battery performance from external pressure requirements, establishing a new paradigm of intrinsic stress regulation for practical SSB commercialization. Future research need focus on novel material systems and innovative interface modification strategies that intrinsically minimize external pressure dependence, thereby enabling scalable manufacturing. Resolving stress-related limitations in ASSLBs requires synergistic advancements in materials chemistry and battery architecture, complemented by industry-academia partnerships to establish unified testing standards and scalable technical implementations.

7.3. Process technology

7.3.1. Pre-lithiation strategies

The design concept of anode pre-lithiation primarily involves preloading a certain amount of active lithium within the anode material. This aims to compensate for irreversible lithium loss caused by the formation of the SEI and other parasitic reactions, ensuring that cathode lithium is utilized for charge transfer within the electrolyte [663]. The principal technological pathways for anode pre-lithiation include mixing lithiation (such as lithium powder or lithiated silicon powder), contact lithiation (such as lithium foil), electrochemical lithiation, and chemical lithiation. The difference in Gibbs free energy between anode and lithium metal enables an internal short circuit for the spontaneous movement of electrons from lithium to anode material. Concurrently, the generated Li^+ reacts with the anode to achieve lithiation.

Ham et al. [664] employed a straightforward pressure-induced pre-lithiation strategy for silicon anodes and characterized these anodes using ss-NMR. They further assessed the performance of pre-lithiated silicon anodes in symmetric, half-cell, and full-cell configurations. A comparison of six electrochemical properties, including radar maps, indicates that the pre-lithiation method could be well-suited for next-generation, high-load ASSLBs (Fig. 34a). Yang et al. [665] proposed an *in situ* pre-lithiation method through direct integration of lithium metal mesh into battery assemblies, as shown in Fig. 34b. They designed tunable-porosity lithium meshes as pre-lithiation reagents applied to silicon anodes, enabling spontaneous electrode lithiation upon electrolyte addition. The pre-lithiation degree was precisely controlled by varying mesh porosity. Lee et al. [666] developed a dry-phase pre-lithiation technique for diffusion-dependent electrodes using direct contact with metallic lithium powder (Fig. 34c). In contrast to traditional pre-lithiation strategies involving additional solvents, gases, and additives, this approach facilitates pre-lithiation reactions in anhydrous conditions, minimizing side reactions while simplifying processing. Incorporating metallic lithium powder into electrodes enhances initial CE by compensating lithium loss of active lithium due to anode degradation during cycling.

Cathode pre-lithiation refers to the addition of extra active lithium sources to compensate for irreversible active lithium loss, ensuring sufficient active lithium within the battery. Compared to anode pre-lithiation techniques, which are characterized by complex processes, high safety risks, and demanding environmental and process requirements, current research in cathode pre-lithiation technology is focused more on the development of cost-effective lithium-rich additives. These lithium-rich additives must meet several requirements, including matching the ESWs, providing sufficiently high lithiation capacity, being compatible with existing lithium battery production environments and processes, and minimizing side reactions such as residue and gas generation.

Yang et al. [667] introduced a lithium replenishment technology that involves the deposition of lithium metal onto the cathode surface (Fig. 34d). This process entails the *in situ* synthesis of a lithium nitride film on the electrode, which decomposes during the initial charging cycle to supply lithium ions to the battery. Additionally, this technology is applicable to lithium-free cathodes, serving as the sole lithium source in the battery. It allows for compatibility with traditional graphite/silicon-based anodes, thus enhancing the lithium-free cathode's application range and improving overall battery safety by avoiding the use of lithium metal negative electrodes. Zhu et al. [668] exploited a defective transition metal-doped lattice engineering to obtain $(Li_{0.906}Co_{0.043-0.051})_2CO_{2.934}$ (Co-Li_2CO_3). The essence of lattice engineering is precisely tuning the position of doped atoms, inspiring bulk phase catalytic regulation and inducing defects, which can modify bandgap and bond strength. Benefiting from this approach, Li_2CO_3 is transformed from an intrinsic insulator to an exceptional sacrificial cathode pre-lithiation agent with reduced bandgap and weakened Li–O bond strength (Fig. 34e). Lu et al. [669] developed a composite pre-lithiation strategy involving a magnetron-sputtered LRMOs coupled with an *in situ* vacuum-evaporated sacrificial Li_3N layer as shown in Fig. 34f, demonstrating superior pre-lithiation efficiency, controllability, and air stability.

7.3.2. Dry electrode technology

Traditional wet electrode manufacturing involves mixing powdered materials with solvents to prepare a slurry, followed by multiple processes such as coating, drying, solvent recovery, and rolling to produce electrodes. However, the drawbacks associated with the wet process include long drying time, high cost of organic solvent recovery, serious environmental pollution, and limitations on high electrode load [670]. In contrast, dry electrode technology bypasses manufacturing steps such as slurry preparation, drying, and solvent recovery, directly compacting dry powder electrode materials containing active materials to form electrodes. Therefore, this method simplifies high-mass-loading electrode production, reducing energy consumption by 45–47 %, and cutting total battery costs by 1–2 % [671,672]. This process integrates six core techniques: adhesive precursor fiberization, electrostatic spray coating, powder compression, vapor deposition, powder spray, and 3D printing. The fiberization technique specifically involves dry-blending powdered active materials with conductive agents, incorporating solid adhesives, and then applying high shear forces to fibrillate the binder. This creates a 3D fibrillated adhesive "mesh" that interconnects electrode powder, forming self-supporting films, which are

subsequently extruded and rolled onto current collectors for final electrode assembly. Therefore, adhesive selection is critical. PTFE is the ideal solid adhesive for dry electrode technology due to its low van der Waals forces, enabling its transformation from agglomerates into a fibrous network that binds electrode powder, unlike traditional PVDF used in wet processes. Furthermore, achieving adequate fiberization is essential, as insufficient fibrillation can prevent film formation or increase electrode impedance due to adhesive agglomeration, compromising electrode strength and battery performance. The specific dry-film technology is chosen based on the battery type, application environment, and manufacturing scale [673].

Generally, dry battery electrode (DBE) procedures include dry mixing, dry coating, calendaring, and slitting. Important manufacturing procedures for DBE are shown in Fig. 35a [674]. In 2016, Zheng et al. [675] first proposed a completely novel, fully dry powder coating process. This hot rolling approach superseded the conventional solvent evaporation process for casting slurry electrode fabrication, significantly reducing both processing time and resource requirements. Fig. 35b illustrates the corresponding hot rolling apparatus configuration. Then, Lee et al. [676] systematically studied the influence of shear force in the dry electrode process by comparing binder-free hand-mixed particles, wet-treated electrodes, and dry-treated electrodes. In traditional wet slurry methods, the binder is generally coated on the surface of the active material, hindering direct contact between electrode particles and restricting the interfacial transfer of Li^+ and e^-. Moreover, achieving satisfactory mechanical properties requires high binder content. In contrast, the solvent-free dry-electrode fabrication method allows the binder to form a 3D fiber network under shear forces, enabling direct and close contact between the active material and the SSE/conductive agent. This configuration ensures rapid ion/electron transport and high mechanical performance. The comparison between wet and dry electrode preparation processes is illustrated in Fig. 35c. Digital image analysis demonstrated that dry electrodes achieve significantly greater electrolyte coverage than binder-free particle mixtures or wet-processed electrodes, where electrolyte coverage represents the percentage of active material surface area covered by electrolyte. This enhanced interfacial contact correlates directly with improved rate capability and cycling stability. Kim et al. [677] pointed out that early laboratory research often overlooked the inherent complexity of large-scale production and specific application challenges. Integrating an understanding of industrial processes into academic research is key to improving the technical readiness. They further summarized the manufacturing and physicochemical issues of roll-to-roll production of high area capacity electrodes, focusing on slurry casting and dry coating processes (Fig. 35d). The dry coating process eliminates solvent processing and avoids the coating and drying problems associated with slurry casting of high area capacity electrodes. However, achieving efficient and stable roll-to-roll continuous production still requires addressing several key issues, including particle aggregation, active materials cracking, adhesion failure, current collector wrinkling delamination and fracture. Overall, the advantages of dry electrodes in SSBs mainly include cost-effectiveness reduction, lower CO_2 emissions, elimination of toxic solvents, stable interfaces, and high energy density (Fig. 35e) [678]. However, further verifying scalability and industrial feasibility remains crucial. Progressing towards industrialization, the USA dry electrode company AM Batteries announced in October 2024 that it had delivered the first sample of a dry electrode consisting of two coils of NCM cathodes to a leading battery supplier. The disclosed process first involves dry mixing of cathode/anode active powder, polymer binders, and conductive additives. The mixed powder is then applied to the substrate using an electrostatic spray deposition system, and finally the particles are mechanically compressed and bonded to the substrate via a thermal calendaring system, as illustrated in Fig. 35f.

7.3.2.1. Dry electrode application. In 2019, Tesla acquired Maxwell, a company known for its adhesive precursor fiberization method in film manufacturing, which Tesla currently employs for producing self-supporting films. The USA and Japan are respectively leading countries in the adhesive precursor fiberization method and electrostatic spray coating process, with Maxwell and Toyota representing these two techniques, respectively. Electrostatic spray coating is a technique within dry spray coating systems, comprising powder storage, distribution units, and electrostatic spray guns. Its main challenge lies in controlling powder dosage, thickness, and uniformity during spraying. Initially, materials including active substances, conductive agents, and adhesive particles are premixed, then propelled by high-pressure gas to acquire a negative charge and sprayed onto a positively charged metal foil current collector. Subsequently, the adhesive-coated current collector undergoes heat pressing, melting the adhesive to bond other powder and extrude into a self-supporting film, ultimately forming the electrode sheet. This limitation hampers its subsequent processability, adhesive stability, electrode flexibility, and durability compared to the adhesive fiberization method. Therefore, the mainstream technique for dry electrodes is gradually shifting towards adhesive precursor fiberization.

7.3.2.2. Thick electrode technique. Compared to slurry-based processes, binder fiberization dry technology enables crack-free fabrication of ultra-thick roll-to-roll electrodes. Thick electrode design approaches can substantially increase the active material loading by decreasing the inactive component ratio at the cell level, thereby leading to increased battery energy density as well as decreased cost [679]. Meng's group [671] developed a PTFE-based dry electrode fabrication method to prepare high voltage spinel oxide LNMO electrodes. Overcoming major limitations with slurry-coated electrodes, this process enables ultra-high loadings ($\approx$ 68 mg cm^{-2} and $\approx$ 240 mm) and excellent cycling stability using a 3.0 mAh cm^{-2} level ($\approx$ 21 mg cm^{-2} and $\approx$ 90 mm) electrode at 1000 cycles with both the baseline and a high-performance fluorinated electrolyte (68 % capacity retention after 1000 cycles for the full cell). Lv et al. [680] employed dry electrode fabrication to produce freestanding sulfur cathodes with a high sulfur content (40 wt%) and areal loading (4.5 mg cm^{-2}). These electrodes exhibited an initial discharge capacity of 1114.8 mAh g^{-1}, along with excellent cycling stability and rate performance. Chen et al. [681] achieved a uniform and thin SSE layer (50 μm) and a high-load cathode layer (5 mAh cm^{-2}) simultaneously through the dry process of co-rolling thick SSE and cathode materials for ASSLBs, and the proportion of cathode active substances reached 80 wt%. Jeong et al. [682] employed single-crystal active materials with reduced particle size in combination with highly porous spherical conductive agents to fabricate high-energy-density dry-processed electrodes. These electrodes achieved an

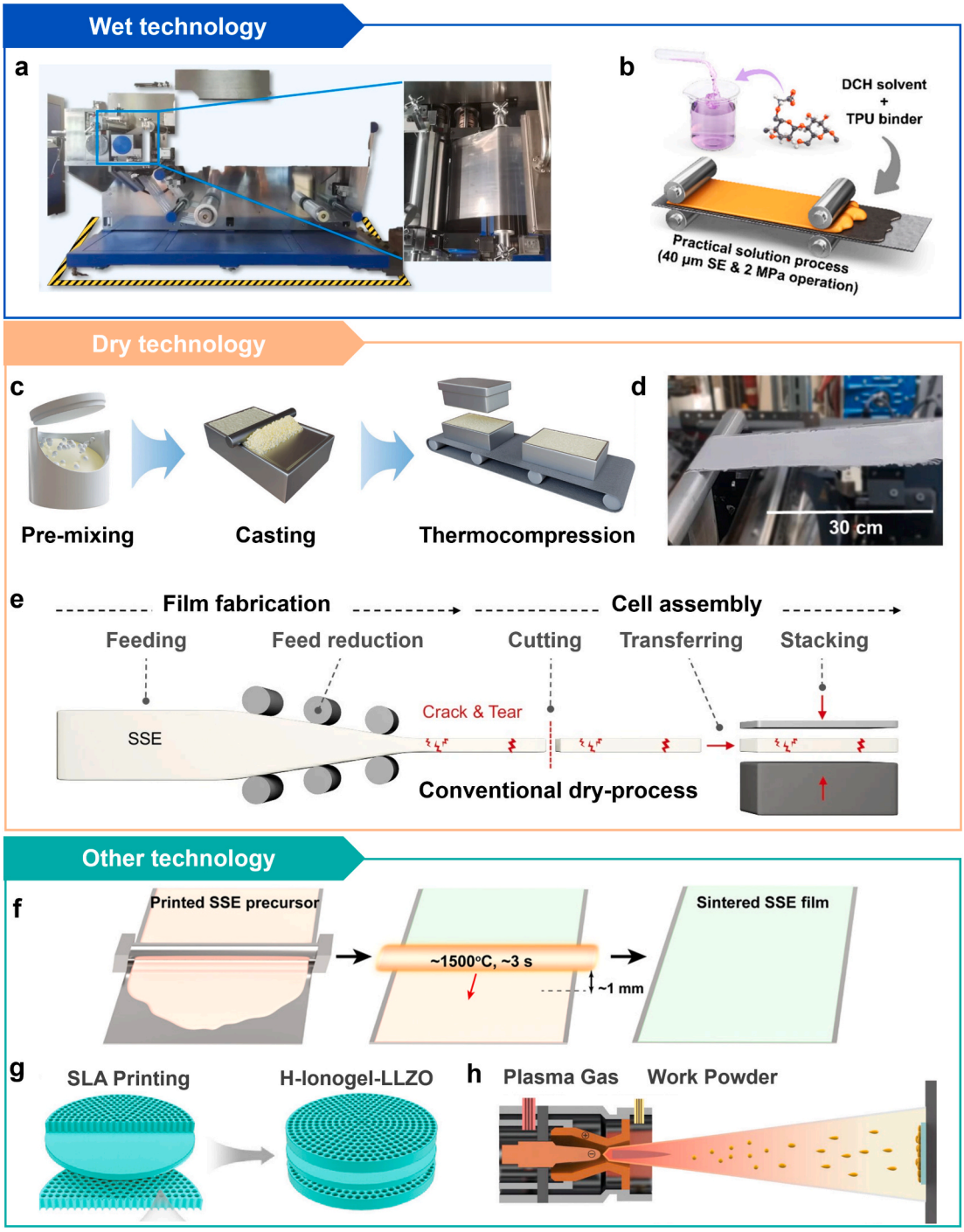

Fig. 36. (a) Optical photos of the industrial-scale continuous casting slurry PEO electrolyte membrane production line. Reproduced with permission from ref. [639]. Copyright 2024, Nature Communications. (b) Schematic diagram of electrolyte membrane preparation by co-coating wet method. Reproduced with permission from ref. [683]. Copyright 2025, ACS Energy Letters. (c) Schematic diagram of electrolyte membrane preparation by melt-dry method. Reproduced with permission from ref. [684]. Copyright 2024, Advanced Materials. (d) Sulfide-based SSE membranes are prepared on non-woven fabrics by dry roll-to-roll technology. Reproduced with permission from ref. [685]. Copyright 2025, Advanced Energy Materials. (e) Dry-process design of co-rolled electrolyte. Reproduced with permission from ref. [681]. Copyright 2025, Nature Communications. (f) Printing and rapid HT sintering processes for the synthesis of ceramic SSE membranes. Reproduced with permission from ref. [175]. Copyright 2020, Science Advances. (g) Schematic diagram of 3D printing technology for LLZO. Reproduced with permission from ref. [686]. Copyright 2025, ACS Nano. (h) Fast preparation of LLZO films by air plasma spraying. Reproduced with permission from ref. [687]. Copyright 2024, Advanced Energy Materials.

exceptional areal capacity of 20 mAh cm^{-2} while maintaining a high composite density of 3.65 g cm^{-3}. To validate their practical feasibility, the authors fabricated double-sided dry-processed thick electrodes and successfully assembled 1 Ah pouch cells, demonstrating the scalability and applicability of this approach in real-world battery systems.

Dry electrode technology is a promising route for ASSLBs thick electrodes, offering high energy density, mechanical stability, and process scalability. Further optimization of binder, conductive networks, and interfacial engineering will enhance its viability for

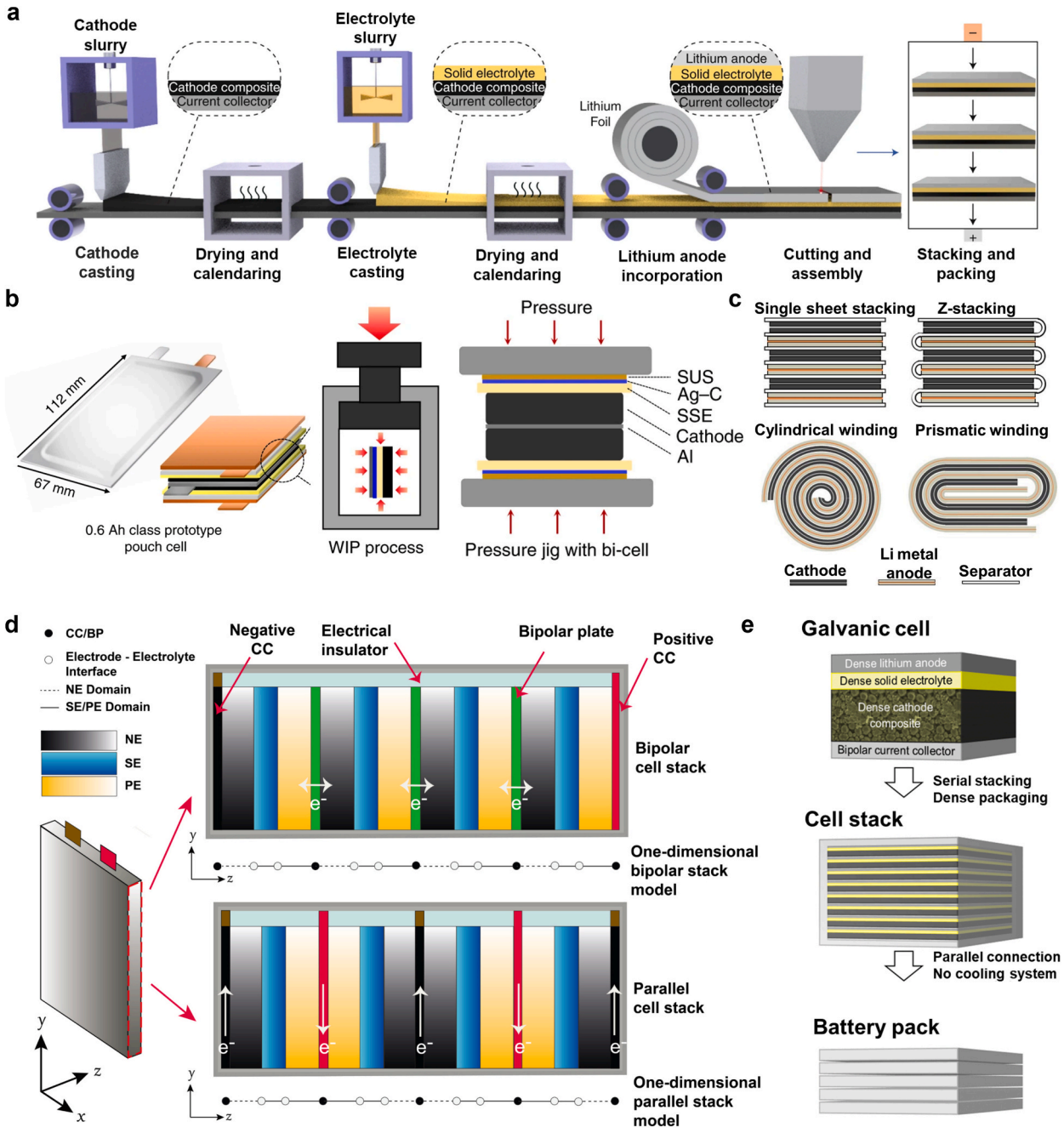

Fig. 37. (a) Schematic of large-scale manufacturing of ASSLBs. Reproduced with permission from ref. [690]. Copyright 2020, Nature Nanotechnology. (b) Characterization of a 0.6 Ah class prototype pouch cell and illustration of a bi-cell structure. Reproduced with permission from ref. [224]. Copyright 2020, Nature Energy. (c) Schematic showing four typical types of LMB manufacturing processes: single sheet stacking, Z-stacking, cylindrical winding, and prismatic winding. Reproduced with permission from ref. [694]. Copyright 2019, Journal of The Electrochemical Society. (d) Configuration diagram of a bipolar and parallel stack assembled pouch battery. Reproduced with permission from ref. [695]. Copyright 2020, Journal of The Electrochemical Society. (e) ASSLBs at the cell, stack, and pack levels with potentials for increased energy density. Reproduced with permission from ref. [696]. Copyright 2018, Journal of Power Sources.

commercial SSBs.

7.3.3. SSE membrane preparation technology

Throughout the entire production process of ASSLBs, the electrolyte film-forming process stands as a critical step. An ideal SSE film should possess a large area, controllable thickness, high ionic conductivity, and good electrode interface compatibility, which could enhance the practical energy density of batteries and reduce manufacturing costs. The selection of an appropriate film-forming method depends on specific performance requirements. This section will focus on introducing techniques including wet methods, dry methods, 3D printing, etc.

Wet methods are preferred due to their simplicity, process maturity, and scalability, making them one of the most promising techniques for mass-producing SSE membranes. The key aspects of wet methods include the selection of binders and solvents, especially for sulfide-based SSEs. Ideally, solvents should have low boiling points for easy evaporation and good solubility and chemical stability with the SSE. Polar solvents like acetonitrile and acetone are commonly used for polymer electrolytes, while non-polar solvents like toluene and xylene are preferred for most sulfides. The addition of binders increases the impedance of SSE membranes, necessitating a balance between ionic conductivity and binding strength. Wang et al. [639] adopted the Lewis-acid synergy strategy to solve the problem of high-voltage instability of PEO. Further, they fabricated a 50 m-long roll of PEO–MG–AL–LiTFSI electrolyte membrane through an industrial-scale continuous casting process, demonstrating the potential of this strategy in engineering applications (Fig. 36a). Choi et al. [683] developed a new type of solvent-binder combination, which significantly improved the performance and solution processability of sulfide electrolytes (Fig. 36b). 1, 6-dichlorohexane (DCH) solvent can effectively dissolve highly adhesive thermoplastic polyurethane (TPU) adhesives while maintaining the ionic conductivity of SSEs. In addition, by taking advantage of the excellent adhesion performance of TPU, a double-layer coating process was successfully achieved. This process demonstrated outstanding performance under actual conditions of thin SSE layer, RT, and low stacking pressure.

One of the drawbacks of wet methods is the potential toxicity and high cost of solvents used, with residual solvents reducing the ionic conductivity of SSE membranes. Dry methods involve dispersing SSEs and polymer binders into high-viscosity mixtures, followed by applying sufficient pressure to form films. Dry methods typically result in thicker SSE membranes, which can lower the energy density of ASSLBs. However, dry methods offer cost advantages by avoiding solvent use and enable higher ionic conductivity due to the absence of solvent residues. Cui et al. [684] proposed an optimal solvent-free strategy using melt bonding technology (Fig. 36c). Kaskel et al. [685] successfully fabricated dry-process thin and flexible sulfide electrolyte membranes containing non-woven fabric substrates by using a continuous, scalable, single-step roll-to-roll process (Fig. 36d). By hot-pressing ($\leq$ 5 MPa), low-viscosity thermoplastic polyamide binder and LPSC were combined to form a percolation network, thereby creating an ultrathin LPSC film ($\leq$ 25 μm). This technology is expected to be used for manufacturing bulk sulfide-based ASSLB with stability, flexibility and large-scale feasibility. Chen et al. [681] proposed a co-rolling dry process. By simultaneously rolling the SSE layer and the cathode material layer, a tightly bonded interface between the SSE and the cathode was directly formed during the processing, as shown in Fig. 36e. During the co-rolling process, the shear force acts on the interface between SSE and the cathode material, causing the binder (such as PTFE) to undergo fibrosis and form a bonding network that runs through the interface. This bonding network significantly enhances the adhesion of the interface, enabling a tight mechanical connection to be formed between the SSE and the cathode material.

In 2020, Hu et al. [688] reported a ceramic synthesis method called UHS, which features uniform temperature distribution, high heating rate (103–104 °C min^{-1}), high cooling rate (up to 104 °C min^{-1}), and high sintering temperature (up to 3000 °C). In the same year, they [175] continued to adopt the printable UHS process, and high-performance ceramic SSE membrane was successfully prepared (Fig. 36f). This method has high scalability, which is suitable for roll-to-roll processing, and rapidity advantages, etc. However, its cost should be further reduced before being applied in large-scale production. Besides this UHS method, 3D structural design can increase the contact area and integrate functional additives to enhance interface stability and reduce ion transfer resistance. The flexibility and precision of 3D printing enable the production of thinner SSEs with custom shapes and functions, thereby enhancing ionic conductivity and processability [689]. Yan et al. [686] successfully prepared a high ceramic content slurry suitable for stereolithography 3D printing by coating ionic liquid on the surface of LLZO nanoparticles, and printed symmetrical honeycomb-shaped brick electrolyte films. This electrolyte achieves low interfacial impedance and high lithium-ion migration number by taking advantage of its unique honeycomb structure, significantly improving the ionic conductivity (Fig. 36g). In the field of large-scale ceramic coating or film processing, the air plasma spraying (APS) method has been widely used since its first development in the 1970s. Its applications include solid oxide full batteries, biomaterial coatings, wear-resistant coatings and thermal barrier coatings. Fig. 36h shows a schematic diagram of the APS process. By controlling the spraying processing time, LLZO films of different thicknesses ranging from 30 to 300 μm can be prepared. This method demonstrates its scalability for industrial production [687].

7.3.4. SSB assembly technology

The novel material systems and battery architectures of ASSLBs render existing LIB manufacturing processes and equipment inadequate for industrial-scale fabrication, necessitating adaptive innovations. Current ASSLBs lack standardized mass-production processes, the production techniques and fabrication procedures vary considerably depending on the battery design and application. Fig. 37a depicts a typical manufacturing process for ASSLBs utilizing wet slurry processing techniques analogous to those employed in conventional LIBs [690]. To address critical challenges in SSBs, particularly interfacial contact resistance and electrode porosity issues, Lee et al. [224] developed an Ah-class ASSLB prototype for electric vehicle applications and introduced a warm isostatic pressing method during the manufacturing process of ASSLBs, applying a pressure of 490 MPa (Fig. 37b). However, the choice of isostatic pressing technology directly affects cost and performance. Belharouak et al. [691] conducted an economic analysis of isostatic pressing technology in the case of large-scale production of SSBs. They found that cold isostatic pressing has a short cycle time,

the lowest cost per cycle, and the best overall cost. In summary, the adoption of isostatic pressing technology must be carefully evaluated in the context of the existing production line and battery system design to ensure cost-effective implementation. Futsher et al. [692] presented a high-power and high-energy SSB design based on monolithically-stacked thin-film cells fabricated by scalable vacuum deposition and predicted the specific energy and power of monolithic stacked thin-film batteries using a thermo-electric model. Wang et al. [693] developed a scalable methodology for pouch cell-level evaluation of lab-scale battery materials (mass loading < 5 g), providing a detailed protocol for pouch cell assembly. With great success in thin SSE membranes and thick SSEs, all-solid-state pouch cells can be fabricated via a roll-to-roll process and assembled by bipolar stacking [690]. Fig. 37c compares four typical manufacturing processes for LIBs, including single sheet stacking, Z-stacking, cylindrical winding, and prismatic winding [694]. The manufacturing processes used for ASSLBs currently can similarly draw from these techniques. For instance, SK ON have exclusive ownership of a stacking method that intersects and stacks cathodes and anodes between the separators in a zigzag shape to achieve the highest level of safety. The Z-folding technology minimizes cell stress and evenly stacks cathodes and anodes to prevent physical contact between electrodes, greatly reducing the potential risk of internal short and ignition of batteries.

The optimal cell format for industry currently manufactured SSBs typically adopts a planar shape, such as prismatic or pouch cells, which effectively preserves the structural integrity of SSEs. Currently, all-solid-state pouch batteries primarily come in two structures: bipolar stacking and parallel stacking. To enhance performance of multi-layer SSB configurations, a bipolar design can be implemented to reduce pack resistance and increase energy density. The working principles of bipolar and parallel stacking as shown in Fig. 37d [695], in a bipolar stack configuration, the electrical current flows from one unit cell to the adjacent unit cell through the bipolar plates, whereas in a parallel stack, the current travels in-plane along the current collectors to the external tabs. Microvast's ASSLB utilizes a bipolar stacking architecture that enables internal series connections within a single battery cell, allowing it to achieve tens of volts or higher depending on application requirements. The manufacturing process of the ASSLBs pack is illustrated in Fig. 37e. Bipolar stacking is advantageous for ASSLBs, as individual cells are connected in series through an electrolyte isolation layer. This configuration can increase the battery voltage, reduce the number of current collectors within the stack, and optimize the packaging design. Additionally, due to the absence of flammable organic components, ASSLBs do not require a cooling system; in fact, higher temperatures can enhance conductivity, further improving the overall performance of the battery [696].

However, bipolar stacking for all-solid-state pouch cells is still in its infancy because several technical challenges remain unresolved [697]. For SPE-based ASSLBs, interface resistance between the SPE membrane and the electrodes can be mitigated through heating. However, for other inorganic SSE membranes, compression treatment is required to enhance the mechanical contact between the SSEs and the electrodes. The core distinctions in production processes between ASSLBs and traditional LIBs manifest across three phases. In front-end processes (SSE and electrode fabrication), ASSLBs exhibit superior compatibility with dry electrode technology, introducing additional steps such as dry mixing and dry coating for SSE membrane preparation, in contrast to the slurry-based wet coating methods employed in LIBs. In mid-end processes (cell assembly), the conventional winding process is replaced by a stacking process combined with printed electrode frames and isostatic pressing technology to ensure optimal interfacial contact, while entirely eliminating LE injection. In rear-end processes (formation and encapsulation), the standard formation and aging procedures evolve into high-voltage conditioning protocols, enhancing the stability of solid–solid interfaces.

7.4. Characterizations

Characterizing materials to obtain their physicochemical properties is fundamental to the development of high-performance ASSLBs. For electrode materials, the characterization methods in the field of ASSLBs are indistinguishable from those in traditional liquid-state LIBs. Therefore, this information will not be further expounded upon here, and this chapter primarily focuses on elucidating the properties of SSEs and the corresponding characterization and testing methodologies.

7.4.1. Material characterizations

Phase composition and crystal structure of ionic conductors is vital for designing new SSEs candidates and enhancing their intrinsic properties. The structure of the SSEs and their structure–property relationship could be evaluated using XRD, XPS, NMR, Raman, and XAS [698,699]. Sun et al. investigated $Li_{6.6}Ge_{0.6}Sb_{0.4}S_5I$ electrolytes and estimated the chemical stability of ASSLBs by *operando* energy dispersive X-ray diffraction (EDXRD) technique, where no significant crystalline change in the cathode or electrolyte was detected (Fig. 38a) [700]. Additionally, the stabilities of SSEs, which refer to chemical stability and thermostability, are vital for their applications. By using magic angle spinning MAS-NMR, it was revealed that $Li_{10}SnP_2S_{12}$ would decompose into Li_3PS_4 and Li_4SnS_4 due to the high thermal and mechanical energy during ball-milling [701]. Su et al. [496] achieved improved thermal stability of the FMC-ASPE membranes through the formation of hydrogen bonds, which was characterized by thermogravimetric analysis (TGA) in accompanied with ^1H NMR spectra, ensuring the steady operation under wide temperature range.

Ionic conductivity is one of the most critical features of SSEs. The development of SSEs with high ionic conductivity has been the focus of research efforts to improve ASSLBs' performance and commercial viability. EIS is applied to calculate the ionic conductivities of SSEs. There is also the calculation of the total ionic conductivity as well as differentiation between the gain boundaries, grain, and electrode impedance [702]. For novel hybrid SSEs, Zheng et al. [703] tracked Li^+ pathways within LLZO-PEO composite electrolytes by combining selective isotope labeling and Li ss-NMR. Their results confirmed that Li ions prefer to maximize the fraction of the LLZO ceramic phase and minimize that of the interface or the PEO polymer phase on their diffusion pathway. Further, fast Li^+ transport in the hybrid electrolyte with different fillers was also determined with tracer-exchange Li NMR in PEO–perovskite and PEO–Li^+ insulating oxides [704,705]. The activation energy is the barrier for ion transport in SSEs which refers to the energy required for an ion to overcome the resistance in the solid lattice structure. The fundamental stage for ion conduction is the energetically/thermally induced

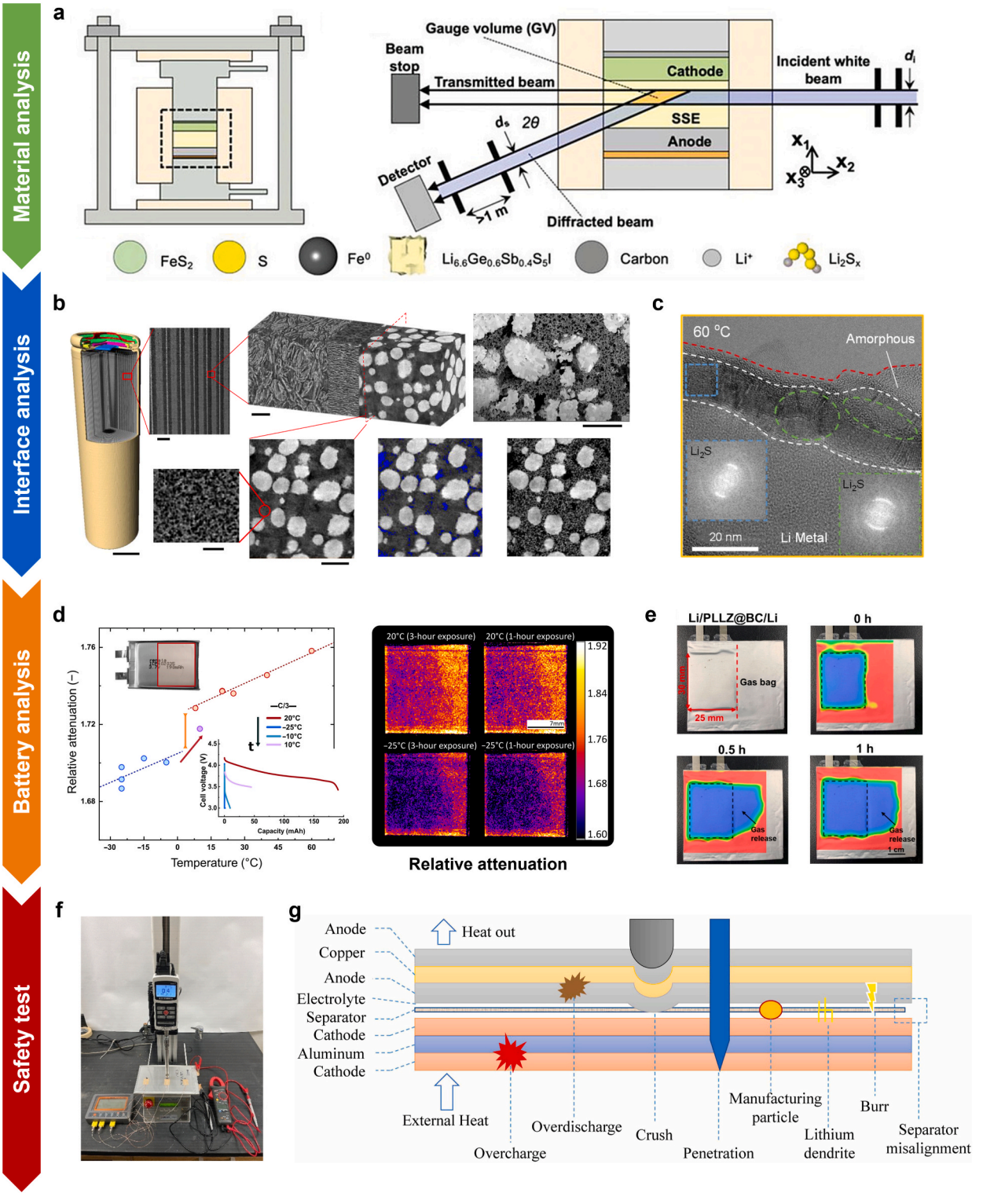

(caption on next page)

Fig. 38. Characterization techniques for SSBs: material characterization, interface characterization, cell characterization, battery safety testing. (a) EDXRD result of half-cell. Schematic of half-cell and major $Li_{6.6}Ge_{0.6}Sb_{0.4}S_5I$ peaks as a function of time in half cell at location 30 in the SSE layer. Reproduced with permission from ref. [700]. Copyright 2021, Advanced Energy Materials. (b) A typical cylindrical LIB scanned by X-ray micro-CT with a corner-cut-out showing the auxiliary components in the cell cap and the internal structure of the cell. Reproduced with permission from ref. [707]. Copyright 2020, Nature Communications. (c) Nanostructure of the interphase layer between a single Li dendrite and sulfide-based electrolyte at different temperatures. Reproduced with permission from ref. [714]. Copyright 2022, ACS Energy Letters. (d) Stability of a commercial Li–Po battery studied via the α_{rel}. Reproduced with permission from ref. [728]. Copyright 2023, Science Advances. (e) Image of the Li/PLLZ@BC/Li pouch cell and Li/PLLZ@BC/Li pouch cell picture and corresponding ultrasonic transmission images of the cell overlapped on each other after storing for 0, 0.5, and 1 h, correspondingly. Reproduced with permission from ref. [732]. Copyright 2022, ACS Energy Letters. (f) Penetration test setup and closer look of penetrating cone. Reproduced with permission from ref. [734]. Copyright 2021, Batteries. (g) Schematic of failure mechanisms of LIBs under crush condition. Reproduced with permission from ref. [735]. Copyright 2021, Renewable and Sustainable Energy Reviews.

hopping between neighboring sites in the potential barrier landscape. The ionic conductivity measurements (via EIS) as a function of temperature are applied for the calculation of the activation energy (E_a) by the Arrhenius Equation.

Ideal SSE should possess a broad ESW. The galvanostatic cycling electrochemical technique shows a stable and smooth Li^+ transport in the symmetric cells over various current densities, which is used to determine the electrode/electrolyte stability. And the best CCD value could be assessed from the voltage versus time graph with step-increased current densities. The current density distribution is outlined as the specific current density at which a battery fails when the Li dendrite propagation from the lithium metal anode spreads towards the cathode side via the SSE, resulting in a self-discharge and hence a safety problem [706]. Besides, the upper limit of the ESW could be explored using the CV method. Han et al. indicated that the ESW of LGPS SSE is determined from the CV scan of the Li|LGPS–C/LGPS|Pt cell. The findings demonstrate that LGPS reduction begins at 1.7 V and LGPS oxidation begins at 2.1 V, which correlates extremely well with the theoretical calculations [235].

7.4.2. Interface characterizations

Interfaces in ASSLBs involve many complex processes and chemical reactions, including interfacial wettability, physical contact, chemical or electrochemical reaction, ionic transport, space-charge layer, etc. In the past few years, researchers have developed many advanced techniques to probe the structural, compositional, and morphological variations occurring at the electrode–SSE interfaces that are associated with the interfacial dynamics and the battery performance.

Physical contact and wettability are imperative in developing high-performance ASSLBs. SEM offers a simple method to observe the physical contact between the active materials and SSEs [254]. To observe the internal as well as the external interfaces at 3D view, X-ray computed tomography (CT) enables high-resolution visualization to identify the underlying mechanism of the electromechanical deformation at cathode-SSE interfaces. Lu et al. conducted *in situ* X-ray CT to investigate the microstructural evolution, porosity and tortuosity variation of NCM811 electrode at incremental calendaring steps to guide the manufacturing process (Fig. 38b) [707]. Lewis et al. [708] investigated the effect of volume changes due to the reductive decomposition of $Li_{10}SnP_2S_{12}$ (LSPS) on the pellet structure via *operando* synchrotron-based CT. The decomposed interphase and voids at the Li metal/LSPS interface were clearly observed. The loss of contact that drives current constriction at the interface was quantitatively measured, indicating that the loss and reconfiguration of interfacial contact is the critical factor that causes cell failure. Besides, Hu et al. [709] conducted a stress-mapping model based on Raman spectroscopy that allowed the characterization of microscopic stress distributions. They examined the stress distribution for the garnet-based SSEs LLZTO under various processing environments, including different rates of cooling and polishing with various mesh sizes of sandpapers. The obtained 3D stress mapping discloses the area's topology under various stress positions, which can be linked to the patterns of electrolyte cracking and Li protrusion creation.

Instability of the electrode–electrolyte interface has been a serious concern for SSBs. The interfacial chemical reaction and the resulting high interfacial resistance are detrimental for ASSLBs performance. Wang et al. [710] performed *in situ* STEM-EELS observation of LCO–LiPON interface. The nanoscale spectroscopic characterization revealed the formation of a disordered interfacial phase that accumulates Li_2O and Li_2O_2 species along with the formation of rocksalt CoO after charging process, which can be attributed to the deposited cathode elements and the oxygen evolution reaction at solid–solid interfaces. The interfacial elemental interdiffusion can be characterized by the combination of FIB with HRTEM. At the Li_xCoO_2–LiPON interfaces, Li accumulation and the interdiffusion of elements was found by STEM-EELS, which can be accounted for the irreversible capacity losses at SSBs [711]. ToF-SIMS is a semi-quantitative method to detect the local enrichments of some fragments at interfaces, and the depth profiles can be reconstructed in 3D to show the spatial fragment distribution. Combining local compositional information from ToF-SIMS and complementary XPS, the degradation mechanism in the NCM622–LPSC composite of an ASSLB was directly visualized and indicated that sulfates and phosphates play an important role in the formation of an SEI at cathode interface [712]. Li metal/SSE interfaces have been characterized in detail by combining cryo-FIB and cryo-EM, which could reduce thermal effects. Cheng et al. [713] observed an 80 nm SEI at the Li metal/LiPON interface. The results showed that the SEI is a mosaic structure of Li_2O, Li_3N, and Li_3PO_4 nanocrystals embedded in an amorphous matrix. The unique multilayer mosaic SEI shields LiPON from the strong reductivity of Li metal and provides extreme stability for Li plating and stripping. Luo et al. [714] also characterized the Li metal/LPSC interface via cryo-EM. Their results indicate that the presence of numerous grain boundaries and dislocations within polycrystalline Li_2S causes a high interfacial resistance (Fig. 38c).

Interfacial ion transport is crucial for understanding solid-state electrochemical reactions. NMR has the unique ability to probe the spontaneous Li^+ exchange between different phases [715]. 2D Li^+ exchange NMR has been employed to access the spontaneous ion transport over the interface between an argyrodite SSE and a sulfide electrode, providing new insight into interfacial ion transport for

SSBs [716]. Besides, interfacial ion-transport properties are also related to 3D electrode microstructure features. With the accurate 3D reconstruction of an electrode, fine microstructural parameters (such as porosity and tortuosity) could be obtained experimentally to determine the occurrence of continuous ionic transport paths [717]. Moreover, chemomechanical fracture processes and interphase growth in LAGP SSEs can be directly visualized using lab X-ray CT. The growth of interphase with volume expansion drives large crack formation in an SSE, which plays a primary role in the increase of ion-transport impedance and electro-chemomechanical degradation [718].

Dendrite formation is another serious issue in SSBs. To unveil the underlying mechanism behind dendrite chemistries, various characterization techniques are expected to investigate fundamental aspects of metallic Li anodes, including optical microscopy (OM), SEM, TEM, scanning transmission electron microscopy (STEM) with EELS, cryo-EM, neutron-depth profiling (NDP) imaging, and CT. SEM and TEM are the most commonly used methods to visualize the physical morphology and elemental distribution of dendrite [719–721]. With the combination of the EELS technique, STEM could offer rich information from bulk phase (dendrite morphology) down to the atomic scale (dendrite microstructure) [710]. Besides, the accumulation of the deposited Li metal within the localized SSEs under high current densities could be deduced from NDP imaging, which lead to poor stripping reversibility and then eventual battery failure [722]. CT is another useful tool in investigating Li plating and stripping using symmetric cells [723]. Ning et al. [724] used synchrotron-based *in situ* CT to observe the relationship between crack formation and lithium dendrite growth within the LPSC layer. SSE spallation and cracks first formed at the edge of Li electrode with high local electric field. The transverse cracks then propagated from the spallation across the SSE layer and reached the Li-metal surface on the opposite side. Cryo-EM technology was also used to investigate the structure of lithium dendrite and SEI layer. Such cryogenic operation is of vital importance to maintain the structure features of the vulnerable samples [725]. However, a single detection technique still has limitations in characterizing the solid–solid interface. Zhang et al. [726] first utilized *in situ* EIS/relaxation time distribution (DRT) analysis combined with *in situ* AFM to reveal the different interface behaviors of LGPS and LPS. Subsequently, *in situ* AFM and *in situ* XPS were combined to reveal the morphology and chemical evolution of the interfaces and related dynamics, demonstrating the wrinkle-like morphology of the SEI and the deposition/stripping kinetics of lithium at these two interfaces. Furthermore, through *in situ* Kelvin probe force microscopy (KPFM), the lithium-ion enrichment phenomenon that occurred at the LGPS/LPS interface under the applied voltage condition was successfully captured.

By elucidating the intricate relations between interfacial behaviors and electrochemical performance, new mechanistic insights into SSB interfaces can be anticipated to provide strategies for the design of high-performance SSBs.

7.4.3. Battery characterizations

Nondestructive detection method is crucial for revealing the operational status of ASSLBs. In terms of internal Li-metal plating, Ishigaki et al. demonstrated a direct Li-metal detection technology that focuses on electromagnetic behavior. They found that internal Li-metal plating can be detected by the decrease in real part of the impedance at high-frequency. Further, they developed a battery sensor that detects and monitors the cycle-by-cycle growth of Li-metal plating [727]. Ruiz et al. [728] quantitatively and qualitatively studied the thermal runaway behavior of battery systems through time-of-flight neutron imaging (ToF-NI), which paves the way for the study of safe and stable operation of portable devices and transportation industries under various environmental conditions (Fig. 38d). Darmet et al. [729] pointed out that the propagation of thermal runaway was consisted of three key steps, i.e., ignition, propagation and ending. As revealed by high-speed X-ray radiography and heat flow measurements, the propagation of thermal runaway in an all-solid-state-battery pack (91 ms) was faster and more brutal than that in a LIB pack (507 ms). Yang et al. [730] developed a hybrid battery thermal management system for the SSB pack, and predicted the temperature, current, and SOC distributions at different cooling conditions. Their results showed that the temperatures of SSB pack could be controlled within 43 °C at 35 °C ambient temperature.

The application of ultrasonic technology is noteworthy for its high sensitivity to porosity, gas, and mechanical properties of materials, making it a suitable choice for such purposes. Deng et al. [731] employed an ultrasonic scanning technique to investigate the characteristics of pouch and prismatic LIBs, which can effectively monitor electrolyte wetting, unwetting, and dry-out processes in lithium-ion pouch cells. Besides, ultrasonic scanning images may depict side reactions and structural evolution at the interfaces, even if only a small amount of gas generation or contact loss is present. Huo et al. [732] monitored the oxidation and gassing phenomena occurring at the interface of SSE/LCO to elucidate the underlying causes of capacity degradation. Ultrasonic imaging offers valuable insights into the interfacial design of SSBs, thereby revealing crucial structural information that can enhance their performance (Fig. 38e).

7.4.4. Safety tests

The commercialization of ASSLBs necessitates rigorous adherence to continuously evolving safety standards and associated testing protocols. These frameworks ensure comprehensive validation of ASSLBs and their constituent materials against predefined safety benchmarks. While collaborative efforts between academia and industry persistently advance safety research and refine regulatory guidelines—often through iterative updates to address emerging risks. This section will focus on outlining the most prevalent testing methodologies currently employed for hazard mitigation and performance certification [733].

The overcharge test evaluates the ability of a ASSLBs to withstand an overcharge condition. The goal is to charge the cell beyond its voltage limits recommended by the manufacturer. Self-cascaded exothermic reactions occur when a cell experiences overcharge, causing massive heat generation and gas exhaustion which can lead to thermal runaway. Most battery safety standards require this test as it is the most hazardous abusive condition leading to thermal runaway. Also, it represents situations that could happen in battery safety accidents. Generally, the overcharge test consists of applying a set charging current to a fully charged cell to a set voltage limit for a defined SOC level or if thermal runaway is triggered before.

The forced discharge (or over-discharge) test is another important scenario of electrical abuse conditions. Similar to an overcharge, a forced discharged test consists of applying a load to a ASSLB beyond its voltage limits. During a forced discharge, the cell is first discharged to 0 % SOC. Then, a continuous discharge at a set current rate is applied for a period varying between 30 min and 90 min depending on the standard or if thermal runaway is triggered during the forced discharge.

The external short-circuit test is designed to evaluate the safety performance when a short circuit occurs. The main effect when connecting the cathode and anode of a cell is a high heat generation rate which can damage the safety of the ASSLB and the circuitry of device. The ESC consists of connecting the cathode and anode of a cell with a resistive load for a specific time (e.g., 10 min or 1 h) or until the device's temperature has returned to 10 °C of the ambient temperature. Some standards indicate two ESC tests: soft ESC and hard ESC. The difference lies with the external load value: $\geq$ 5 mΩ and $\leq$ 5 mΩ, respectively.

The nail penetration test is a mechanical abuse condition consisting of reproducing an internal short circuit (ISC) that may happen when a ASSLB's shell is punctured by a foreign object [734]. In such situations, a sharp steel nail of Ø3 mm is forced to pierce the center of the cell at a specific speed. The metallic nail creates a thermal and electrical bridge when piercing the separator, thus an ISC and massive heat are generated (Fig. 38f). However, several standards do not indicate nail penetration as a requirement which questions the utility of this test. several factors can influence the results of the nail penetration test such as the nail speed, the nail size and the material.

A collision (or crush test) is designed to represent a vehicle accident or any collision that may occur to the ASSLB and their casing [735]. During this test, an external load force mechanically causes the deformation of the cell and its enclosure by compressing it (Fig. 38g). To do so, the cell is placed on a flat surface and crushed using a ribbed plat or a textured tool. The test is stopped until a sudden voltage drop is reached, the cell is deformed by a certain percentage of its original thickness or a certain compression force is achieved.

The vibration test is an important test for battery manufacturers and standards because it represents what ASSLBs experience when moving. This test aims to observe the long-term vibration profiles on the ASSLBs to identify any design flaws, the durability of the system or the looseness of any contacts. In a vibration test, the cell is firmly secured to the platform of the vibration machine and a vibration profile is applied. The frequency of the signal varies with the standards from 10 Hz up to 2000 Hz for a specific duration (e.g., 90 min, 3 h, or 8 h).

The thermal heating test is used to assess the thermal stability of ASSLBs at an elevated temperature. When the temperature of a cell rises beyond its normal operating range, exothermic reactions occur inside the cells (e.g., electrolyte decomposition, cathode dissolution, anode-electrolyte interface reaction, etc.) that may lead to thermal runaway. the test consists of placing a cell inside a temperature-controlled environment for which the temperature rises sequentially in 5 °C steps with a holding time of 30 min between each step. The test stops when the maximum temperature environment is reached (e.g., 130 °C, 150 °C or 300 °C) or if the cell starts self-heating at a rate of 1 °C min^{-1} which could indicate the start of the thermal runaway process. The thermal heating test also covers another test protocol called thermal shock (or temperature cycling test). This test evaluates the cell's integrity and internal electrical connections when exposed to extreme and sudden changes in temperature. The test is conducted using a temperature profile involving rapid and extreme temperature changes. Generally, two temperature limits are selected which correspond to an extremely LT environment (e.g., −40 °C) and an extremely HT environment (e.g., 70 °C or 85 °C).

As research pivots from academic exploration to industrial validation, the limitations of isolated analytical techniques become

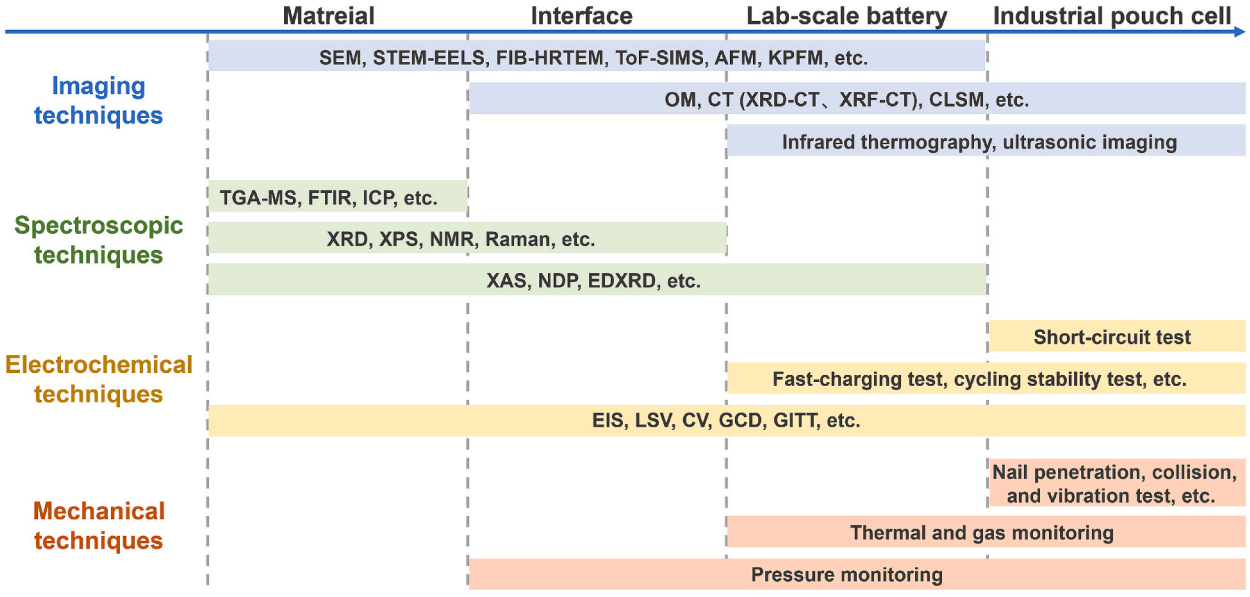

Fig. 39. Summary of cross-scale applications of imaging, spectroscopic, electrochemical, and mechanical characterization techniques.

starkly apparent across hierarchical scales. This paradigm shift necessitates integrated characterization platforms that bridge materials, interfaces, lab-scale batteries, and industrial pouch cells (Fig. 39), thereby simultaneously tracking ionic, electronic, thermal, and mechanical behaviors across scales.

7.5. Industrialization adaptability

7.5.1. Recycling and cost efficiency

Currently, research in the field of SSBs primarily focuses on the synthesis of SSEs and the optimization of their electrochemical performance. However, studies on sustainable and environmentally friendly recycling strategies for SSBs remain relatively underdeveloped. Implementing an effective recycling strategy for SSBs could enable the recovery of key materials from used batteries, facilitating their reintegration into the industrial economy. This would contribute to the shift from a linear to a circular economy and significantly advance the development of green, low-carbon, and sustainable energy storage systems. According to the upcoming battery passport, ALSSBs will be pre-classified. After classification, the same type of ALSSBs can be pre-crushed in batches and then processed using either dry or wet methods based on the SSEs [736]. At present, there are two promising methods that may achieve the "direct" recovery of electrolyte components, namely physical separation and dissolution separation. The physical separation process is usually based on the principle of separating the collector and housing components from other battery components, and this principle may also be applicable to SSB systems. For example, the density of copper/aluminum is significantly different from that of oxide cathode materials, so the density differences of different components can be used to simplify separation without affecting the material properties of each component. In different solvents, the difference in the dissolution of SSEs (such as sulfides, thiophosphates and halides) relative to the electrode material is the key to the separation effect. Therefore, such methods need to choose the solvent according to the dissolution characteristics of the SSEs. The hydrometallurgical treatment involves mechanical crushing to recover polymers and conductive salts. For oxides, mechanical separation is employed to recover active materials and electrolytes separately. In the case of sulfides, halides, or hydrides, the electrolyte is dissolved and separated for recovery in an anhydrous environment, such as a drying chamber or inert gas atmosphere. In the long term, non-destructive (or damage-reducing) separation of materials could also guide sustainable battery design. By optimizing design, existing recycling strategies may also influence the production process, such as product recycling oriented production process design [737].

The production cost of SSBs is currently significantly higher than that of liquid-based batteries, which hampers their competitiveness in large-scale commercial applications. Reducing production costs has become a critical challenge that the SSB industry must address. As most SSB concepts are still in the R&D stage, statements about future prices are highly speculative and based not only on material and processing costs, but also on corporate strategies. The current price for state-of-the-art LIBs ranges between 90 and 180 EUR kWh^{-1} and is expected to drop to as low as 45 EUR kWh^{-1} in the coming decade, according to some original equipment manufacturer announcements. However, this price should be considered a lower limit that requires optimistic developments in raw material costs, energy prices, smart fabrication technologies, and vanishing margins which are profitable only at very large production scales [738]. Crucially, the optimal performance solution identified in the laboratory is often cost-prohibitive for industrial implementation. Only by integrating cost considerations into basic research and development can bridge the gap between academia and industry. The academic community needs to introduce industrial cost accounting tools such as total cost of ownership (TCO) analysis to

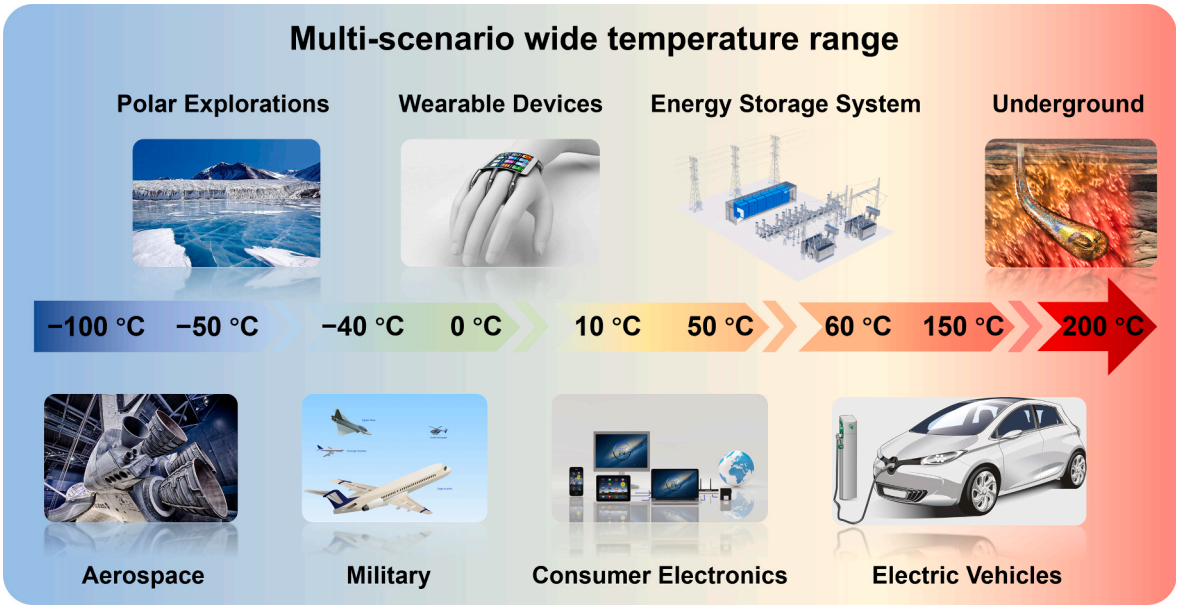

Fig. 40. Diagram of application scenarios for SSBs across wide temperature ranges.

avoid high-cost elements and processes in the material design stage. The industrial sector and universities jointly build pilot platforms to verify cost feasibility in advance. For instance, Tesla's dry-process electrode technology originated from Maxwell's academic collaboration. At the policy level, an industrial-oriented fund should be established to give priority to supporting low-cost technologies, such as the funding from the USA DOE for cobalt-free cathodes.

7.5.2. Market demand and application scenarios

The global LIBs market, valued at approximately €35 billion in 2020, is expected to experience significant growth, with projected revenues rising to €125–225 billion by 2030, driven by increasing global demand that could surpass 3 TWh annually. Long-term projections indicate a global battery demand exceeding 10 TWh per year is realistic [739].

The industrial adoption of SSBs is progressing from specialized applications toward mass-market implementation. Fig. 40 illustrates the broad temperature range of SSBs across different application scenarios. Initial commercialization has focused on micro-electronics, expanding progressively into mainstream consumer electronics including smartphones and laptops, which are sensitive to energy density improvements. This evolution is now reaching the transportation sector, where electric vehicles and aerospace applications are positioned to benefit most significantly from SSBs' superior energy and power densities. The automotive industry, in particular, has responded with substantial R&D investments targeting extended range and fast-charging capabilities, with major manufacturers like Toyota, Honda, Nissan, Ford, BMW, and Volkswagen actively developing SSB solutions for their next-generation electric vehicle platforms [740].

Furthermore, there are specific temperature tolerance requirements for batteries in other application scenarios. Such as, Medical-grade LIBs worn on sterilization equipment require operation at temperatures exceeding 120 °C. Military-grade batteries are expected to operate from −40 °C to 60 °C, electric vehicles require battery systems capable of having stable performance in both colder regions and hot desert conditions. Apart from extending the operability of conventional batteries, task-specific applications also call for energy storage at further extremes [741]. In hybrid electric vehicles, temperatures under the hood can surpass 140 °C. During underground oil and gas exploration, localized drilling temperatures can exceed 200 °C. LIBs used in turbine engines, generators, motors, as well as rocket and aerospace casings, necessitate operation at temperatures exceeding 250 °C. Besides terrestrial environments, the deep ocean and outer space can experience even more extreme cold temperatures. Hence, developing ASSLBs with outstanding wide temperature range adaptability is essential for their widespread application [742].

7.5.3. Collaboration between academia and industry

The commercialization of ASSLBs necessitates deep collaboration between academia and industry, which serves as a critical bridge connecting fundamental scientific discoveries with practical technological applications. However, significant disparities in objectives, evaluation criteria, and resource allocation have created a substantial gap between laboratory innovation and industrial implementation. While academia explores the novel materials, reaction mechanisms, and scientific issues, industry prioritizes scalability, cost-effectiveness, and real-world integration. This section highlights collaborative models and key disconnects, while proposing synergistic pathways to bridge this gap.

Currently, many companies have established partnerships with universities and research institutes to explore new materials and technologies. For instance, Toyota is collaborating with Kyoto University and other academic institutions to advance sulfide-based SSEs. In terms of technology transfer, academic breakthroughs are often licensed to industry for further development. CATL has collaborated with Tsinghua University and the Chinese Academy of Sciences to develop sulfide-based SSEs. The company has achieved energy densities exceeding 400 Wh kg^{-1} and plans to commercialize SSBs by 2025. Qing Tao Energy, a spin-off from the Chinese Academy of Sciences, focuses on SPEs. The company has established pilot production lines and is collaborating with automakers for electric vehicle applications. At Baima Lake Laboratory, collaborative technology transfer initiatives have been established with Fudan University and Nanjing University of Aeronautics and Astronautics since 2024. Researchers there identify that hydride-based SSEs exhibit substantial technological potential and promising commercialization prospects. Solid Power, in partnership with BMW and Ford, has focused on sulfide-based SSEs. The company has delivered prototype cells to automakers and aims to begin mass production by 2026. Last year, QuantumScape announced the successful development, delivery and installation of next-generation heat treatment equipment for its separator production process. This advancement enables initial separator treatment and represents a critical milestone toward delivering larger-volume samples of its first commercial product (QSE-5) in 2025. The achievement marks significant progress in the company's SSB commercialization roadmap for electric vehicle applications. ProLogium has developed oxide-based SSEs through collaborations with academic partners, resulting in its Large-Footprint Ceramic SSBs. This advancement has facilitated a strategic partnership with Germany's FEV Group to commercialize innovative SSBs for automotive applications.

Despite the progress, ASSLB industrialization remains immature, requiring collaborative solutions by the academic community and the industry. Many SSE materials developed in academic labs face difficulties in large-scale production due to high costs and complex manufacturing processes. The lack of standardized testing protocols and performance metrics hinders the comparison and optimization of SSE materials. Although successful discoveries in the laboratory are widely publicized in academic journals, start-up companies prefer to protect successful practices, making information availability for pilot-scale prototyping limited [743]. Academic research prioritizes "peak performance metrics" such as breakthroughs in single parameters, while industry requires "comprehensive balancing" of factors including cost ($< \$100$ kWh^{-1}) and production speed (> 20 m min^{-1} winding rate). For instance, sulfide electrolytes demonstrate excellent performance in 1 cm^2 test cells but exhibit exponential growth of interfacial side reactions when scaled to Ah-level batteries. Laboratory evaluations typically employ symmetric cells with low-loading electrodes (< 2 mAh cm^{-2}), whereas industrial standards demand rigorous conditions (> 4 mAh cm^{-2} loading density, > 80 % capacity retention after 1000 cycles). This discrepancy renders much academic data non-comparable or non-representative for industrial applications. Current

mainstream sulfide-based SSEs, despite achieving LE-comparable ionic conductivity (10 mS cm^{-1}), suffer from extreme chemical instability. Exposure to moisture/oxygen generates toxic H_2S, necessitating oxygen-free production environments. Furthermore, critical rare metals (Ge, Zr) maintain prohibitively high prices, sulfide electrolyte costs reached \$1000 kg^{-1} in 2025, approximately 100 conventional LEs. From process engineering perspectives, academia typically employs energy-intensive methods such as LLZO sintering ($>$ 1000 °C) and inert-atmosphere glovebox handling, accepting low yields ($<$ 60 %) for small-area samples (1 cm^2 ALD-coated specimens). In contrast, industrial production demands ambient/LT processes (e.g., polymer electrolyte coating $<$ 100 °C) with stringent requirements for high yields ($>$ 95 %) and production-compatible speeds ($>$ 20 m min^{-1} dry electrode calendaring). The scale-up challenge manifests starkly when transitioning from lab-scale equipment (ball mills processing $<$ 100 g batches) to industrial manufacturing, where equipment investments must remain below \$100 M GWh^{-1} (liquid battery benchmark) a threshold exceeded by advanced processes like LLZO microwave sintering ($>$ \$300 M GWh^{-1}) that must simultaneously address material uniformity issues. Crucially, academic studies frequently overlook hidden cost factors including environmental control systems and end-of-life processing, while industrial implementations must incorporate full lifecycle cost accounting (including disassembly/recycling) and comply with stringent regulations such as EU REACH H_2S emission limits, creating fundamental disparities in technology evaluation metrics between research and commercialization environments. To address challenges in ASSLB development, standardized protocols should be established through academia-industry consensus, accompanied by integrated research platforms enabling synergistic collaboration across fundamental and applied research. Additionally, systematic knowledge sharing, robust collaborative networks, increased funding, and targeted policy incentives are essential to foster innovation, eliminate redundant efforts, and accelerate SSB industrialization.

8. Conclusions and perspectives

SSEs are emerging as the cornerstone of next-generation lithium battery technology due to their superior safety and high energy density potential, positioning them to replace LEs. This review systematically examines recent academic breakthroughs and industrialization progress in SSEs. By analyzing the performance characteristics, modification strategies, fabrication processes, and development prospects of five major types of SSEs—oxide-based, sulfide-based, halide-based, hydride-based, and polymer-based—this study provides scientific insights for developing commercially applicable SSEs for ASSLBs.

In material innovation, significant advancements have enhanced ionic conductivity. Common strategies include constructing low-energy-barrier ion migration pathways through lattice doping to introduce defects, designing 3D transport networks using porous materials, and creating additional ion conduction channels via multi-electrolyte composites. Implementing these approaches requires coupling advanced characterization techniques (e.g., *in situ* CT, ss-NMR) with computational simulations (e.g., AIMD, DFT) to probe ion transport mechanisms. Targeted solutions address application-specific bottlenecks: the brittleness of oxide-based SSEs is mitigated through organic composites, while humidity sensitivity is managed via elemental doping and grain boundary engineering. Sulfide-based SSEs achieve widened ESWs through oxygen doping or core–shell structures, with air instability alleviated by soft-acid cation substitution or hydrophobic coatings. The stability of halide-based SSEs at electrodes is enhanced through fluorine doping (cathode side) or inert central metal ions (anode side). The limitations of hydride-based SSEs in CCD are optimized via ligand complexation, whereas the thermal and mechanical properties of SPEs are reinforced with inorganic fillers. Notably, nitride-based electrolytes like Li_3N and LiPON demonstrate exceptional lithium metal compatibility. Machine learning and big data analytics are accelerating the efficient development of novel SSEs.

Interfacial engineering employs *in situ* construction or artificial introduction of functional interlayers to enhance electrode–electrolyte compatibility, suppress dendrite growth, and optimize ion transport. Specifically, flexible buffer layers and dynamically adaptive conformal interfaces address poor solid–solid physical contact by accommodating electrode volume changes. At the anode, constructing inorganic-rich SEI layers (e.g., LiF/Li_3N/LiH) blocks electron tunneling and homogenizes lithium deposition. The cathode side utilizes MIECI to regulate ion/electron distribution while resisting electrochemical oxidation. For air-sensitive materials like sulfides, hydrophobic/oxygen-blocking interfaces are particularly critical. Multilayer electrolyte architectures can synergistically improve electrode compatibility, though interlayer side reactions must be prevented. Advanced characterization techniques such as cryo-EM, *in situ* X-ray CT, NPD and ToF-SIMS provide essential insights into interfacial behavior by enabling real-time monitoring of reactions and contact status. Synergistic integration of interfacial engineering with high-capacity electrodes will propel ASSLB energy density beyond 500 Wh kg^{-1}.

Industrial-scale deployment of SSE-based ASSLBs hinges on overcoming manufacturing bottlenecks. For large-area, high-conductivity SSE thin films, wet processing enables simplicity and scalability but suffers from solvent toxicity, while dry processing offers cost advantages and higher ionic conductivity via solvent-free operation yet faces challenges in thickness control. High-precision 3D printing enables customized ultrathin SSEs but remains constrained by equipment costs. Crucially, ASSLBs require external pressure to maintain stable solid–solid interfacial contact. MP governs electrode porosity, AP ensures interfacial intimacy, and OP impacts cycling stability. Mechano-electrochemical dynamic compensation mechanisms are emerging as vital strategies for low-pressure operation, reducing industrial implementation barriers. Among stacking technologies, bipolar stacking enhances voltage through series-connected cells while simplifying packaging—though still in early industrialization stages.

Advancing commercialization demands interdisciplinary collaboration across materials science, electrochemistry, engineering, and computer science. Academia must continue delivering novel material systems and fundamental mechanisms, while industry focuses on process scaling and cost control. Deep integration of these domains is essential for accelerating laboratory-to-factory translation. Concurrently, establishing ASSLB performance standards, testing protocols, and safety regulations is critical for coordinated progress across research, development, and production.

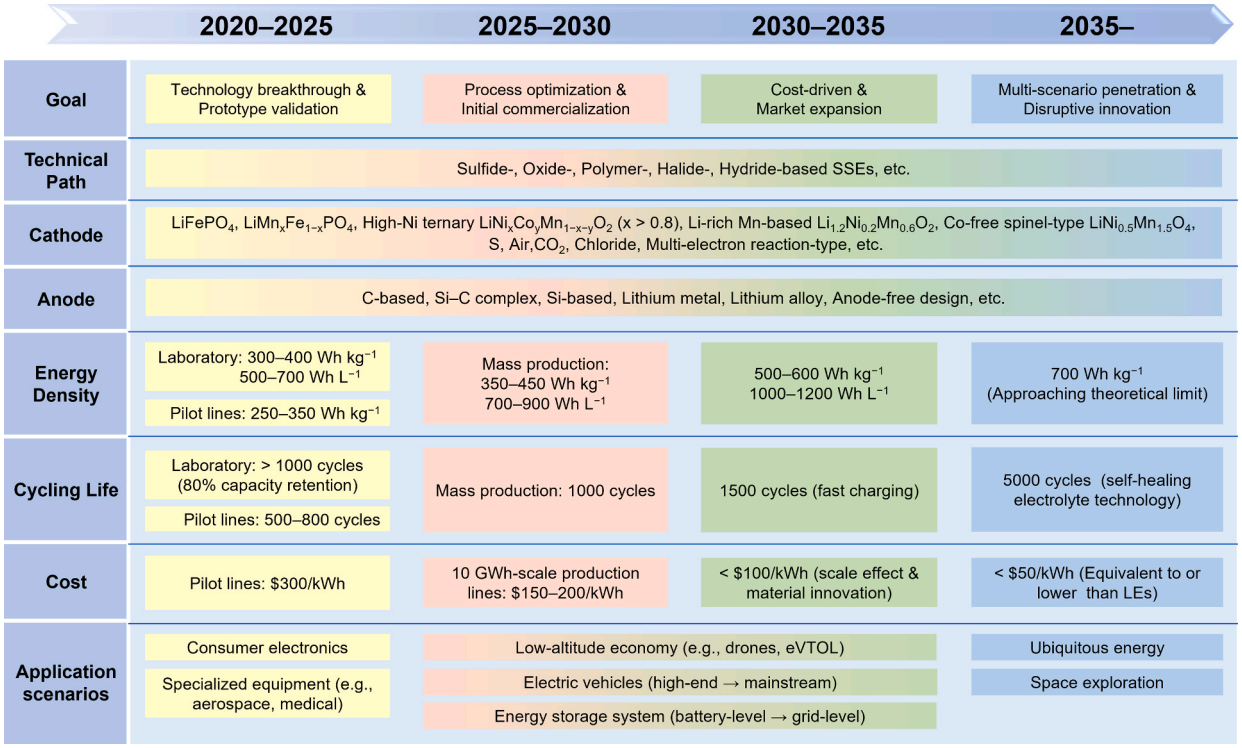

Fig. 41. The industrialization roadmap for ASSLBs.

The commercialization of ASSLB technology constitutes both a transformative advancement in energy storage and a critical strategic imperative within the global energy transition. Current technology roadmaps reveal a diversified landscape. Polymer, sulfide, and oxide systems dominate development efforts, halide-based SSEs are entering pilot-scale production, while hydride-based SSEs demonstrate significant potential for high-energy-density applications owing to their inherent lithium stability. A schematic assessment of SSE industrialization progress is presented in Fig. 41. Positioned at a critical juncture of SSE technological advancement, this review synthesizes cutting-edge research with industrial-scale development pathways to inform academic innovation and guide strategic industrial planning, thereby accelerating the clean energy transition.

CRediT authorship contribution statement

Qing Qiao: Writing – review & editing, Writing – original draft, Visualization, Methodology, Investigation, Conceptualization. **Yingxue Li:** Writing – review & editing, Writing – original draft, Visualization, Investigation. **Chang Song:** Writing – original draft, Investigation. **Mariyam Niyaz:** Writing – original draft, Investigation. **Yang Zhang:** Writing – original draft, Investigation. **Songqiang Zhu:** Writing – review & editing, Resources, Formal analysis. **Tengfei Zhang:** Writing – review & editing, Supervision, Funding acquisition, Conceptualization. **Weiming Teng:** Writing – review & editing, Supervision, Methodology, Funding acquisition. **Hongge Pan:** Writing – review & editing, Supervision, Methodology, Funding acquisition. **Xuebin Yu:** Writing – review & editing, Supervision, Resources, Funding acquisition, Formal analysis, Conceptualization.

Declaration of competing interest

The authors declare that they have no known competing financial interests or personal relationships that could have appeared to influence the work reported in this paper.

Acknowledgements

This work was partially supported by the National Key R&D Program of China (No. 2023YFB2504000), the Innovation Program of Shanghai Municipal Education Commission (No. 2025GDZKZD01), and the Key R&D Program of Zhejiang (No. 2024SSYS0062).

Data availability

No data was used for the research described in the article.

References

[1] Zeng X, Li M, Abd El-Hady D, Alshitari W, Al-Bogami AS, Lu J, et al. Commercialization of Lithium Battery Technologies for Electric Vehicles. Adv Energy Mater 2019;9:1900161. https://doi.org/10.1002/aenm.201900161.

[2] Zhang H, Chen P, Xia H, Xu G, Wang Y, Zhang T, et al. An integrated self-healing anode assembled *via* dynamic encapsulation of liquid metal with a 3D $Ti_3C_2T_x$ network for enhanced lithium storage. Energy Environ Sci 2022;15:5240–50. https://doi.org/10.1039/D2EE02147A.

[3] Guo M, Yuan C, Zhang T, Yu X. Solid-state electrolytes for rechargeable magnesium-ion batteries: from structure to mechanism. Small 2022;18:2106981. https://doi.org/10.1002/smll.202106981.

[4] Yu Y, Wang J, Qin Z, Lv Y, Pei Q, Chen Tan K, et al. Sodium Carbazolide and Derivatives as Solid-State Electrolytes for Sodium-Ion Batteries. Angew Chem Int Ed 2023;62:e202302679. https://doi.org/10.1002/anie.202302679.

[5] Fan X, Wang C. High-voltage liquid electrolytes for Li batteries: progress and perspectives. Chem Soc Rev 2021;50:10486–566. https://doi.org/10.1039/d1cs00450f.

[6] Du H, Wang Y, Kang Y, Zhao Y, Tian Y, Wang X, et al. Side reactions/changes in lithium-ion batteries: mechanisms and strategies for creating safer and better batteries. Adv Mater 2024;36:2401482. https://doi.org/10.1002/adma.202401482.

[7] Manthiram A, Yu X, Wang S. Lithium battery chemistries enabled by solid-state electrolytes. Nat Rev Mater 2017;2:16103. https://doi.org/10.1038/natrevmats.2016.103.

[8] Zheng Y, Yao Y, Ou J, Li M, Luo D, Dou H, et al. A review of composite solid-state electrolytes for lithium batteries: fundamentals, key materials and advanced structures. Chem Soc Rev 2020;49:8790–839. https://doi.org/10.1039/D0CS00305K.

[9] Zhao Q, Stalin S, Zhao C-Z, Archer LA. Designing solid-state electrolytes for safe, energy-dense batteries. Nat Rev Mater 2020;5:229–52. https://doi.org/10.1038/s41578-019-0165-5.

[10] Zhang Z, Wang X, Li X, Zhao J, Liu G, Yu W, et al. Review on composite solid electrolytes for solid-state lithium-ion batteries. Mater Today Sustainability 2023;21:100316. https://doi.org/10.1016/j.mtsust.2023.100316.

[11] Cao D, Sun X, Li Q, Natan A, Xiang P, Zhu H. Lithium dendrite in all-solid-state batteries: growth mechanisms, suppression strategies, and characterizations. Matter 2020;3:57–94. https://doi.org/10.1016/j.matt.2020.03.015.

[12] Famprikis T, Canepa P, Dawson JA, Islam MS, Masquelier C. Fundamentals of inorganic solid-state electrolytes for batteries. Nat Mater 2019;18:1278–91. https://doi.org/10.1038/s41563-019-0431-3.

[13] Janek J, Zeier WG. Challenges in speeding up solid-state battery development. Nat Energy 2023;8:230–40. https://doi.org/10.1038/s41560-023-01208-9.

[14] Banerjee A, Wang X, Fang C, Wu EA, Meng YS. Interfaces and Interphases in All-Solid-State Batteries with Inorganic Solid Electrolytes. Chem Rev 2020;120:6878–933. https://doi.org/10.1021/acs.chemrev.0c00101.

[15] Yang X, Yin Q, Wang C, Doyle-Davis K, Sun X, Li X. Towards practically accessible high-voltage solid-state lithium batteries: from fundamental understanding to engineering design. Prog Mater Sci 2023;140:101193. https://doi.org/10.1016/j.pmatsci.2023.101193.

[16] Wu D, Chen L, Li H, Wu F. Solid-state lithium batteries-from fundamental research to industrial progress. Prog Mater Sci 2023;139:101182. https://doi.org/10.1016/j.pmatsci.2023.101182.

[17] Sand SC, Rupp JLM, Yildiz B. A critical review on Li-ion transport, chemistry and structure of ceramic–polymer composite electrolytes for solid state batteries. Chem Soc Rev 2025;54:178–200. https://doi.org/10.1039/D4CS00214H.

[18] Zhang T, He W, Zhang W, Wang T, Li P, Sun Z, et al. Designing composite solid-state electrolytes for high performance lithium ion or lithium metal batteries. Chem Sci 2020;11:8686–707. https://doi.org/10.1039/D0SC03121F.

[19] Hull S. Superionics: crystal structures and conduction processes. Rep Prog Phys 2004;67:1233. https://doi.org/10.1088/0034-4885/67/7/R05.

[20] Tubandt C, Lorenz E. Molekularzustand und elektrisches Leitvermögen kristallisierter Salze. Z Phys Chem 1914;87U:513–42. https://doi.org/10.1515/zpch-1914-8737.

[21] Fan X, Zhong C, Liu J, Ding J, Deng Y, Han X, et al. Opportunities of flexible and Portable Electrochemical Devices for Energy Storage: Expanding the Spotlight onto Semi-solid/Solid Electrolytes. Chem Rev 2022;122:17155–239. https://doi.org/10.1021/acs.chemrev.2c00196.

[22] Takahashi T, Yamamoto O. The $Ag/Ag_3SI/I_2$ solid-electrolyte cell. Electrochim Acta 1966;11:779–89. https://doi.org/10.1016/0013-4686(66)87055-X.

[23] Yung-Fang YY, Kummer JT. Ion exchange properties of and rates of ionic diffusion in beta-alumina. J Inorg Nucl Chem 1967;29:2453–75. https://doi.org/10.1016/0022-1902(67)80301-4.

[24] Vu TT, Cheon HJ, Shin SY, Jeong G, Wi E, Chang M. Hybrid electrolytes for solid-state lithium batteries: challenges, progress, and prospects. Energy Storage Mater 2023;61:102876. https://doi.org/10.1016/j.ensm.2023.102876.

[25] Zhang H, Li C, Eshetu GG, Laruelle S, Grugeon S, Zaghib K, et al. From Solid-solution Electrodes and the Rocking-Chair Concept to Today's Batteries. Angew Chem Int Ed 2020;59:534–8. https://doi.org/10.1002/anie.201913923.

[26] Fenton DE, Parker JM, Wright PV. Complexes of alkali metal ions with poly(ethylene oxide). Polymer 1973;14:589. https://doi.org/10.1016/0032-3861(73)90146-8.

[27] Armand M, Chabagno J, Duclot M. Poly (ethylene oxide) is a medium capable of dissolving salt to form a conductive polymer. Scotland: St Andrews; 1978.

[28] Goodenough JB, Hong HYP, Kafalas JA. Fast Na^+-ion transport in skeleton structures. Mater Res Bull 1976;11:203–20. https://doi.org/10.1016/0025-5408(76)90077-5.

[29] Li C, Li R, Liu K, Si R, Zhang Z, Hu Y-S. NaSICON: a promising solid electrolyte for solid-state sodium batteries. Interdiscip Mater 2022;1:396–416. https://doi.org/10.1002/idm2.12044.

[30] Aono H, Imanaka N, Adachi G-y. High Li^+ conducting ceramics. Acc Chem Res 1994;27:265–70. https://doi.org/10.1021/ar00045a002.

[31] Fu J. Fast Li^+ ion conducting glass-ceramics in the system Li_2O–Al_2O_3–GeO_2–P_2O_5. Solid State Ion 1997;104:191–4. https://doi.org/10.1016/S0167-2738(97)00434-7.

[32] Ribes M, Barrau B, Souquet JL. Sulfide glasses: Glass forming region, structure and ionic conduction of glasses in Na_2S-XS_2 (X=Si; Ge), Na_2S-P_2S_5 and Li_2S-GeS_2 systems. J Non Cryst Solids 1980;38–39:271–6. https://doi.org/10.1016/0022-3093(80)90430-5.

[33] Kennedy JH, Sahami S, Shea SW, Zhang Z. Preparation and conductivity measurements of SiS_2-Li_2S glasses doped with LiBr and LiCl. Solid State Ion 1986;18–19:368–71. https://doi.org/10.1016/0167-2738(86)90142-6.

[34] Mercier R, Malugani J-P, Fahys B, Robert G. Superionic conduction in Li_2S - P_2S_5 - LiI - glasses. Solid State Ion 1981;5:663–6. https://doi.org/10.1016/0167-2738(81)90341-6.

[35] Liu H, Liang Y, Wang C, Li D, Yan X, Nan C-W, et al. Priority and Prospect of Sulfide-based Solid-Electrolyte Membrane. Adv Mater 2023;35:2206013. https://doi.org/10.1002/adma.202206013.

[36] Coetzer J. A new high energy density battery system. J Power Sources 1986;18:377–80. https://doi.org/10.1016/0378-7753(86)80093-3.

[37] Bates J, Dudney N, Gruzalski G, Zuhr R, Choudhury A, Luck C, et al. Electrical properties of amorphous lithium electrolyte thin films. Solid State Ion 1992;53:647–54. https://doi.org/10.1016/0167-2738(92)90442-R.

[38] Inaguma Y, Liquan C, Itoh M, Nakamura T, Uchida T, Ikuta H, et al. High ionic conductivity in lithium lanthanum titanate. Solid State Commun 1993;86:689–93. https://doi.org/10.1016/0038-1098(93)90841-A.

[39] Thangadurai V, Kaack H, Weppner WJF. Novel Fast Lithium Ion Conduction in Garnet-Type $Li_5La_3M_2O_{12}$ (M = Nb, Ta). J Am Ceram Soc 2004;86:437–40. https://doi.org/10.1111/j.1151-2916.2003.tb03318.x.

[40] Kanno R, Maruyama M. Lithium ionic conductor thio-LISICON-: the Li_2S-GeS_2-P_2S_5 system. J Electrochem Soc 2001;148:A742–6. https://doi.org/10.1149/1.1379028.

[41] Kamaya N, Homma K, Yamakawa Y, Hirayama M, Kanno R, Yonemura M, et al. A lithium superionic conductor. Nat Mater 2011;10:682–6. https://doi.org/10.1038/nmat3066.

[42] Matsuo M, Nakamori Y, Orimo S-i, Maekawa H, Takamura H. Lithium superionic conduction in lithium borohydride accompanied by structural transition. Appl Phys Lett 2007;91:224103. https://doi.org/10.1063/1.2817934.

[43] Zhang T, Shao Y, Zhang X, Huang Y, Wang S, Zhou W, et al. Fast Lithium Ionic Conductivity in complex Hydride-Sulfide Electrolytes by double Anions Substitution. Small Methods 2021;5:2100609. https://doi.org/10.1002/smtd.202100609.

[44] Liu H, Ren Z, Zhang X, Hu J, Gao M, Pan H, et al. Incorporation of Ammonia Borane groups in the Lithium Borohydride Structure Enables Ultrafast Lithium Ion Conductivity at Room Temperature for Solid-State Batteries. Chem Mater 2020;32:671–8. https://doi.org/10.1021/acs.chemmater.9b03188.

[45] Grinderslev JB, Skov LN, Andreasen JG, Ghorwal S, Skibsted J, Jensen TR. Methylamine Lithium Borohydride as Electrolyte for All-Solid-State Batteries. Angew Chem Int Ed 2022;61:e202203484. https://doi.org/10.1002/anie.202203484.

[46] Wei Y, Yang Y, Chen Z, Gao P, Ma Q, Gao M, et al. In-Situ-Generated Electron-Blocking LiH Enabling an Unprecedented critical Current Density of over 15 mA cm^{-2} for Solid-State Hydride Electrolytes. Adv Mater 2023;35:2304285. https://doi.org/10.1002/adma.202304285.

[47] Wei Y, Li Z, Chen Z, Gao P, Gao M, Yan C, et al. A wide temperature 10 V solid-state electrolyte with a critical current density of over 20 mA cm^{-2}. Energy Environ Sci 2023;16:4679–92. https://doi.org/10.1039/D3EE02301J.

[48] Lv Y-T, Zhang T-F, Hu Z-T, Xia G-L, Huang Z-Y, Liu Z-H, et al. High critical current density in $Li_{6.4}La_3Zr_{1.4}Ta_{0.6}O_{12}$ electrolyte via interfacial engineering with complex hydride. Rare Met 2024;43:692–701. https://doi.org/10.1007/s12598-023-02479-7.

[49] Gao Y, Sun S, Zhang X, Liu Y, Hu J, Huang Z, et al. Amorphous Dual-Layer Coating: Enabling High Li-Ion Conductivity of Non-Sintered Garnet-Type Solid Electrolyte. Adv Funct Mater 2021;31:2009692. https://doi.org/10.1002/adfm.202009692.

[50] Zhang X, Zhang T, Shao Y, Cao H, Liu Z, Wang S, et al. Composite Electrolytes based on Poly(Ethylene Oxide) and Lithium Borohydrides for All-Solid-State Lithium–Sulfur Batteries. ACS Sustain Chem Eng 2021;9:5396–404. https://doi.org/10.1021/acssuschemeng.1c00381.

[51] Shan C, Wang R, Zhang X, Li L, Sun W, Gao M, et al. Remarkably improved ionic conductivity and lithium metal compatibility of LLZTO-$Li_4(BH_4)_3I$ composite solid-state electrolyte. J Alloy Compd 2024;980:173554. https://doi.org/10.1016/j.jallcom.2024.173554.

[52] Maekawa H, Matsuo M, Takamura H, Ando M, Noda Y, Karahashi T, et al. Halide-Stabilized $LiBH_4$, a Room-Temperature Lithium Fast-Ion Conductor. J Am Chem Soc 2009;131:894–5. https://doi.org/10.1021/ja807392k.

[53] Pitt MP, Paskevicius M, Brown DH, Sheppard DA, Buckley CE. Thermal stability of $Li_2B_{12}H_{12}$ and its role in the decomposition of $LiBH_4$. J Am Chem Soc 2013;135:6930–41. https://doi.org/10.1021/ja400131b.

[54] Zhang T, Wang Y, Song T, Miyaoka H, Shinzato K, Miyaoka H, et al. Ammonia, a Switch for Controlling High Ionic Conductivity in Lithium Borohydride Ammoniates. Joule 2018;2:1522–33. https://doi.org/10.1016/j.joule.2018.04.015.

[55] Gao P, Ju S, Liu Z, Xia G, Sun D, Yu X. Metal Hydrides with In Situ built Electron/Ion Dual-Conductive Framework for Stable All-Solid-State Li-Ion Batteries. ACS Nano 2022;16:8040–50. https://doi.org/10.1021/acsnano.2c01038.

[56] Zhang X, Lou Z, Gao M, Pan H, Liu Y. Metal Hydrides for Advanced Hydrogen/Lithium Storage and Ionic Conduction applications. Acc Mater Res 2024;5:371–84. https://doi.org/10.1021/accountsmr.3c00267.

[57] Lv Y, Zhang X, Chen W, Ju S, Liu Z, Xia G, et al. Ion diffusion, and hysteresis of magnesium hydride conversion electrode materials. J Mater Sci Technol 2023;155:47–53. https://doi.org/10.1016/j.jmst.2023.01.028.

[58] Zhong S, Ju S, Shao Y, Chen W, Zhang T, Huang Y, et al. Magnesium hydride nanoparticles anchored on MXene sheets as high capacity anode for lithium-ion batteries. J Energy Chem 2021;62:431–9. https://doi.org/10.1016/j.jechem.2021.03.049.

[59] Gao P, Ju S, Huang Y, Xia G, Sun D, Yu X. Porous Magnesium Hydride Nanoparticles Uniformly Coated by Mg-based Composites toward Advanced Lithium Storage Performance. Small Struct 2024;5:2300365. https://doi.org/10.1002/sstr.202300365.

[60] Huang Y, Gao P, Zhang T, Zhang X, Xia G, Fang F, et al. An Ultra-Stable Electrode-Solid Electrolyte Composite for High-Performance All-Solid-State Li-Ion Batteries. Small 2023;19:2207210. https://doi.org/10.1002/smll.202207210.

[61] Guo M, Yuan C, Xu T, Zhong S, Wang W, Zou T, et al. In Situ built Nanoconfined TiO_2 Particles in Robust-Flexible MXene@rGO Conductive Framework Enabling High-Performance Hybrid Magnesium–Sulfur Batteries. Adv Energy Mater 2023;13:2300417. https://doi.org/10.1002/aenm.202300417.

[62] Asano T, Sakai A, Ouchi S, Sakaida M, Miyazaki A, Hasegawa S. Solid Halide Electrolytes with High Lithium-Ion Conductivity for Application in 4 V Class Bulk-Type All-Solid-State Batteries. Adv Mater 2018;30:1803075. https://doi.org/10.1002/adma.201803075.

[63] Li X, Liang J, Luo J, Norouzi Banis M, Wang C, Li W, et al. Air-stable Li_3InCl_6 electrolyte with high voltage compatibility for all-solid-state batteries. Energy Environ Sci 2019;12:2665–71. https://doi.org/10.1039/c9ee02311a.

[64] Li X, Liang J, Chen N, Luo J, Adair KR, Wang C, et al. Water-Mediated Synthesis of a Superionic Halide Solid Electrolyte. Angew Chem Int Ed 2019;58:16427–32. https://doi.org/10.1002/anie.201909805.

[65] Ding F, Doi A, Ogawa T, Ubukata H, Zhu T, Kato D, et al. Anionic Sublattices in Halide Solid Electrolytes: a Case Study with the High-pressure phase of Li_3ScCl_6. Angew Chem Int Ed 2024;63:e202401779. https://doi.org/10.1002/anie.202401779.

[66] Patel SV, Lacivita V, Liu H, Truong E, Jin Y, Wang E, et al. Charge-clustering induced fast ion conduction in 2LiX-GaF_3: a strategy for electrolyte design. Sci Adv 2023;9:eadj9930. https://doi.org/10.1126/sciadv.adj9930.

[67] Zhang H, Armand M, Rojo T. Editors' Choice—Review—Innovative Polymeric Materials for Better Rechargeable Batteries: Strategies from CIC Energigune. J Electrochem Soc 2019;166:A679–86. https://doi.org/10.1149/2.0811904jes.

[68] Liu H, Cheng X-B, Huang J-Q, Yuan H, Lu Y, Yan C, et al. Controlling Dendrite Growth in Solid-State Electrolytes. ACS Energy Lett 2020;5:833–43. https://doi.org/10.1021/acsenergylett.9b02660.

[69] Samson AJ, Hofstetter K, Bag S, Thangadurai V. A bird's-eye view of Li-stuffed garnet-type $Li_7La_3Zr_2O_{12}$ ceramic electrolytes for advanced all-solid-state Li batteries. Energy Environ Sci 2019;12:2957–75. https://doi.org/10.1039/c9ee01548e.

[70] Murugan R, Thangadurai V, Weppner W. Fast Lithium Ion Conduction in Garnet-Type $Li_7La_3Zr_2O_{12}$. Angew Chem Int Ed 2007;46:7778–81. https://doi.org/10.1002/anie.200701144.

[71] Awaka J, Kijima N, Hayakawa H, Akimoto J. Synthesis and structure analysis of tetragonal $Li_7La_3Zr_2O_{12}$ with the garnet-related type structure. J Solid State Chem 2009;182:2046–52. https://doi.org/10.1016/j.jssc.2009.05.020.

[72] Awaka J, Takashima A, Kataoka K, Kijima N, Idemoto Y, Akimoto J. Crystal Structure of Fast Lithium-ion-conducting Cubic $Li_7La_3Zr_2O_{12}$. Chem Lett 2011;40:60–2. https://doi.org/10.1246/cl.2011.60.

[73] Tsai C-L, Ma Q, Dellen C, Lobe S, Vondahlen F, Windmüller A, et al. A garnet structure-based all-solid-state Li battery without interface modification: resolving incompatibility issues on positive electrodes. Sustainable Energy Fuels 2019;3:280–91. https://doi.org/10.1039/c8se00436f.

[74] Chen Y, Rangasamy E, dela Cruz CR, Liang C, An K. A study of suppressed formation of low-conductivity phases in doped $Li_7La_3Zr_2O_{12}$ garnets by *in situ* neutron diffraction. J Mater Chem A 2015;3:22868–76. https://doi.org/10.1039/c5ta04902d.

[75] Geiger CA, Alekseev E, Lazic B, Fisch M, Armbruster T, Langner R, et al. Crystal Chemistry and Stability of "$Li_7La_3Zr_2O_{12}$" Garnet: a Fast Lithium-Ion Conductor. Inorg Chem 2010;50:1089–97. https://doi.org/10.1021/ic101914e.

[76] Xia W, Xu B, Duan H, Guo Y, Kang H, Li H, et al. Ionic Conductivity and Air Stability of Al-Doped $Li_7La_3Zr_2O_{12}$ Sintered in Alumina and Pt Crucibles. ACS Appl Mater Interfaces 2016;8:5335–42. https://doi.org/10.1021/acsami.5b12186.

[77] Qin S, Zhu X, Jiang Y, Ling Me HZ, Zhu J. Growth of self-textured Ga^{3+}-substituted $Li_7La_3Zr_2O_{12}$ ceramics by solid state reaction and their significant enhancement in ionic conductivity. Appl Phys Lett 2018;112:113901. https://doi.org/10.1063/1.5019179.

[78] Zhu Y, Connell JG, Tepavcevic S, Zapol P, Garcia-Mendez R, Taylor NJ, et al. Dopant-Dependent Stability of Garnet Solid Electrolyte Interfaces with Lithium Metal. Adv Energy Mater 2019;9:1803440. https://doi.org/10.1002/aenm.201803440.

[79] Xiang W, Ma R, Liu X, Kong X, Shen S, Wang L, et al. Rapid Li compensation toward highly conductive solid state electrolyte film. Nano Energy 2023;116:108816. https://doi.org/10.1016/j.nanoen.2023.108816.

[80] Rettenwander D, Wagner R, Reyer A, Bonta M, Cheng L, Doeff MM, et al. Interface instability of Fe-stabilized $Li_7La_3Zr_2O_{12}$ versus Li metal. J Phys Chem C 2018;122:3780–5. https://doi.org/10.1021/acs.jpcc.7b12387.

[81] Jung S-K, Gwon H, Kim H, Yoon G, Shin D, Hong J, et al. Unlocking the hidden chemical space in cubic-phase garnet solid electrolyte for efficient quasi-all-solid-state lithium batteries. Nat Commun 2022;13:7638. https://doi.org/10.1038/s41467-022-35287-1.

[82] Wang S, Wen X, Huang Z, Xu H, Fan F, Wang X, et al. High-Entropy Strategy Flattening Lithium Ion Migration Energy Landscape to Enhance the Conductivity of Garnet-Type Solid-State Electrolytes. Adv Funct Mater 2025;35:2416389. https://doi.org/10.1002/adfm.202416389.

[83] Zhao Y, Liu Z, Xu J, Zhang T, Zhang F, Zhang X. Synthesis and characterization of a new perovskite-type solid-state electrolyte of $Na_{1/3}La_{1/3}Sr_{1/3}ZrO_3$ for all-solid-state sodium-ion batteries. J Alloy Compd 2019;783:219–25. https://doi.org/10.1016/j.jallcom.2018.12.289.

[84] Paengson S, Pilasuta P, Mori D, Seetawan T. Effect of Sr and Ta co-substitution on microstructure and ionic conductivity of cubic-$Li_{0.5}La_{0.5}TiO_3$ electrolyte for applications in Li batteries. J Alloy Compd 2024;979:173512. https://doi.org/10.1016/j.jallcom.2024.173512.

[85] Ma C, Chen K, Liang C, Nan C-W, Ishikawa R, More K, et al. Atomic-scale origin of the large grain-boundary resistance in perovskite Li-ion-conducting solid electrolytes. Energy Environ Sci 2014;7:1638–42. https://doi.org/10.1039/C4EE00382A.

[86] Yan S, Yim C-H, Pankov V, Bauer M, Baranova E, Weck A, et al. Perovskite Solid-State Electrolytes for Lithium Metal Batteries. Batteries 2021;7:75. https://doi.org/10.3390/batteries7040075.

[87] Chambers MS, Chen J, Sacci RL, McAuliffe RD, Sun W, Veith GM. Memory effect on the Synthesis of Perovskite-Type Li-Ion Conductor $Li_xLa_{2/3-x/3}TiO_3$ (LLTO). Chem Mater 2024;36:1197–213. https://doi.org/10.1021/acs.chemmater.3c01928.

[88] Gao C, Zhou X, Yu R, Li C, Gao X, Yang W, et al. Synergistic Modulation of Grain Boundary and Domain Boundary Enhances the Ionic Conductivity of $Li_{0.33}La_{0.56}TiO_3$ Solid Electrolyte. ACS Nano 2025;19:10902–11. https://doi.org/10.1021/acsnano.4c15481.

[89] Lu J, Li Y. Perovskite-type Li-ion solid electrolytes: a review. J Mater Sci Mater Electron 2021;32:9736–54. https://doi.org/10.1007/s10854-021-05699-8.

[90] Sutorik AC, Green MD, Cooper C, Wolfenstine J, Gilde G. The comparative influences of structural ordering, grain size, Li-content, and bulk density on the Li^+-conductivity of $Li_{0.29}La_{0.57}TiO_3$. J Mater Sci 2012;47:6992–7002. https://doi.org/10.1007/s10853-012-6650-5.

[91] Hagman L-O, Kierkegaard P, Karvonen P, Virtanen AI, Paasivirta J. The Crystal Structure of $NaM_2IV(PO_4)_3$; MeIV = Ge, Ti, Zr. Acta Chem Scand 1968;22:1822–32. https://doi.org/10.3891/acta.chem.scand.22-1822.

[92] Xiao W, Wang J, Fan L, Zhang J, Li X. Recent advances in $Li_{1+x}Al_xTi_{2-x}(PO_4)_3$ solid-state electrolyte for safe lithium batteries. Energy Storage Mater 2019;19:379–400. https://doi.org/10.1016/j.ensm.2018.10.012.

[93] Zhang B, Tan R, Yang L, Zheng J, Zhang K, Mo S, et al. Mechanisms and properties of ion-transport in inorganic solid electrolytes. Energy Storage Mater 2018;10:139–59. https://doi.org/10.1016/j.ensm.2017.08.015.

[94] Huang X, Li T, Fan W, Xiao R, Cheng XB. Challenges and Solutions of Solid-State Electrolyte Film for Large-Scale applications. Adv Energy Mater 2024;14:2303850. https://doi.org/10.1002/aenm.202303850.

[95] Chen S, Nie L, Hu X, Zhang Y, Zhang Y, Yu Y, et al. Ultrafast Sintering for Ceramic-Based All-Solid-State Lithium-Metal Batteries. Adv Mater 2022;34:2200430. https://doi.org/10.1002/adma.202200430.

[96] Yao X, Chen S, Wang C, Chen T, Li J, Xue S, et al. Interface Welding via thermal Pulse Sintering to Enable 4.6 V Solid-State Batteries. Adv Energy Mater 2023;14:2303422. https://doi.org/10.1002/aenm.202303422.

[97] Hong H-P. Crystal structure and ionic conductivity of $Li_{14}Zn(GeO_4)_4$ and other new Li^+ superionic conductors. Mater Res Bull 1978;13:117–24. https://doi.org/10.1016/0025-5408(78)90075-2.

[98] Tao B, Ren C, Li H, Liu B, Jia X, Dong X, et al. Thio-/LISICON and LGPS-Type Solid Electrolytes for All-Solid-State Lithium-Ion Batteries. Adv Funct Mater 2022;32:2203551. https://doi.org/10.1002/adfm.202203551.

[99] Okumura T, Taminato S, Miyazaki Y, Kitamura M, Saito T, Takeuchi T, et al. LISICON-Based Amorphous Oxide for Bulk-Type All-Solid-State Lithium-Ion Battery. ACS Appl Energy Mater 2020;3:3220–9. https://doi.org/10.1021/acsaem.9b01949.

[100] Kuwano J, West AR. New Li^+ ion conductors in the system, Li_4GeO_4-Li_3VO_4. Mater Res Bull 1980;15:1661–7. https://doi.org/10.1016/0025-5408(80)90249-4.

[101] Bruce PG, West A. The A-C conductivity of polycrystalline LISICON, $Li_{2+2x}Zn_{1-x}GeO_4$, and a model for intergranular constriction resistances. J Electrochem Soc 1983;130:662. https://doi.org/10.1149/1.2119778.

[102] Kuwata N, Kawamura J, Toribami K, Hattori T, Sata N. Thin-film lithium-ion battery with amorphous solid electrolyte fabricated by pulsed laser deposition. Electrochem Commun 2004;6:417–21. https://doi.org/10.1016/j.elecom.2004.02.010.

[103] Kataoka K. Oxide single crystals with high lithium-ion conductivity as solid electrolytes for all-solid-state lithium secondary battery applications. J Ceram Soc Jpn 2020;128:7–18. https://doi.org/10.2109/jcersj2.19094.

[104] Moy AC, Manjón-Sanz A, Caracciolo TC, Lobanov MV, Veith GM, Sakamoto J. Effects of Al concentration on the structure and conductivity of lithium lanthanum zirconium oxide. J Mater Chem A 2024;12:28193–210. https://doi.org/10.1039/d4ta04862h.

[105] Kobi S, Sharma A, Mukhopadhyay A. Low Interfacial Resistance and Superior suppression to Li-Dendrite Penetration Facilitated by Air-Stable and Mechanically Robust Al/Mg-Co-Doped Li-La-Zirconate as Electrolyte for Li-based Solid-State Cells. ACS Appl Mater Interfaces 2023;15:39276–90. https://doi.org/10.1021/acsami.3c05954.

[106] Gao J, Zhu J, Li X, Li J, Guo X, Li H, et al. Rational Design of mixed Electronic-Ionic Conducting Ti-Doping $Li_7La_3Zr_2O_{12}$ for Lithium Dendrites suppression. Adv Funct Mater 2020;31:2001918. https://doi.org/10.1002/adfm.202001918.

[107] Li Y, Chen X, Dolocan A, Cui Z, Xin S, Xue L, et al. Garnet Electrolyte with an Ultralow Interfacial Resistance for Li-Metal Batteries. J Am Chem Soc 2018;140:6448–55. https://doi.org/10.1021/jacs.8b03106.

[108] Chen L, Huang X, Ma R, Xiang W, Ma J, Wu Y, et al. A nanocrystal garnet skeleton-derived high-performance composite solid-state electrolyte membrane. Energy Storage Mater 2024;65:103140. https://doi.org/10.1016/j.ensm.2023.103140.

[109] Deng T, Ji X, Zhao Y, Cao L, Li S, Hwang S, et al. Tuning the anode–electrolyte interface chemistry for garnet-based solid-state Li metal batteries. Adv Mater 2020;32:2000030. https://doi.org/10.1002/adma.202000030.

[110] Qin Z, Xie Y, Meng X, Qian D, Shan C, Mao D, et al. Interface engineering for garnet-type electrolyte enables low interfacial resistance in solid-state lithium batteries. Chem Eng J 2022;447:137538. https://doi.org/10.1016/j.cej.2022.137538.

[111] Meng J, Zhang Y, Zhou X, Lei M, Li C. Li_2CO_3-affiliative mechanism for air-accessible interface engineering of garnet electrolyte via facile liquid metal painting. Nat Commun 2020;11:3716. https://doi.org/10.1038/s41467-020-17493-x.

[112] Kobi S, Amardeep VA, Bhargava P, Mukhopadhyay A. Al and Mg Co-Doping Towards Development of Air-Stable and Li-Ion Conducting Li-La-Zirconate based Solid Electrolyte Exhibiting Low Electrode/Electrolyte Interfacial Resistance. J Electrochem Soc 2020;167:120519. https://doi.org/10.1149/1945-7111/abad66.

[113] Jeong W, Park SS, Yun J, Shin HR, Moon J, Lee J-W. Tailoring grain boundary structures and chemistry of $Li_7La_3Zr_2O_{12}$ solid electrolytes for enhanced air stability. Energy Storage Mater 2023;54:543–52. https://doi.org/10.1016/j.ensm.2022.10.044.

[114] Abrha LH, Hagos TT, Nikodimos Y, Bezabh HK, Berhe GB, Hagos TM, et al. Dual-Doped Cubic Garnet Solid Electrolytes with Superior Air Stability. ACS Appl Mater Interfaces 2020;12:25709–17. https://doi.org/10.1021/acsami.0c01289.

[115] Donzelli M, Ferber T, Vanita V, Waidha AI, Muller P, Mellin M, et al. On the Surface Modification of LLZTO with LiF via a Gas-phase Approach and the Characterization of the Interfaces of LiF with LLZTO as well as PEO+LiTFSI. Materials (Basel) 2022;15:6900. https://doi.org/10.3390/ma15196900.

[116] Jia M, Bi Z, Shi C, Zhao N, Guo X. Air-stable dopamine-treated garnet ceramic particles for high-performance composite electrolytes. J Power Sources 2021;486:229363. https://doi.org/10.1016/j.jpowsour.2020.229363.

[117] Wu B, Wang S, Lochala J, Desrochers D, Liu B, Zhang W, et al. The role of the solid electrolyte interphase layer in preventing Li dendrite growth in solid-state batteries. Energy Environ Sci 2018;11:1803–10. https://doi.org/10.1039/c8ee00540k.

[118] Zheng H, Li G, Liu J, Wu S, Zhang X, Wu Y, et al. A rational design of garnet-type $Li_7La_3Zr_2O_{12}$ with ultrahigh moisture stability. Energy Storage Mater 2022;49:278–90. https://doi.org/10.1016/j.ensm.2022.04.027.

[119] Zhang LC, Yang JF, Gao YX, Wang XP, Fang QF, Chen CH. Influence of Li_3BO_3 additives on the Li^+ conductivity and stability of Ca/Ta-substituted $Li_{6.55}(La_{2.95}Ca_{0.05})(Zr_{1.5}Ta_{0.5})O_{12}$ electrolytes. J Power Sources 2017;355:69–73. https://doi.org/10.1016/j.jpowsour.2017.04.044.

[120] Zhang S, Zhao H, Wang J, Xu T, Zhang K, Du Z. Enhanced densification and ionic conductivity of Li-garnet electrolyte: Efficient Li_2CO_3 elimination and fast grain-boundary transport construction. Chem Eng J 2020;393:124797. https://doi.org/10.1016/j.cej.2020.124797.
[121] Li J, Gong Z, Xie W, Yu S, Wei Y, Li D, et al. Growth Process and Removal of Interface Contaminants for Garnet-based Solid-State Lithium Metal Batteries. ACS Appl Energy Mater 2023;6:12432–41. https://doi.org/10.1021/acsaem.3c02319.
[122] Huo H, Chen Y, Zhao N, Lin X, Luo J, Yang X, et al. In-situ formed Li_2CO_3-free garnet/Li interface by rapid acid treatment for dendrite-free solid-state batteries. Nano Energy 2019;61:119–25. https://doi.org/10.1016/j.nanoen.2019.04.058.
[123] Zhang J, Wang C, Zheng M, Ye M, Zhai H, Li J, et al. Rational design of air-stable and intact anode-electrolyte interface for garnet-type solid-state batteries. Nano Energy 2022;102:107672. https://doi.org/10.1016/j.nanoen.2022.107672.
[124] Dai Q, Yao J, Du C, Ye H, Gao Z, Zhao J, et al. Cryo-EM Studies of Atomic-Scale Structures of Interfaces in Garnet-Type Electrolyte based Solid-State Batteries. Adv Funct Mater 2022;32:2208682. https://doi.org/10.1002/adfm.202208682.
[125] Lu G, Dong Z, Liu W, Jiang X, Yang Z, Liu Q, et al. Universal lithiophilic interfacial layers towards dendrite-free lithium anodes for solid-state lithium-metal batteries. Sci Bull 2021;66:1746–53. https://doi.org/10.1016/j.scib.2021.04.034.
[126] Jiang J, Ou Y, Lu S, Shen C, Li B, Liu X, et al. *In-situ* construction of Li-Mg/LiF conductive layer to achieve an intimate lithium-garnet interface for all-solid-state Li metal battery. Energy Storage Mater 2022;50:810–8. https://doi.org/10.1016/j.ensm.2022.06.011.
[127] Duan J, Zheng Y, Luo W, Wu W, Wang T, Xie Y, et al. Is graphite lithiophobic or lithiophilic? Natl Sci Rev 2020;7:1208–17. https://doi.org/10.1093/nsr/nwz222.
[128] Wen J, Huang Y, Duan J, Wu Y, Luo W, Zhou L, et al. Highly Adhesive Li-BN Nanosheet Composite Anode with Excellent Interfacial Compatibility for Solid-State Li Metal Batteries. ACS Nano 2019;13:14549–56. https://doi.org/10.1021/acsnano.9b08803.
[129] Wang T, Duan J, Zhang B, Luo W, Ji X, Xu H, et al. A self-regulated gradient interphase for dendrite-free solid-state Li batteries. Energy Environ Sci 2022;15:1325–33. https://doi.org/10.1039/d1ee03604a.
[130] Lu G, Li M, Chen P, Zheng W, Yang Z, Wang R, et al. Built-in superionic conductive phases enabling dendrite-free, long lifespan and high specific capacity composite lithium for stable solid-state lithium batteries. Energy Environ Sci 2023;16:1049–61. https://doi.org/10.1039/d2ee03709b.
[131] Du M, Sun Y, Liu B, Chen B, Liao K, Ran R, et al. Smart Construction of an Intimate Lithium | Garnet Interface for All-Solid-State Batteries by Tuning the Tension of Molten Lithium. Adv Funct Mater 2021;31:2101556. https://doi.org/10.1002/adfm.202101556.
[132] Zhu F, Hu X, Xu L, Zhang B, Wang H, Ni L, et al. Restrained Li|Garnet Interface Contact Deterioration Manipulated by Lithium Modification for Solid-State Batteries. Adv Funct Mater 2024;34:2314994. https://doi.org/10.1002/adfm.202314994.
[133] Lei M, Fan S, Yu Y, Hu J, Chen K, Gu Y, et al. NASICON-based solid state Li-Fe-F conversion batteries enabled by multi-interface-compatible sericin protein buffer layer. Energy Storage Mater 2022;47:551–60. https://doi.org/10.1016/j.ensm.2022.02.031.
[134] Kong W, Jiang Z, Liu Y, Han Q, Ding LX, Wang S, et al. Stabilizing $Li_{1.3}Al_{0.3}Ti_{1.7}(PO_4)_3$|Li Metal Anode Interface in Solid-State Batteries by Kevlar Aramid Nanofiber-based protective Coating. Adv Funct Mater 2023;33:2306748. https://doi.org/10.1002/adfm.202306748.
[135] Wang L, Wang L, Shi Q, Zhong C, Gong D, Wang X, et al. In-situ constructed SnO_2 gradient buffer layer as a tight and robust interphase toward Li metal anodes in LATP solid state batteries. J Energy Chem 2023;80:89–98. https://doi.org/10.1016/j.jechem.2023.01.040.
[136] Wang C, Sun Q, Liu Y, Zhao Y, Li X, Lin X, et al. Boosting the performance of lithium batteries with solid-liquid hybrid electrolytes: Interfacial properties and effects of liquid electrolytes. Nano Energy 2018;48:35–43. https://doi.org/10.1016/j.nanoen.2018.03.020.
[137] Yu J, Liu Q, Hu X, Wang S, Wu J, Liang B, et al. Smart construction of multifunctional $Li_{1.5}Al_{0.5}Ge_{1.5}(PO_4)_3$|Li intermediate interfaces for solid-state batteries. Energy Storage Mater 2022;46:68–75. https://doi.org/10.1016/j.ensm.2021.12.043.
[138] Gu Y, Hu J, Lai C, Li C. NASICON-Based Solid State Li-Fluoride Conversion Batteries Enabled by Constructing a Fluorine-Rich Trap for Ti^{4+}. Adv Energy Mater 2023;13:2203679. https://doi.org/10.1002/aenm.202203679.
[139] Bi Z, Sun Q, Jia M, Zuo M, Zhao N, Guo X. Molten Salt Driven Conversion Reaction Enabling Lithiophilic and Air-Stable Garnet Surface for Solid-State Lithium Batteries. Adv Funct Mater 2022;32:2208751. https://doi.org/10.1002/adfm.202208751.
[140] Bi Z, Shi R, Liu X, Liu K, Jia M, Guo X. In Situ Conversion Reaction Triggered Alloy@Antiperovskite Hybrid Layers for Lithiophilic and Robust Lithium/Garnet Interfaces. Adv Funct Mater 2023;33:2307701. https://doi.org/10.1002/adfm.202307701.
[141] Gao Z, Sun H, Fu L, Ye F, Zhang Y, Luo W, et al. Promises, challenges, and recent Progress of Inorganic Solid-State Electrolytes for All-Solid-State Lithium Batteries. Adv Mater 2018;30:1705702. https://doi.org/10.1002/adma.201705702.
[142] Liu Y, Li C, Li B, Song H, Cheng Z, Chen M, et al. Germanium Thin Film Protected Lithium Aluminum Germanium Phosphate for Solid-State Li Batteries. Adv Energy Mater 2018;8:1702374. https://doi.org/10.1002/aenm.201702374.
[143] Wang G, Liu H, Liang Y, Wang C, Fan L-Z. Composite polymer electrolyte with three-dimensional ion transport channels constructed by NaCl template for solid-state lithium metal batteries. Energy Storage Mater 2022;45:1212–9. https://doi.org/10.1016/j.ensm.2021.11.021.
[144] Zhou W, Wang S, Li Y, Xin S, Manthiram A, Goodenough JB. Plating a Dendrite-Free Lithium Anode with a Polymer/Ceramic/Polymer Sandwich Electrolyte. J Am Chem Soc 2016;138:9385–8. https://doi.org/10.1021/jacs.6b05341.
[145] Zhu L, Wang Y, Wu Y, Feng W, Liu Z, Tang W, et al. Boron Nitride-Based Release Agent Coating Stabilizes $Li_{1.3}Al_{0.3}Ti_{1.7}(PO_4)_3$/Li Interface with Superior Lean-Lithium Electrochemical Performance and thermal Stability. Adv Funct Mater 2022;32:2201136. https://doi.org/10.1002/adfm.202201136.
[146] Ci N, Zhang L, Li J, Li D, Cheng J, Sun Q, et al. In situ construction of a flexible interlayer for durable solid-state lithium metal batteries. Carbon 2022;187:13–21. https://doi.org/10.1016/j.carbon.2021.10.070.
[147] Krauskopf T, Mogwitz B, Rosenbach C, Zeier WG, Janek J. Diffusion Limitation of Lithium Metal and Li–Mg Alloy Anodes on LLZO Type Solid Electrolytes as a Function of Temperature and pressure. Adv Energy Mater 2019;9:1902568. https://doi.org/10.1002/aenm.201902568.
[148] Han F, Westover AS, Yue J, Fan X, Wang F, Chi M, et al. High electronic conductivity as the origin of lithium dendrite formation within solid electrolytes. Nat Energy 2019;4:187–96. https://doi.org/10.1038/s41560-018-0312-z.
[149] Wang C, He Y, Zou P, He Q, Li J, Xin HL. Nanoscale Origin of the Soft-to-Hard Short-Circuit transition in Inorganic Solid-State Electrolytes. J Am Chem Soc 2025;147:19084–92. https://doi.org/10.1021/jacs.5c04113.
[150] Yang M, Liu Y, Mo Y. Lithium crystallization at solid interfaces. Nat Commun 2023;14:2986. https://doi.org/10.1038/s41467-023-38757-2.
[151] Huo H, Gao J, Zhao N, Zhang D, Holmes NG, Li X, et al. A flexible electron-blocking interfacial shield for dendrite-free solid lithium metal batteries. Nat Commun 2021;12:176. https://doi.org/10.1038/s41467-020-20463-y.
[152] Fan X, Ji X, Han F, Yue J, Chen J, Chen L, et al. Fluorinated solid electrolyte interphase enables highly reversible solid-state Li metal battery. Sci Adv 2018;4:eaau9245. https://doi.org/10.1126/sciadv.aau9245.
[153] Kim JS, Yoon G, Kim S, Sugata S, Yashiro N, Suzuki S, et al. Surface engineering of inorganic solid-state electrolytes via interlayers strategy for developing long-cycling quasi-all-solid-state lithium batteries. Nat Commun 2023;14:782. https://doi.org/10.1038/s41467-023-36401-7.
[154] Lu Y, Huang X, Ruan Y, Wang Q, Kun R, Yang J, et al. An *in situ* element permeation constructed high endurance Li–LLZO interface at high current densities. J Mater Chem A 2018;6:18853–8. https://doi.org/10.1039/C8TA07241H.
[155] Lee S, Lee K-s, Kim S, Yoon K, Han S, Lee MH, et al. Design of a lithiophilic and electron-blocking interlayer for dendrite-free lithium-metal solid-state batteries. Sci Adv 2022;8:eabq0153. https://doi.org/10.1126/sciadv.abq0153.
[156] Alexander GV, Shi C, O'Neill J, Wachsman ED. Extreme lithium-metal cycling enabled by a mixed ion- and electron-conducting garnet three-dimensional architecture. Nat Mater 2023;22:1136–43. https://doi.org/10.1038/s41563-023-01627-9.
[157] Zou P, Wang C, He Y, Xin HL. Broadening solid ionic conductor selection for sustainable and earth-abundant solid-state lithium metal batteries. Energy Environ Sci 2023;16:5871–80. https://doi.org/10.1039/d3ee02657d.
[158] Sarkar S, Santos C, Glenneberg J, Bardenhagen I, Schwenzel J, Thangadurai V. Probing Alkaline-Earth-Doped Garnet-Type $Li_7La_{2.75}A_{0.25}Zr_{1.75}M_{0.25}O_{12}$ (a = Ca, Sr, Ba; M = Nb, Ta) Electrolytes for All-Solid-State Li Metal Batteries. Chem Mater 2024;36:2685–97. https://doi.org/10.1021/acs.chemmater.3c02615.
[159] Mishra AK, Sau S, Patel Y, Shaikh N, Odedra H, Vagadiya B, et al. Stabilization of cubic $Li_7La_3Zr_2O_{12}$ phase solid electrolyte by gallium doping and its effect on structural and energy storage properties. J Energy Storage 2025;121:116537. https://doi.org/10.1016/j.est.2025.116537.

[160] Zeng C, Feng W, Shi Y, Zhang X, Yang Y, Zheng X, et al. In Situ Fabrication of High Ionic and Electronic Conductivity Interlayers Enabling Long-Life Garnet-based Solid-State Lithium Batteries. ACS Appl Mater Interfaces 2024;16:30462–70. https://doi.org/10.1021/acsami.3c19215.

[161] Hao X, Zhao Q, Su S, Zhang S, Ma J, Shen L, et al. Constructing Multifunctional Interphase between $Li_{1.4}Al_{0.4}Ti_{1.6}(PO_4)_3$ and Li Metal by Magnetron Sputtering for Highly Stable Solid-State Lithium Metal Batteries. Adv Energy Mater 2019;9:1901604. https://doi.org/10.1002/aenm.201901604.

[162] Zhao G, Luo C, Hua Q. Li^+ selective transport network-assisted high-performance of garnet-based solid electrolyte for Li metal batteries. J Mater Chem A 2023; 11:20174–86. https://doi.org/10.1039/d3ta04229d.

[163] Lee K, Han S, Lee J, Lee S, Kim J, Ko Y, et al. Multifunctional Interface for High-Rate and Long-durable Garnet-Type Solid Electrolyte in Lithium Metal Batteries. ACS Energy Lett 2021;7:381–9. https://doi.org/10.1021/acsenergylett.1c02332.

[164] McConohy G, Xu X, Cui T, Barks E, Wang S, Kaeli E, et al. Mechanical regulation of lithium intrusion probability in garnet solid electrolytes. Nat Energy 2023; 8:241–50. https://doi.org/10.1038/s41560-022-01186-4.

[165] Raj V, Venturi V, Kankanallu VR, Kuiri B, Viswanathan V, Aetukuri NPB. Direct correlation between void formation and lithium dendrite growth in solid-state electrolytes with interlayers. Nat Mater 2022;21:1050–6. https://doi.org/10.1038/s41563-022-01264-8.

[166] Park J-H, Kim M, Kim M-Y, Jeong J, Jung H-G, Yoon WY, et al. Correlation between the particle size of $Li_{1.3}A_{l0.3}Ti_{1.7}(PO_4)_3$ solid electrolyte and lithium-ion transport in composite cathodes for all-solid-state lithium-ion batteries. Chem Eng J 2024;481:148436. https://doi.org/10.1016/j.cej.2023.148436.

[167] Wei R, Chen S, Gao T, Liu W. Challenges, fabrications and horizons of oxide solid electrolytes for solid-state lithium batteries. Nano Select 2021;2:2256–74. https://doi.org/10.1002/nano.202100110.

[168] Dai W, Qiao Y, Ma Z, Wang T, Fu Z. All-solid-state thin-film batteries based on lithium phosphorus oxynitrides. Mater Futures 2022;1:032101. https://doi.org/10.1088/2752-5724/ac7db2.

[169] Li J, Ma C, Chi M, Liang C, Dudney NJ. Solid Electrolyte: the Key for High-Voltage Lithium Batteries. Adv Energy Mater 2014;5:1401408. https://doi.org/10.1002/aenm.201401408.

[170] Deng R, Ke B, Xie Y, Cheng S, Zhang C, Zhang H, et al. All-Solid-State Thin-Film Lithium-Sulfur Batteries Nanomicro Lett 2023;15:73. https://doi.org/10.1007/s40820-023-01064-y.

[171] Westover AS, Sacci RL, Dudney N. Electroanalytical Measurement of Interphase Formation at a Li Metal–Solid Electrolyte Interface. ACS Energy Lett 2020;5: 3860–7. https://doi.org/10.1021/acsenergylett.0c01840.

[172] Cheng D, Wynn T, Lu B, Marple M, Han B, Shimizu R, et al. A free-standing lithium phosphorus oxynitride thin film electrolyte promotes uniformly dense lithium metal deposition with no external pressure. Nat Nanotechnol 2023;18:1448–55. https://doi.org/10.1038/s41565-023-01478-0.

[173] Yi E, Wang W, Kieffer J, Laine RM. Key parameters governing the densification of cubic-$Li_7La_3Zr_2O_{12}$ Li^+ conductors. J Power Sources 2017;352:156–64. https://doi.org/10.1016/j.jpowsour.2017.03.126.

[174] Kwon G, Gwon H, Bae Y, Jung C, Ko D-S, Kim MG, et al. Disorder-driven sintering-free garnet-type solid electrolytes. Nat Commun 2025;16:3256. https://doi.org/10.1038/s41467-025-58108-7.

[175] Ping W, Wang C, Wang R, Dong Q, Lin Z, Brozena AH, et al. Printable, high-performance solid-state electrolyte films. Sci Adv 2020;6:eabc8641. https://doi.org/10.1126/sciadv.abc8641.

[176] Chen W-P, Duan H, Shi J-L, Qian Y, Wan J, Zhang X-D, et al. Bridging interparticle Li^+ conduction in a soft ceramic oxide electrolyte. J Am Chem Soc 2021;143: 5717–26. https://doi.org/10.1021/jacs.0c12965.

[177] Li C-L, Zhang B, Fu Z-W. Physical and electrochemical characterization of amorphous lithium lanthanum titanate solid electrolyte thin-film fabricated by e-beam evaporation. Thin Solid Films 2006;515:1886–92. https://doi.org/10.1016/j.tsf.2006.07.026.

[178] Kim S, Hirayama M, Cho W, Kim K, Kobayashi T, Kaneko R, et al. Low temperature synthesis and ionic conductivity of the epitaxial $Li_{0.17}La_{0.61}TiO_3$ film electrolyte. CrstEngComm 2014;16:1044–9. https://doi.org/10.1039/c3ce42003e.

[179] Aaltonen T, Alnes M, Nilsen O, Costelle L, Fjellvåg H. Lanthanum titanate and lithium lanthanum titanate thin films grown by atomic layer deposition. J Mater Chem 2010;20:2877. https://doi.org/10.1039/b923490j.

[180] Wu XM, Chen S, Mai FR, Zhao JH, He ZQ. Influence of the annealing technique on the properties of Li ion-conductive $Li_{1.3}Al_{0.3}Ti_{1.7}(PO_4)_3$ films. Ionics 2012; 19:589–93. https://doi.org/10.1007/s11581-012-0788-7.

[181] Inada R, Ishida K-i, Tojo M, Okada T, Tojo T, Sakurai Y. Properties of aerosol deposited NASICON-type $Li_{1.5}Al_{0.5}Ge_{1.5}(PO_4)_3$ solid electrolyte thin films. Ceram Int 2015;41:11136–42. https://doi.org/10.1016/j.ceramint.2015.05.062.

[182] Ling Q, Yu Z, Xu H, Zhu G, Zhang X, Zhao Y, et al. Preparation and electrical properties of amorphous Li-Al-Ti-P-O thin film electrolyte. Mater Lett 2016;169: 42–5. https://doi.org/10.1016/j.matlet.2016.01.089.

[183] Li H, Zhang X, Huang H, Liu H, Lin Y, Pan H, et al. Ionic liquid reinforced NaSICON-type oxide electrolyte films enabling solid state conversion metal fluoride-lithium batteries. Energy Storage Mater 2024;70:103452. https://doi.org/10.1016/j.ensm.2024.103452.

[184] Huang X, Lu Y, Song Z, Rui K, Wang Q, Xiu T, et al. Manipulating Li_2O atmosphere for sintering dense $Li_7La_3Zr_2O_{12}$ solid electrolyte. Energy Storage Mater 2019;22:207–17. https://doi.org/10.1016/j.ensm.2019.01.018.

[185] Jiang H, Liu J, Tang B, Yang Z, Liang X, Yu X, et al. Regulation Mechanism on a Bilayer Li_2O-Rich Interface between Lithium Metal and Garnet-Type Solid Electrolytes. Adv Funct Mater 2023;34:2306399. https://doi.org/10.1002/adfm.202306399.

[186] Leng J, Liang H, Wang H, Xiao Z, Wang S, Zhang Z, et al. A facile and low-cost wet-chemistry artificial interface engineering for garnet-based solid-state Li metal batteries. Nano Energy 2022;101:107603. https://doi.org/10.1016/j.nanoen.2022.107603.

[187] Luo L, Sun Z, Gao H, Lan C, Huang X, Han X, et al. Insights into the Enhanced Interfacial Stability Enabled by Electronic Conductor Layers in Solid-State Li Batteries. Adv Energy Mater 2023;13:2203517. https://doi.org/10.1002/aenm.202203517.

[188] Li S-Y, Wang W-P, Xin S, Zhang J, Guo Y-G. A facile strategy to reconcile 3D anodes and ceramic electrolytes for stable solid-state Li metal batteries. Energy Storage Mater 2020;32:458–64. https://doi.org/10.1016/j.ensm.2020.07.029.

[189] Cui C, Zeng C, Huang G, Feng X, Zhang Y, Zhai T, et al. In Situ Visualizing the Interfacial failure Mechanism and Modification Promotion of LAGP Solid Electrolyte toward Li Metal Anode. Adv Energy Mater 2022;12:2202250. https://doi.org/10.1002/aenm.202202250.

[190] Li W, Wang Q, Jin J, Li Y, Wu M, Wen Z. Constructing dual interfacial modification by synergetic electronic and ionic conductors: Toward high-performance LAGP-Based Li-S batteries. Energy Storage Mater 2019;23:299–305. https://doi.org/10.1016/j.ensm.2019.04.044.

[191] Zhang Z, Chen S, Yao X, Cui P, Duan J, Luo W, et al. Enabling high-areal-capacity all-solid-state lithium-metal batteries by tri-layer electrolyte architectures. Energy Storage Mater 2020;24:714–8. https://doi.org/10.1016/j.ensm.2019.06.006.

[192] Jiang P, Cao J, Wei B, Qian G, Wang S, Shi Y, et al. LiF involved interphase layer enabling thousand cycles of LAGP-based solid-state Li metal batteries with 80% capacity retention. Energy Storage Mater 2022;48:145–54. https://doi.org/10.1016/j.ensm.2022.03.017.

[193] Xiong S, Liu Y, Jankowski P, Liu Q, Nitze F, Xie K, et al. Design of a Multifunctional Interlayer for NASCION-Based Solid-State Li Metal Batteries. Adv Funct Mater 2020;30:2001444. https://doi.org/10.1002/adfm.202001444.

[194] Paolella A, Liu X, Daali A, Xu W, Hwang I, Savoie S, et al. Enabling High-Performance NASICON-Based Solid-State Lithium Metal Batteries Towards Practical Conditions. Adv Funct Mater 2021;31:2102765. https://doi.org/10.1002/adfm.202102765.

[195] Liu Q, Yu Q, Li S, Wang S, Zhang L, Cai B, et al. Safe LAGP-based all solid-state Li metal batteries with plastic super-conductive interlayer enabled by in-situ solidification. Energy Storage Mater 2020;25:613–20. https://doi.org/10.1016/j.ensm.2019.09.023.

[196] Wang Z, Zhao J, Zhang X, Rong Z, Tang Y, Liu X, et al. Tailoring lithium concentration in alloy anodes for long cycling and high areal capacity in sulfide-based all solid-state batteries. eScience 2023;3:100087. https://doi.org/10.1016/j.esci.2022.100087.

[197] Yang S, Tang Y, Yao Y, He S, Wu Z, Yang Y, et al. Sulfide electrolytes for all-solid-state sodium batteries: fundamentals and modification strategies. Mater Horiz 2025;12:1058–83. https://doi.org/10.1039/D4MH01218F.

[198] Wu J, Liu S, Han F, Yao X, Wang C. Lithium/Sulfide All-Solid-State Batteries using Sulfide Electrolytes. Adv Mater 2021;33:2000751. https://doi.org/10.1002/adma.202000751.

[199] Nakashima S, Kondo S, Ooura Y, Machida N, Hirano A, Imanishi N, et al. Low-Temperature Synthesis of the Li_2S–P_2S_5 Electrolytes by a Milling Process combined with Heat Treatment. Electrochemistry 2011;79:701–5. https://doi.org/10.5796/electrochemistry.79.701.

[200] Kim J, Yoon Y, Lee J, Shin D. Formation of the high lithium ion conducting phase from mechanically milled amorphous Li_2S–P_2S_5 system. J Power Sources 2011;196:6920–3. https://doi.org/10.1016/j.jpowsour.2010.12.020.

[201] Hayashi A, Hama S, Morimoto H, Tatsumisago M, Minami T. Preparation of Li_2S–P_2S_5 amorphous solid electrolytes by mechanical milling. J Am Ceram Soc 2001;84:477–9. https://doi.org/10.1111/j.1151-2916.2001.tb00685.x.

[202] Hayashi A. Preparation and characterization of glassy materials for all-solid-state lithium secondary batteries. J Ceram Soc Jpn 2007;115:110–7. https://doi.org/10.2109/jcersj.115.110.

[203] Muramatsu H, Hayashi A, Ohtomo T, Hama S, Tatsumisago M. Structural change of Li_2S–P_2S_5 sulfide solid electrolytes in the atmosphere. Solid State Ion 2011; 182:116–9. https://doi.org/10.1016/j.ssi.2010.10.013.

[204] Ohtomo T, Mizuno F, Hayashi A, Tadanaga K, Tatsumisago M. Mechanochemical synthesis of lithium ion conducting glasses and glass–ceramics in the system Li_2S–P–S. Solid State Ion 2005;176:2349–53. https://doi.org/10.1016/j.ssi.2005.03.025.

[205] Fukushima A, Hayashi A, Yamamura H, Tatsumisago M. Mechanochemical synthesis of high lithium ion conducting solid electrolytes in a Li_2S-P_2S_5-Li_3N system. Solid State Ion 2017;304:85–9. https://doi.org/10.1016/j.ssi.2017.03.010.

[206] Deck MJ, Chien PH, Poudel TP, Jin Y, Liu H, Hu YY. Oxygen-Induced Structural Disruption for improved Li^+ Transport and Electrochemical Stability of Li_3PS_4. Adv Energy Mater 2023;14:2302785. https://doi.org/10.1002/aenm.202302785.

[207] Wu Z, Xie Z, Yoshida A, An X, Wang Z, Hao X, et al. Novel SeS_2 doped Li_2S-P_2S_5 solid electrolyte with high ionic conductivity for all-solid-state lithium sulfur batteries. Chem Eng J 2020;380:122419. https://doi.org/10.1016/j.cej.2019.122419.

[208] Mizuno F, Hayashi A, Tadanaga K, Tatsumisago M. New, highly ion-conductive crystals precipitated from Li_2S–P_2S_5 glasses. Adv Mater 2005;17:918–21. https://doi.org/10.1002/adma.200401286.

[209] Mizuno F, Hayashi A, Tadanaga K, Tatsumisago M. New lithium-ion conducting crystal obtained by crystallization of the Li_2S–P_2S_5 glasses. Electrochemical and Solid State Letters 2005;8:A603–6. https://doi.org/10.1149/1.2056487.

[210] Tatsumisago M, Hama S, Hayashi A, Morimoto H, Minami T. New lithium ion conducting glass-ceramics prepared from mechanochemical Li_2S–P_2S_5 glasses. Solid State Ion 2002;154:635–40. https://doi.org/10.1016/s0167-2738(02)00509-x.

[211] Yamane H, Shibata M, Shimane Y, Junke T, Seino Y, Adams S, et al. Crystal structure of a superionic conductor, $Li_7P_3S_{11}$. Solid State Ion 2007;178:1163–7. https://doi.org/10.1016/j.ssi.2007.05.020.

[212] Zhou J, Chen P, Wang W, Zhang X. $Li_7P_3S_{11}$ electrolyte for all-solid-state lithium-ion batteries: structure, synthesis, and applications. Chem Eng J 2022;446: 137041. https://doi.org/10.1016/j.cej.2022.137041.

[213] Xiong K, Longo RC, Santosh KC, Wang W, Cho K. Behavior of Li defects in solid electrolyte lithium thiophosphate $Li_7P_3S_{11}$: a first principles study. Comput Mater Sci 2014;90:44–9. https://doi.org/10.1016/j.commatsci.2014.03.030.

[214] Chu I-H, Nguyen H, Hy S, Lin Y-C, Wang Z, Xu Z, et al. Insights into the Performance Limits of the $Li_7P_3S_{11}$ Superionic Conductor: a combined First-Principles and Experimental Study. ACS Appl Mater Interfaces 2016;8:7843–53. https://doi.org/10.1021/acsami.6b00833.

[215] Deiseroth HJ, Kong ST, Eckert H, Vannahme J, Reiner C, Zaiß T, et al. Li_6PS_5X: a Class of Crystalline Li-Rich Solids with an Unusually High Li^+ Mobility. Angew Chem 2008;120:767–70. https://doi.org/10.1002/ange.200703900.

[216] Kato Y, Hori S, Saito T, Suzuki K, Hirayama M, Mitsui A, et al. High-power all-solid-state batteries using sulfide superionic conductors. Nat Energy 2016;1: 16030. https://doi.org/10.1038/nenergy.2016.30.

[217] Kraft MA, Ohno S, Zinkevich T, Koerver R, Culver SP, Fuchs T, et al. Inducing High Ionic Conductivity in the Lithium Superionic Argyrodites $Li_{6+x}P_{1-x}Ge_xS_5I$ for All-Solid-State Batteries. J Am Chem Soc 2018;140:16330–9. https://doi.org/10.1021/jacs.8b10282.

[218] Liang J, Chen N, Li X, Li X, Adair KR, Li J, et al. $Li_{10}Ge(P_{1-x}Sb_x)_2S_{12}$ Lithium-Ion Conductors with Enhanced Atmospheric Stability. Chem Mater 2020;32: 2664–72. https://doi.org/10.1021/acs.chemmater.9b04764.

[219] Li Y, Song S, Kim H, Nomoto K, Kim H, Sun X, et al. A lithium superionic conductor for millimeter-thick battery electrode. Science 2023;381:50–3. https://doi.org/10.1126/science.add7138.

[220] Ma Y, Jin D, Shi H, Li R, Niu Y, Xu Y, et al. A Superionic Conductor Lithium Argyrodite Sulfide of $Li_{7-x}(GeSi)_{(1-x)/2}Sb_xS_5I$ toward All-Solid-State Lithium-Ion Batteries. ACS Energy Lett 2025;10:1374–81. https://doi.org/10.1021/acsenergylett.4c03115.

[221] Sun Y, Suzuki K, Hori S, Hirayama M, Kanno R. Superionic Conductors: $Li_{10+\delta}[Sn_ySi_{1-y}]_{1+\delta}P_{2-\delta}S_{12}$ with a $Li_{10}GeP_2S_{12}$-type Structure in the Li_3PS_4–Li_4SnS_4–Li_4SiS_4 Quasi-ternary System. Chem Mater 2017;29:5858–64. https://doi.org/10.1021/acs.chemmater.7b00886.

[222] Adeli P, Bazak JD, Park KH, Kochetkov I, Huq A, Goward GR, et al. Boosting Solid-State Diffusivity and Conductivity in Lithium Superionic Argyrodites by Halide Substitution. Angew Chem Int Ed 2019;58:8681–6. https://doi.org/10.1002/anie.201814222.

[223] Li S, Lin J, Schaller M, Indris S, Zhang X, Brezesinski T, et al. High-Entropy Lithium Argyrodite Solid Electrolytes Enabling Stable All-Solid-State Batteries. Angew Chem Int Ed 2023;62:e202314155. https://doi.org/10.1002/anie.202314155.

[224] Lee Y-G, Fujiki S, Jung C, Suzuki N, Yashiro N, Omoda R, et al. High-energy long-cycling all-solid-state lithium metal batteries enabled by silver–carbon composite anodes. Nat Energy 2020;5:299–308. https://doi.org/10.1038/s41560-020-0575-z.

[225] Kim J, Yoon Y, Eom M, Shin D. Characterization of amorphous and crystalline Li_2S–P_2S_5–P_2Se_5 solid electrolytes for all-solid-state lithium ion batteries. Solid State Ion 2012;225:626–30. https://doi.org/10.1016/j.ssi.2012.05.013.

[226] Tao Y, Chen S, Liu D, Peng G, Yao X, Xu X. Lithium Superionic Conducting Oxysulfide Solid Electrolyte with Excellent Stability against Lithium Metal for All-Solid-State Cells. J Electrochem Soc 2016;163:A96–. https://doi.org/10.1149/2.0311602jes.

[227] Xu R, Xia X, Li S, Zhang S, Wang X, Tu J. All-solid-state lithium–sulfur batteries based on a newly designed $Li_7P_{2.9}Mn_{0.1}S_{10.7}I_{0.3}$ superionic conductor. J Mater Chem A 2017;5:6310–7. https://doi.org/10.1039/c7ta01147d.

[228] Sun Y, Yan W, An L, Wu B, Zhong K, Yang R. A facile strategy to improve the electrochemical stability of a lithium ion conducting $Li_{10}GeP_2S_{12}$ solid electrolyte. Solid State Ion 2017;301:59–63. https://doi.org/10.1016/j.ssi.2017.01.014.

[229] Kim K-H, Martin SW. Structures and Properties of Oxygen-Substituted $Li_{10}SiP_2S_{12-x}O_x$ Solid-State Electrolytes. Chem Mater 2019;31:3984–91. https://doi.org/10.1021/acs.chemmater.9b00505.

[230] Swamy T, Chen X, Chiang Y-M. Electrochemical Redox Behavior of Li Ion Conducting Sulfide Solid Electrolytes. Chem Mater 2019;31:707–13. https://doi.org/10.1021/acs.chemmater.8b03420.

[231] Zhang Z, Zhang L, Yan X, Wang H, Liu Y, Yu C, et al. All-in-one improvement toward Li_6PS_5Br-based solid electrolytes triggered by compositional tune. J Power Sources 2019;410–411:162–70. https://doi.org/10.1016/j.jpowsour.2018.11.016.

[232] Wu F, Fitzhugh W, Ye L, Ning J, Li X. Advanced sulfide solid electrolyte by core-shell structural design. Nat Commun 2018;9:4037. https://doi.org/10.1038/s41467-018-06123-2.

[233] Wang X, He K, Li S, Zhang J, Lu Y. Realizing high-performance all-solid-state batteries with sulfide solid electrolyte and silicon anode: a review. Nano Res 2022;16:3741–65. https://doi.org/10.1007/s12274-022-4526-9.

[234] Kim T, Chang H, Song G, Lee S, Kim K, Lee S, et al. Critical Factors Contributing to the Thermal Runaway of Thiophosphate Solid Electrolytes for All-Solid-State Batteries 2024;34:2404806. https://doi.org/10.1002/adfm.202404806.

[235] Han F, Zhu Y, He X, Mo Y, Wang C. Electrochemical Stability of $Li_{10}GeP_2S_{12}$ and $Li_7La_3Zr_2O_{12}$ Solid Electrolytes. Adv Energy Mater 2016;6:1501590. https://doi.org/10.1002/aenm.201501590.

[236] Richards WD, Miara LJ, Wang Y, Kim JC, Ceder G. Interface Stability in Solid-State Batteries. Chem Mater 2016;28:266–73. https://doi.org/10.1021/acs.chemmater.5b04082.

[237] Hori S, Suzuki K, Hirayama M, Kato Y, Kanno R. Lithium Superionic Conductor $Li_{9.42}Si_{1.02}P_{2.1}S_{9.96}O_{2.04}$ with $Li_{10}GeP_2S_{12}$-Type Structure in the Li_2S–P_2S_5–SiO_2 Pseudoternary System: Synthesis, Electrochemical Properties, and Structure–Composition Relationships. Front Energy Res 2016;4:38. https://doi.org/10.3389/fenrg.2016.00038.

[238] Sun Z, Lai Y, Lv N, Hu Y, Li B, Jiang L, et al. Insights on the Properties of the O-Doped Argyrodite Sulfide Solid Electrolytes ($Li_6PS_{5-x}ClO_x$, x = 0–1). ACS Appl Mater Interfaces 2021;13:54914–25. https://doi.org/10.1021/acsami.1c14573.

[239] Xie D, Chen S, Zhang Z, Ren J, Yao L, Wu L, et al. High ion conductive Sb_2O_5-doped β-Li_3PS_4 with excellent stability against Li for all-solid-state lithium batteries. J Power Sources 2018;389:140–7. https://doi.org/10.1016/j.jpowsour.2018.04.021.

[240] Zhu Y, Mo Y. Materials Design Principles for Air-Stable Lithium/Sodium Solid Electrolytes. Angew Chem Int Ed 2020;59:17472–6. https://doi.org/10.1002/anie.202007621.

[241] Zhao F, Liang J, Yu C, Sun Q, Li X, Adair K, et al. A Versatile Sn-Substituted Argyrodite Sulfide Electrolyte for All-Solid-State Li Metal Batteries. Adv Energy Mater 2020;10:1903422. https://doi.org/10.1002/aenm.201903422.

[242] Lu P, Xia Y, Sun G, Wu D, Wu S, Yan W, et al. TiS_2 batteries using $Li_{6+x}M_xAs_{1-x}S_5I$ (M = Si, Sn) sulfide solid electrolytes. Nat Commun 2023;14:4077. https://doi.org/10.1038/s41467-023-39686-w.

[243] Liu G, Xie D, Wang X, Yao X, Chen S, Xiao R, et al. High air-stability and superior lithium ion conduction of $Li_{3+3x}P_{1-x}Zn_xS_{4-x}O_x$ by aliovalent substitution of ZnO for all-solid-state lithium batteries. Energy Storage Mater 2019;17:266–74. https://doi.org/10.1016/j.ensm.2018.07.008.

[244] Jung WD, Jeon M, Shin SS, Kim J-S, Jung H-G, Kim B-K, et al. Functionalized Sulfide Solid Electrolyte with Air-Stable and Chemical-Resistant Oxysulfide Nanolayer for All-Solid-State Batteries. ACS Omega 2020;5:26015–22. https://doi.org/10.1021/acsomega.0c03453.

[245] Sang J, Pan K, Tang B, Zhang Z, Liu Y, Zhou Z. One Stone, three Birds: an Air and Interface Stable Argyrodite Solid Electrolyte with Multifunctional Nanoshells. Adv Sci 2023;10:2304117. https://doi.org/10.1002/advs.202304117.

[246] Xu J, Li Y, Lu P, Yan W, Yang M, Li H, et al. Water-Stable Sulfide Solid Electrolyte Membranes Directly Applicable in All-Solid-State Batteries Enabled by Superhydrophobic Li^+-Conducting Protection Layer. Adv Energy Mater 2022;12:2102348. https://doi.org/10.1002/aenm.202102348.

[247] Yu Z, Shang S-L, Ahn K, Marty DT, Feng R, Engelhard MH, et al. Enhancing Moisture Stability of Sulfide Solid-State Electrolytes by Reversible Amphipathic Molecular Coating. ACS Appl Mater Interfaces 2022;14:32035–42. https://doi.org/10.1021/acsami.2c07388.

[248] Li J, Chen H, Shen Y, Hu C, Cheng Z, Lu W, et al. Covalent interfacial coupling for hybrid solid-state Li ion conductor. Energy Storage Mater 2019;23:277–83. https://doi.org/10.1016/j.ensm.2019.12.001.

[249] Zhang Y, Chen R, Wang S, Liu T, Xu B, Zhang X, et al. Free-standing sulfide/polymer composite solid electrolyte membranes with high conductance for all-solid-state lithium batteries. Energy Storage Mater 2020;25:145–53. https://doi.org/10.1016/j.ensm.2019.10.020.

[250] Zhang Z, Zhao Y, Chen S, Xie D, Yao X, Cui P, et al. An advanced construction strategy of all-solid-state lithium batteries with excellent interfacial compatibility and ultralong cycle life. J Mater Chem A 2017;5:16984–93. https://doi.org/10.1039/c7ta04320a.

[251] Liu M, Hong JJ, Sebti E, Zhou K, Wang S, Feng S, et al. Surface molecular engineering to enable processing of sulfide solid electrolytes in humid ambient air. Nat Commun 2025;16:213. https://doi.org/10.1038/s41467-024-55634-8.

[252] Lu P, Liu L, Wang S, Xu J, Peng J, Yan W, et al. Superior All-Solid-State Batteries Enabled by a Gas-Phase-Synthesized Sulfide Electrolyte with Ultrahigh Moisture Stability and Ionic Conductivity. Adv Mater 2021;33:2100921. https://doi.org/10.1002/adma.202100921.

[253] Yang Y, Yang S, Xue X, Zhang X, Li Q, Yao Y, et al. Inorganic All-Solid-State Sodium Batteries: Electrolyte Designing and Interface Engineering. Adv Mater 2024;36:2308332. https://doi.org/10.1002/adma.202308332.

[254] Koerver R, Ayguen I, Leichtweiss T, Dietrich C, Zhang W, Binder JO, et al. Capacity Fade in Solid-State Batteries: Interphase Formation and Chemomechanical Processes in Nickel-Rich Layered Oxide Cathodes and Lithium Thiophosphate Solid Electrolytes. Chem Mater 2017;29:5574–82. https://doi.org/10.1021/acs.chemmater.7b00931.

[255] Wu J, Shen L, Zhang Z, Liu G, Wang Z, Zhou D, et al. All-Solid-State Lithium Batteries with Sulfide Electrolytes and Oxide Cathodes. Electrochem Energy Rev 2020;4:101–35. https://doi.org/10.1007/s41918-020-00081-4.

[256] Zhang W, Leichtweiss T, Culver SP, Koerver R, Das D, Weber DA, et al. The Detrimental Effects of Carbon Additives in $Li_{10}GeP_2S_{12}$-based Solid-State Batteries. ACS Appl Mater Interfaces 2017;9:35888–96. https://doi.org/10.1021/acsami.7b11530.

[257] Meng R, Wu J, Zhu M, Xie W, Yang M, Tian F, et al. MoS_2-C superlattice cathodes for conductive additive-free sulfide electrolyte-based all-solid-state lithium batteries. Chem Eng J 2024;493:152540. https://doi.org/10.1016/j.cej.2024.152540.

[258] Haruyama J, Sodeyama K, Han L, Takada K, Tateyama Y. Space–Charge Layer effect at Interface between Oxide Cathode and Sulfide Electrolyte in All-Solid-State Lithium-Ion Battery. Chem Mater 2014;26:4248–55. https://doi.org/10.1021/cm5016959.

[259] Haruyama J, Sodeyama K, Tateyama Y. Cation Mixing Properties toward Co Diffusion at the $LiCoO_2$ Cathode/Sulfide Electrolyte Interface in a Solid-State Battery. ACS Appl Mater Interfaces 2017;9:286–92. https://doi.org/10.1021/acsami.6b08435.

[260] Li X, Ren Z, Norouzi Banis M, Deng S, Zhao Y, Sun Q, et al. Unravelling the Chemistry and Microstructure Evolution of a Cathodic Interface in Sulfide-based All-Solid-State Li-Ion Batteries. ACS Energy Lett 2019;4:2480–8. https://doi.org/10.1021/acsenergylett.9b01676.

[261] Li X, Liang M, Sheng J, Song D, Zhang H, Shi X, et al. Constructing double buffer layers to boost electrochemical performances of NCA cathode for ASSLB. Energy Storage Mater 2019;18:100–6. https://doi.org/10.1016/j.ensm.2018.10.003.

[262] Zhang M, Zhang S, Li M, Xiao D, Fu W, Zhang S, et al. Self-Sacrificing Reductive Interphase for Robust and High-Performance Sulfide-based All-Solid-State Lithium Batteries. Adv Energy Mater 2024;14:2303647. https://doi.org/10.1002/aenm.202303647.

[263] Zhang B, He Z, Liu T, Li Z, Zhang S, Zhao W, et al. Reducing gases Triggered Cathode Surface Reconstruction for Stable Cathode–Electrolyte Interface in Practical All-Solid-State Lithium Batteries. Adv Mater 2024;36:2305748. https://doi.org/10.1002/adma.202305748.

[264] Zhang X, Li X, Weng S, Wu S, Liu Q, Cao M, et al. Spontaneous gas–solid reaction on sulfide electrolytes for high-performance all-solid-state batteries. Energy Environ Sci 2023;16:1091–9. https://doi.org/10.1039/d2ee03358e.

[265] Zou C, Yang L, Zang Z, Tao X, Yi L, Chen X, et al. $LiAlO_2$-coated $LiNi_{0.8}Co_{0.1}Mn_{0.1}O_2$ and chlorine-rich argyrodite enabling high-performance all-solid-state lithium batteries at suitable stack pressure. Ceram Int 2023;49:443–9. https://doi.org/10.1016/j.ceramint.2022.09.010.

[266] Li X, Sun Y, Wang Z, Wang X, Zhang H, Song D, et al. High-rate and long-life Ni-rich oxide cathode under high mass loading for sulfide-based all-solid-state lithium batteries. Electrochim Acta 2021;391:138917. https://doi.org/10.1016/j.electacta.2021.138917.

[267] Zou C, Zang Z, Tao X, Yi L, Chen X, Zhang X, et al. Stabilized Cathode/Sulfide Electrolyte Interface through Conformally Interfacial Nanocoating for All-Solid-State Batteries. ACS Appl Energy Mater 2023;6:3599–607. https://doi.org/10.1021/acsaem.3c00255.

[268] Shen B, Li L, Yao X, Huang B. Interfacial engineering of $LiCoO_2$/$Li_{10}GeP_2S_{12}$ with electron-ion mixed conductor $Li_{7.5}La_3Zr_{1.5}Co_{0.5}O_{12}$ for high stable all-solid-state batteries. Ceram Int 2024;50:7150–5. https://doi.org/10.1016/j.ceramint.2023.12.082.

[269] Huang Y, Zhou L, Li C, Yu Z, Nazar LF. Waxing Bare High-Voltage Cathode Surfaces to Enable Sulfide Solid-State Batteries. ACS Energy Lett 2023;8:4949–56. https://doi.org/10.1021/acsenergylett.3c01717.

[270] Wei L, Tao J, Yang Y, Fan X, Ran X, Li J, et al. Surface sulfidization of spinel $LiNi_{0.5}Mn_{1.5}O_4$ cathode material for enhanced electrochemical performance in lithium-ion batteries. Chem Eng J 2020;384:123268. https://doi.org/10.1016/j.cej.2019.123268.

[271] Wang K, Liang Z, Weng S, Ding Y, Su Y, Wu Y, et al. Surface Engineering Strategy Enables 4.5 V Sulfide-based All-Solid-State Batteries with High Cathode Loading and Long Cycle Life. ACS Energy Lett 2023;8:3450–9. https://doi.org/10.1021/acsenergylett.3c01047.

[272] Bandyopadhyay S, Nandan B. A review on design of cathode, anode and solid electrolyte for true all-solid-state lithium sulfur batteries. Mater Today Energy 2023;31:101201. https://doi.org/10.1016/j.mtener.2022.101201.

[273] Umeshbabu E, Zheng B, Yang Y. Recent Progress in All-Solid-State Lithium−Sulfur Batteries using High Li-Ion Conductive Solid Electrolytes. Electrochem Energy Rev 2019;2:199–230. https://doi.org/10.1007/s41918-019-00029-3.

[274] Geng C, Qu W, Han Z, Wang L, Lv W, Yang Q-H. Superhigh Coulombic Efficiency Lithium−Sulfur Batteries Enabled by In Situ Coating Lithium Sulfide with Polymerizable Electrolyte Additive. Adv Energy Mater 2023;13:2204246. https://doi.org/10.1002/aenm.202204246.

[275] Tanibata N, Tsukasaki H, Deguchi M, Mori S, Hayashi A, Tatsumisago M. A novel discharge−charge mechanism of a S−P_2S_5 composite electrode without electrolytes in all-solid-state Li/S batteries. J Mater Chem A 2017;5:11224–8. https://doi.org/10.1039/c7ta01481c.

[276] Nagao M, Suzuki K, Imade Y, Tateishi M, Watanabe R, Yokoi T, et al. All-solid-state lithium−sulfur batteries with three-dimensional mesoporous electrode structures. J Power Sources 2016;330:120–6. https://doi.org/10.1016/j.jpowsour.2016.09.009.

[277] Yang G, Tan J, Jin H, Kim YH, Yang X, Son DH, et al. Creating Effective Nanoreactors on Carbon Nanotubes with Mechanochemical Treatments for High-Areal-Capacity Sulfur Cathodes and Lithium Anodes. Adv Funct Mater 2018;28:1800595. https://doi.org/10.1002/adfm.201800595.
[278] Yao X, Huang N, Han F, Zhang Q, Wan H, Mwizerwa JP, et al. High-Performance All-Solid-State Lithium−Sulfur Batteries Enabled by Amorphous Sulfur-Coated Reduced Graphene Oxide Cathodes. Adv Energy Mater 2017;7:1602923. https://doi.org/10.1002/aenm.201602923.
[279] Wan H, Zhang B, Liu S, Wang Z, Xu J, Wang C. Interface Design for High-Performance All-Solid-State Lithium Batteries. Adv Energy Mater 2024;14:2303046. https://doi.org/10.1002/aenm.202303046.
[280] Hao W, Li Y, Hwang GS, Liu Y, Liang Z. Origin of Lithium Dendrite Formation in Sulfide-based Electrolyte. Angew Chem Int Ed Engl 2025;64:e202500245. https://doi.org/10.1002/anie.202500245.
[281] Zhang H, Chen X, Xia G, Yu X. Stable Li Metal Anode Enabled by Simultaneous Regulation of Electrolyte Solvation Chemistry and the Solid Electrolyte Interphase. Adv Funct Mater 2023;33:2301976. https://doi.org/10.1002/adfm.202301976.
[282] Zhang H, Wang Y, Ju S, Gao P, Zou T, Zhang T, et al. 3D artificial electron and ion conductive pathway enabled by MgH_2 nanoparticles supported on g-C_3N_4 towards dendrite-free Li metal anode. Energy Storage Mater 2022;52:220–9. https://doi.org/10.1016/j.ensm.2022.08.001.
[283] Zeng D, Yao J, Zhang L, Xu R, Wang S, Yan X, et al. Promoting favorable interfacial properties in lithium-based batteries using chlorine-rich sulfide inorganic solid-state electrolytes. Nat Commun 2022;13:1901. https://doi.org/10.1038/s41467-022-29596-8.
[284] Lim H, Jun S, Song YB, Baeck KH, Bae H, Lee G, et al. Rationally Designed Conversion-Type Lithium Metal protective Layer for All-Solid-State Lithium Metal Batteries. Adv Energy Mater 2024;14:2303762. https://doi.org/10.1002/aenm.202303762.
[285] Wan H, Wang Z, Liu S, Zhang B, He X, Zhang W, et al. Critical interphase overpotential as a lithium dendrite-suppression criterion for all-solid-state lithium battery design. Nat Energy 2023;8:473–81. https://doi.org/10.1038/s41560-023-01231-w.
[286] Wan H, Wang Z, Zhang W, He X, Wang C. Interface design for all-solid-state lithium batteries. Nature 2023;623:739–44. https://doi.org/10.1038/s41586-023-06653-w.
[287] Wang Z, Xia J, Ji X, Liu Y, Zhang J, He X, et al. Lithium anode interlayer design for all-solid-state lithium-metal batteries. Nat Energy 2024;9:251–62. https://doi.org/10.1038/s41560-023-01426-1.
[288] Yan W, Mu Z, Wang Z, Huang Y, Wu D, Lu P, et al. Hard-carbon-stabilized Li–Si anodes for high-performance all-solid-state Li-ion batteries. Nat Energy 2023;8:800–13. https://doi.org/10.1038/s41560-023-01279-8.
[289] Park N-Y, Lee H-U, Yu T-Y, Lee I-S, Kim H, Park S-M, et al. High-energy, long-life Ni-rich cathode materials with columnar structures for all-solid-state batteries. Nat Energy 2025;10:479–89. https://doi.org/10.1038/s41560-025-01726-8.
[290] Koerver R, Zhang W, de Biasi L, Schweidler S, Kondrakov AO, Kolling S, et al. Chemo-mechanical expansion of lithium electrode materials – on the route to mechanically optimized all-solid-state batteries. Energy Environ Sci 2018;11:2142–58. https://doi.org/10.1039/c8ee00907d.
[291] Wang C, Yu R, Duan H, Lu Q, Li Q, Adair KR, et al. Solvent-Free Approach for Interweaving Freestanding and Ultrathin Inorganic Solid Electrolyte Membranes. ACS Energy Lett 2022;7:410–6. https://doi.org/10.1021/acsenergylett.1c02261.
[292] Zhang Z, Wu L, Zhou D, Weng W, Yao X. Flexible Sulfide Electrolyte Thin Membrane with Ultrahigh Ionic Conductivity for All-Solid-State Lithium Batteries. Nano Lett 2021;21:5233–9. https://doi.org/10.1021/acs.nanolett.1c01344.
[293] Nam YJ, Cho S-J, Oh DY, Lim J-M, Kim SY, Song JH, et al. Bendable and Thin Sulfide Solid Electrolyte Film: a New Electrolyte Opportunity for Free-standing and Stackable High-Energy All-Solid-State Lithium-Ion Batteries. Nano Lett 2015;15:3317–23. https://doi.org/10.1021/acs.nanolett.5b00538.
[294] Jiang Z, Peng H, Li J, Liu Y, Zhong Y, Gu C, et al. A facile path from fast synthesis of Li-argyrodite conductor to dry forming ultrathin electrolyte membrane for high-energy-density all-solid-state lithium batteries. J Energy Chem 2022;74:309–16. https://doi.org/10.1016/j.jechem.2022.07.029.
[295] Kim D, Lee H, Roh Y, Lee J, Song J, Dzakpasu CB, et al. Thin, Highly Ionic Conductive, and Mechanically Robust Frame-based Solid Electrolyte Membrane for All-Solid-State Li Batteries. Adv Energy Mater 2023;14:2302596. https://doi.org/10.1002/aenm.202302596.
[296] Zhao X, Xiang P, Wu J, Liu Z, Shen L, Liu G, et al. Toluene Tolerated $Li_{9.88}GeP_{1.96}Sb_{0.04}S_{11.88}Cl_{0.12}$ Solid Electrolyte toward Ultrathin Membranes for All-Solid-State Lithium Batteries. Nano Lett 2022;23:227–34. https://doi.org/10.1021/acs.nanolett.2c04140.
[297] Li H, Lin Q, Wang J, Hu L, Chen F, Zhang Z, et al. A Cost-Effective Sulfide Solid Electrolyte $Li_7P_3S_{7.5}O_{3.5}$ with Low Density and Excellent Anode Compatibility. Angew Chem Int Ed 2024;63:e202407892. https://doi.org/10.1002/anie.202407892.
[298] Xue X, Liu G, Zhao X, Xie W, He H, Yao X. Superior Air-Stable $Li_4P_{0.9}Sb_{0.1}S_4I$ Solid Electrolyte for All-Solid-State Lithium Batteries. Energy Technol 2023;11:2201320. https://doi.org/10.1002/ente.202201320.
[299] Liu H, Zhu Q, Liang Y, Wang C, Li D, Zhao X, et al. Versatility of Sb-doping enabling argyrodite electrolyte with superior moisture stability and Li metal compatibility towards practical all-solid-state Li metal batteries. Chem Eng J 2023;462:142183. https://doi.org/10.1016/j.cej.2023.142183.
[300] Wang C, Hao J, Wu J, Shi H, Fan L, Wang J, et al. Enhanced Air Stability and Li Metal Compatibility of Li-Argyrodite Electrolytes Triggered by In_2O_3 Co-Doping for All-Solid-State Li Metal Batteries. Adv Funct Mater 2024;34:2313308. https://doi.org/10.1002/adfm.202313308.
[301] Wang K, Ren Q, Gu Z, Duan C, Wang J, Zhu F, et al. A cost-effective and humidity-tolerant chloride solid electrolyte for lithium batteries. Nat Commun 2021;12:4410. https://doi.org/10.1038/s41467-021-24697-2.
[302] Zhou L, Zuo T-T, Kwok CY, Kim SY, Assoud A, Zhang Q, et al. High areal capacity, long cycle life 4 V ceramic all-solid-state Li-ion batteries enabled by chloride solid electrolytes. Nat Energy 2022;7:83–93. https://doi.org/10.1038/s41560-021-00952-0.
[303] Tanaka Y, Ueno K, Mizuno K, Takeuchi K, Asano T, Sakai A. New Oxyhalide Solid Electrolytes with High Lithium Ionic Conductivity >10 mS cm^{-1} for All-Solid-State Batteries. Angew Chem Int Ed Engl 2023;62:e202217581. https://doi.org/10.1002/anie.202217581.
[304] Yin Y-C, Yang J-T, Luo J-D, Lu G-X, Huang Z, Wang J-P, et al. A $LaCl_3$-based lithium superionic conductor compatible with lithium metal. Nature 2023;616:77–83. https://doi.org/10.1038/s41586-023-05899-8.
[305] Hu L, Wang J, Wang K, Gu Z, Xi Z, Li H, et al. A cost-effective, ionically conductive and compressible oxychloride solid-state electrolyte for stable all-solid-state lithium-based batteries. Nat Commun 2023;14:3807. https://doi.org/10.1038/s41467-023-39522-1.
[306] Wang Y, Ren Z, Zhang J, Lu S, Hua C, Yuan H, et al. Prediction of Novel Trigonal Chloride Superionic Conductors as Promising Solid Electrolytes for All-Solid-State Lithium Batteries. Adv Sci 2024;11:2404213. https://doi.org/10.1002/advs.202404213.
[307] Poudel TP, Truong E, Oyekunle IP, Deck MJ, Ogbolu B, Chen Y, et al. Sliceable, Moldable, and Highly Conductive Electrolytes for All-Solid-State Batteries. ACS Energy Lett 2025;10:40–7. https://doi.org/10.1021/acsenergylett.4c02788.
[308] Kwak H, Wang S, Park J, Liu Y, Kim KT, Choi Y, et al. Emerging Halide Superionic Conductors for All-Solid-State Batteries: Design, Synthesis, and Practical applications. ACS Energy Lett 2022;7:1776–805. https://doi.org/10.1021/acsenergylett.2c00438.
[309] Nikodimos Y, Su WN, Hwang BJ. Halide Solid-State Electrolytes: Stability and Application for High Voltage All-Solid-State Li Batteries. Adv Energy Mater 2022;13:2202854. https://doi.org/10.1002/aenm.202202854.
[310] Tuo K, Sun C, Liu S. Recent Progress in and Perspectives on Emerging Halide Superionic Conductors for All-Solid-State Batteries. Electrochem Energy Rev 2023;6:17. https://doi.org/10.1007/s41918-023-00179-5.
[311] Li X, Liang J, Yang X, Adair KR, Wang C, Zhao F, et al. Progress and perspectives on halide lithium conductors for all-solid-state lithium batteries. Energy Environ Sci 2020;13:1429–61. https://doi.org/10.1039/c9ee03828k.
[312] Ginnings DC, Phipps TE. Temperature-conductance curves of solid salts. III. Halides of lithium. J Am Chem Soc 1930;52:1340–5. https://doi.org/10.1021/ja01367a006.
[313] Tomita Y, Fuji-i A, Ohki H, Yamada K, Okuda T. New lithium ion conductor Li_3InBr_6 studied by ^7Li NMR. Chem Lett 1998:223–4. https://doi.org/10.1246/cl.1998.223.
[314] Lutz HD, Schmidt W, Haeuseler H. Chloride spinels: a new group of solid lithium electrolytes. J Phys Chem Solid 1981;42:287–9. https://doi.org/10.1016/0022-3697(81)90142-6.
[315] Weppner W, Huggins RA. Ionic-conductivity of solid and liquid $LiAlCl_4$. J Electrochem Soc 1977;124:35–8. https://doi.org/10.1149/1.2133238.
[316] Weppner W, Huggins RA. Ionic-conductity of alkali-metal chloroaluminates. Phys Lett A 1976;58:245–8. https://doi.org/10.1016/0375-9601(76)90087-6.

[317] Esaka T, Okuyama R, Iwahara H. Ionic conduction in sintered fluorocomplexes Li_mMF_6, M = Al, Ti. Solid State Ion 1989;34:201–5. https://doi.org/10.1016/0167-2738(89)90040-4.

[318] Kanno R, Takeda Y, Takada K, Yamamoto O. Phase-diagram and ionic-conductivity of the lithium-chloride iron(II) chloride system. Solid State Ion 1983;9–10:153–6. https://doi.org/10.1016/0167-2738(83)90225-4.

[319] Schlem R, Muy S, Prinz N, Banik A, Shao-Horn Y, Zobel M, et al. Mechanochemical Synthesis: a Tool to Tune Cation Site Disorder and Ionic Transport Properties of Li_3MCl_6 (M = Y, Er) Superionic Conductors. Adv Energy Mater 2019;10:1903719. https://doi.org/10.1002/aenm.201903719.

[320] Wang C, Liang J, Jiang M, Li X, Mukherjee S, Adair K, et al. Interface-assisted in-situ growth of halide electrolytes eliminating interfacial challenges of all-inorganic solid-state batteries. Nano Energy 2020;76:105015. https://doi.org/10.1016/j.nanoen.2020.105015.

[321] Wang C, Liang J, Luo J, Liu J, Li X, Zhao F, et al. A universal wet-chemistry synthesis of solid-state halide electrolytes for all-solid-state lithium-metal batteries. Sci Adv 2021;7:eabh1896. https://doi.org/10.1126/sciadv.abh1896.

[322] Wang G, Zhang S, Wu H, Zheng M, Zhao C, Liang J, et al. Oxychloride Polyanion Clustered Solid-State Electrolytes via Hydrate-Assisted Synthesis for All-Solid-State Batteries. Adv Mater 2025;37:2410402. https://doi.org/10.1002/adma.202410402.

[323] Luo X, Cai D, Wang X, Xia X, Gu C, Tu J. A Novel Ethanol-Mediated Synthesis of Superionic Halide Electrolytes for High-Voltage All-Solid-State Lithium–Metal Batteries. ACS Appl Mater Interfaces 2022;14:29844–55. https://doi.org/10.1021/acsami.2c06216.

[324] Shao Q, Yan C, Gao M, Du W, Chen J, Yang Y, et al. New Insights into the Effects of Zr Substitution and Carbon Additive on $Li_{3-x}Er_{1-x}Zr_xCl_6$ Halide Solid Electrolytes. ACS Appl Mater Interfaces 2022;14:8095–105. https://doi.org/10.1021/acsami.1c25087.

[325] Wang H, Li Y, Tang Y, Ye D, He T, Zhao H, et al. Electrochemically Stable $Li_{3-x}In_{1-x}Hf_xCl_6$ Halide Solid Electrolytes for All-Solid-State Batteries. ACS Appl Mater Interfaces 2023;15:5504–11. https://doi.org/10.1021/acsami.2c21022.

[326] Kim SY, Kaup K, Park K-H, Assoud A, Zhou L, Liu J, et al. Lithium Ytterbium-based Halide Solid Electrolytes for High Voltage All-Solid-State Batteries. ACS Mater Lett 2021;3:930–8. https://doi.org/10.1021/acsmaterialslett.1c00142.

[327] Liang J, van der Maas E, Luo J, Li X, Chen N, Adair KR, et al. A Series of Ternary Metal Chloride Superionic Conductors for High-Performance All-Solid-State Lithium Batteries. Adv Energy Mater 2022;12:2103921. https://doi.org/10.1002/aenm.202103921.

[328] Helm B, Schlem R, Wankmiller B, Banik A, Gautam A, Ruhl J, et al. Exploring Aliovalent Substitutions in the Lithium Halide Superionic Conductor $Li_{3-x}In_{1-x}Zr_xCl_6$ ($0 \leq x \leq 0.5$). Chem Mater 2021;33:4773–82. https://doi.org/10.1021/acs.chemmater.1c01348.

[329] Sebti E, Evans HA, Chen H, Richardson PM, White KM, Giovine R, et al. Stacking Faults Assist Lithium-Ion Conduction in a Halide-based Superionic Conductor. J Am Chem Soc 2022;144:5795–811. https://doi.org/10.1021/jacs.1c11335.

[330] Yu S, Noh J, Kim B, Song J-H, Oh K, Yoo J, et al. Design of a trigonal halide superionic conductor by regulating cation order-disorder. Science 2023;382:573–9. https://doi.org/10.1126/science.adg6591.

[331] Li R, Lu P, Liang X, Liu L, Avdeev M, Deng Z, et al. Superionic Conductivity Invoked by Enhanced Correlation Migration in Lithium Halides Solid Electrolytes. ACS Energy Lett 2024;9:1043–52. https://doi.org/10.1021/acsenergylett.3c02496.

[332] Park K-H, Kaup K, Assoud A, Zhang Q, Wu X, Nazar LF. High-Voltage Superionic Halide Solid Electrolytes for All-Solid-State Li-Ion Batteries. ACS Energy Lett 2020;5:533–9. https://doi.org/10.1021/acsenergylett.9b02599.

[333] Liu Z, Chien PH, Wang S, Song S, Lu M, Chen S, et al. Tuning collective anion motion enables superionic conductivity in solid-state halide electrolytes. Nat Chem 2024;16:1584–91. https://doi.org/10.1038/s41557-024-01634-6.

[334] Wang S, Bai Q, Nolan AM, Liu Y, Gong S, Sun Q, et al. Lithium Chlorides and Bromides as Promising Solid-State Chemistries for Fast Ion Conductors with Good Electrochemical Stability. Angew Chem Int Ed 2019;58:8039–43. https://doi.org/10.1002/anie.201901938.

[335] Li X, Kim JT, Luo J, Zhao C, Xu Y, Mei T, et al. Structural regulation of halide superionic conductors for all-solid-state lithium batteries. Nat Commun 2024;15:53. https://doi.org/10.1038/s41467-023-43886-9.

[336] Wang C, Liang J, Kim JT, Sun X. Prospects of halide-based all-solid-state batteries: from material design to practical application. Sci Adv 2022;8:eadc9516. https://doi.org/10.1126/sciadv.adc9516.

[337] Luo J-D, Zhang Y, Cheng X, Li F, Tan H-Y, Zhou M-Y, et al. Halide Superionic Conductors with Non-Close-Packed Anion Frameworks. Angew Chem Int Ed 2024;63:e202400424. https://doi.org/10.1002/anie.202400424.

[338] Li X, Xu Y, Zhao C, Wu D, Wang L, Zheng M, et al. The Universal Super Cation-Conductivity in Multiple-cation mixed Chloride Solid-State Electrolytes. Angew Chem Int Ed 2023;62:e202306433. https://doi.org/10.1002/anie.202306433.

[339] Li F, Cheng X, Lu G, Yin Y-C, Wu Y-C, Pan R, et al. Amorphous Chloride Solid Electrolytes with High Li-Ion Conductivity for Stable Cycling of All-Solid-State High-Nickel Cathodes. J Am Chem Soc 2023;145:27774–87. https://doi.org/10.1021/jacs.3c10602.

[340] Zhang S, Zhao F, Chang L-Y, Chuang Y-C, Zhang Z, Zhu Y, et al. Amorphous Oxyhalide matters for Achieving Lithium Superionic Conduction. J Am Chem Soc 2024;146:2977–85. https://doi.org/10.1021/jacs.3c07343.

[341] Singh B, Wang Y, Liu J, Bazak JD, Shyamsunder A, Nazar LF. Critical Role of Framework Flexibility and Disorder in Driving High Ionic Conductivity in $LiNbOCl_4$. J Am Chem Soc 2024;146:17158–69. https://doi.org/10.1021/jacs.4c03142.

[342] Zhao F, Zhang S, Wang S, Andrei CM, Yuan H, Zhou J, et al. Revealing unprecedented cathode interface behavior in all-solid-state batteries with oxychloride solid electrolytes. Energy Environ Sci 2024;17:4055–63. https://doi.org/10.1039/d4ee00750f.

[343] Feinauer M, Euchner H, Fichtner M, Reddy MA. Unlocking the potential of Fluoride-based Solid Electrolytes for Solid-State Lithium Batteries. ACS Appl Energy Mater 2019;2:7196–203. https://doi.org/10.1021/acsaem.9b01166.

[344] Yu Y, Huang Y, Xu Z, Wu Z, Wang Z, Shao G. A High-Voltage Solid State Electrolyte based on Spinel-like Chloride made of Low-cost and Abundant Resources. Adv Funct Mater 2024;34:2315512. https://doi.org/10.1002/adfm.202315512.

[345] Gu Y, Yang K, Yao H, Li W, Zhan H, Ming X, et al. Surface modification of Li_3InCl_6 provides superior electrochemical performance for $LiMn_2O_4$ cathode materials. Chin Chem Lett 2023;34:108047. https://doi.org/10.1016/j.cclet.2022.108047.

[346] Zhou L, Kwok CY, Shyamsunder A, Zhang Q, Wu X, Nazar LF. A new halospinel superionic conductor for high-voltage all solid state lithium batteries. Energy Environ Sci 2020;13:2056–63. https://doi.org/10.1039/d0ee01017k.

[347] Zhang S, Zhao F, Wang S, Liang J, Wang J, Wang C, et al. Advanced High-Voltage All-Solid-State Li-Ion Batteries Enabled by a Dual-Halogen Solid Electrolyte. Adv Energy Mater 2021;11:2100836. https://doi.org/10.1002/aenm.202100836.

[348] Yu T, Liang J, Luo L, Wang L, Zhao F, Xu G, et al. Superionic Fluorinated Halide Solid Electrolytes for Highly Stable Li-Metal in All-Solid-State Li Batteries. Adv Energy Mater 2021;11:2101915. https://doi.org/10.1002/aenm.202101915.

[349] Song Z, Wang T, Yang H, Kan WH, Chen Y, Yu Q, et al. Promoting high-voltage stability through local lattice distortion of halide solid electrolytes. Nat Commun 2024;15:1481. https://doi.org/10.1038/s41467-024-45864-1.

[350] Lee D, Cui Z, Goodenough JB, Manthiram A. Interphase Stabilization of $LiNi_{0.5}Mn_{1.5}O_4$ Cathode for 5 V-Class All-Solid-State Batteries. Small 2023;20:2306053. https://doi.org/10.1002/smll.202306053.

[351] Zhang H-S, Lei X-C, Su D, Guo S-J, Zhu J-C, Wang X-F, et al. Surface Lattice Modulation Enables Stable Cycling of High-Loading All-solid-state Batteries at High Voltages. Angew Chem Int Ed 2024;63:e202400562. https://doi.org/10.1002/anie.202400562.

[352] Wu J, Li J, Yao X. Exploring the potential of Halide Electrolytes for Next-Generation All-Solid-State Lithium Batteries. Adv Funct Mater 2024;35:2416671. https://doi.org/10.1002/adfm.202416671.

[353] Riegger LM, Schlem R, Sann J, Zeier WG, Janek J. Lithium-Metal Anode Instability of the Superionic Halide Solid Electrolytes and the Implications for Solid-State Batteries. Angew Chem Int Ed 2021;60:6718–23. https://doi.org/10.1002/anie.202015238.

[354] Chun GH, Shim JH, Yu S. Computational Investigation of the Interfacial Stability of Lithium Chloride Solid Electrolytes in All-Solid-State Lithium Batteries. ACS Appl Mater Interfaces 2021;14:1241–8. https://doi.org/10.1021/acsami.1c22104.

[355] Koç T, Marchini F, Rousse G, Dugas R, Tarascon J-M. In Search of the best Solid Electrolyte-Layered Oxide Pairing for Assembling Practical All-Solid-State Batteries. ACS Appl Energy Mater 2021;4:13575–85. https://doi.org/10.1021/acsaem.1c02187.

[356] Koç T, Hallot M, Quemin E, Hennequart B, Dugas R, Abakumov AM, et al. Toward Optimization of the Chemical/Electrochemical Compatibility of Halide Solid Electrolytes in All-Solid-State Batteries. ACS Energy Lett 2022;7:2979–87. https://doi.org/10.1021/acsenergylett.2c01668.
[357] Rosenbach C, Walther F, Ruhl J, Hartmann M, Hendriks TA, Ohno S, et al. Visualizing the Chemical Incompatibility of Halide and Sulfide-based Electrolytes in Solid-State Batteries. Adv Energy Mater 2022;13:2203673. https://doi.org/10.1002/aenm.202203673.
[358] Deng Z, Jin Z, Chen D, Ni D, Tian M, Zhan Y, et al. Bilayer Halide Electrolytes for All-Inorganic Solid-State Lithium-Metal Batteries with Excellent Interfacial Compatibility. ACS Appl Mater Interfaces 2022;14:48619–26. https://doi.org/10.1021/acsami.2c12444.
[359] Wang S, Xu X, Cui C, Zeng C, Liang J, Fu J, et al. Air Sensitivity and Degradation Evolution of Halide Solid State Electrolytes upon Exposure. Adv Funct Mater 2021;32:2108805. https://doi.org/10.1002/adfm.202108805.
[360] Wang K, Gu Z, Liu H, Hu L, Wu Y, Xu J, et al. High-Humidity-Tolerant Chloride Solid-State Electrolyte for All-Solid-State Lithium Batteries. Adv Sci 2024;11:2305394. https://doi.org/10.1002/advs.202305394.
[361] Li X, Liang J, Adair KR, Li J, Li W, Zhao F, et al. Origin of Superionic $Li_3Y_{1-x}In_xCl_6$ Halide Solid Electrolytes with High Humidity Tolerance. Nano Lett 2020;20:4384–92. https://doi.org/10.1021/acs.nanolett.0c01156.
[362] Lei P, Wu G, Liu H, Qi X, Wu M, Li D, et al. Boosting Ion Conduction and Moisture Stability through Zn^{2+} Substitution of Chloride Electrolytes for All-Solid-State Lithium Batteries. Adv Energy Mater 2025;2405760. https://doi.org/10.1002/aenm.202405760.
[363] Wang S, Liao Y, Li S, Cui C, Liang J, Du G, et al. Ultrathin All-Inorganic Halide Solid-State Electrolyte Membranes for All-Solid-State Li-Ion Batteries. Adv Energy Mater 2023;14:2303641. https://doi.org/10.1002/aenm.202303641.
[364] Zhao B, Lu Y, Yuan B, Wang Z, Han X. Preparation of free-standing Li_3InCl_6 solid electrolytes film with infiltration-method enable roll-to-roll manufacture. Mater Lett 2022;310:131463. https://doi.org/10.1016/j.matlet.2021.131463.
[365] Mei H-x, Piccardo P, Carraro G, Smerieri M, Spotorno R. Thin-film Li_3InCl_6 electrolyte prepared by solution casting method for all-solid-state batteries. J Energy Storage 2023;72:108244. https://doi.org/10.1016/j.est.2023.108244.
[366] Dai T, Wu S, Lu Y, Yang Y, Liu Y, Chang C, et al. Inorganic glass electrolytes with polymer-like viscoelasticity. Nat Energy 2023;8:1221–8. https://doi.org/10.1038/s41560-023-01356-y.
[367] Thenuwara AC, Thompson EL, Malkowski TF, Parrotte KD, Lostracco KE, Narayan S, et al. Interplay among Metallic Interlayers, Discharge Rate, and pressure in LLZO-Based Lithium–Metal Batteries. ACS Energy Lett 2023;8:4016–23. https://doi.org/10.1021/acsenergylett.3c01514.
[368] Sun H, Liu Z, Xin M, Shi Y, Wang Y, Ma S, et al. Enabling long-term oxide based solid-state lithium metal battery through a near room-temperature sintering process. J Colloid Interface Sci 2024;653:908–16. https://doi.org/10.1016/j.jcis.2023.09.125.
[369] Kim S, Kim J-S, Miara L, Wang Y, Jung S-K, Park SY, et al. High-energy and durable lithium metal batteries using garnet-type solid electrolytes with tailored lithium-metal compatibility. Nat Commun 2022;13:1883. https://doi.org/10.1038/s41467-022-29531-x.
[370] Zhang Q, Cao D, Ma Y, Natan A, Aurora P, Zhu H. Sulfide-based Solid-State Electrolytes: Synthesis, Stability, and potential for All-Solid-State Batteries. Adv Mater 2019;31:1901131. https://doi.org/10.1002/adma.201901131.
[371] Yu C, Zhao F, Luo J, Zhang L, Sun X. Recent development of lithium argyrodite solid-state electrolytes for solid-state batteries: Synthesis, structure, stability and dynamics. Nano Energy 2021;83:105858. https://doi.org/10.1016/j.nanoen.2021.105858.
[372] Shen L, Wang Z, Xu S, Law HM, Zhou Y, Ciucci F. Harnessing database-supported high-throughput screening for the design of stable interlayers in halide-based all-solid-state batteries. Nat Commun 2025;16:3687. https://doi.org/10.1038/s41467-025-58522-x.
[373] Cuan J, Zhou Y, Zhou T, Ling S, Rui K, Guo Z, et al. Borohydride-Scaffolded Li/Na/Mg Fast Ionic Conductors for Promising Solid-State Electrolytes. Adv Mater 2019;31:1803533. https://doi.org/10.1002/adma.201803533.
[374] Pang Y, Liu Y, Yang J, Zheng S, Wang C. Hydrides for solid-state batteries: a review. Mater Today Nano 2022;18:100194. https://doi.org/10.1016/j.mtnano.2022.100194.
[375] Mohtadi R, Orimo S-i. The renaissance of hydrides as energy materials. Nat Rev Mater 2016;2:16091. https://doi.org/10.1038/natrevmats.2016.91.
[376] Schlesinger HI, Brown HC, Abraham B, Bond AC, Davidson N, Finholt AE, et al. New Developments in the Chemistry of Diborane and the Borohydrides. I. General Summary1. J Am Chem Soc 1953;75:186–90. https://doi.org/10.1021/ja01097a049.
[377] Comanescu C. Recent Development in Nanoconfined Hydrides for Energy Storage. Int J Mol Sci 2022;23:7111. https://doi.org/10.3390/ijms23137111.
[378] Boukamp BA, Huggins RA. Ionic conductivity in lithium imide. Phys Lett A 1979;72:464–6. https://doi.org/10.1016/0375-9601(79)90846-6.
[379] Bogdanović B, Schwickardi M. Ti-doped alkali metal aluminium hydrides as potential novel reversible hydrogen storage materials. J Alloy Compd 1997;253:1–9. https://doi.org/10.1016/S0925-8388(96)03049-6.
[380] Züttel A, Wenger P, Rentsch S, Sudan P, Mauron P, Emmenegger C. $LiBH_4$ a new hydrogen storage material. J Power Sources 2003;118:1–7. https://doi.org/10.1016/s0378-7753(03)00054-5.
[381] Unemoto A, Matsuo M, Orimo S-i. Complex Hydrides for Electrochemical Energy Storage. Adv Funct Mater 2014;24:2267–79. https://doi.org/10.1002/adfm.201303147.
[382] Matsuo M, Remhof A, Martelli P, Caputo R, Ernst M, Miura Y, et al. Complex Hydrides with $(BH_4)^-$ and $(NH_2)^-$ Anions as New Lithium Fast-Ion Conductors. J Am Chem Soc 2009;131:16389–91. https://doi.org/10.1021/ja907249p.
[383] Hwang S-J, Bowman RC, Reiter JW, Rijssenbeek SGL, Zhao J-C, et al. NMR Confirmation for Formation of $[B_{12}H_{12}]^{2-}$ Complexes during Hydrogen Desorption from Metal Borohydrides. J Phys Chem C 2008;112:3164–9. https://doi.org/10.1021/jp710894t.
[384] Zhang Y, Majzoub E, Ozoliņš V, Wolverton C. Theoretical Prediction of Metastable Intermediates in the Decomposition of $Mg(BH_4)_2$. J Phys Chem C 2012;116:10522–8. https://doi.org/10.1021/jp302303z.
[385] Paskevicius M, Pitt MP, Brown DH, Sheppard DA, Chumphongphan S, Buckley CE. First-order phase transition in the $Li_2B_{12}H_{12}$ system. PCCP 2013;15:15825–8. https://doi.org/10.1039/C3CP53090F.
[386] Teprovich JA, Colón-Mercado H, Washington Ii AL, Ward PA, Greenway S, Missimer DM, et al. Bi-functional $Li_2B_{12}H_{12}$ for energy storage and conversion applications: solid-state electrolyte and luminescent down-conversion dye. J Mater Chem A 2015;3:22853–9. https://doi.org/10.1039/C5TA06549F.
[387] Sau K, Ikeshoji T, Kim S, Takagi S, Orimo S-i. Comparative Molecular Dynamics Study of the Roles of Anion–Cation and Cation–Cation Correlation in Cation Diffusion in $Li_2B_{12}H_{12}$ and $LiCB_{11}H_{12}$. Chem Mater 2021;33:2357–69. https://doi.org/10.1021/acs.chemmater.0c04473.
[388] Campos dos Santos E, Sato R, Kisu K, Sau K, Jia X, Yang F, et al. Explore the Ionic Conductivity Trends on $B_{12}H_{12}$ Divalent *Closo*-Type complex Hydride Electrolytes. Chem Mater 2023;35:5996–6004. https://doi.org/10.1021/acs.chemmater.3c00975.
[389] Orimo S-I, Nakamori Y, Ohba N, Miwa K, Aoki M, Towata S-i, et al. Experimental studies on intermediate compound of $LiBH_4$. Appl Phys Lett 2006;89:021920. https://doi.org/10.1063/1.2221880.
[390] Her J-H, Yousufuddin M, Zhou W, Jalisatgi SS, Kulleck JG, Zan JA, et al. Crystal Structure of $Li_2B_{12}H_{12}$: a possible Intermediate Species in the Decomposition of $LiBH_4$. Inorg Chem 2008;47:9757–9. https://doi.org/10.1021/ic801345h.
[391] Wang Z, Lin X, Han Y, Cai J, Wu S, Yu X, et al. Harnessing artificial intelligence to holistic design and identification for solid electrolytes. Nano Energy 2021;89:106337. https://doi.org/10.1016/j.nanoen.2021.106337.
[392] Merchant A, Batzner S, Schoenholz SS, Aykol M, Cheon G, Cubuk ED. Scaling deep learning for materials discovery. Nature 2023;624:80–5. https://doi.org/10.1038/s41586-023-06735-9.
[393] Wang Q, Yang F, Wang Y, Zhang D, Sato R, Zhang L, et al. Unraveling the Complexity of Divalent Hydride Electrolytes in Solid-State Batteries via a Data-Driven Framework with Large Language Model. Angew Chem Int Ed 2025;64:e202506573. https://doi.org/10.1002/anie.202506573.
[394] Ley MB, Boulineau S, Janot R, Filinchuk Y, Jensen TR. New Li Ion Conductors and Solid State Hydrogen Storage Materials: $LiM(BH_4)_3Cl$, M = La, Gd. J Phys Chem C 2012;116:21267–76. https://doi.org/10.1021/jp307762g.
[395] Tang WS, Unemoto A, Zhou W, Stavila V, Matsuo M, Wu H, et al. Unparalleled lithium and sodium superionic conduction in solid electrolytes with large monovalent cage-like anions. Energy Environ Sci 2015;8:3637–45. https://doi.org/10.1039/C5EE02941D.
[396] Tang WS, Matsuo M, Wu H, Stavila V, Zhou W, Talin AA, et al. Liquid-like Ionic Conduction in Solid Lithium and Sodium Monocarba-*closo*-Decaborates Near or at Room Temperature. Adv Energy Mater 2016;6:1502237. https://doi.org/10.1002/aenm.201502237.

[397] Xu G, Zhang X, Sun S, Zhou Y, Liu Y, Yang H, et al. Synergized Tricomponent All-Inorganics Solid Electrolyte for Highly Stable Solid-State Li-Ion Batteries. Adv Sci 2023;10:2207627. https://doi.org/10.1002/advs.202207627.

[398] Han J-H, Kim DK, Lee YJ, Lee Y-S, Yi K-W, Cho YW. Borohydride and halide dual-substituted lithium argyrodites. Mater Horiz 2024;11:251–61. https://doi.org/10.1039/D3MH01450A.

[399] Liu H, Zhou X, Ye M, Shen J. Ion Migration Mechanism Study of Hydroborate/Carborate Electrolytes for All-Solid-State Batteries. Electrochem Energy Rev 2023;6:31. https://doi.org/10.1007/s41918-023-00191-9.

[400] Yin LC, Wang P, Kang XD, Sun CH, Cheng HM. Functional anion concept: effect of fluorine anion on hydrogen storage of sodium alanate. PCCP 2007;9: 1499–502. https://doi.org/10.1039/b610257c.

[401] Yin L, Wang P, Fang Z, Cheng H. Thermodynamically tuning $LiBH_4$ by fluorine anion doping for hydrogen storage: a density functional study. Chem Phys Lett 2008;450:318–21. https://doi.org/10.1016/j.cplett.2007.11.060.

[402] Matsuo M, Orimo S-i. Lithium Fast-Ionic Conduction in complex Hydrides: Review and prospects. Adv Energy Mater 2011;1:161–72. https://doi.org/10.1002/aenm.201000012.

[403] Ikeshoji T, Tsuchida E, Morishita T, Ikeda K, Matsuo M, Kawazoe Y, et al. Fast-ionic conductivity of Li^+ in $LiBH_4$. Phys Rev B 2011;83:144301. https://doi.org/10.1103/PhysRevB.83.144301.

[404] Arnbjerg LM, Ravnsbæk DB, Filinchuk Y, Vang RT, Cerenius Y, Besenbacher F, et al. Structure and Dynamics for $LiBH_4$−LiCl Solid Solutions. Chem Mater 2009; 21:5772–82. https://doi.org/10.1021/cm902013k.

[405] Cascallana-Matias I, Keen DA, Cussen EJ, Gregory DH. Phase Behavior in the $LiBH_4$–LiBr System and Structure of the Anion-Stabilized Fast Ionic. High Temperature Phase Chem Mater 2015;27:7780–7. https://doi.org/10.1021/acs.chemmater.5b03642.

[406] Gulino V, Brighi M, Dematteis EM, Murgia F, Nervi C, Černý R, et al. Phase Stability and Fast Ion Conductivity in the Hexagonal $LiBH_4$–LiBr–LiCl Solid solution. Chem Mater 2019;31:5133–44. https://doi.org/10.1021/acs.chemmater.9b01035.

[407] Li S, Qiu P, Kang J, Ma Y, Zhang Y, Yan Y, et al. Iodine-Substituted Lithium/Sodium *closo*-Decaborates: Syntheses, Characterization, and Solid-State Ionic Conductivity. ACS Appl Mater Interfaces 2021;13:17554–64. https://doi.org/10.1021/acsami.1c01659.

[408] Toyama N, Kim S, Oguchi H, Sato T, Takagi S, Tazawa M, et al. Lithium ion conductivity of complex hydrides incorporating multiple *closo*-type complex anions. J Energy Chem 2019;38:84–7. https://doi.org/10.1016/j.jechem.2019.01.009.

[409] Kim S, Oguchi H, Toyama N, Sato T, Takagi S, Otomo T, et al. A complex hydride lithium superionic conductor for high-energy-density all-solid-state lithium metal batteries. Nat Commun 2019;10:1081. https://doi.org/10.1038/s41467-019-09061-9.

[410] Payandeh S, Rentsch D, Łodziana Z, Asakura R, Bigler L, Černý R, et al. Nido-Hydroborate-based Electrolytes for All-Solid-State Lithium Batteries. Adv Funct Mater 2021;31:2010046. https://doi.org/10.1002/adfm.202010046.

[411] Braun H, Asakura R, Remhof A, Battaglia C. Hydroborate Solid-State Lithium Battery with High-Voltage NMC811 Cathode. ACS Energy Lett 2024;9:707–14. https://doi.org/10.1021/acsenergylett.3c02117.

[412] Zhou C, Grinderslev JB, Skov LN, Jørgensen M, Li Y, Skibsted J, et al. Polymorphism, ionic conductivity and electrochemical properties of lithium *closo*-deca- and dodeca-borates and their composites, $Li_2B_{10}H_{10}$–$Li_2B_{12}H_{12}$. J Mater Chem A 2022;10:16137–51. https://doi.org/10.1039/D2TA00337F.

[413] He T, Pachfule P, Wu H, Xu Q, Chen P. Hydrogen carriers. Nat Rev Mater 2016;1:16059. https://doi.org/10.1038/natrevmats.2016.59.

[414] Xiong Z, Wu G, Hu J, Chen P. Ternary Imides for Hydrogen Storage. Adv Mater 2004;16:1522–5. https://doi.org/10.1002/adma.200400571.

[415] Luo W. ($LiNH_2$–MgH_2): a viable hydrogen storage system. J Alloy Compd 2004;381:284–7. https://doi.org/10.1016/j.jallcom.2004.03.119.

[416] Leng HY, Ichikawa T, Hino S, Hanada N, Isobe S, Fujii H. New Metal−N−H System Composed of $Mg(NH_2)_2$ and LiH for Hydrogen Storage. J Phys Chem B 2004;108:8763–5. https://doi.org/10.1021/jp048002j.

[417] Zhang T, Isobe S, Matsuo M, Orimo S-i, Wang Y, Hashimoto N, et al. Effect of Lithium Ion Conduction on Hydrogen Desorption of $LiNH_2$–LiH Solid Composite. ACS Catal 2015;5:1552–5. https://doi.org/10.1021/cs501782y.

[418] Matsuo M, Sato T, Miura Y, Oguchi H, Zhou Y, Maekawa H, et al. Synthesis and Lithium Fast-Ion Conductivity of a New complex Hydride $Li_3(NH_2)_2I$ with Double-Layered Structure. Chem Mater 2010;22:2702–4. https://doi.org/10.1021/cm1006857.

[419] Yan Y, Kühnel R-S, Remhof A, Duchêne L, Reyes EC, Rentsch D, et al. A Lithium Amide-Borohydride Solid-State Electrolyte with Lithium-Ion Conductivities Comparable to Liquid Electrolytes. Adv Energy Mater 2017;7:1700294. https://doi.org/10.1002/aenm.201700294.

[420] Skoryunov RV, Babanova OA, Soloninin AV, Skripov AV, Orimo S. Nuclear magnetic resonance study of atomic motion in the mixed borohydride-amide $Li_2(BH_4)$ (NH_2). J Alloy Compd 2020;823:153821. https://doi.org/10.1016/j.jallcom.2020.153821.

[421] Ebechidi N, Ahmed R, Oyewole O, Bello A, Ngene P, Soboyejo W. Charge-discharge-induced local strain distributions in a lithium amide-borohydride-iodide [$LiBH_4$-$LiNH_2$-LiI] solid electrolyte. J Energy Storage 2022;47:103600. https://doi.org/10.1016/j.est.2021.103600.

[422] Fang Z-Z, Kang X-D, Luo J-H, Wang P, Li H-W, Orimo S-i. Formation and Hydrogen Storage Properties of Dual-Cation (Li, Ca) Borohydride. J Phys Chem C 2010;114:22736–41. https://doi.org/10.1021/jp109260g.

[423] Lee JY, Ravnsbæk D, Lee Y-S, Kim Y, Cerenius Y, Shim J-H, et al. Decomposition Reactions and Reversibility of the $LiBH_4$−$Ca(BH_4)_2$ Composite. J Phys Chem C 2009;113:15080–6. https://doi.org/10.1021/jp904400b.

[424] Sveinbjörnsson D, Blanchard D, Myrdal JSG, Younesi R, Viskinde R, Riktor MD, et al. Ionic conductivity and the formation of cubic CaH_2 in the $LiBH_4$–Ca $(BH_4)_2$ composite. J Solid State Chem 2014;211:81–9. https://doi.org/10.1016/j.jssc.2013.12.006.

[425] Xiang M, Zhang Y, Zhan L, Zhu Y, Guo X, Chen J, et al. Study on x$LiBH_4$-$NaBH_4$ (x = 1.6, 2.3, and 4) composites with enhanced lithium ionic conductivity. J Alloy Compd 2017;729:936–41. https://doi.org/10.1016/j.jallcom.2017.08.253.

[426] Yu XB, Grant DM, Walker GS. A new dehydrogenation mechanism for reversible multicomponent borohydride systems—The role of Li–Mg alloys. Chem Commun 2006:3906–8. https://doi.org/10.1039/B607869A.

[427] Zhan L, Zhang Y, Xiang M, Zhu Y, Guo X, Chen J, et al. The lithium ionic conductivity of 2$LiBH_4$-MgH_2 composite as solid electrolyte. Inorg Chem Commun 2017;83:62–5. https://doi.org/10.1016/j.inoche.2017.05.010.

[428] Xiang M, Zhang Y, Zhu Y, Guo X, Chen J, Li L. Ternary $LiBH_4$-$NaBH_4$-MgH_2 composite as fast ionic conductor. Solid State Ion 2018;324:109–13. https://doi.org/10.1016/j.ssi.2018.06.015.

[429] Ley MB, Ravnsbæk DB, Filinchuk Y, Lee Y-S, Janot R, Cho YW, et al. $LiCe(BH_4)_3Cl$, a New Lithium-Ion Conductor and Hydrogen Storage Material with Isolated Tetranuclear Anionic Clusters. Chem Mater 2012;24:1654–63. https://doi.org/10.1021/cm300792t.

[430] Guo Y, Xia G, Zhu Y, Gao L, Yu X. Hydrogen release from amminelithium borohydride, $LiBH_4{\cdot}NH_3$. Chem Commun 2010;46:2599–601. https://doi.org/10.1039/B924057H.

[431] Tan Y, Guo Y, Li S, Sun W, Zhu Y, Li Q, et al. A liquid-based eutectic system: $LiBH_4{\cdot}NH_3$–nNH_3BH_3 with high dehydrogenation capacity at moderate temperature. J Mater Chem 2011;21:14509–15. https://doi.org/10.1039/C1JM11158B.

[432] Tan Y, Chen X, Xia G, Yu X. Efficient chemical regeneration of $LiBH_4NH_3$ spent fuel for hydrogen storage. Int J Hydrogen Energy 2015;40:146–50. https://doi.org/10.1016/j.ijhydene.2014.11.040.

[433] Skoryunov RV, Babanova OA, Soloninin AV, Grinderslev JB, Skripov AV, Jensen TR. Dynamical properties of lithium borohydride – ammine composite $LiBH_4{\cdot}NH_3$: a nuclear magnetic resonance study. J Alloy Compd 2022;894:162446. https://doi.org/10.1016/j.jallcom.2021.162446.

[434] Zhu M, Pang Y, Lu F, Shi X, Yang J, Zheng S. In Situ formed Li–B–H complex with High Li-Ion Conductivity as a potential Solid Electrolyte for Li Batteries. ACS Appl Mater Interfaces 2019;11:14136–41. https://doi.org/10.1021/acsami.9b01326.

[435] Shi X, Pang Y, Wang B, Sun H, Wang X, Li Y, et al. In situ forming LiF nanodecorated electrolyte/electrode interfaces for stable all-solid-state batteries. Mater Today Nano 2020;10:100079. https://doi.org/10.1016/j.mtnano.2020.100079.

[436] de Kort LM, Gulino V, Blanchard D, Ngene P. Effects of $LiBF_4$ Addition on the Lithium-Ion Conductivity of $LiBH_4$. Molecules 2022;27:2187. https://doi.org/10.3390/molecules27072187.

[437] Zhao W, Zhang R, Li H, Zhang Y, Wang Y, Wu C, et al. Li-Ion Conductivity Enhancement of $LiBH_4{\cdot}xNH_3$ with *In Situ* formed Li_2O Nanoparticles. ACS Appl Mater Interfaces 2021;13:31635–41. https://doi.org/10.1021/acsami.1c06164.

[438] Zhang R, Zhao W, Liu Z, Wei S, Yan Y, Chen Y. Enhanced room temperature ionic conductivity of the $LiBH_4{\cdot}1/2NH_3$–Al_2O_3 composite. Chem Commun 2021; 57:2380–3. https://doi.org/10.1039/D0CC07296F.
[439] Zhang R, Li H, Wang Q, Wei S, Yan Y, Chen Y. Size effect of MgO on the Ionic Conduction Properties of a $LiBH_4{\cdot}1/2NH_3$–MgO Nanocomposite. ACS Appl Mater Interfaces 2022;14:8947–54. https://doi.org/10.1021/acsami.1c20976.
[440] Zettl R, Gombotz M, Clarkson D, Greenbaum SG, Ngene P, de Jongh PE, et al. Li-Ion Diffusion in Nanoconfined $LiBH_4$-LiI/Al_2O_3: from 2D Bulk Transport to 3D Long-Range Interfacial Dynamics. ACS Appl Mater Interfaces 2020;12:38570–83. https://doi.org/10.1021/acsami.0c10361.
[441] Scheiber T, Gadermaier B, Hogrefe K, Zettl R, Wilkening HMR. Thermoresistant Defects Preserve Fast Ion Conduction in $LiBH_4$–ZrO_2 Conductor–Insulator Nanocomposites. Chem Mater 2023;35:10504–14. https://doi.org/10.1021/acs.chemmater.3c02026.
[442] Lu F, Pang Y, Zhu M, Han F, Yang J, Fang F, et al. A High-Performance Li–B–H Electrolyte for All-Solid-State Li Batteries. Adv Funct Mater 2019;29:1809219. https://doi.org/10.1002/adfm.201809219.
[443] Hu L, Wang H, Liu Y, Fang F, Yuan B, Hu R. Interface Modification and Halide Substitution to Achieve High Ionic Conductivity in $LiBH_4$-based Electrolytes for all-Solid-State Batteries. ACS Appl Mater Interfaces 2022;14:1260–9. https://doi.org/10.1021/acsami.1c22561.
[444] Wu Z, Wang K, Sun W, Li Z, Ma Z, Zhu Y, et al. Defective Boron Nitride Inducing the Lithium-ion Migration on the Sub-Surface of $LiBH_4$. Adv Funct Mater 2022; 32:2205677. https://doi.org/10.1002/adfm.202205677.
[445] Blanchard D, Nale A, Sveinbjörnsson D, Eggenhuisen TM, Verkuijlen MHW, Suwarno, et al. Nanoconfined $LiBH_4$ as a Fast Lithium Ion Conductor. Adv Funct Mater 2015;25:184–92. https://doi.org/10.1002/adfm.201402538.
[446] de Kort LM, Harmel J, de Jongh PE, Ngene P. The effect of nanoscaffold porosity and surface chemistry on the Li-ion conductivity of $LiBH_4$–$LiNH_2$/metal oxide nanocomposites. J Mater Chem A 2020;8:20687–97. https://doi.org/10.1039/D0TA07600G.
[447] Liu Z, Zhang T, Ju S, Ji Y, Hu Z, Lv Y, et al. Fast Ionic Migration from Bulk to Interface in the $Li(NH_3)_xBH_4$@SiO_2 Composite. ACS Appl Energy Mater 2022;5: 14301–10. https://doi.org/10.1021/acsaem.2c02871.
[448] Yamauchi A, Sakuda A, Hayashi A, Tatsumisago M. Preparation and ionic conductivities of $(100-x)(0.75Li_2S{\cdot}0.25P_2S_5){\cdot}xLiBH_4$ glass electrolytes. J Power Sources 2013;244:707–10. https://doi.org/10.1016/j.jpowsour.2012.12.001.
[449] Sakuda A, Yamauchi A, Yubuchi S, Kitamura N, Idemoto Y, Hayashi A, et al. Mechanochemically Prepared Li_2S–P_2S_5–$LiBH_4$ Solid Electrolytes with an Argyrodite Structure. ACS Omega 2018;3:5453–8. https://doi.org/10.1021/acsomega.8b00377.
[450] Jang Y-J, Seo H, Lee Y-S, Kang S, Cho W, Cho YW, et al. Lithium Superionic Conduction in BH_4-Substituted Thiophosphate Solid Electrolytes. Adv Sci 2023;10: 2204942. https://doi.org/10.1002/advs.202204942.
[451] Seo H, Jang Y-J, Yoo J, Han J-H, Lee Y-S, Jung JY, et al. Enhancement of ionic conductivity in Li argyrodite solid electrolytes with bromide and borohydride anions for all-solid-state batteries. J Mater Chem A 2024;12:27022–30. https://doi.org/10.1039/D4TA04426F.
[452] Kim T, Lee T, Kim S. Synthesis and Electrochemical Properties of Hydrosulfide Solid Electrolytes. Korean J Chem Eng 2024. https://doi.org/10.1007/s11814-024-00243-w.
[453] Lee T, Park H, Joo S, Kim H, Kim J, Kim T, et al. Hydrogen-Rich Argyrodite Solid Electrolytes for NCM/Li All-Solid-State batteries. ACS Energy Lett 2024;9: 4493–500. https://doi.org/10.1021/acsenergylett.4c01639.
[454] Wei Y, Li Z, Chen Z, Gao P, Ma Q, Gao M, et al. Polymeric Electronic Shielding Layer Enabling Superior Dendrite suppression for All-Solid-State Lithium Batteries. ACS Nano 2024;18:5965–80. https://doi.org/10.1021/acsnano.4c00279.
[455] Pang Y, Wang X, Shi X, Xu F, Sun L, Yang J, et al. Solid-State Prelithiation Enables High-Performance Li-Al-H Anode for Solid-State Batteries. Adv Energy Mater 2020;10:1902795. https://doi.org/10.1002/aenm.201902795.
[456] Kisu K, Kim S, Yoshida R, Oguchi H, Toyama N, Orimo S-i. Microstructural analyses of all-solid-state Li–S batteries using $LiBH_4$-based solid electrolyte for prolonged cycle performance. J Energy Chem 2020;50:424–9. https://doi.org/10.1016/j.jechem.2020.03.069.
[457] Wang J, Yang J, Xie J, Xu N. A Novel Conductive Polymer–Sulfur Composite Cathode Material for Rechargeable Lithium Batteries. Adv Mater 2002;14:963–5. https://doi.org/10.1002/1521-4095(20020705)14:13/14<963::AID-ADMA963>3.0.CO;2-P.
[458] Huang J, Shao Y, Liu Z, Lv Y, Guo F, Tu Y, et al. Nano sulfurized polyacrylonitrile cathode for high performance solid-state lithium–sulfur batteries. J Power Sources 2023;570:233045. https://doi.org/10.1016/j.jpowsour.2023.233045.
[459] Unemoto A, Ikeshoji T, Yasaku S, Matsuo M, Stavila V, Udovic TJ, et al. Stable Interface Formation between TiS_2 and $LiBH_4$ in Bulk-Type All-Solid-State Lithium Batteries. Chem Mater 2015;27:5407–16. https://doi.org/10.1021/acs.chemmater.5b02110.
[460] Wang L, Xu S, Wang Z, Yang E, Jiang W, Zhang S, et al. A nano fiber–gel composite electrolyte with high Li^+ transference number for application in quasi-solid batteries. eScience 2023;3:100090. https://doi.org/10.1016/j.esci.2022.100090.
[461] Yi T, Zhao E, He Y, Liang T, Wang H. Quantification and visualization of spatial distribution of dendrites in solid polymer electrolytes. eScience 2024;4: 100182. https://doi.org/10.1016/j.esci.2023.100182.
[462] Watanabe M, Kanba M, Matsuda H, Tsunemi K, Mizoguchi K, Tsuchida E, et al. High lithium ionic conductivity of polymeric solid electrolytes. Makromol Chem Rapid Commun 1981;2:741–4. https://doi.org/10.1002/marc.1981.030021208.
[463] Weston J, Steele B. Effects of inert fillers on the mechanical and electrochemical properties of lithium salt-poly(ethylene oxide) polymer electrolytes. Solid State Ion 1982;7:75–9. https://doi.org/10.1016/0167-2738(82)90072-8.
[464] Armand M, Moursli F. Agence Nationale de Valorisation de la Recherche. France Patent 1983:2527602A1.
[465] Croce F, Appetecchi GB, Persi L, Scrosati B. Nanocomposite polymer electrolytes for lithium batteries. Nature 1998;394:456–8. https://doi.org/10.1038/28818.
[466] Lee MJ, Han J, Lee K, Lee YJ, Kim BG, Jung K-N, et al. Elastomeric electrolytes for high-energy solid-state lithium batteries. Nature 2022;601:217–22. https://doi.org/10.1038/s41586-021-04209-4.
[467] Zhang W, Koverga V, Liu S, Zhou J, Wang J, Bai P, et al. Single-phase local-high-concentration solid polymer electrolytes for lithium-metal batteries. Nat Energy 2024;9:386–400. https://doi.org/10.1038/s41560-023-01443-0.
[468] Robitaille CD, Fauteux D. Phase Diagrams and Conductivity Characterization of some PEO–LiX Electrolytes. J Electrochem Soc 1986;133:315. https://doi.org/10.1149/1.2108569.
[469] Chen L, Li Y, Li S-P, Fan L-Z, Nan C-W, Goodenough JB. PEO/garnet composite electrolytes for solid-state lithium batteries: from "ceramic-in-polymer" to "polymer-in-ceramic". Nano Energy 2018;46:176–84. https://doi.org/10.1016/j.nanoen.2017.12.037.
[470] Xue Z, He D, Xie X. Poly(ethylene oxide)-based electrolytes for lithium-ion batteries. J Mater Chem A 2015;3:19218–53. https://doi.org/10.1039/C5TA03471J.
[471] Bruce PG. Ion–polyether coordination complexes: crystalline ionic conductors for clean energy storage. Dalton Trans 2006:1365–9. https://doi.org/10.1039/B517247K.
[472] Judez X, Martinez-Ibañez M, Santiago A, Armand M, Zhang H, Li C. Quasi-solid-state electrolytes for lithium sulfur batteries: advances and perspectives. J Power Sources 2019;438:226985. https://doi.org/10.1016/j.jpowsour.2019.226985.
[473] Yang X, Jiang M, Gao X, Bao D, Sun Q, Holmes N, et al. Determining the limiting factor of the electrochemical stability window for PEO-based solid polymer electrolytes: main chain or terminal –OH group? Energy Environ Sci 2020;13:1318–25. https://doi.org/10.1039/D0EE00342E.
[474] Feuillade G, Perche P. Ion-conductive macromolecular gels and membranes for solid lithium cells. J Appl Electrochem 1975;5:63–9. https://doi.org/10.1007/BF00625960.
[475] Xi G, Xiao M, Wang S, Han D, Li Y, Meng Y. Polymer-Based Solid Electrolytes: Material selection, Design, and Application. Adv Funct Mater 2020;31:2007598. https://doi.org/10.1002/adfm.202007598.
[476] Ebadi M, Marchiori C, Mindemark J, Brandell D, Araujo CM. Assessing structure and stability of polymer/lithium-metal interfaces from first-principles calculations. J Mater Chem A 2019;7:8394–404. https://doi.org/10.1039/C8TA12147H.
[477] Yang K, Chen L, Ma J, Lai C, Huang Y, Mi J, et al. Stable Interface Chemistry and Multiple Ion Transport of Composite Electrolyte Contribute to Ultra-long Cycling Solid-State $LiNi_{0.8}Co_{0.1}Mn_{0.1}O_2$/Lithium Metal Batteries. Angew Chem Int Ed 2021;60:24668–75. https://doi.org/10.1002/anie.202110917.

[478] Huang YF, Zeng JP, Li SF, Dai C, Liu JF, Liu C, et al. Conformational Regulation of Dielectric Poly(Vinylidene Fluoride)-Based Solid-State Electrolytes for Efficient Lithium Salt Dissociation and Lithium-Ion Transportation. Adv Energy Mater 2023;13:2203888. https://doi.org/10.1002/aenm.202203888.
[479] Zhai P, Yang Z, Wei Y, Guo X, Gong Y. Two-Dimensional Fluorinated Graphene Reinforced Solid Polymer Electrolytes for High-Performance Solid-State Lithium Batteries. Adv Energy Mater 2022;12:2200967. https://doi.org/10.1002/aenm.202200967.
[480] Xu H, Zhang H, Ma J, Xu G, Dong T, Chen J, et al. Overcoming the challenges of 5 V Spinel $LiNi_{0.5}Mn_{1.5}O_4$ Cathodes with Solid Polymer Electrolytes. ACS Energy Lett 2019;4:2871–86. https://doi.org/10.1021/acsenergylett.9b01871.
[481] Iijima T, Toyoguchi Y, Eda N. Quasi-solid organic electrolytes gelatinized with polymethyl-methacrylate and their applications for lithium batteries. Cell Rep Phys Sci 1985;53:619–23. https://doi.org/10.1016/j.xcrp.2021.100722.
[482] Huo S, Sheng L, Xue W, Wang L, Xu H, Zhang H, et al. Challenges of polymer electrolyte with wide electrochemical window for high energy solid-state lithium batteries. InfoMat 2023;5:e12394. https://doi.org/10.1002/inf2.12394.
[483] Wang S, Li J, Li T, Huang W, Wang L, Tao S. Li^+ affinity ultra-thin solid polymer electrolyte for advanced all-solid-state lithium-ion battery. Chem Eng J 2023; 461:141995. https://doi.org/10.1016/j.cej.2023.141995.
[484] Chen Z, Ma X, Hou Y, Cui H, Li X, Yang Q, et al. Grafted MXenes based Electrolytes for 5V-Class Solid-State Batteries. Adv Funct Mater 2023;33:2214539. https://doi.org/10.1002/adfm.202214539.
[485] Xiao G, Xu H, Bai C, Liu M, He Y-B. Progress and perspectives of in situ polymerization method for lithium-based batteries. Interdiscip Mater 2023;2:609–34. https://doi.org/10.1002/idm2.12109.
[486] Ren Z, Li J, Cai M, Yin R, Liang J, Zhang Q, et al. An *in situ* formed copolymer electrolyte with high ionic conductivity and high lithium-ion transference number for dendrite-free solid-state lithium metal batteries. J Mater Chem A 2023;11:1966–77. https://doi.org/10.1039/d2ta07516d.
[487] Wen S, Luo C, Wang Q, Wei Z, Zeng Y, Jiang Y, et al. Integrated design of ultrathin crosslinked network polymer electrolytes for flexible and stable all-solid-state lithium batteries. Energy Storage Mater 2022;47:453–61. https://doi.org/10.1016/j.ensm.2022.02.035.
[488] Mu K, Wang D, Dong W, Liu Q, Song Z, Xu W, et al. Hybrid Crosslinked Solid Polymer Electrolyte via In-Situ Solidification Enables High-Performance Solid-State Lithium Metal Batteries. Adv Mater 2023;35:2304686. https://doi.org/10.1002/adma.202304686.
[489] Wang H, Song J, Zhang K, Fang Q, Zuo Y, Yang T, et al. A strongly complexed solid polymer electrolyte enables a stable solid state high-voltage lithium metal battery. Energy Environ Sci 2022;15:5149–58. https://doi.org/10.1039/d2ee02904a.
[490] Guo K, Wang J, Shi Z, Wang Y, Xie X, Xue Z. One-step In Situ Polymerization: a Facile Design Strategy for Block Copolymer Electrolytes. Angew Chem Int Ed 2023;62:e202213606. https://doi.org/10.1002/anie.202213606.
[491] Gong Y, Wang C, Xin M, Chen S, Xu P, Li D, et al. Ultra-thin and high-voltage-stable Bi-phasic solid polymer electrolytes for high-energy-density Li metal batteries. Nano Energy 2024;119:109054. https://doi.org/10.1016/j.nanoen.2023.109054.
[492] Zhang D, Liu Y, Sun Z, Liu Z, Xu X, Xi L, et al. Eutectic-based Polymer Electrolyte with the Enhanced Lithium Salt Dissociation for High-Performance Lithium Metal Batteries. Angew Chem Int Ed 2023;62:e202310006. https://doi.org/10.1002/anie.202310006.
[493] Liu Y, Zeng Q, Li Z, Chen A, Guan J, Wang H, et al. Recent Development in Topological Polymer Electrolytes for Rechargeable Lithium Batteries. Adv Sci 2023; 10:2206978. https://doi.org/10.1002/advs.202206978.
[494] Li S, Guo K, Chen G, Wang J, Wang Y, Zhou X, et al. A self-catalyzed strategy towards facile fabrication of bottlebrush polyester-based solid polymer electrolytes. Energy Storage Mater 2022;46:461–71. https://doi.org/10.1016/j.ensm.2022.01.029.
[495] Guo K, Li S, Chen G, Wang J, Wang Y, Xie X, et al. One-Pot Synthesis of Polyester-based Linear and Graft Copolymers for Solid Polymer Electrolytes. CCS Chem 2022;4:3134–49. https://doi.org/10.31635/ccschem.021.202101364.
[496] Su Y, Rong X, Gao A, Liu Y, Li J, Mao M, et al. Rational design of a topological polymeric solid electrolyte for high-performance all-solid-state alkali metal batteries. Nat Commun 2022;13:4181. https://doi.org/10.1038/s41467-022-31792-5.
[497] Su Y, Rong X, Li H, Huang X, Chen L, Liu B, et al. High-Entropy Microdomain Interlocking Polymer Electrolytes for Advanced All-Solid-State Battery Chemistries. Adv Mater 2023;35:2209402. https://doi.org/10.1002/adma.202209402.
[498] Kei H, Toru S, Hiroyuki A, Hideaki Y, Koichi M, Kohzo I. Strain-induced crystallization and phase separation used for fabricating a tough and stiff slide-ring solid polymer electrolyte. Sci Adv 2023;9:eadi8505. https://doi.org/10.1126/sciadv.adi8505.
[499] Liu J, Shen X, Zhou J, Wang M, Niu C, Qian T, et al. Nonflammable and High-Voltage-Tolerated Polymer Electrolyte Achieving High Stability and Safety in 4.9 V-Class Lithium Metal Battery. ACS Appl Mater Interfaces 2019;11:45048–56. https://doi.org/10.1021/acsami.9b14147.
[500] Jia M, Wen P, Wang Z, Zhao Y, Liu Y, Lin J, et al. Fluorinated Bifunctional Solid Polymer Electrolyte Synthesized under Visible Light for Stable Lithium Deposition and Dendrite-Free All-Solid-State Batteries. Adv Funct Mater 2021;31:2101736. https://doi.org/10.1002/adfm.202101736.
[501] Tang L, Chen B, Zhang Z, Ma C, Chen J, Huang Y, et al. Polyfluorinated crosslinker-based solid polymer electrolytes for long-cycling 4.5 V lithium metal batteries. Nat Commun 2023;14:2301. https://doi.org/10.1038/s41467-023-37997-6.
[502] Qin S, Wang Z, Ren Y, Yu Y, Xiao Y, Chen J, et al. A meltblown cloth reinforced partially fluorinated solid polymer electrolyte for ultrastable lithium metal batteries. Nano Energy 2024;119:109075. https://doi.org/10.1016/j.nanoen.2023.109075.
[503] Yan S, Liu H, Lu Y, Feng Q, Zhou H, Wu Y, et al. Selectively fluorinated aromatic lithium salts regulate the solvation structure and interfacial chemistry for all-solid-state batteries. Sci Adv 2025;11:eads4014. https://doi.org/10.1126/sciadv.ads4014.
[504] Li Y, Ma S, Zhao Y, Chen S, Xiao T, Yin H, et al. Synergetic Control of Li^+ Transport Ability and Solid Electrolyte Interphase by Boron-Rich Hexagonal Skeleton Structured All-Solid-State Polymer Electrolyte. Energy Environ Mater 2023;7:e12648. https://doi.org/10.1002/eem2.12648.
[505] Zhu J, Zhang Z, Zhao S, Westover AS, Belharouak I, Cao PF. Single-ion conducting polymer electrolytes for solid-state lithium–metal batteries: design, performance, and challenges. Adv Energy Mater 2021;11:2003836. https://doi.org/10.1002/aenm.202003836.
[506] Cao C, Li Y, Feng Y, Peng C, Li Z, Feng W. A solid-state single-ion polymer electrolyte with ultrahigh ionic conductivity for dendrite-free lithium metal batteries. Energy Storage Mater 2019;19:401–7. https://doi.org/10.1016/j.ensm.2019.03.004.
[507] Li Z, Wang L, Liu Y, Yu M, Liu B, Men Y, et al. Single-Ion Polymer Electrolyte based on Lithium-Rich Imidazole Anionic Porous Aromatic Framework for High Performance Lithium-Ion Batteries. Small 2023;19:2302818. https://doi.org/10.1002/smll.202302818.
[508] Han S, Wen P, Wang H, Zhou Y, Gu Y, Zhang L, et al. Sequencing polymers to enable solid-state lithium batteries. Nat Mater 2023;22:1515–22. https://doi.org/10.1038/s41563-023-01693-z.
[509] Lin R, He Y, Wang C, Zou P, Hu E, Yang X-Q, et al. Characterization of the structure and chemistry of the solid–electrolyte interface by cryo-EM leads to high-performance solid-state Li-metal batteries. Nat Nanotechnol 2022;17:768–76. https://doi.org/10.1038/s41565-022-01148-7.
[510] Fan Z, Ding B, Zhang T, Lin Q, Malgras V, Wang J, et al. Solid/Solid Interfacial Architecturing of Solid Polymer Electrolyte–Based All-Solid-State Lithium–Sulfur Batteries by Atomic Layer Deposition. Small 2019;15:1903952. https://doi.org/10.1002/smll.201903952.
[511] Xu H, Zhang J, Zhang H, Long J, Xu L, Mai L. In Situ Topological Interphases Boosting Stable Solid-State Lithium Metal Batteries. Adv Energy Mater 2023;13: 2204411. https://doi.org/10.1002/aenm.202204411.
[512] Yan M, Liang JY, Zuo TT, Yin YX, Xin S, Tan SJ, et al. Stabilizing Polymer–Lithium Interface in a Rechargeable Solid Battery. Adv Funct Mater 2019;30: 1908047. https://doi.org/10.1002/adfm.201908047.
[513] Zheng J, Sun C, Wang Z, Liu S, An B, Sun Z, et al. Double Ionic–Electronic transfer Interface Layers for All-Solid-State Lithium Batteries. Angew Chem Int Ed 2021;60:18448–53. https://doi.org/10.1002/anie.202104183.
[514] Hu L, Gao X, Li Z, Liu Y, Wang H, Liu J, et al. Layered Polymer Stacking for Stable Interfaces and Dendrite Growth Inhibition in All-Solid-State Lithium Batteries. ACS Appl Mater Interfaces 2023;15:38485–95. https://doi.org/10.1021/acsami.3c07794.
[515] Lv H, Chu X, Zhang Y, Liu Q, Wu F, Mu D. Self-healing solid-state polymer electrolytes for high-safety and long-cycle lithium-ion batteries. Mater Today 2024; 78:181–208. https://doi.org/10.1016/j.mattod.2024.06.018.
[516] Liu B, Wu M, Du W, Jiang L, Li H, Wang L, et al. The Application of Self-Healing Microcapsule Technology in the Field of Cement-based Materials: a Review and Prospect. Polymers 2023;15:2718. https://doi.org/10.3390/polym15122718.
[517] Park J-H, Braun PV. Coaxial Electrospinning of Self-Healing Coatings. Adv Mater 2010;22:496–9. https://doi.org/10.1002/adma.200902465.

[518] Lu S, Chu X, Li C, Zhao Z, Xiao J, Wu B, et al. A self-supporting solid electrolyte membrane with fibrous network structure for solid state lithium metal batteries. J Power Sources 2023;556:232472. https://doi.org/10.1016/j.jpowsour.2022.232472.
[519] Li Z, Fu J, Zheng S, Li D, Guo X. Self-Healing Polymer Electrolyte for Dendrite-Free Li Metal Batteries with Ultra-High-Voltage Ni-Rich Layered Cathodes. Small 2022;18:2200891. https://doi.org/10.1002/smll.202200891.
[520] Pei F, Wu L, Zhang Y, Liao Y, Kang Q, Han Y, et al. Interfacial self-healing polymer electrolytes for long-cycle solid-state lithium-sulfur batteries. Nat Commun 2024;15:351. https://doi.org/10.1038/s41467-023-43467-w.
[521] Zhou W, Wang Z, Pu Y, Li Y, Xin S, Li X, et al. Double-Layer Polymer Electrolyte for High-Voltage All-Solid-State Rechargeable Batteries. Adv Mater 2018;31:1805574. https://doi.org/10.1002/adma.201805574.
[522] Sun J, Yao X, Li Y, Zhang Q, Hou C, Shi Q, et al. Facilitating Interfacial Stability Via Bilayer Heterostructure Solid Electrolyte Toward High-energy, Safe and Adaptable Lithium Batteries. Adv Energy Mater 2020;10:2000709. https://doi.org/10.1002/aenm.202000709.
[523] Qi S, Li M, Gao Y, Zhang W, Liu S, Zhao J, et al. Enabling Scalable Polymer Electrolyte with Dual-Reinforced Stable Interface for 4.5 V Lithium-Metal Batteries. Adv Mater 2023;35:2304951. https://doi.org/10.1002/adma.202304951.
[524] Ma Q, Fu S, Wu AJ, Deng Q, Li WD, Yue D, et al. Designing Bidirectionally Functional Polymer Electrolytes for Stable Solid Lithium Metal Batteries. Adv Energy Mater 2023;13:2203892. https://doi.org/10.1002/aenm.202203892.
[525] He X, Zhu Z, Wen G, Lv S, Yang S, Hu T, et al. Design of High-Entropy Tape Electrolytes for Compression-Free Solid-State Batteries. Adv Mater 2023;36:2307599. https://doi.org/10.1002/adma.202307599.
[526] Yang J, Li R, Zhang P, Zhang J, Meng J, Li L, et al. Crosslinked polymer-in-salt solid electrolyte with multiple ion transport paths for solid-state lithium metal batteries. Energy Storage Mater 2024;64:103088. https://doi.org/10.1016/j.ensm.2023.103088.
[527] Liang Q, Chen L, Tang J, Liu X, Liu J, Tang M, et al. Large-scale preparation of ultrathin composite polymer electrolytes with excellent mechanical properties and high thermal stability for solid-state lithium-metal batteries. Energy Storage Mater 2023;55:847–56. https://doi.org/10.1016/j.ensm.2022.12.039.
[528] Liu W, Yi C, Li L, Liu S, Gui Q, Ba D, et al. Designing Polymer-in-Salt Electrolyte and fully Infiltrated 3D Electrode for Integrated Solid-State Lithium Batteries. Angew Chem Int Ed 2021;60:12931–40. https://doi.org/10.1002/anie.202101537.
[529] Zhang J, Zeng Y, Li Q, Tang Z, Sun D, Huang D, et al. Polymer-in-salt electrolyte enables ultrahigh ionic conductivity for advanced solid-state lithium metal batteries. Energy Storage Mater 2023;54:440–9. https://doi.org/10.1016/j.ensm.2022.10.055.
[530] Xu S, Xu R, Yu T, Chen K, Sun C, Hu G, et al. Decoupling of ion pairing and ion conduction in ultrahigh-concentration electrolytes enables wide-temperature solid-state batteries. Energy Environ Sci 2022;15:3379–87. https://doi.org/10.1039/d2ee01053d.
[531] Yang X, Adair KR, Gao X, Sun X. Recent advances and perspectives on thin electrolytes for high-energy-density solid-state lithium batteries. Energy Environ Sci 2021;14:643–71. https://doi.org/10.1039/D0EE02714F.
[532] Wu J, Yuan L, Zhang W, Li Z, Xie X, Huang Y. Reducing the thickness of solid-state electrolyte membranes for high-energy lithium batteries. Energy Environ Sci 2021;14:12–36. https://doi.org/10.1039/D0EE02241A.
[533] Randau S, Weber DA, Kötz O, Koerver R, Braun P, Weber A, et al. Benchmarking the performance of all-solid-state lithium batteries. Nat Energy 2020;5:259–70. https://doi.org/10.1038/s41560-020-0565-1.
[534] Wu J, Rao Z, Cheng Z, Yuan L, Li Z, Huang Y. Ultrathin, Flexible Polymer Electrolyte for Cost-Effective Fabrication of All-Solid-State Lithium Metal Batteries. Adv Energy Mater 2019;9:1902767. https://doi.org/10.1002/aenm.201902767.
[535] Yuan B, Zhao B, Wang Q, Bai Y, Cheng Z, Cong Z, et al. A thin composite polymer electrolyte with high room-temperature conductivity enables mass production for solid-state lithium-metal batteries. Energy Storage Mater 2022;47:288–96. https://doi.org/10.1016/j.ensm.2022.01.052.
[536] Wang Z, Shen L, Deng S, Cui P, Yao X. 10 μm-Thick High-Strength Solid Polymer Electrolytes with Excellent Interface Compatibility for Flexible All-Solid-State Lithium-Metal Batteries. Adv Mater 2021;33:2100353. https://doi.org/10.1002/adma.202100353.
[537] Zhang Y, Yu J, Shi H, Wang S, Lv Y, Zhang Y, et al. Fiber-Reinforced Ultrathin Solid Polymer Electrolyte for Solid-State Lithium-Metal Batteries. Adv Funct Mater 2025;2421054. https://doi.org/10.1002/adfm.202421054.
[538] He F, Tang W, Zhang X, Deng L, Luo J. High Energy Density Solid State Lithium Metal Batteries Enabled by Sub-5 μm Solid Polymer Electrolytes. Adv Mater 2021;33:2105329. https://doi.org/10.1002/adma.202105329.
[539] Wan J, Xie J, Kong X, Liu Z, Liu K, Shi F, et al. Ultrathin, flexible, solid polymer composite electrolyte enabled with aligned nanoporous host for lithium batteries. Nat Nanotechnol 2019;14:705–11. https://doi.org/10.1038/s41565-019-0465-3.
[540] Han L, Liu Y, Liao C, Zhao Y, Cao Y, Kan Y, et al. Noncombustible 7 μm-thick solid polymer electrolyte for highly energy density solid state lithium batteries. Nano Energy 2023;112:108448. https://doi.org/10.1016/j.nanoen.2023.108448.
[541] Bao W, Zhang Y, Cao L, Jiang Y, Zhang H, Zhang N, et al. An H_2O-initiated Crosslinking Strategy for Ultrafine-Nanoclusters-Reinforced High-Toughness Polymer-In-Plasticizer Solid Electrolyte. Adv Mater 2023;35:2304712. https://doi.org/10.1002/adma.202304712.
[542] Tan J, Ao X, Dai A, Yuan Y, Zhuo H, Lu H, et al. Polycation ionic liquid tailored PEO-based solid polymer electrolytes for high temperature lithium metal batteries. Energy Storage Mater 2020;33:173–80. https://doi.org/10.1016/j.ensm.2020.08.009.
[543] Fu C, Homann G, Grissa R, Rentsch D, Zhao W, Gouveia T, et al. A Polymerized-Ionic-Liquid-Based Polymer Electrolyte with High Oxidative Stability for 4 and 5 V Class Solid-State Lithium Metal Batteries. Adv Energy Mater 2022;12:2200412. https://doi.org/10.1002/aenm.202200412.
[544] Wang Y, Zanelotti CJ, Wang X, Kerr R, Jin L, Kan WH, et al. Solid-state rigid-rod polymer composite electrolytes with nanocrystalline lithium ion pathways. Nat Mater 2021;20:1255–63. https://doi.org/10.1038/s41563-021-00995-4.
[545] Wu H, Xu Y, Ren X, Liu B, Engelhard MH, Ding MS, et al. Polymer-in-"Quasi-Ionic Liquid" Electrolytes for High-Voltage Lithium Metal Batteries. Adv Energy Mater 2019;9:1902108. https://doi.org/10.1002/aenm.201902108.
[546] Li X, Zheng Y, Li CY. Dendrite-free, wide temperature range lithium metal batteries enabled by hybrid network ionic liquids. Energy Storage Mater 2020;29:273–80. https://doi.org/10.1016/j.ensm.2020.04.037.
[547] Wang S, Zhou L, Tufail MK, Yang L, Zhai P, Chen R, et al. In-Situ synthesized Non-flammable gel polymer electrolyte enable highly safe and Dendrite-Free lithium metal batteries. Chem Eng J 2021;415:128846. https://doi.org/10.1016/j.cej.2021.128846.
[548] Fu X, Li C, Wang Y, Kovatch LP, Scudiero L, Liu J, et al. Building Ion-Conduction highways in Polymeric Electrolytes by Manipulating Protein Configuration. ACS Appl Mater Interfaces 2018;10:4726–36. https://doi.org/10.1021/acsami.7b17156.
[549] Li J, Jing M-x, Li R, Li L-x, Huang Z-h, Yang H, et al. Al_2O_3 Fiber-Reinforced Polymer Solid Electrolyte Films with Excellent Lithium-Ion Transport Properties for High-Voltage Solid-State Lithium Batteries. ACS Appl Polym Mater 2022;4:7144–51. https://doi.org/10.1021/acsapm.2c01034.
[550] Wang C, Yang T, Zhang W, Huang H, Gan Y, Xia Y, et al. Hydrogen bonding enhanced SiO_2/PEO composite electrolytes for solid-state lithium batteries. J Mater Chem A 2022;10:3400–8. https://doi.org/10.1039/D1TA10607D.
[551] Hu C, Shen Y, Shen M, Liu X, Chen H, Liu C, et al. Superionic Conductors *via* Bulk Interfacial Conduction. J Am Chem Soc 2020;142:18035–41. https://doi.org/10.1021/jacs.0c07060.
[552] Yang X, Sun Q, Zhao C, Gao X, Adair KR, Liu Y, et al. High-areal-capacity all-solid-state lithium batteries enabled by rational design of fast ion transport channels in vertically-aligned composite polymer electrodes. Nano Energy 2019;61:567–75. https://doi.org/10.1016/j.nanoen.2019.05.002.
[553] Liang Y, Dong L, Zhong S, Yuan B, Ji Y, Yang C, et al. Asbestos-functionalized solid polymer electrolyte for uniform Li deposition in lithium metal batteries. Chem Eng J 2023;451:138599. https://doi.org/10.1016/j.cej.2022.138599.
[554] Lin Y, Wang X, Liu J, Miller JD. Natural halloysite nano-clay electrolyte for advanced all-solid-state lithium-sulfur batteries. Nano Energy 2017;31:478–85. https://doi.org/10.1016/j.nanoen.2016.11.045.
[555] Tao F, Wang X, Jin S, Tian L, Liu Z, Kang X, et al. A Composite of Hierarchical Porous MOFs and Halloysite Nanotubes as Single-Ion-Conducting Electrolyte Toward High-Performance Solid-State Lithium-Ion Batteries. Adv Mater 2023;35:2300687. https://doi.org/10.1002/adma.202300687.
[556] Lv S, He X, Ji Z, Yang S, Feng L, Fu X, et al. A Supertough and Highly-Conductive Nano-Dipole Doped Composite Polymer Electrolyte with Hybrid Li^+-Solvation Microenvironment for Lithium Metal Batteries. Adv Energy Mater 2023;13:2302711. https://doi.org/10.1002/aenm.202302711.

[557] Wu Q, Fang M, Jiao S, Li S, Zhang S, Shen Z, et al. Phase regulation enabling dense polymer-based composite electrolytes for solid-state lithium metal batteries. Nat Commun 2023;14:6296. https://doi.org/10.1038/s41467-023-41808-3.

[558] Xia S, Yang B, Zhang H, Yang J, Liu W, Zheng S. Ultrathin Layered double Hydroxide Nanosheets Enabling Composite Polymer Electrolyte for All-Solid-State Lithium Batteries at Room Temperature. Adv Funct Mater 2021;31:2101168. https://doi.org/10.1002/adfm.202101168.

[559] Pan Q, Zheng Y, Kota S, Huang W, Wang S, Qi H, et al. 2D MXene-containing polymer electrolytes for all-solid-state lithium metal batteries. Nanoscale Adv 2019;1:395–402. https://doi.org/10.1039/c8na00206a.

[560] Shi Y, Li B, Zhu Q, Shen K, Tang W, Xiang Q, et al. MXene-Based Mesoporous Nanosheets Toward Superior Lithium Ion Conductors. Adv Energy Mater 2020;10:1903534. https://doi.org/10.1002/aenm.201903534.

[561] Xu Z, Huang H, Tang Q, Peng H, Huang J, He H, et al. Coaxially MXene-confined solid-state electrolyte for flexible high-rate lithium metal battery. Nano Energy 2024;122:109312. https://doi.org/10.1016/j.nanoen.2024.109312.

[562] Zhao CZ, Zhao Q, Liu X, Zheng J, Stalin S, Zhang Q, et al. Rechargeable Lithium Metal Batteries with an In-built Solid-State Polymer Electrolyte and a High Voltage/Loading Ni-Rich Layered Cathode. Adv Mater 2020;32:1905629. https://doi.org/10.1002/adma.201905629.

[563] Hu J, Lai C, Chen K, Wu Q, Gu Y, Wu C, et al. Dual fluorination of polymer electrolyte and conversion-type cathode for high-capacity all-solid-state lithium metal batteries. Nat Commun 2022;13:7914. https://doi.org/10.1038/s41467-022-35636-0.

[564] Cheng Y, Liu X, Guo Y, Dong G, Hu X, Zhang H, et al. Monodispersed Sub-1 nm Inorganic Cluster Chains in Polymers for Solid Electrolytes with Enhanced Li-Ion Transport. Adv Mater 2023;35:2303226. https://doi.org/10.1002/adma.202303226.

[565] Qian S, Zhu H, Sun C, Li M, Zheng M, Wu Z, et al. Liquid Metal Loaded Molecular Sieve: Specialized Lithium Dendrite Blocking Filler for Polymeric Solid-State Electrolyte. Adv Mater 2024;36:2313456. https://doi.org/10.1002/adma.202313456.

[566] Yang W, Liu Y, Sun X, He Z, He P, Zhou H. Solvation-tailored PVDF-based Solid-state Electrolyte for High-voltage Lithium Metal Batteries. Angew Chem Int Ed 2024;63:e202401428. https://doi.org/10.1002/anie.202401428.

[567] Lee MJ, Shin DO, Kim JY, Oh J, Kang SH, Kim J, et al. Interfacial barrier free organic-inorganic hybrid electrolytes for solid state batteries. Energy Storage Mater 2021;37:306–14. https://doi.org/10.1016/j.ensm.2021.02.013.

[568] Bohnke O. The fast lithium-ion conducting oxides $Li_{3x}La_{2/3-x}TiO_3$ from fundamentals to application. Solid State Ion 2008;179:9–15. https://doi.org/10.1016/j.ssi.2007.12.022.

[569] Zhang K, Wu F, Wang X, Weng S, Yang X, Zhao H, et al. 8.5 μm-Thick Flexible-Rigid Hybrid Solid–Electrolyte/Lithium Integration for Air-Stable and Interface-Compatible All-Solid-State Lithium Metal Batteries. Adv Energy Mater 2022;12:2200368. https://doi.org/10.1002/aenm.202200368.

[570] Alireza Kondori ME, Harzandi AM, Amine R. Mahmoud Tamadoni Saray. a room temperature rechargeable Li_2O-based lithium-air battery enabled by a solid electrolyte. Science 2023;379:499–505. https://doi.org/10.1126/science.abq1347.

[571] Su Y, Zhang X, Du C, Luo Y, Chen J, Yan J, et al. An All-Solid-State Battery based on Sulfide and PEO Composite Electrolyte. Small 2022;18:2202069. https://doi.org/10.1002/smll.202202069.

[572] Luo J, Sun Q, Liang J, Adair K, Zhao F, Deng S, et al. Rapidly In Situ Cross-Linked Poly(butylene oxide) Electrolyte Interface Enabling Halide-based All-Solid-State Lithium Metal Batteries. ACS Energy Lett 2023;8:3676–84. https://doi.org/10.1021/acsenergylett.3c01157.

[573] Zheng J, Hu YY. New Insights into the Compositional Dependence of Li-Ion Transport in Polymer–Ceramic Composite Electrolytes. ACS Appl Mater Interfaces 2018;10:4113–20. https://doi.org/10.1021/acsami.7b17301.

[574] Huo H, Chen Y, Luo J, Yang X, Guo X, Sun X. Rational Design of Hierarchical "Ceramic-in-Polymer" and "Polymer-in-Ceramic" Electrolytes for Dendrite-Free Solid-State Batteries. Adv Energy Mater 2019;9:1804004. https://doi.org/10.1002/aenm.201804004.

[575] He Y, Wang C, Zhang R, Zou P, Chen Z, Bak S-M, et al. A self-healing plastic ceramic electrolyte by an aprotic dynamic polymer network for lithium metal batteries. Nat Commun 2024;15:10015. https://doi.org/10.1038/s41467-024-53869-z.

[576] Song S, Wu Y, Tang W, Deng F, Yao J, Liu Z, et al. Composite Solid Polymer Electrolyte with Garnet Nanosheets in Poly(ethylene oxide). ACS Sustain Chem Eng 2019;7:7163–70. https://doi.org/10.1021/acssuschemeng.9b00143.

[577] Jiang B, Li F, Hou T, Liu Y, Cheng H, Wang H, et al. Polymer electrolytes shielded by 2D $Li_{0.46}Mn_{0.77}PS_3$ Li^+-conductors for all-solid-state lithium-metal batteries. Energy Storage Mater 2023;56:183–91. https://doi.org/10.1016/j.ensm.2023.01.011.

[578] Chen L, Li W, Fan LZ, Nan CW, Zhang Q. Intercalated Electrolyte with High Transference Number for Dendrite-Free Solid-State Lithium Batteries. Adv Funct Mater 2019;29:1901047. https://doi.org/10.1002/adfm.201901047.

[579] Gong Y, Fu K, Xu S, Dai J, Hamann TR, Zhang L, et al. Lithium-ion conductive ceramic textile: a new architecture for flexible solid-state lithium metal batteries. Mater Today 2018;21:594–601. https://doi.org/10.1016/j.mattod.2018.01.001.

[580] Gou J, Cui K, Wang S, Zhang Z, Huang J, Wang H. An anisotropic strategy for developing polymer electrolytes endowing lithium metal batteries with electrochemo-mechanically stable interface. Nat Commun 2025;16:3626. https://doi.org/10.1038/s41467-025-58916-x.

[581] Wang G, Zhu X, Rashid A, Hu Z, Sun P, Zhang Q, et al. Organic polymeric filler-amorphized poly(ethylene oxide) electrolyte enables all-solid-state lithium–metal batteries operating at 35 °C. J Mater Chem A 2020;8:13351–63. https://doi.org/10.1039/d0ta00335b.

[582] Xu Y, Xue H, Li X, Fan X, Li P, Zhang T, et al. Application of metal-organic frameworks, covalent organic frameworks and their derivates for the metal-air batteries. Nano Research Energy 2023;2:e9120052. https://doi.org/10.26599/NRE.2023.9120052.

[583] Ye Z, Jiang Y, Li L, Wu F, Chen R. Rational Design of MOF-Based Materials for Next-Generation Rechargeable Batteries. Nano Micro Lett 2021;13:203. https://doi.org/10.1007/s40820-021-00726-z.

[584] Yuan C, Li J, Han P, Lai Y, Zhang Z, Liu J. Enhanced electrochemical performance of poly(ethylene oxide) based composite polymer electrolyte by incorporation of nano-sized metal-organic framework. J Power Sources 2013;240:653–8. https://doi.org/10.1016/j.jpowsour.2013.05.030.

[585] Huo H, Wu B, Zhang T, Zheng X, Ge L, Xu T, et al. Anion-immobilized polymer electrolyte achieved by cationic metal-organic framework filler for dendrite-free solid-state batteries. Energy Storage Mater 2019;18:59–67. https://doi.org/10.1016/j.ensm.2019.01.007.

[586] Li C, Xue P, Chen L, Liu J, Wang Z. Reducing the crystallinity of PEO-based composite electrolyte for high performance lithium batteries. Compos B Eng 2022;234:109729. https://doi.org/10.1016/j.compositesb.2022.109729.

[587] Lin R, Jin Y, Zhang X, Li Y, Zhang Y, Xiong Y. Hierarchical bulk-interface design of MOFs framework for polymer electrolyte towards ultra-stable quasi-solid-state Li metal batteries. Chem Eng J 2024;479:147558. https://doi.org/10.1016/j.cej.2023.147558.

[588] Zhai Y, Hou W, Tao M, Wang Z, Chen Z, Zeng Z, et al. Enabling High-Voltage "Superconcentrated Ionogel-in-Ceramic" Hybrid Electrolyte with Ultrahigh Ionic Conductivity and Single Li^+-Ion Transference Number. Adv Mater 2022;34:2205560. https://doi.org/10.1002/adma.202205560.

[589] Guo D, Shinde DB, Shin W, Abou-Hamad E, Emwas AH, Lai Z, et al. Foldable Solid-State Batteries Enabled by Electrolyte Mediation in Covalent Organic Frameworks. Adv Mater 2022;34:2201410. https://doi.org/10.1002/adma.202201410.

[590] Liu J, Zhang Y, Ji H, Zhang J, Zhou P, Cao Y, et al. Cationic Covalent Organic Framework with Ultralow HOMO Energy used as Scaffolds for 5.2 V Solid Polycarbonate Electrolytes. Adv Sci 2022;9:2200390. https://doi.org/10.1002/advs.202200390.

[591] Liu Q, Liu Y, Jiao X, Song Z, Sadd M, Xu X, et al. Enhanced ionic conductivity and interface stability of hybrid solid-state polymer electrolyte for rechargeable lithium metal batteries. Energy Storage Mater 2019;23:105–11. https://doi.org/10.1016/j.ensm.2019.05.023.

[592] Zhang X, Fu C, Cheng S, Zhang C, Zhang L, Jiang M, et al. Novel PEO-based composite electrolyte for low-temperature all-solid-state lithium metal batteries enabled by interfacial cation-assistance. Energy Storage Mater 2023;56:121–31. https://doi.org/10.1016/j.ensm.2022.12.048.

[593] Sun Y-Y, Zhang Q, Fan L, Han D-D, Li L, Yan L, et al. Engineering the interface of organic/inorganic composite solid-state electrolyte by amino effect for all-solid-state lithium batteries. J Colloid Interface Sci 2022;628:877–85. https://doi.org/10.1016/j.jcis.2022.08.111.

[594] Fang C, Huang K, Zhao J, Tian S, Dou H, Zhang X. Dual-filler reinforced PVDF-HFP based polymer electrolyte enabling high-safety design of lithium metal batteries. Nano Res 2024;17:5251–60. https://doi.org/10.1007/s12274-024-6502-z.

[595] Yin J, Xu X, Jiang S, Wu H, Wei L, Li Y, et al. High ionic conductivity PEO-based electrolyte with 3D framework for Dendrite-free solid-state lithium metal batteries at ambient temperature. Chem Eng J 2022;431:133352. https://doi.org/10.1016/j.cej.2021.133352.

[596] Lv C, Zhou X, Zhong L, Yan C, Srinivasan M, Seh ZW, et al. Machine Learning: an Advanced Platform for Materials Development and State Prediction in Lithium-Ion Batteries. Adv Mater 2022;34:2101474. https://doi.org/10.1002/adma.202101474.
[597] Dong S, Sheng L, Wang L, Liang J, Zhang H, Chen Z, et al. Challenges and prospects of All-Solid-State Electrodes for Solid-State Lithium Batteries. Adv Funct Mater 2023;33:2304371. https://doi.org/10.1002/adfm.202304371.
[598] Jiang P, Du G, Cao J, Zhang X, Zou C, Liu Y, et al. Solid-State Li Ion Batteries with Oxide Solid Electrolytes: Progress and Perspective. Energy Technol 2023;11:2201288. https://doi.org/10.1002/ente.202201288.
[599] Ren Z, Li J, Gong Y, Shi C, Liang J, Li Y, et al. Insight into the integration way of ceramic solid-state electrolyte fillers in the composite electrolyte for high performance solid-state lithium metal battery. Energy Storage Mater 2022;51:130–8. https://doi.org/10.1016/j.ensm.2022.06.037.
[600] Zhang X, Xie J, Shi F, Lin D, Liu Y, Liu W, et al. Vertically aligned and continuous nanoscale ceramic–polymer interfaces in composite solid polymer electrolytes for enhanced ionic conductivity. Nano Lett 2018;18:3829–38. https://doi.org/10.1021/acs.nanolett.8b01111.
[601] Takeda H, Fukuda H, Nakano K, Hashimura S, Tanibata N, Nakayama M, et al. Process optimisation for NASICON-type solid electrolyte synthesis using a combination of experiments and bayesian optimisation. Mater Adv 2022;3:8141–8. https://doi.org/10.1039/d2ma00731b.
[602] Xie W, Deng Z, Liu Z, Famprikis T, Butler KT, Canepa P. Effects of Grain Boundaries and Surfaces on Electronic and Mechanical Properties of Solid Electrolytes. Adv Energy Mater 2024;14:2304230. https://doi.org/10.1002/aenm.202304230.
[603] Hou M, Liang F, Chen K, Dai Y, Xue D. Challenges and perspectives of NASICON-type solid electrolytes for all-solid-state lithium batteries. Nanotechnology 2020;31:132003. https://doi.org/10.1088/1361-6528/ab5be7.
[604] Du W, Shao Q, Wei Y, Yan C, Gao P, Lin Y, et al. High-Energy and Long-Cycling All-Solid-State Lithium-Ion Batteries with Li- and Mn-Rich Layered Oxide Cathodes and Sulfide Electrolytes. ACS Energy Lett 2022;7:3006–14. https://doi.org/10.1021/acsenergylett.2c01637.
[605] Lau J, DeBlock RH, Butts DM, Ashby DS, Choi CS, Dunn BS. Sulfide solid electrolytes for lithium battery applications. Adv Energy Mater 2018;8:1800933. https://doi.org/10.1002/aenm.201800933.
[606] Park KH, Bai Q, Kim DH, Oh DY, Zhu Y, Mo Y, et al. Design strategies, practical considerations, and new solution processes of sulfide solid electrolytes for all-solid-state batteries. Adv Energy Mater 2018;8:1800035. https://doi.org/10.1002/aenm.201800035.
[607] Lu P, Wu D, Chen L, Li H, Wu F. Air stability of solid-state sulfide batteries and electrolytes. Electrochem Energy Rev 2022;5:3. https://doi.org/10.1007/s41918-022-00149-3.
[608] Ni Y, Huang C, Liu H, Liang Y, Fan LZ. A High Air-Stability and Li-Metal-Compatible $Li_{3+2x}P_{1-x}Bi_xS_{4-1.5x}O_{1.5x}$ sulfide Electrolyte for All-Solid-State Li–Metal Batteries. Adv Funct Mater 2022;32:2205998. https://doi.org/10.1002/adfm.202205998.
[609] Zhang S, Zhao F, Su H, Zhong Y, Liang J, Chen J, et al. Cubic Iodide Li_xYI_{3+x} Superionic Conductors through defect Manipulation for All-Solid-State Li Batteries. Angew Chem Int Ed 2024;136:e202316360. https://doi.org/10.1002/anie.202316360.
[610] Wu Z, Yan C, Gao P, She L, Zhang X, Lin Y, et al. Redox couple strategy for improving the Oxygen Redox activity and Reversibility of Li- and Mn-Rich Cathode Materials. Nano Lett 2024;24:13496–503. https://doi.org/10.1021/acs.nanolett.4c02588.
[611] Zhu G, Xia G, Pan H, Yu X. Size-Controllable Nickel Sulfide Nanoparticles embedded in Carbon Nanofibers as High-Rate Conversion Cathodes for Hybrid Mg-based Battery. Adv Sci 2022;9:2106107. https://doi.org/10.1002/advs.202106107.
[612] Yan C, Shao Q, Yao Z, Gao M, Zhang C, Chen G, et al. Multifunctional Surface Construction for Long-Term Cycling Stability of Li-Rich Mn-based Layered Oxide Cathode for Li-Ion Batteries. Small 2022;18:2107910. https://doi.org/10.1002/smll.202107910.
[613] Huang H, Xia Y, Hao Y, Li H, Yousaf M, Iqbal S, et al. Local Electronic Structure Regulation Enabling Fluorophosphates Cathode with improved Redox potential and Reversible Capacity for Sodium-Ion Batteries. J Am Chem Soc 2024;146:28906–13. https://doi.org/10.1021/jacs.4c09379.
[614] Gao M, Yan C, Shao Q, Chen J, Zhang C, Chen G, et al. A Novel Perovskite Electron–Ion Conductive Coating to simultaneously Enhance Cycling Stability and Rate Capability of $Li_{1.2}Ni_{0.13}Co_{0.13}Mn_{0.54}O_2$ Cathode Material for Lithium-Ion Batteries. Small 2021;17:2008132. https://doi.org/10.1002/smll.202008132.
[615] Wu Z, Yan C, Gao P, She L, Zhang X, Lin Y, et al. Cu-N Synergism Regulation to Enhance Anionic Redox Reversibility and activity of Li- and Mn-Rich Layered Oxides Cathode. Small 2024;20:2401645. https://doi.org/10.1002/smll.202401645.
[616] Shao Q, Gao P, Yan C, Gao M, Du W, Chen J, et al. A Redox couple Strategy Enables Long-Cycling Li- and Mn-Rich Layered Oxide Cathodes by Suppressing Oxygen Release. Adv Mater 2022;34:2108543. https://doi.org/10.1002/adma.202108543.
[617] Ju S, Ye J, Zhang H, Wang W, Xia G, Cui W, et al. Recognizing the contrasting role of N, O dual-coordinated single-atom iron catalyst in Li−S and Al−S batteries. Energy Storage Mater 2023;56:1–12. https://doi.org/10.1016/j.ensm.2023.01.002.
[618] Zhang Z, Wang B, Ju S, Wu Z, Yang Y, Pan H, et al. Progress and prospects for solving the "shuttle effect" in magnesium-sulfur batteries. Energy Storage Mater 2023;62:102933. https://doi.org/10.1016/j.ensm.2023.102933.
[619] Zou T, Xu T, Ju S, Yu X. Single atom iron as an efficient electrocatalyst for enhanced kinetics in magnesium-sulfur batteries. Chem Eng J 2023;477:147207. https://doi.org/10.1016/j.cej.2023.147207.
[620] Zheng J, Zhang H, Xu T, Ju S, Xia G, Yu X. Copper and Cobalt Nanoparticles Enable Highly Stable and Fast Kinetics of Al–S Batteries. Adv Funct Mater 2024;34:2307486. https://doi.org/10.1002/adfm.202307486.
[621] Ju S, Yuan C, Zheng J, Yao L, Zhang T, Xia G, et al. Identifying single-atom catalysts for boosted Al–S conversion reactions. Energy Storage Mater 2022;52:524–33. https://doi.org/10.1016/j.ensm.2022.08.030.
[622] Song H, Münch K, Liu X, Shen K, Zhang R, Weintraut T, et al. All-solid-state Li–S batteries with fast solid–solid sulfur reaction. Nature 2025;637:846–53. https://doi.org/10.1038/s41586-024-08298-9.
[623] Frith JTT, Lacey MJJ, Ulissi U. A non-academic perspective on the future of lithium-based batteries. Nat Commun 2023;14:420. https://doi.org/10.1038/s41467-023-35933-2.
[624] Zhang H, Ju S, Xia G, Yu X. Identifying the positive role of lithium hydride in stabilizing Li metal anodes. Sci Adv 2022;8:eabl8245. https://doi.org/10.1126/sciadv.abl8245.
[625] Lai Y, Zhang H, Xia G, Yu X. Long-term stable Li metal anode enabled by strengthened and protected lithiophilic LiZn alloys. J Power Sources 2022;543:231839. https://doi.org/10.1016/j.jpowsour.2022.231839.
[626] You L, Ju S, Liu J, Xia G, Guo Z, Yu X. Synergistic effect of lithiophilic Zn nanoparticles and N-doping for stable Li metal anodes. J Energy Chem 2022;65:439–47. https://doi.org/10.1016/j.jechem.2021.06.001.
[627] You L, Liu J, Zhang H, Zhang T, Wang J, Guo Z, et al. Building a House for stabilizing Lithium-Metal Anodes. Batteries Supercaps 2022;5:e202100408. https://doi.org/10.1002/batt.202100408.
[628] Burton M, Narayanan S, Jagger B, Olbrich LF, Dhir S, Shibata M, et al. Techno-economic assessment of thin lithium metal anodes for solid-state batteries. Nat Energy 2025;10:135–47. https://doi.org/10.1038/s41560-024-01676-7.
[629] Zhang Z, Zhang X, Liu Y, Lan C, Han X, Pei S, et al. Silicon-based all-solid-state batteries operating free from external pressure. Nat Commun 2025;16:1013. https://doi.org/10.1038/s41467-025-56366-z.
[630] Fang L, Bahlawane N, Sun W, Pan H, Xu BB, Yan M, et al. Conversion-Alloying Anode Materials for Sodium Ion Batteries. Small 2021;17:2101137. https://doi.org/10.1002/smll.202101137.
[631] Liu L, Cai Z, Yang S, Yang Y, Yao Y, He S, et al. Multifunctional High-Entropy Alloy Nanolayer Toward Long-Life Anode-Free Sodium Metal Battery. Adv Mater 2025;37:2413331. https://doi.org/10.1002/adma.202413331.
[632] Wang Y, Wang S, Xue L, Wang F, Qi F, Zhou Y, et al. An Ultrastable Integrated Anode with ~95 wt.% SiO_x via In Situ Electrode-Scale Conformal Coating. ACS Nano 2025;19:1660–75. https://doi.org/10.1021/acsnano.4c15386.
[633] Cui L, Zhang S, Ju J, Liu T, Zheng Y, Xu J, et al. A cathode homogenization strategy for enabling long-cycle-life all-solid-state lithium batteries. Nat Energy 2024;9:1084–94. https://doi.org/10.1038/s41560-024-01596-6.
[634] Chen L, Gu T, Mi J, Li Y, Yang K, Ma J, et al. Homogeneous polymer-ionic solvate electrolyte with weak dipole-dipole interaction enabling long cycling pouch lithium metal battery. Nat Commun 2025;16:3517. https://doi.org/10.1038/s41467-025-58689-3.

[635] Zhang J, Xiao X, Chen J, Wan H, Zhang N, Liu G, et al. All wet-coating process for chemical stable antimony and selenium dual-doped argyrodite electrolyte based all-solid-state lithium batteries. Mater Sci Eng R Rep 2025;164:100972. https://doi.org/10.1016/j.mser.2025.100972.
[636] Lee W, Lee J, Yu T, Kim H-J, Kim MK, Jang S, et al. Advanced parametrization for the production of high-energy solid-state lithium pouch cells containing polymer electrolytes. Nat Commun 2024;15:5860. https://doi.org/10.1038/s41467-024-50075-9.
[637] Wang Z, Mu Z, Ma T, Yan W, Wu D, Li Y, et al. In Situ formed Li_3N Networks by Soft Carbon-Si_3N_4 for Superior All-Solid-State Lithium-Metal Batteries. Adv Energy Mater 2024;14:2400003. https://doi.org/10.1002/aenm.202400003.
[638] Xu X, Chu S, Xu S, Li H, Sheng C, Dong M, et al. Integrating Prelithiation and Interface Protection to Achieve High-Energy All-Solid-State Batteries. Angew Chem Int Ed 2025;64:e202415891. https://doi.org/10.1002/anie.202415891.
[639] An H, Li M, Liu Q, Song Y, Liu J, Yu Z, et al. Strong Lewis-acid coordinated PEO electrolyte achieves 4.8 V-class all-solid-state batteries over 580 Wh kg^{-1}. Nat Commun 2024;15:9150. https://doi.org/10.1038/s41467-024-53094-8.
[640] Vishnugopi BS, Kazyak E, Lewis JA, Nanda J, McDowell MT, Dasgupta NP, et al. Challenges and Opportunities for Fast Charging of Solid-State Lithium Metal Batteries. ACS Energy Lett 2021;6:3734–49. https://doi.org/10.1021/acsenergylett.1c01352.
[641] Yang Y, Dong R, Cheng H, Wang L, Tu J, Zhang S, et al. 2D Layered Materials for Fast-Charging Lithium-Ion Battery Anodes. Small 2023;19:2301574. https://doi.org/10.1002/smll.202301574.
[642] Ye L, Lu Y, Wang Y, Li J, Li X. Fast cycling of lithium metal in solid-state batteries by constriction-susceptible anode materials. Nat Mater 2024;23:244–51. https://doi.org/10.1038/s41563-023-01722-x.
[643] Wang Y, Li X. Fast Kinetics Design for Solid-State Battery Device. Adv Mater 2024;36:2309306. https://doi.org/10.1002/adma.202309306.
[644] Ma Y, Qiu Y, Yang K, Lv S, Li Y, An X, et al. Competitive Li-ion Coordination Constructing Three-Dimensional Transport Network for Ultra-High Ionic Conductivity of Composite Solid-State Electrolyte. Energy Environ Sci 2024;17:8274–83. https://doi.org/10.1039/D4EE03134B.
[645] Song Y, Sun X, Lou S, Sun F, Wang J. Alleviating range anxiety: Solid-state batteries and extreme fast charging. Prog Mater Sci 2025;147:101339. https://doi.org/10.1016/j.pmatsci.2024.101339.
[646] Lim H-D, Park J-H, Shin H-J, Jeong J, Kim JT, Nam K-W, et al. A review of challenges and issues concerning interfaces for all-solid-state batteries. Energy Storage Mater 2020;25:224–50. https://doi.org/10.1016/j.ensm.2019.10.011.
[647] Wu Z, He S, Zheng C, Gan J, She L, Zhang M, et al. Fabrication pressures and stack pressures in solid-state battery. eScience 2024;4:100247. https://doi.org/10.1016/j.esci.2024.100247.
[648] Xu H, Yang S, Li B. Pressure Effects and Countermeasures in Solid-State Batteries: a Comprehensive Review. Adv Energy Mater 2024;14:2303539. https://doi.org/10.1002/aenm.202303539.
[649] Zhang F, Guo Y, Zhang L, Jia P, Liu X, Qiu P, et al. A review of the effect of external pressure on all-solid-state batteries. Etransportation 2023;15:100220. https://doi.org/10.1016/j.etran.2022.100220.
[650] Mussa AS, Klett M, Lindbergh G, Lindström RW. Effects of external pressure on the performance and ageing of single-layer lithium-ion pouch cells. J Power Sources 2018;385:18–26. https://doi.org/10.1016/j.jpowsour.2018.03.020.
[651] Doux J-M, Yang Y, Tan DHS, Han N, Wu EA, Wang X, et al. Pressure effects on sulfide electrolytes for all solid-state batteries. J Mater Chem A 2020;8:5049–55. https://doi.org/10.1039/c9ta12889a.
[652] Sang J, Tang B, Qiu Y, Fang Y, Pan K, Zhou Z. How does Stacking pressure Affect the Performance of Solid Electrolytes and All-Solid-State Lithium Metal Batteries? Energy Environ Mater 2023;7:e12670. https://doi.org/10.1002/eem2.12670.
[653] Zhang X, Wang QJ, Harrison KL, Roberts SA, Harris SJ. Pressure-Driven Interface Evolution in Solid-State Lithium Metal Batteries. Cell Rep Phys Sci 2020;1:100012. https://doi.org/10.1016/j.xcrp.2019.100012.
[654] Sakka Y, Yamashige H, Watanabe A, Takeuchi A, Uesugi M, Uesugi K, et al. Pressure dependence on the three-dimensional structure of a composite electrode in an all-solid-state battery. J Mater Chem A 2022;10:16602–9. https://doi.org/10.1039/d2ta02378d.
[655] Kalnaus S, Dudney NJ, Westover AS, Herbert E, Hackney S. Solid-state batteries: the critical role of mechanics. Science 2023;381:eabg5998. https://doi.org/10.1126/science.abg5998.
[656] Gao X, Liu B, Hu B, Ning Z, Jolly DS, Zhang S, et al. Solid-state lithium battery cathodes operating at low pressures. Joule 2022;6:636–46. https://doi.org/10.1016/j.joule.2022.02.008.
[657] Lee C, Kim JY, Bae KY, Kim T, Jung S-J, Son S, et al. Enhancing electrochemomechanics: how stack pressure regulation affects all-solid-state batteries. Energy Storage Mater 2024;66:103196. https://doi.org/10.1016/j.ensm.2024.103196.
[658] Hu X, Zhang Z, Zhang X, Wang Y, Yang X, Wang X, et al. External-pressure–electrochemistry coupling in solid-state lithium metal batteries. Nat Rev Mater 2024;9:305–20. https://doi.org/10.1038/s41578-024-00669-y.
[659] Hu Z, Gao P, Ju S, Li Y, Zhang T, Lu C, et al. Dynamic volume compensation realizing Ah-level all-solid-state silicon-sulfur batteries. Nat Commun 2025;16:3979. https://doi.org/10.1038/s41467-025-59224-0.
[660] Yoon SG, Vishnugopi BS, Nelson DL, Yong AXB, Wang Y, Sandoval SE, et al. Interface morphogenesis with a deformable secondary phase in solid-state lithium batteries. Science 2025;388:1062–8. https://doi.org/10.1126/science.adt5229.
[661] Zhang W, Wang Z, Wan H, Li A-M, Liu Y, Liou S-C, et al. Revitalizing interphase in all-solid-state Li metal batteries by electrophile reduction. Nat Mater 2025;24:414–23. https://doi.org/10.1038/s41563-024-02064-y.
[662] Xu F, Wu Y, Wang L, Zhang Z, Liu G, Guo C, et al. Low-pressure Sulfide All-Solid-State Lithium-Metal Pouch Cell by Self-limiting Electrolyte Design. Adv Energy Mater 2025;15:2405369. https://doi.org/10.1002/aenm.202405369.
[663] Zou K, Deng W, Cai P, Deng X, Wang B, Liu C, et al. Prelithiation/Presodiation Techniques for Advanced Electrochemical Energy Storage Systems: Concepts, applications, and Perspectives. Adv Funct Mater 2020;31:2005581. https://doi.org/10.1002/adfm.202005581.
[664] Ham SY, Sebti E, Cronk A, Pennebaker T, Deysher G, Chen YT, et al. Overcoming low initial coulombic efficiencies of Si anodes through prelithiation in all-solid-state batteries. Nat Commun 2024;15:2991. https://doi.org/10.1038/s41467-024-47352-y.
[665] Yang Y, Wang J, Kim SC, Zhang W, Peng Y, Zhang P, et al. *In Situ* Prelithiation by Direct Integration of Lithium Mesh into Battery Cells. Nano Lett 2023;23:5042–7. https://doi.org/10.1021/acs.nanolett.3c00859.
[666] Lee J, Jin D, Kim JY, Roh Y, Lee H, Kang SH, et al. Dry Pre-Lithiation for Graphite-Silicon Diffusion-Dependent Electrode for All-Solid-State Battery. Adv Energy Mater 2023;13:2300172. https://doi.org/10.1002/aenm.202300172.
[667] Yang S-Y, Yue X-Y, Xia H-Y, Li X-L, Wang T, Li H, et al. Battery prelithiation enabled by lithium fixation on cathode. J Power Sources 2020;480:229109. https://doi.org/10.1016/j.jpowsour.2020.229109.
[668] Zhu Y, Chen Y, Chen J, Yin J, Sun Z, Zeng G, et al. Lattice Engineering on Li_2CO_3-based Sacrificial Cathode Prelithiation Agent for improving the Energy Density of Li-Ion Battery Full-Cell. Adv Mater 2024;36:2312159. https://doi.org/10.1002/adma.202312159.
[669] Lu J, Wang Y, Qiao Y, Yang S, Cheng X, Yang M, et al. A high-efficient stable surface-prelithiated $Li_{1.2}Ni_{0.13}Co_{0.13}Mn_{0.54}O_2$ cathode enabled by sacrificial lithium nitrides for high-energy-density lithium-ion batteries. Energy Storage Mater 2024;66:103204. https://doi.org/10.1016/j.ensm.2024.103204.
[670] Nam YJ, Oh DY, Jung SH, Jung YS. Toward practical all-solid-state lithium-ion batteries with high energy density and safety: Comparative study for electrodes fabricated by dry- and slurry-mixing processes. J Power Sources 2018;375:93–101. https://doi.org/10.1016/j.jpowsour.2017.11.031.
[671] Yao WL, Chouchane M, Li WK, Bai S, Liu Z, Li LT, et al. A 5 V-class cobalt-free battery cathode with high loading enabled by dry coating. Energy Environ Sci 2023;16:1620–30. https://doi.org/10.1039/d2ee03840d.
[672] Liu Y, Zhang R, Wang J, Wang Y. Current and future lithium-ion battery manufacturing. iScience 2021;24:102332. https://doi.org/10.1016/j.isci.2021.102332.
[673] Li YX, Wu YJ, Wang ZX, Xu JR, Ma TH, Chen LQ, et al. Progress in solvent-free dry-film technology for batteries and supercapacitors. Mater Today 2022;55:92–109. https://doi.org/10.1016/j.mattod.2022.04.008.
[674] Lu Y, Zhao CZ, Yuan H, Hu JK, Huang JQ, Zhang Q. Dry electrode technology, the rising star in solid-state battery industrialization. Matter 2022;5:876–98. https://doi.org/10.1016/j.matt.2022.01.011.

[675] Ludwig B, Zheng Z, Shou W, Wang Y, Pan H. Solvent-Free Manufacturing of Electrodes for Lithium-ion Batteries. Sci Rep 2016;6:23150. https://doi.org/10.1038/srep23150.
[676] Lee D, Shim Y, Kim Y, Kwon G, Choi SH, Kim K, et al. Shear force effect of the dry process on cathode contact coverage in all-solid-state batteries. Nat Commun 2024;15:4763. https://doi.org/10.1038/s41467-024-49183-3.
[677] Kim J-H, Kim N-Y, Ju Z, Hong Y-K, Kang K-D, Pang J-H, et al. Upscaling high-areal-capacity battery electrodes. Nat. Energy 2025;10:295–307. https://doi.org/10.1038/s41560-025-01720-0.
[678] Mun J, Song T, Park M-S, Kim JH. Paving the way for Next-Generation All-Solid-State Batteries: Dry Electrode Technology. Adv Mater 2025;2506123. https://doi.org/10.1002/adma.202506123.
[679] Sun H, Zhu J, Baumann D, Peng L, Xu Y, Shakir I, et al. Hierarchical 3D electrodes for electrochemical energy storage. Nat Rev Mater 2019;4:45–60. https://doi.org/10.1038/s41578-018-0069-9.
[680] Lv Z, Liu J, Li C, Peng J, Zheng C, Zheng X, et al. High-areal-capacity all-solid-state Li-S battery enabled by dry process technology. eTransportation 2024;19:100298. https://doi.org/10.1016/j.etran.2023.100298.
[681] Lee DJ, Jeon Y, Lee J-P, Zhang L, Koh KH, Li F, et al. Robust interface and reduced operation pressure enabled by co-rolling dry-process for stable all-solid-state batteries. Nat Commun 2025;16:4200. https://doi.org/10.1038/s41467-025-59363-4.
[682] Oh H, Kim G-S, Bang J, Kim S, Jeong K-M. Dry-processed thick electrode design with a porous conductive agent enabling 20 mA h cm^{-2} for high-energy-density lithium-ion batteries. Energy Environ Sci 2025;18:645–58. https://doi.org/10.1039/D4EE04106B.
[683] Oh J, Choi SH, Kim H, Chung WJ, Kim M, Kim I, et al. Solvent–Binder Engineering for a Practically Viable solution Process for Fabricating Sulfide-based All-Solid-State Batteries. ACS Energy Lett 2025;10:2831–8. https://doi.org/10.1021/acsenergylett.5c00762.
[684] Hu L, Ren Y, Wang C, Li J, Wang Z, Sun F, et al. Fusion Bonding Technique for Solvent-Free Fabrication of All-Solid-State Battery with Ultrathin Sulfide Electrolyte. Adv Mater 2024;36:2401909. https://doi.org/10.1002/adma.202401909.
[685] Rosner M, Cangaz S, Dupuy A, Hippauf F, Dörfler S, Abendroth T, et al. Toward Higher Energy Density All-Solid-State Batteries by production of Freestanding Thin Solid Sulfidic Electrolyte Membranes in a Roll-to-Roll Process. Adv Energy Mater 2025;15:2404790. https://doi.org/10.1002/aenm.202404790.
[686] Wei L, Feng Y, Ge S, Liu S, Ma Y, Yan J. Three-Dimensionally Printed Ionogel-Coated Ceramic Electrolytes for Solid-State Lithium Batteries. ACS Nano 2025;19:5789–800. https://doi.org/10.1021/acsnano.4c17761.
[687] Wu Y, Wang K, Liu K, Long Y, Yang C, Zhang H, et al. Rapid Processing of Uniform, thin, Robust, and Large-Area Garnet Solid Electrolyte by Atmospheric Plasma Spraying. Adv Energy Mater 2023;13:2300809. https://doi.org/10.1002/aenm.202300809.
[688] Wang C, Ping W, Bai Q, Cui H, Hensleigh R, Wang R, et al. A general method to synthesize and sinter bulk ceramics in seconds. Science 2020;368:521–6. https://doi.org/10.1126/science.aaz7681.
[689] Song J, Shang W, Zhou W, Li J, Wu X, Li W, et al. From issues to solutions: 3D printing for overcoming challenges in liquid- and solid-state batteries. Energy Storage Mater 2025;79:104342. https://doi.org/10.1016/j.ensm.2025.104342.
[690] Tan DHS, Banerjee A, Chen Z, Meng YS. From nanoscale interface characterization to sustainable energy storage using all-solid-state batteries. Nat Nanotechnol 2020;15:170–80. https://doi.org/10.1038/s41565-020-0657-x.
[691] Dixit M, Beamer C, Amin R, Shipley J, Eklund R, Muralidharan N, et al. The Role of Isostatic Pressing in Large-Scale production of Solid-State Batteries. ACS Energy Lett 2022;7:3936–46. https://doi.org/10.1021/acsenergylett.2c01936.
[692] Futscher MH, Brinkman L, Müller A, Casella J, Aribia A, Romanyuk YE. Monolithically-stacked thin-film solid-state batteries Commun Chem 2023;6:110. https://doi.org/10.1038/s42004-023-00901-w.
[693] Wang Y, Li Z, Li X, Ma ZF, Li L. Catalyzing Battery Materials Research via Lab-Made, Sub-Ampere-Hour-Scale Pouch Cells, and Long-Term Electrochemical monitoring by a Reparable Reference Electrode. Adv Energy Mater 2024;14:2304512. https://doi.org/10.1002/aenm.202304512.
[694] Wu B, Yang Y, Liu D, Niu C, Gross M, Seymour L, et al. Good Practices for Rechargeable Lithium Metal Batteries. J Electrochem Soc 2019;166:A4141–9. https://doi.org/10.1149/2.0691916jes.
[695] Pang M-C, Wei Y, Wang H, Marinescu M, Yan Y, Offer GJ. Large-Format Bipolar and Parallel Solid-State Lithium-Metal Cell Stacks: a Thermally coupled Model-based Comparative Study. J Electrochem Soc 2020;167:160555. https://doi.org/10.1149/1945-7111/abd493.
[696] Schnell J, Günther T, Knoche T, Vieider C, Köhler L, Just A, et al. All-solid-state lithium-ion and lithium metal batteries – paving the way to large-scale production. J Power Sources 2018;382:160–75. https://doi.org/10.1016/j.jpowsour.2018.02.062.
[697] Jung K-N, Shin H-S, Park M-S, Lee J-W. Solid-State Lithium Batteries: Bipolar Design, Fabrication, and Electrochemistry. ChemElectroChem 2019;6:3842–59. https://doi.org/10.1002/celc.201900736.
[698] Ahmad N, Sun S, Yu P, Yang W. Design Unique Air-Stable and Li–Metal Compatible Sulfide Electrolyte via Exploration of Anion Functional units for All-Solid-State Lithium–Metal Batteries. Adv Funct Mater 2022;32:2201528. https://doi.org/10.1002/adfm.202201528.
[699] Liu X, Liang Z, Xiang Y, Lin M, Li Q, Liu Z, et al. Solid-State NMR and MRI Spectroscopy for Li/Na Batteries: Materials, Interface, and In Situ Characterization. Adv Mater 2021;33:2005878. https://doi.org/10.1002/adma.202005878.
[700] Sun X, Stavola AM, Cao D, Bruck AM, Wang Y, Zhang Y, et al. Operando EDXRD Study of All-Solid-State Lithium Batteries Coupling Thioantimonate Superionic Conductors with Metal Sulfide. Adv Energy Mater 2021;11:2002861. https://doi.org/10.1002/aenm.202002861.
[701] Zheng B, Liu X, Zhu J, Zhao J, Zhong G, Xiang Y, et al. Unraveling (electro)-chemical stability and interfacial reactions of $Li_{10}SnP_2S_{12}$ in all-solid-state Li batteries. Nano Energy 2020;67:104252. https://doi.org/10.1016/j.nanoen.2019.104252.
[702] Bron P, Dehnen S, Roling B. $Li_{10}Si_{0.3}Sn_{0.7}P_2S_{12}$ – a low-cost and low-grain-boundary-resistance lithium superionic conductor. J Power Sources 2016;329:530–5. https://doi.org/10.1016/j.jpowsour.2016.08.115.
[703] Zheng J, Tang M, Hu YY. Lithium Ion Pathway within $Li_7La_3Zr_2O_{12}$-Polyethylene Oxide Composite Electrolytes. Angew Chem Int Ed Engl 2016;55:12538–42. https://doi.org/10.1002/anie.201607539.
[704] Wu N, Chien PH, Qian Y, Li Y, Xu H, Grundish NS, et al. Enhanced Surface Interactions Enable Fast Li^+ Conduction in Oxide/Polymer Composite Electrolyte. Angew Chem Int Ed Engl 2020;59:4131–7. https://doi.org/10.1002/anie.201914478.
[705] Xu H, Chien PH, Shi J, Li Y, Wu N, Liu Y, et al. High-performance all-solid-state batteries enabled by salt bonding to perovskite in poly(ethylene oxide). PNAS 2019;116:18815–21. https://doi.org/10.1073/pnas.1907507116.
[706] Wang C, Liang J, Zhao Y, Zheng M, Li X, Sun X. All-solid-state lithium batteries enabled by sulfide electrolytes: from fundamental research to practical engineering design. Energy Environ Sci 2021;14:2577–619. https://doi.org/10.1039/D1EE00551K.
[707] Lu X, Bertei A, Finegan DP, Tan C, Daemi SR, Weaving JS, et al. 3D microstructure design of lithium-ion battery electrodes assisted by X-ray nano-computed tomography and modelling. Nat Commun 2020;11:2079. https://doi.org/10.1038/s41467-020-15811-x.
[708] Lewis JA, Cortes FJQ, Liu Y, Miers JC, Verma A, Vishnugopi BS, et al. Linking void and interphase evolution to electrochemistry in solid-state batteries using operando X-ray tomography. Nat Mater 2021;20:503–10. https://doi.org/10.1038/s41563-020-00903-2.
[709] Hu J, Sun Z, Gao Y, Li P, Wu Y, Chen S, et al. 3D stress mapping reveals the origin of lithium-deposition heterogeneity in solid-state lithium-metal batteries. Cell Rep Phys Sci 2022;3:100938. https://doi.org/10.1016/j.xcrp.2022.100938.
[710] Wang Z, Santhanagopalan D, Zhang W, Wang F, Xin HL, He K, et al. In Situ STEM-EELS Observation of Nanoscale Interfacial Phenomena in All-Solid-State Batteries. Nano Lett 2016;16:3760–7. https://doi.org/10.1021/acs.nanolett.6b01119.
[711] Santhanagopalan D, Qian D, McGilvray T, Wang Z, Wang F, Camino F, et al. Interface Limited Lithium Transport in Solid-State Batteries. J Phys Chem Lett 2014;5:298–303. https://doi.org/10.1021/jz402467x.
[712] Walther F, Koerver R, Fuchs T, Ohno S, Sann J, Rohnke M, et al. Visualization of the Interfacial Decomposition of Composite Cathodes in Argyrodite-based All-Solid-State Batteries using Time-of-Flight Secondary-Ion Mass Spectrometry. Chem Mater 2019;31:3745–55. https://doi.org/10.1021/acs.chemmater.9b00770.
[713] Cheng D, Wynn TA, Wang X, Wang S, Zhang M, Shimizu R, et al. Unveiling the Stable Nature of the Solid Electrolyte Interphase between Lithium Metal and LiPON via Cryogenic Electron Microscopy. Joule 2020;4:2484–500. https://doi.org/10.1016/j.joule.2020.08.013.

[714] Luo S, Liu X, Zhang X, Wang X, Wang Z, Zhang Y, et al. Nanostructure of the Interphase Layer between a Single Li Dendrite and Sulfide Electrolyte in All-Solid-State Li Batteries. ACS Energy Lett 2022;7:3064–71. https://doi.org/10.1021/acsenergylett.2c01543.
[715] Yu C, Ganapathy S, de Klerk NJ, Roslon I, van Eck ER, Kentgens AP, et al. Unravelling Li-Ion Transport from Picoseconds to seconds: Bulk versus Interfaces in an Argyrodite Li_6PS_5Cl-Li_2S All-Solid-State Li-Ion Battery. J Am Chem Soc 2016;138:11192–201. https://doi.org/10.1021/jacs.6b05066.
[716] Yu C, Ganapathy S, Eck E, Wang H, Basak S, Li Z, et al. Accessing the bottleneck in all-solid state batteries, lithium-ion transport over the solid-electrolyte-electrode interface. Nat Commun 2017;8:1086. https://doi.org/10.1038/s41467-017-01187-y.
[717] Dixit MB, Regala M, Shen F, Xiao X, Hatzell KB. Tortuosity Effects in Garnet-Type $Li_7La_3Zr_2O_{12}$ Solid Electrolytes. ACS Appl Mater Interfaces 2019;11:2022–30. https://doi.org/10.1021/acsami.8b16536.
[718] Tippens J, Miers JC, Afshar A, Lewis JA, Cortes FJQ, Qiao H, et al. Visualizing Chemomechanical Degradation of a Solid-State Battery Electrolyte. ACS Energy Lett 2019;4:1475–83. https://doi.org/10.1021/acsenergylett.9b00816.
[719] Zheng G, Lee SW, Liang Z, Lee HW, Yan K, Yao H, et al. Interconnected hollow carbon nanospheres for stable lithium metal anodes. Nat Nanotechnol 2014;9:618–23. https://doi.org/10.1038/nnano.2014.152.
[720] Zhao CZ, Zhang XQ, Cheng XB, Zhang R, Xu R, Chen PY, et al. An anion-immobilized composite electrolyte for dendrite-free lithium metal anodes. PNAS 2017;114:11069–74. https://doi.org/10.1073/pnas.1708489114.
[721] Yan K, Lu Z, Lee H-W, Xiong F, Hsu P-C, Li Y, et al. Selective deposition and stable encapsulation of lithium through heterogeneous seeded growth. Nat Energy 2016;1:16010. https://doi.org/10.1038/nenergy.2016.10.
[722] Wang C, Gong Y, Dai J, Zhang L, Xie H, Pastel G, et al. *In Situ* Neutron Depth Profiling of Lithium Metal-Garnet Interfaces for Solid State Batteries. J Am Chem Soc 2017;139:14257–64. https://doi.org/10.1021/jacs.7b07904.
[723] Harry KJ, Hallinan DT, Parkinson DY, MacDowell AA, Balsara NP. Detection of subsurface structures underneath dendrites formed on cycled lithium metal electrodes. Nat Mater 2014;13:69–73. https://doi.org/10.1038/nmat3793.
[724] Ning Z, Jolly DS, Li G, De Meyere R, Pu SD, Chen Y, et al. Visualizing plating-induced cracking in lithium-anode solid-electrolyte cells. Nat Mater 2021;20:1121–9. https://doi.org/10.1038/s41563-021-00967-8.
[725] Li Y, Li Y, Pei A, Yan K, Sun Y, Wu C-L, et al. Atomic structure of sensitive battery materials and interfaces revealed by cryo–electron microscopy. Science 2017;358:506–10. https://doi.org/10.1126/science.aam6014.
[726] Zhang X-S, Wan J, Shen Z-Z, Lang S-Y, Xin S, Wen R, et al. *In Situ* Analysis of Interfacial Morphological and Chemical Evolution in All-Solid-State Lithium-Metal Batteries. Angew Chem Int Ed 2024;63:e202409435. https://doi.org/10.1002/anie.202409435.
[727] Ishigaki M, Ishikawa K, Usuki T, Kondo H, Komagata S, Sasaki T. Operando Li metal plating diagnostics via MHz band electromagnetics. Nat Commun 2023;14:7275. https://doi.org/10.1038/s41467-023-43138-w.
[728] Carreon Ruiz ER, Lee J, Strobl M, Stalder N, Burca G, Gubler L, et al. Revealing the impact of temperature in battery electrolytes via wavelength-resolved neutron imaging. Sci Adv 2023;9:eadi0586. https://doi.org/10.1126/sciadv.adi0586.
[729] Darmet N, Charbonnel J, Reytier M, Broche L, Vincent R. First Experimental Assessment of All-Solid-State Battery thermal Runaway Propagation in a Battery Pack. ACS Appl Energy Mater 2024;7:4365–75. https://doi.org/10.1021/acsaem.4c00248.
[730] Yang R, Xie Y, Li K, Li W, Hu X, Fan Y, et al. Thermal characteristics of solid-state battery and its thermal management system based on flat heat pipe. Appl Therm Eng 2024;252:123575. https://doi.org/10.1016/j.applthermaleng.2024.123575.
[731] Deng Z, Huang Z, Shen Y, Huang Y, Ding H, Luscombe A, et al. Ultrasonic Scanning to Observe Wetting and "Unwetting" in Li-Ion Pouch Cells. Joule 2020;4:2017–29. https://doi.org/10.1016/j.joule.2020.07.014.
[732] Huo H, Huang K, Luo W, Meng J, Zhou L, Deng Z, et al. Evaluating Interfacial Stability in Solid-State Pouch Cells via Ultrasonic Imaging. ACS Energy Lett 2022;7:650–8. https://doi.org/10.1021/acsenergylett.1c02363.
[733] Jaguemont J, Bardé F. A critical review of lithium-ion battery safety testing and standards. Appl Therm Eng 2023;231:121014. https://doi.org/10.1016/j.applthermaleng.2023.121014.
[734] Liu Y, Li Y, Liao YG, Lai M-C. Effects of State-of-Charge and Penetration Location on Variations in Temperature and Terminal Voltage of a Lithium-Ion Battery Cell during Penetration Tests. Batteries 2021;7:81. https://doi.org/10.3390/batteries7040081.
[735] Zhang G, Wei X, Tang X, Zhu J, Chen S, Dai H. Internal short circuit mechanisms, experimental approaches and detection methods of lithium-ion batteries for electric vehicles: a review. Renew Sustain Energy Rev 2021;141:110790. https://doi.org/10.1016/j.rser.2021.110790.
[736] Ahuis M, Doose S, Vogt D, Michalowski P, Zellmer S, Kwade A. Recycling of solid-state batteries. Nat. Energy 2024;9:373–85. https://doi.org/10.1038/s41560-024-01463-4.
[737] Jacob M, Wissel K, Clemens O. Recycling of solid-state batteries—challenge and opportunity for a circular economy? Mater Futures 2024;3:012101. https://doi.org/10.1088/2752-5724/acfb28.
[738] Duffner F, Kronemeyer N, Tübke J, Leker J, Winter M, Schmuch R. Post-lithium-ion battery cell production and its compatibility with lithium-ion cell production infrastructure. Nat Energy 2021;6:123–34. https://doi.org/10.1038/s41560-020-00748-8.
[739] Kong L, Wang L, Zhu J, Bian J, Xia W, Zhao R, et al. Configuring solid-state batteries to power electric vehicles: a deliberation on technology, chemistry and energy. Chem Commun 2021;57:12587–94. https://doi.org/10.1039/d1cc04368d.
[740] Thomas F, Mahdi L, Lemaire J, Santos DMF. Technological advances and Market Developments of Solid-State Batteries: a Review. Materials 2024;17:239. https://doi.org/10.3390/ma17010239.
[741] Rodrigues M-T-F, Babu G, Gullapalli H, Kalaga K, Sayed FN, Kato K, et al. A materials perspective on Li-ion batteries at extreme temperatures. Nat. Energy 2017;2:17108. https://doi.org/10.1038/nenergy.2017.108.
[742] Lu P, Zhou Z, Xiao Z, Lu J, Zhang J, Hu G, et al. Materials and chemistry design for low-temperature all-solid-state batteries. Joule 2024;8:635–57. https://doi.org/10.1016/j.joule.2024.01.027.
[743] Tan DHS, Meng YS, Jang J. Scaling up high-energy-density sulfidic solid-state batteries: a lab-to-pilot perspective. Joule 2022;6:1755–69. https://doi.org/10.1016/j.joule.2022.07.002.